Deformation mechanisms and inter-granular stresses in Zircaloy-4 and Zr-2.5%Nb

Thesis

UNRESTRICTED

Deformation Mechanisms and Inter-Granular Stresses in Zircaloy-4 and Zr-2.5%Nb

A thesis submitted to The Open University for the degree of Doctor of Philosophy in the Faculty of Maths, Computing and Technology

by

Olivier Zanellato

Submission date: 22nd June 2009
Date of award: 17th September 2009

Abstract

Zirconium alloys have interesting properties for structural applications in the core of a nuclear reactor: they are transparent to neutrons and have good mechanical and corrosion properties. Zircaloy-4 is used for tube cladding or pressure vessels while the main application of Zr2.5%Nb is pressure tubes. However the crystal structure of the dominant phase at room temperature is hexagonal close packed (hcp) and shows a very strong thermo-mechanical anisotropy that can affect the deformation behaviour of a polycrystal aggregate and give rise to intergranular stresses. It is particularly important to understand the deformation mechanisms at the microscopic length-scale both for processing optimisation and for service life predictions and improvements.

This thesis presents the results of compression tests preformed in-situ in a neutron diffractometer so as to determine grains and aggregate behaviours. The analysis shows that there is a strong anisotropy in the response at both the microscopic and macroscopic levels. An elasto-plastic self consistent model is also implemented to try to reproduce these results and determine values for the laws that describe the deformation mechanisms.

The study of the deformation mechanisms is also complemented by an analysis of texture evolution during deformation. This analysis is particularly successful for evaluating the volume fraction of twinning during deformation.

ALL
MISSING
PAGES ARE
BLANK

Acknowledgements

During the last three and a half years I have had the privilege of meeting a number of people that supported me in my studies and from whom I have learnt a lot. Please forgive the length of this acknowledgement but, in a selfish way, I am writing this page essentially for myself rather than anybody else: it is a way of remembering who I owe to be where I am now and that I wouldn't have made it on my own. I would like to first thank my supervisors: Lyndon for giving me a great start in my PhD activities, Mike for your great help and your encouragements at all levels and Mark for joining the supervising team and providing a valuable expertise on the topic. I am grateful for the incredible opportunities you have given me. Besides my supervisors, there have been key figures that shaped the course of my studies: Javier Santisteban (thanks for taking the time to share your knowledge and company), Ondrej Muransky (I enjoy the frankness and openness of our discussions), Ed Oliver (you have been an outstanding instrument scientist and inspiration). I would like to thank also Dr. Carlos Tomé for sharing the EPSC code and for the helpful discussions at conferences, Dr. Sven Vogel for the neutron texture measurements and helping with the analysis, and the other instrument scientists I have had the privilege of working with (Ania Paradowska, Darren Hugh, Shu Yan Zhang...).

The people in the department of materials engineering were fabulous. I had a great time with my office mates Jeffrey, David and Boon (good work and good laughs). I can't forget the friendships built with Sumit, Moshiur, Mulyadi, João, Mehmet, Himanshu, Ashwin, Supriyo, Murat, Kashif, Shiv, Sue, Bama, Asim, Burak... The technicians Pete, Stan and Gordon were also fantastic to help me carry out my work.

I was fortunate enough to have an active life outside university thanks to friends such as Swarup, Evelyn, Shon and Kim, Liezel, Anish and Sanjana, Cobus and Ulrike and the rest of the famous 'Boycott Beavers', Hmad and Hannah and the small group, the music team

at MKCC... And my "far from the eyes, close to the heart" friends: Etienne, Cris, Tim, Matthieu, Luc, Rémi...

My family deserves all my gratitude for their support despite the distance.

Finally I want to thank God for his faithfulness.

Table of contents

Table of Figures

Chapter 1 Introduction

1.1 Background on the use of Zr alloys

The potential of zirconium for nuclear structural applications was discovered in the late 1950s. The most attractive property of pure Zr for non-nuclear applications is certainly its excellent corrosion resistance. A major breakthrough for nuclear applications was when hafnium, which is highly neutron absorbent, could be removed from raw zirconium: pure zirconium is very transparent to neutrons, but the two elements naturally occur together. Pure Zr is also moderately stiff at room temperature (Young's modulus of around 100GPa) and with small alloying additions, its mechanical properties are comparable to steels. This is the final major asset of Zr: without compromising too much on the neutron absorption quality and the corrosion properties by the addition of alloying elements, the gains in terms of strength and ductility are significant and very satisfying for structural applications.

Since these discoveries have been made, several zirconium alloys have been developed to be used in the core of nuclear reactors. Since this environment is very harsh, their corrosion resistance is very much appreciated. Because of the low neutron absorption property, they can be used for fuel cladding, fuel rods and pressure tubes – components within the heart of the operating reactor - without impairing or reducing the efficiency of the nuclear reaction by stopping neutrons travelling from one fuel assembly to the other. Finally the mechanical properties are a crucial aspect for manufacturability and structural integrity.

1.2 Scope of the thesis

The crystal structure of zirconium is hexagonal close packed (hcp) at room temperature. This arrangement has low symmetry and is very anisotropic: the response of the crystal under an external load (mechanical or thermal) varies significantly according to the direction considered. This anisotropy is seen in both thermal and mechanical properties. As a result, in polycrystals, the behaviour of the grains will change according to their crystalline orientation relative to the applied load. A direct consequence is that the material is not homogeneous: under thermal or mechanical loads, each grain will have its own orientation dependant response, which is a priori different from its neighbouring grain. A critical outcome is that some strain misfit can easily arise between the grains. These intergranular strains are potentially high enough to compromise the structural integrity of components. They can act as manufacturing pre-strains which superimpose on the service loading and can be responsible for unexpected failures. In the harsh environment of the core of a nuclear reactor, they can be catalysts for chemically induced embrittlement: for example, it is well known that in zirconium alloys, hydrogen segregates in zones of higher stresses to precipitate and form brittle hydrides. A literature review of the mechanisms responsible for the crystal anisotropy in Zr alloys will be presented in Chapter 2. We will study experimentally the development of these intergranular misfits under applied load (Chapter 5). The experiments are based on neutron diffraction measurements performed during the deformation process, and the technique is explained in Chapter 2.

Nowadays neutron and X-ray diffraction are used extensively for the measurement of residual stresses for structural integrity purposes. However the techniques probe grain family strains which are actually a superposition of macroscopic and microscopic average strains. In general microscopic strains are neglected and the measurement is assumed to represent solely macroscopic misfits. This is not true for highly anisotropic materials such as Zr alloys and the assumption can lead to over or under estimations of the strain the

material is experiencing. Understanding the development of the intergranular misfit can help deconvolute macroscopic and microscopic strains in a diffraction measurement.

Another reason for studying the anisotropy of zirconium alloys is to help in defining manufacturing processes that would reduce the amount of intergranular stresses.

The grain level response and the development of intergranular stresses in a case as simple as uniaxial loading already involve complex mechanisms: the problem is not uniaxial at the grain level but can be very much three dimensional given the neighbouring constraints. Understanding the intergranular strain development therefore provides insight into the deformation modes (e.g. slip systems) operating. The relationships between the operating deformation mode and intergranular strain development are not straightforward, however, and can most readily be studied through the use of models.

Modelling the behaviour is however no trivial task. Some models have been developed to simulate thermo-mechanical loading situations, as explained in Chapter 2. A model has been used in Chapter 6 and has been compared with the diffraction experimental results.

In order to link the crystal behaviour and the macroscopic response, it is necessary to know how the crystallites are organized in terms of their orientation in a statistical way. Hence texture information is the building block of the bridge between the different length scales (details about texture are provided in Chapter 2). The texture measurements performed on the materials studied in this thesis (Zircaloy-4 and Zr-2.5%Nb) are presented in Chapter 4 with the results incorporated into the subsequent modelling.

The deformation mechanisms operating can also affect the development of texture. Thus looking at the texture changes during deformation gives valuable information about these mechanisms as shown in the experimental work presented in Chapter 7.

Chapter 2 Experimental methods

In this chapter I will describe the different basic tools and concepts used in the rest of the thesis. In the first part I will focus on measurements of elastic strains with diffraction techniques, then I will develop the idea of texture in polycrystalline materials and describe some of the measurement methods. The last part of this chapter deals with self-consistent modelling.

2.1 Diffraction elastic strains

2.1.1 Principle

In crystalline materials, if a stress field is applied, the atoms tend to displace in an elastic manner relative to each other. The displacements are proportional to the stress applied to the given crystal, so if one had a tool for probing these atomic displacements, one could derive the elastic strain and ultimately the stress state in the measurement direction. Such a tool exists in terms of the diffraction of waves with wavelengths of the order of the atomic distances.

With diffraction techniques we are actually able to measure the absolute atomic spacings in the crystal. This is a particular use of Bragg's law, which states that diffraction can happen on a crystalline arrangement of atoms bombarded by a beam of X-rays or neutrons (or other wave) only if a set of conditions is fulfilled. They are usually referred to as Bragg's conditions. An important condition for our purposes is that the angle of diffraction θ, the wavelength of the diffracted beam λ and the atomic spacing in the measurement direction (or planar spacing) d must be linked by the relationship:

$$n.\lambda = 2.d.\sin\theta \qquad \textit{Eq. 1}$$

In other words once two variables are known the third one is available by means of Bragg's equation. Our interest is to set up experiments where Bragg's conditions are fulfilled and deduce the inter-planar spacing from measurements of the wavelength at a given diffraction angle. If a reference atomic spacing is available it is then easy to compute a value of elastic strain based on the change in atomic spacing.

There are actually two main ways of carrying out a diffraction experiment depending which parameter in Bragg's equation is fixed by the instrumental set up and which is measured. In both cases, as one parameter is fixed and the other measured, the atomic spacing (third variable in Bragg's equation) is resolved. If the incoming beam is monochromatic (wavelength fixed) the instrument will measure the angular position of the diffracted beam; if the beam is 'white', the instrument will probe the wavelength of the diffracted beam at a given angle. The latter method is usually more advantageous for the diffraction of polycrystals or powders: the detectors can usually collect neutrons or photons with a large range of wavelength, so several diffraction peaks can be collected at once. On the other hand where the wavelength is fixed, most detectors collect data over a small portion of the diffraction angle range and few peaks are available. Moreover with such angle-dispersive methods, the spectrum is physically limited to diffraction angles θ between 0° and 90° for a fixed wavelength. As a result only a limited number of diffraction peaks can be observed even with a detector covering the whole 2θ space. With wavelength-dispersive techniques, it is theoretically possible to access all the diffraction peaks.

2.1.2 Diffraction from a perfect crystal

We will look at diffraction between photons (X-rays) or neutron waves on the atomic lattice. As diffraction is a case of constructive interference, two conditions are to be fulfilled: the waves must be coherent and they must be in phase.

Let's consider a monochromatic X-ray beam of wavelength λ striking an atom. A photon arriving on the atom will generally interact with its electrons and be deflected in any direction. Two types of collisions are possible [1]. If there has been a momentum transfer, we talk about inelastic scattering and the wavelength is increased because of the loss of energy. If the collision is elastic (no momentum transfer), the scattered ray has the same wavelength λ. Only the latter case can lead to a diffraction pattern and from now on, we will only consider this kind of coherent elastic scattering.

Let's now consider a row of atoms irradiated by the same X-ray beam. As seen before, each atom scatters in all directions and sometimes coherently. The waves coherently scattered from different atoms can interfere constructively only if they are in phase, i.e. the difference of path lengths is proportional to λ. Figure 1 shows a row of atoms hit by an X-ray beam.

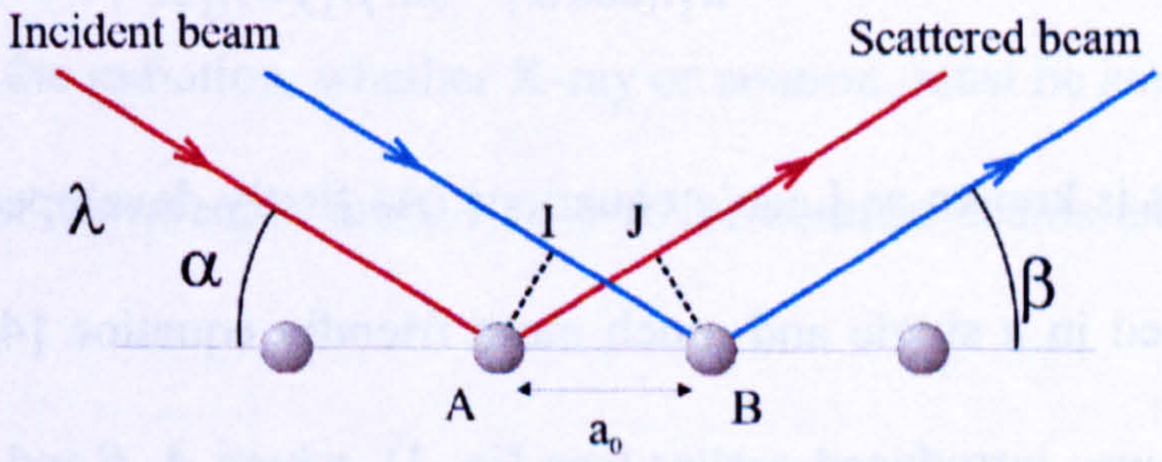

Figure 1 *Conditions for diffraction on a row of atoms*

The scattered beams are in phase if Eq. 2 is fulfilled, where the integer h represents the order of diffraction:

Eq. 2 $$IB - AJ = a_0.(\cos\alpha - \sin\beta) = h.\lambda$$

The row of atoms diffracts a set of diffraction cones with different apertures for each order of diffraction *h* (Figure 2).

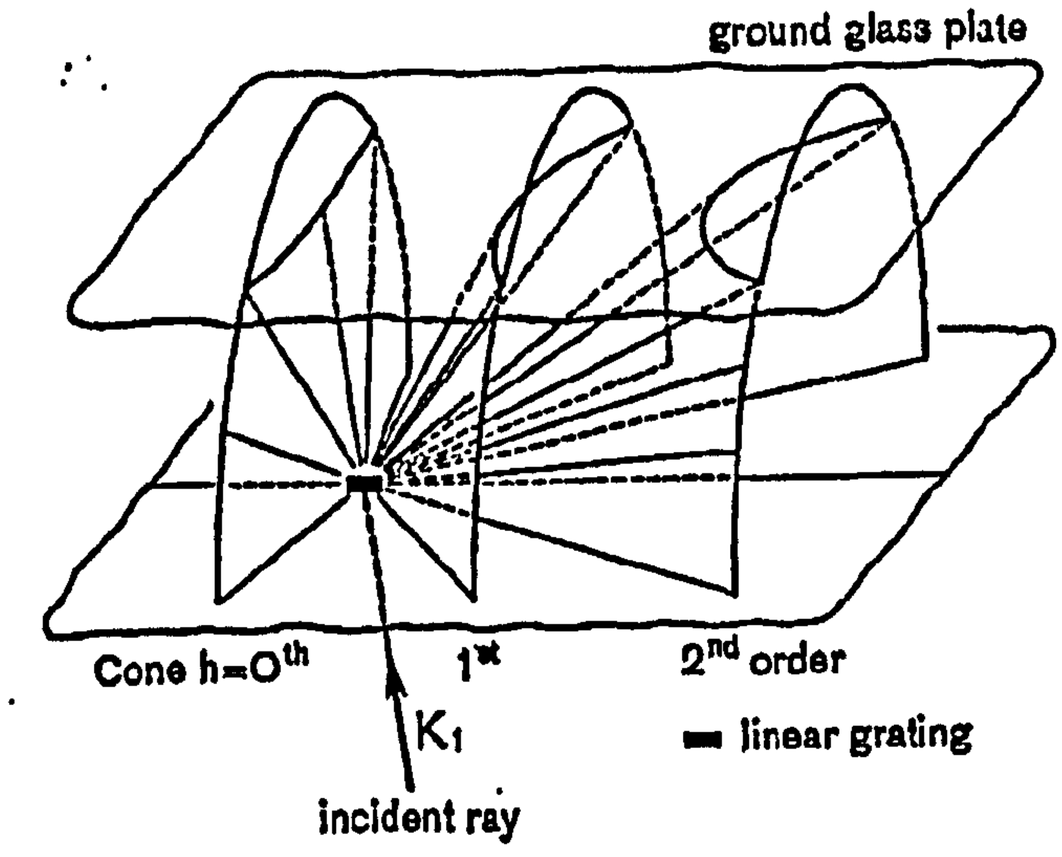

Figure 2 *Diffraction cones from a row of atoms [2]*

Any crystal can be considered as an arrangement of rows of atoms in the three directions of space. Diffraction occurs when Eq. 2 is fulfilled in the three crystallographic directions $\mathbf{a_1}$, $\mathbf{a_2}$, $\mathbf{a_3}$ simultaneously, i.e. when the following system is fulfilled:

$$\text{Eq. 3} \qquad \begin{aligned} a_1.(\cos\alpha_1 - \sin\beta_1) &= h_1.\lambda \\ a_2.(\cos\alpha_2 - \sin\beta_2) &= h_2.\lambda \\ a_3.(\cos\alpha_3 - \sin\beta_3) &= h_3.\lambda \end{aligned}$$

This set of equations is known as Laue's equations. As firstly developed by Bragg [3] the system can be derived in a single and much more friendly equation [4] called the Bragg equation and which was introduced earlier (see Eq. 1), where d, θ and n are respectively the interplanar spacing, the diffraction angle and the order of diffraction (Figure 3). The derivation of Bragg's equation is accompanied by some geometric conditions: the incident and diffracted beams are in the same plane and both form an angle θ with the diffraction planes. Those conditions and the equation compose what is called Bragg's law. One can

note that the geometry has strong similarities with a simple reflection on the diffraction planes.

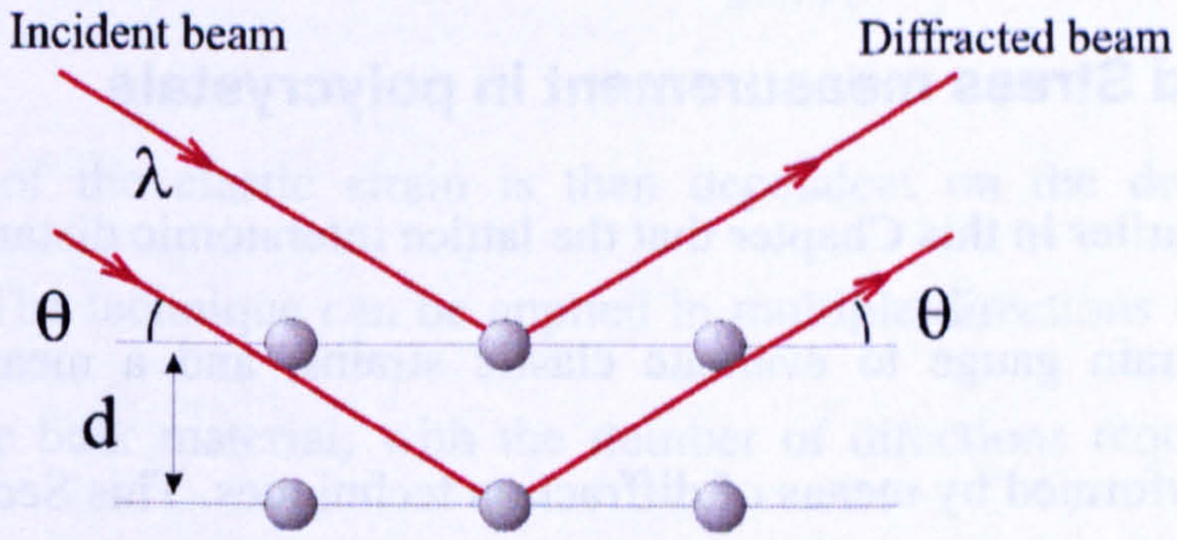

Figure 3 *Bragg's law geometry in the plane of diffraction*

Bragg's law defines the conditions of diffraction of X-rays on a single crystal, but it can be easily extended to neutron radiation [5]. While photons are mainly scattered by the outer electron shell, the scattering sites of neutrons are the atom nuclei [6]. Apart from that, the Laue's equations and Bragg's law are derived similarly.

There are some restrictions on the wavelength for diffraction to occur. By some simple operations on Eq. 1, we have the inequality:

Eq. 4
$$\lambda = \frac{2.d.\sin\theta}{n} \leq \frac{2.d}{n} \leq 2d$$

The wavelength of the radiation, whether X-ray or neutron, must be smaller than two times *d*. Typical ranges of wavelength are 0.1 to 4 Å for neutron beams and 0.06 to 0.2 Å for high energy X-rays.

2.1.3 Diffraction on polycrystals

Powders and polycrystals are composed of many crystallites with different orientations. As a result there are more geometrical opportunities for diffraction to happen than in a single crystal. Usually an incident beam can be diffracted by several crystallites for which

Bragg's law is satisfied. The observed diffraction peak will then be obtained from that subset of the crystallites that are suitably oriented for that particular diffraction condition.

2.1.4 Strain and Stress measurement in polycrystals

I have mentioned earlier in this Chapter that the lattice interatomic distances can be used as an atomic scale strain gauge to evaluate elastic strains, and a measurement of these distances can be performed by means of diffraction techniques. This Section develops how this can be done.

2.1.4.a Strain measurement

Amongst a lot of applications, diffraction techniques have proved to be particularly valuable for local strain field determination in crystalline materials. Let's consider a set of atomic planes in a stress free crystal and call d_0 their d-spacing. A monochromatic beam of wavelength λ hits the planes to be diffracted with a Bragg's angle θ_0 (Figure 4(a)).

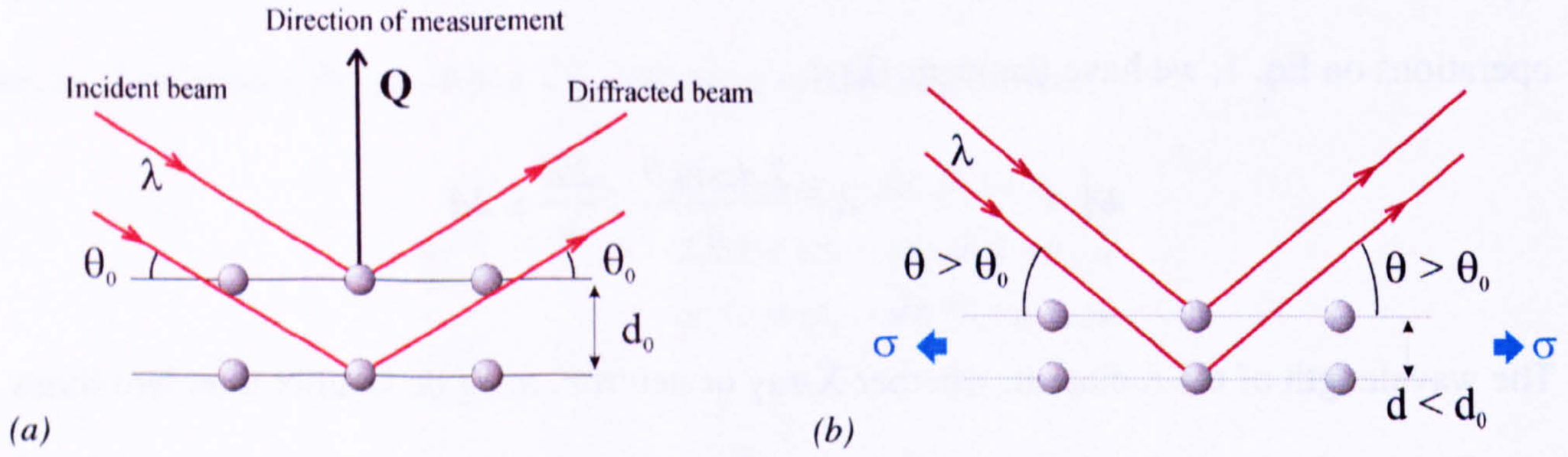

Figure 4 *Diffraction (a) on a stress-free and (b) on a stressed material*

When the material is subjected to a stress field, the atoms are elastically displaced (Figure 4 (b)). This displacement manifests itself by a change in d-spacing which can be derived in local elastic strain in the measurement direction **Q**:

Eq. 5
$$\varepsilon_Q^{elast.} = \frac{d - d_0}{d_0}$$

Assuming that Bragg's law is still fulfilled, measuring the new diffraction angle θ is a way of obtaining the d-spacing and from Bragg's equation:

$$d = \frac{n.\lambda}{2.\sin\theta} \qquad \textit{Eq. 6}$$

The computation of the elastic strain is then dependent on the determination of the diffraction angle. The technique can be applied in multiple directions to obtain the whole strain tensor in the bulk material, with the number of directions required for the whole tensor dependent on the symmetry.

2.1.4.b Stress derivation

For most materials used, the elastic strain is linked to the local stress by a linear relationship called Hooke's law:

$$\sigma_{ij} = \sum_{kl} C_{ijkl} \varepsilon_{kl}^{elast.} \qquad \textit{Eq. 7}$$

Where (σ_{ij}) and (ε^{e}_{ij}) are the local stress and elastic strain tensors and (C_{ijkl}) is the stiffness tensor which contains the elastic coefficients. Knowing the elastic strain field from diffraction, stresses are easily computed.

The derivation described above is generally used for computing macroscopic stresses from the diffraction elastic strains (for residual stress measurements for example). However it is not strictly true in the sense that it does not discriminate between the local and the macroscopic stress states. The formulation is valid only for perfectly homogeneous materials where macroscopic and microscopic entities can be interchanged. For crystalline materials with small crystal anisotropy, the errors induced by this approximation are usually considered small enough to be neglected for the purpose of structural integrity. There are also some diffraction techniques that give spectra containing multiple diffraction

reflections (Time of Flight or Energy Dispersive methods) and where an average elastic strain can be obtained by a full spectrum fit. In the case of single reflection instruments, a careful choice of the reflection is important: for example in FCC materials, the {311} reflections are usually considered as representative of the aggregate [7].

For crystals with a strong crystal anisotropy, questions must be asked on how to deduce macroscopic stress states from the diffraction lattice strains. Usually measurements are done in the principal macroscopic directions so that three strain measurements are sufficient to obtain the full strain and hence stress tensor. However the lattice strains in the macroscopic principal directions are not necessarily principal elastic strains at the grain level. Moreover there is an issue with measuring in different directions: the family of grains represented by a reflection along sample direction 1 is not the same family as represented by the same reflection along sample direction 2, complicating the conversion from strain to stress.

Another problem arises from the methods usually used for obtaining a reference d-spacing. The general method consists of small coupons with a size of the order of the macroscopic heterogeneities. The idea is to remove all the type I stresses so that the measured d-spacings account only for the chemistry and the type II stresses.

Daymond [8] proposed several methods to derive the macroscopic strain and stress (or 'continuum equivalent' strain and stress as he describes) from the diffraction multi peak spectra. Some of the methods will be discussed later with a new approach using the elasto-plastic self consistent model (see Section 6.3.5).

2.1.5 TOF diffraction

The beam in a Time of Flight (TOF) neutron diffraction instrument presents the advantage of covering a large range of wavelength. Thus many reflections of a polycrystal can

diffract at a particular 2θ angle and the diffraction spectrum, collected over a short time period, contains several peaks.

2.1.5.a ENGIN-X

ENGIN-X [9] is the neutron diffraction instrument that has been used to carry out the strain measurements in the current work. It is an engineering dedicated instrument at the spallation source ISIS, UK.

The first step of neutron generation at ISIS consists of creating protons and accelerating them in a synchrotron. With a frequency of 50Hz, pulses of protons are sent on a heavy material target. This process generates short pulses of neutrons every 20ms which are then moderated and sent to the different instruments. Some neutrons travel through a guide and reach ENGIN-X, 50m away from the target. In the experimental hutch, two detectors are placed at $2\theta = +90^{\circ}$ and -90° from the incident beam. They collect neutrons that have been diffracted by grains for which Bragg's law is fulfilled for the range of wavelength in the white beam.

The velocity v at which a neutron travels is directly linked to its wavelength λ as shown in Eq. 8, where h is Planck's constant and m the mass of the neutron. Hence by measuring the time it takes for neutrons to travel all the way from the target to the detector (a known distance L) it is possible to determine their wavelength (Eq. 9). This is the method used at ENGIN-X.

Eq. 8 $$v = \frac{h}{m\lambda}$$

Eq. 9 $$TOF = \frac{L}{v} = \frac{Lm\lambda}{h}$$

For better counting times and statistics, the detectors actually have an angular span of +/- 14° horizontally and +/- 21° vertically; hence grains that diffract with a slightly different 2θ or **Q** vector than ideal 2θ=+/-90° case also participate to the collected intensity.

2.1.5.b Basics of analysis

A TOF neutron diffraction spectrum usually includes several peaks. The number of peaks depends on the range of wavelength of the incoming neutrons. Typically for the instrument settings used in this work, a Zr hcp spectrum collected at ENGIN-X contains 11 diffraction peaks. Each of them corresponds to one reflection and represents a family of diffracting grains: a family of grains is a set of grains for which a specific lattice plane (the diffracting plane as it happens) is normal to a common direction of space (the measurement direction). The condition is only a projection condition so a family doesn't contain only crystallites with the exact same crystal orientation: the orientation of the grains in the family can differ by rotation around the projection axis.

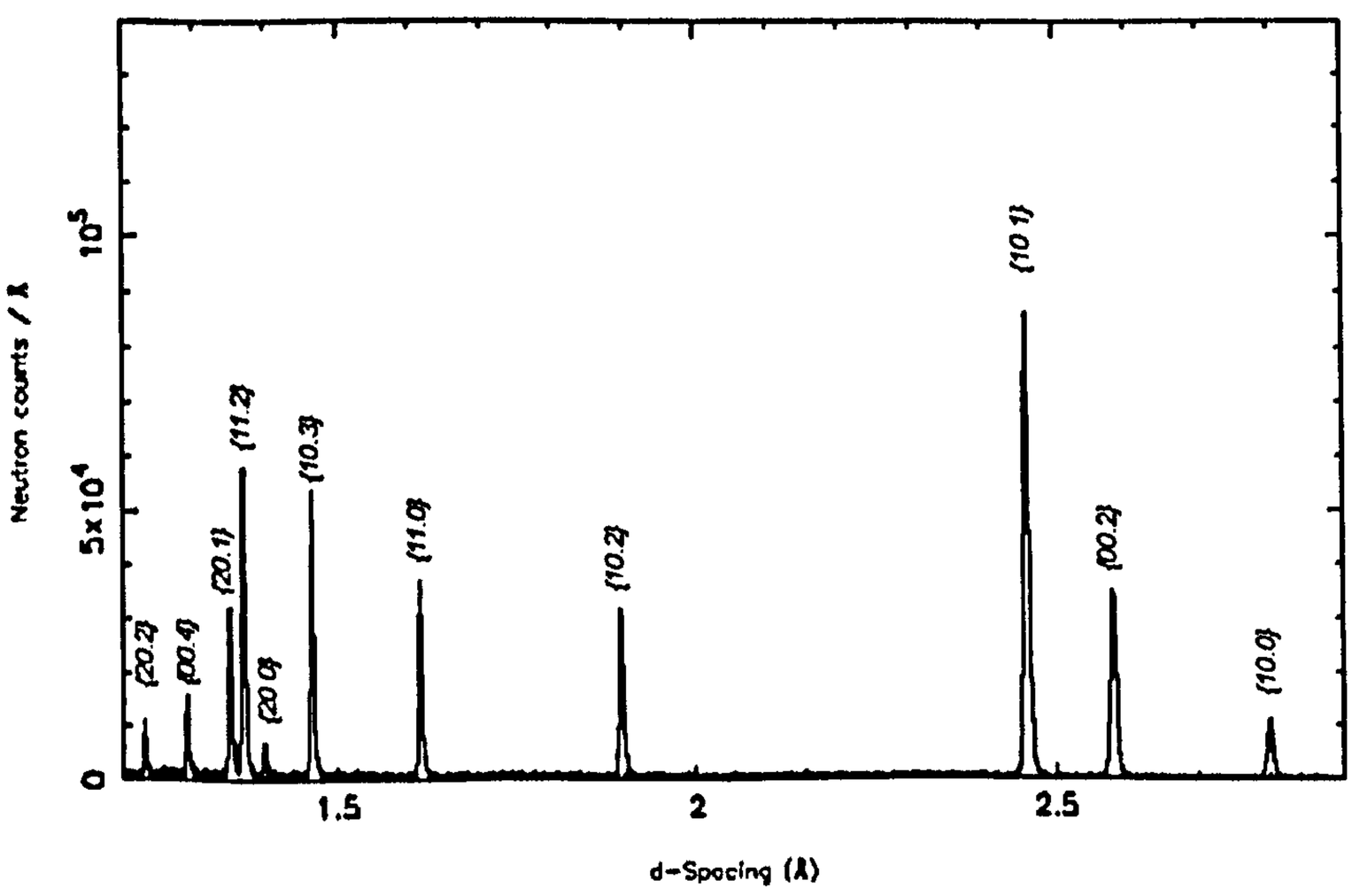

Figure 5 *Typical diffraction spectrum of a Zr at ENGIN-X (Zircaloy-4 plate – Q vector along the transverse direction)*

- *Single peak fitting*

In order to extract the d-spacing of individual reflections, a single peak method is used. This consists of refining a profile of two back-to-back exponentials convolved with a pseudo-Voigt to fit the diffraction peak. The exponential terms are fixed by the instrument calibration (and represent the way that the neutrons are moderated before travelling to the instrument) while the symmetric Gaussian and Lorentzian parts of the pseudo-Voigt fit can be varied to fit the sample contributions to diffraction peak width. The routines used for refinement for this work are from OpenGenie [10] or GSAS [11] software.

- *Full spectrum refinement methods*

Various methods are available for fitting the full diffraction spectrum at once. These methods are generally useful for finding the average lattice spacing in the aggregate. The Rietveld refinement method [12] is very common for powders and polycrystals. Rietveld considered that a diffraction pattern is the superposition of a background function and a set of Gaussian functions corresponding to the diffraction peaks. The fitting function is fully parametrised. For example the position of a Gauss profile corresponds to the d-spacing of the diffracting plane derived geometrically from the crystal structure parameters (geometry of the cell, dimensions and angles). Depending on the application and the desired output, a set of parameters are fixed to a known value while the others are refined so that the Rietveld profile fits the experimental spectrum. Later work introduced other peak shape terms to correctly describe the asymmetry found in TOF neutrons. Typical parameters varied in the present work are the cell dimensions (defining the peaks positions), the peak width parameters and the spherical harmonics coefficients (which alter the relative peak intensities when the grains are not randomly orientated in the aggregate).

2.2 Texture

2.2.1 Definition

The characteristics of crystalline solids can be classified in three categories: the crystal structure (face centred cubic fcc, Body Centred Cubic bcc, Hexagonal Close Packed hcp...), the lattice defects and the arrangement of the crystalline domains. The last refers to the shape, size, position and orientation of the grains. The shape and size of the grains can highly influence the overall response of the material. It is well established that small grains harden the material [13-15], the grain boundaries being obstacles to the propagation of dislocations. The disposition of the grains also influences the response. If the material contains clusters of grains with comparable crystallographic orientations, the dislocations can travel more easily through the grain boundaries. A cluster would behave similarly to a big crystalline domain. By crystallographic orientation we mean the way the coordinate system of the unit cells in the grains are orientated with reference to a macroscopic coordinate system. In polycrystals, the grain orientations can affect the overall behaviour, particularly if there is a preferred orientation shared by most of the grains. The term texture is a synonym of preferred orientation in polycrystals. By extension, a material is referred as more or less textured depending on the amount of grains whose orientations follow a global pattern. A material without a particular preferred crystal orientation (a powder for example) is said to have a 'random texture'. Random texture is used as a reference for quantifying the strength of textures in the units of 'multiple of random'. This unit defines how many more grains have a particular orientation as compared to a non textured reference material.

2.2.2 Reasons for studying texture

Texture analysis is a major element in the bridge between crystalline and macroscopic behaviours. Bunge makes it clear: "Since most of the physical properties of the crystals are anisotropic, the macroscopic mean values are mainly controlled by texture" [16]. As a result a given material can show very different macroscopic responses depending on its texture. Texture can influence both the formability and the performance of materials.

Service life calculations can be severely affected by texture. In some cases if predictions for a heavily textured material are performed based on the properties of the non textured material they can lead to major under or over estimations of the component's service life. The former case would result in over dimensioning and a waste of money. The latter case however can lead to unexpected component failures with potentially serious consequences. Analysing texture can help in optimising some manufacturing processes and reducing waste.

For these reasons texture measurements are often part of quality control and executed on manufacturing lines. In a reverse approach the texture of materials can be engineered in order to optimize their response depending on the application and the external solicitations. Studying texture also is very useful for prediction and characterisation or for post process analysis. It is also an image of the 'history' of the material in terms of mechanical processes. It is thus a useful tool to learn about the processes used to manufacture some ancient archaeological artifacts [17]. Cast or hammered specimens will show a very different texture. It also has geological applications: the texture of rocks can tell about the history of the deformations they have undergone, and influence the speed with which seismic waves travel.

Finally, the texture of materials both affects and is affected by the activation of deformation mechanisms such as slip and twinning. By studying the evolution of texture during deformation, we can learn a lot about the mechanisms (as we will see in Chapter 7).

2.2.3 Origin of texture

In nature, virtually all crystalline metals are textured, at some length scale, and randomly textured materials are rare: random textures usually result from powder compression.

2.2.3.a Deformation texture

As a result of slip and twinning during manufacture and processing, metallic materials are often produced in a textured state. Usually, the higher the applied strain, the more textured the material.

- *Slip induced reorientation:*

The most common process of plastic deformation in crystals is slip. As described in Section 3.2.3.a, slip is a shear mechanism, in the sense that the movements of dislocations preferentially occur on crystallographic planes for which the highest shear component of stress is applied. In other words, slip accommodates shear stresses and does it by introducing shear displacements. The crystal undergoes a shear change of shape without change of volume - this must be accommodated by rotation because of the grain boundary constraints.

Figure 6 is a schematic illustration of the uniaxial tensile deformation of a single crystal by slip on a unique system of planes. When load is applied and slip is activated on a set of parallel planes, the loading loses its coaxiality (Figure 6(b)). When there is a constraint of coaxiality, such as in a real tensile specimen griped at its ends, the crystal has to rotate (Figure 6(c)).

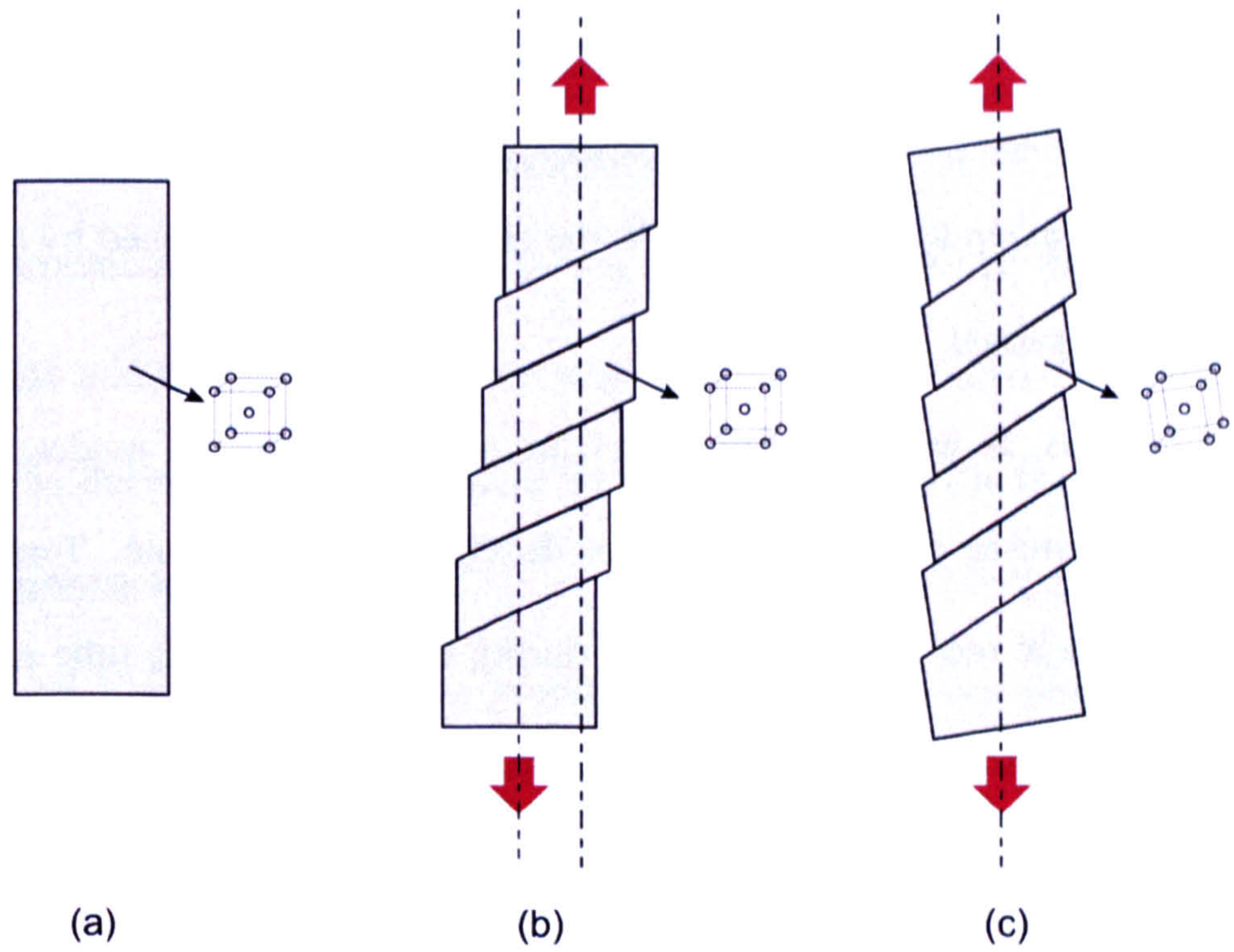

Figure 6 Deformation of a single crystal through one slip system under uniaxial tension. (a) Crystal before deformation, (b) under plastic loading without constraint, (c) with constraint.

For polycrystals things are more complicated due to the higher grain to grain constraints and the number of slip systems activated. A grain in the polycrystal is highly constrained by its neighbours. Some crystal rotation is necessary to accommodate the shear induced by slip and maintain integrity at grain boundaries. The reorientation of individual crystallites takes place throughout the loading process until a stable orientation is found. There is usually a limited and restricted set of stable orientations for a given deformation process. As a result grains will tend to have a preferred crystallographic orientation.

One should note that as a crystallite rotates, the loading configuration might not be favourable any more for the activation of the primary systems. On the other hand, the new loading condition (relative to the grain coordinate system) might generate shear stresses to initiate slip on a different set of planes.

- *Twinning induced reorientation:*

Section 3.2.3.b gives some details on twinning mechanisms. Twinning induces a volume reorientation of the crystal: contrary to slip, crystal rotation is inherent to the mechanism

rather than a result of the combination of shear strain and boundary constraints. The misorientation angle between the parent grain and the twin lamella can be anything between a few degrees up to 90°. As a result, the texture changes induced by twinning are discrete rather than gradual.

In hexagonal systems, as well as being one of the major deformation modes, twinning is also a major mechanism contributing to the development of texture. Tenckhoff [18] describes how the twin mechanisms activated during the sheet rolling, tube reducing and wire drawing of α phase zirconium alloys determine the final texture. During rolling for example, the combination of the reorientation induced by the different twin modes leads to an accumulation of basal planes towards the normal direction. As we will see again in this thesis, different deformation mechanisms tend to orient the basal planes towards the direction of compression.

2.2.3.b Transformation textures

During phase transformations, there is generally a geometrical relationship between the parent and child crystals. As a result if a material is processed at high temperature above the transformation temperature, on cooling some texture components of the parent phase are likely to be passed on to the transformed phase.

The orientation relationship is often characterised by a common plane between the two phases. There is usually a variety of geometrical possibilities (variants). However it has been frequently observed that there is a preferential selection of variants. Indeed although the variants have in principle all the same probabilities of occurrence with respect to the crystal coordinate system, they are not equivalent with regards to the sample symmetry and this implies a variant selection [19].

In the case of the β/α transformation in zirconium and its alloys, there is such a relationship. It follows the Burger's relationship [20], so that the $\{110\}_\beta$ and $\{00.2\}_\alpha$ planes are parallel and the directions $<1\text{-}11>_\beta$ and $<11\text{-}20>_\alpha$ are co-linear. For the β to α transformation and for reasons of crystal symmetries, there are only two variants for each $(110)_\beta$ plane in the cubic cell. Since there are six of these planes in the bcc crysal, the total number of variants is twelve.

Some other relationships have been proposed and observed, but they are very close to Burgers' and differ by a small angle (see [21] for more details).

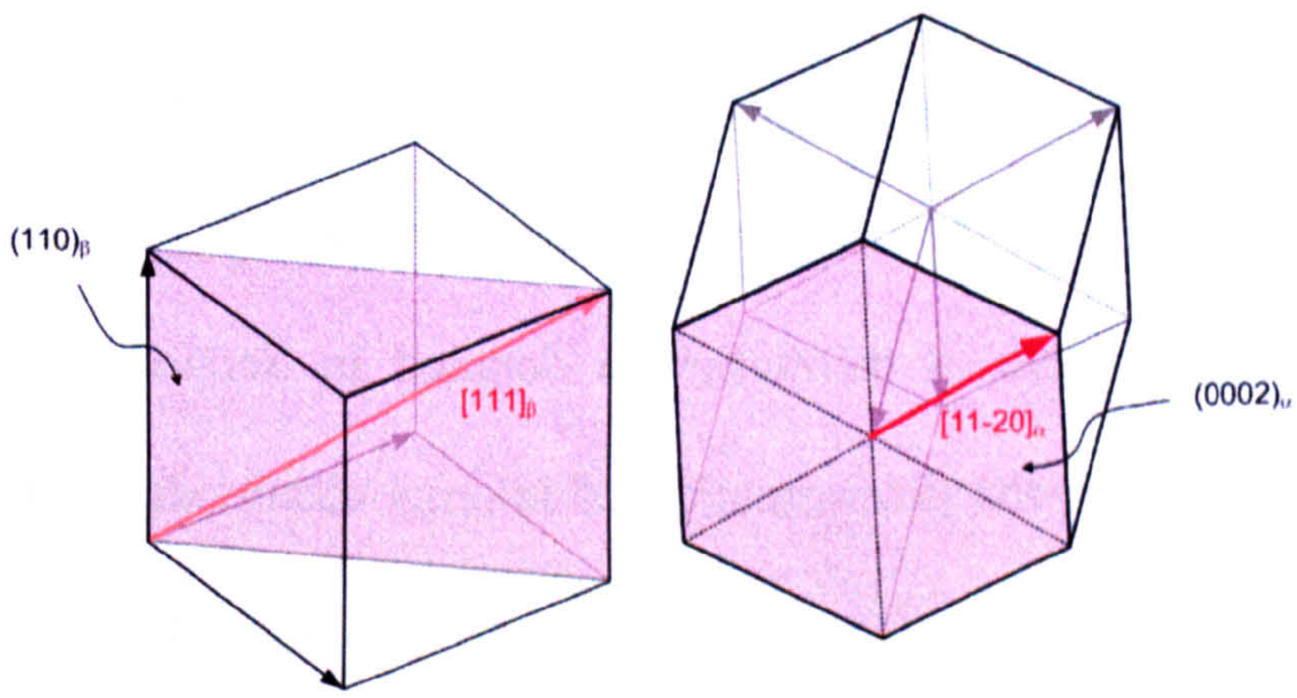

Figure 7 Representation of a Burgers relationship between the cubic and hexagonal cells

Wenk et al. [22] studied the texture changes during this allotropic transformation for a hot rolled Zircalloy-4 sheet. They observed the same hcp textures after two heating-cooling cycles between the α and β phases. This is an evidence of the variant selection. In the same paper, the textures measured by Wenk et al. changed during the annealing of the hcp phase: the crystals are rotated by 30° around the <c> axis. This kind of annealing texture can be considered in the category of transformation textures. Although texture changes don't happen during recovery, they are frequent during recrystallisation. Generally the reorientations consist of rotations around one of the crystal axes. In zirconium and its alloys for example, the annealing usually rotates the hcp crystal by 30° around the <c> axis and also possibly 90° around a <10.0> direction [23]. Mahmood and Murty observed the

same rotation Wenk observed [24]. Murty evidenced the effect this small texture change can have on creep behaviour.

Texture patterns can also arise from casting or welding. Carr et al. [25] studied a case of solidification texture in a weld in a Zircaloy-4 rolled plate.

2.2.4 Measurement techniques

2.2.4.a Volume texture measurement

Volume texture measurement techniques, also called macro texture measurement techniques, determine the crystallographic orientations over a finite volume of material. The main techniques in this category are neutron and X-ray diffraction texture measurements. The principle of diffraction is detailed in Section 2.1. In that section diffraction was applied for the determination of internal elastic strains by looking at the shift of the diffraction peaks. For texture measurement peak intensities are the key output. The intensity of a diffraction peak depends on a number of parameters: parameters relative to the reflection considered (multiplicity, structure factor...), some instrument parameters, the incoming intensity, and most importantly for our purpose the volume of diffracting grains in the gauge volume (one can consult [6] for more information). If the diffraction conditions are kept constant (reflection fixed by the diffraction angle and wavelength, constant gauge volume, constant path length, same incoming beam and counting time) any changes in intensity in the collected peak are only due to changes in the volume of diffracting grains. In other words, the relative intensities represent the relative proportion of grains oriented such as to diffract.

To determine complete texture information from neutron and X-ray diffraction, the intensities of several reflections are acquired in many directions of the sample space. There are two main ways of getting diffraction data in all directions: by covering the whole space

with an arrangement of fixed detectors or by moving the generation-detection system and the sample relative to each other. The first method is usually used for white beams while the second one can be used with any set-up.

HIPPO, the neutron texture instrument at the Los Alamos National Laboratory (LANL), is dotted with a set of 1,360 detector tubes arranged in ring panels covering a range of angles from 10^{o} to 150^{o}. However for low diffraction angles the resolution is quite poor (this will be discussed in Chapter 7). So practically it is not advantageous to have detectors covering the whole space and the method must be combined with some sample rotation.

Usually for lab X-ray diffractometers, the detector is fixed, set at a specific 2θ angle, and the sample is tilted in a range of directions. Figure 8 shows a lab X-ray set up with an Eulerian cradle for sample rotation.

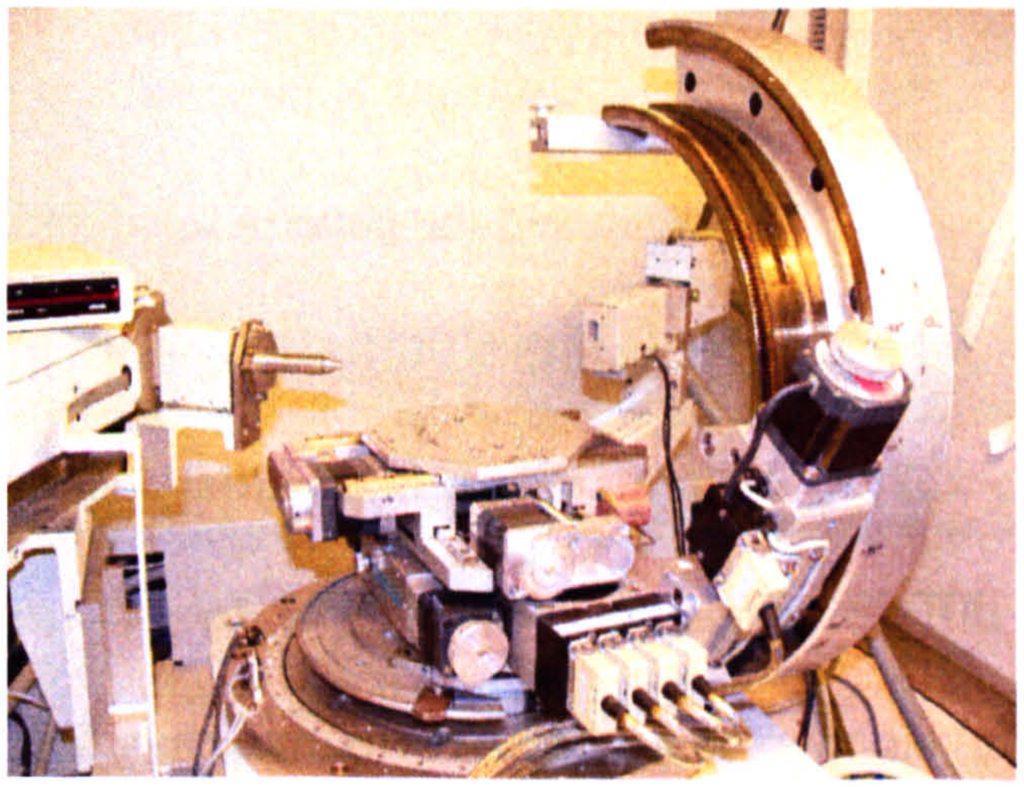

Figure 8 *Bruker lab X-ray gonioimeter at the Open University*

The multiple detector systems present the advantage of being quicker than for a goniometer with single detector, as far fewer sample rotations are required. Moreover as the former is usually performed with white incoming beams several reflections can be collected at once. Typically at HIPPO it takes 1 hour to collect enough information for a complete determination of the texture, while it takes up to 24 hours on a lab X-ray diffractometer or up to 12 hours on a monochromatic neutron instrument. However in

defence of goniometer systems one should mention that the angular resolution is poorer in the multiple detector method: each detector panel has a finite angular coverage (necessary for achieving good counting times) and thus the collected intensity collected on each panel is an average over that solid angle. As a result sharp textures tend to be smoothed. The resolution with goniometer systems is defined by the sample tilt increments and is generally much higher.

2.2.4.b Point texture measurement

These microtexture techniques present a big advantage over classic techniques. They allow local, i.e. spatially mapped, measurements. It is then possible to have access to the grains' sizes, shapes and positions as well as their orientation.

Electron Back Scattering Diffraction (EBSD) is the main measurement technique for microtextures. A nanometer size beam of electrons is targeted at a point on the surface of the sample. In general the size of the beam and the penetration depth are much smaller than the grain size. The thin irradiated volume thus diffracts as a single crystal would and a CCD detector collects a Kikuchi pattern, which is a partial section of Kossel diffraction cones. By fitting the diffraction bands, one is able to determine the complete 3D orientation of the crystal at this point (relative to the chamber or sample coordinate system).

According to Bragg's law, when a monochromatic beam hits the lattice of a single crystal, the electrons should be diffracted as beams, visible as spots on a Laue detector and each corresponding to a specific diffracting lattice plane. So one can wonder why in the present case the planes diffract in the form of cones rather than beams of diffraction. This is a result of the diffuse scattering that happens when the electron beam penetrates the material: a large proportion of electrons are inelastically scattered in all directions and the lattice

planes instead of being hit by a single beam of electrons are showered by electron waves from all directions. Each wave incident on a lattice plane with an angle equal to Bragg's angle will be diffracted as a beam. It is the combination of all these beams that form a diffraction cone (Kossel's cone). It may be worth mentioning that these cones are different from the Debye cones: while the former result from the divergence in the incident rays, the latter results from the multitude of crystal orientations in the irradiated volume (in a powder or a polycrystal). Hence the axis of a Kossel cone is the normal of the diffracting plane whereas the axis of a Debye cone is aligned with the incident beam. More details on EBSD can be found in [26].

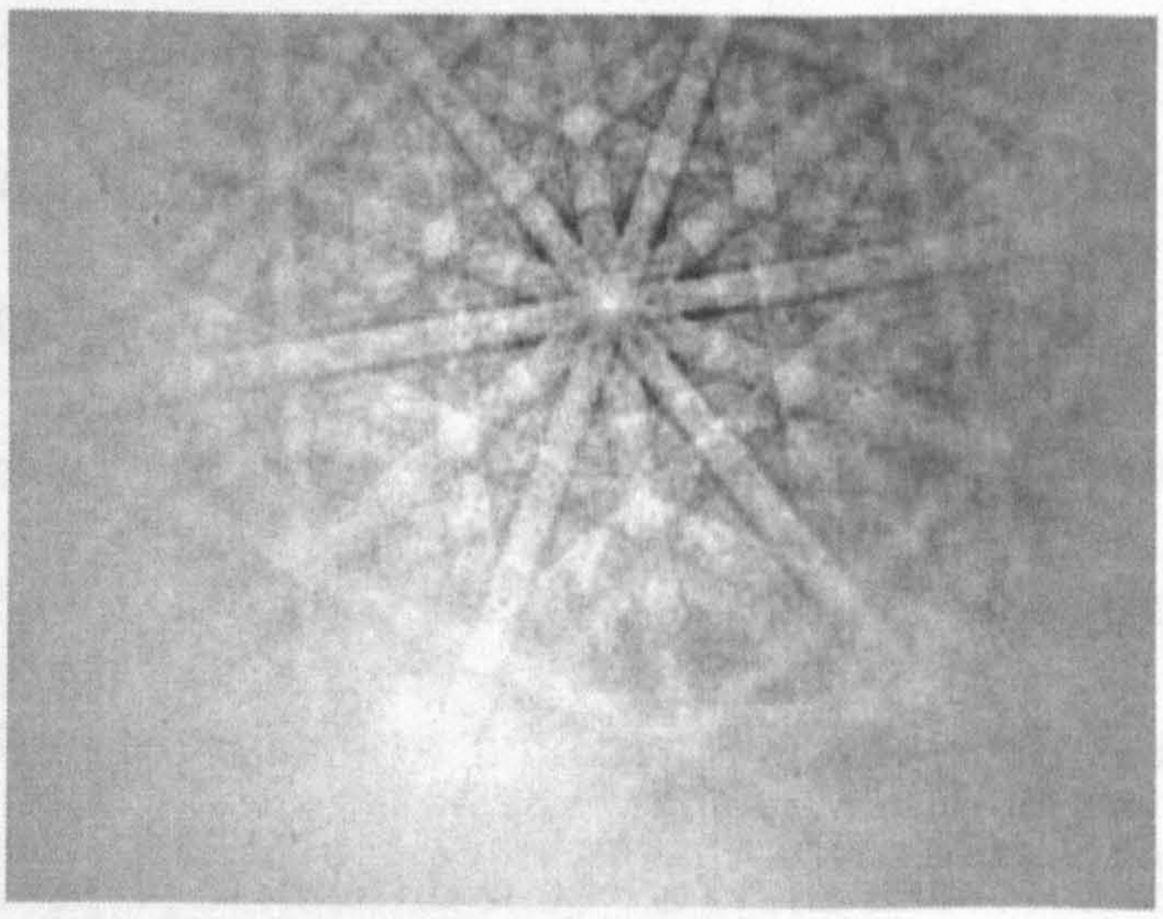

Figure 9 Typical Kikuchi pattern in zirconium alloys (obtained on Zry-4)

2.2.4.c Advantages and drawbacks

Lab X-ray diffraction is certainly the most commonly used technique for texture measurements. It doesn't require much sample preparation and it is relatively cheap. However it presents several limitations. It is quite time consuming: for each reflection desired, the whole orientation space must be scanned (although practically only 70 to 80% of the orientation space is available with the traditional reflection set up). The high absorption of X-rays by matter and the low energy of lab X-rays don't allow for bulk measurements. The technique is thus limited to near surface measurements which do not

necessarily represent the texture of the whole sample: several authors have observed through thickness variations in rolled sheets or tubes ([18, 27] on Zr alloys). Similarly to neutron diffraction, the measurements are indirect: it measures a set of projections of the texture (pole figures). At least 3 sets of pole figures need to be obtained in order to back-calculate the full texture information, and the derivation of the orientation distribution function requires a significant amount of computation. Moreover, the full pole figure is generally not available in a reflection mode only and transmission measurements are required to complete the pole figure. Since transmission geometry requires very thin samples to allow the beam to go through, it is not practical and seldom preformed. Hence X-ray pole figures are generally incomplete (typically up to an radial angle of 70° to 80°) and although there are some ways of extrapolation, it can be a quite tedious procedure. Despite these limitations, the technique stays very popular in industry because it is relatively easy to use on a routine basis.

Sample preparation and accessibility is not as easy for EBSD as it is for Lab X-rays. A very smooth and smear free surface is required to obtain reasonable Kikuchi patterns. Some materials such as zirconium alloys are quite difficult to prepare for this purpose. The technique moreover requires access to a Scanning Electron Microscope equipped with a dedicated CCD camera, so bulky samples can't be measured. Some drawbacks shared with Lab X-rays are that it can only perform surface measurements and that it is time consuming, as several thousand patterns need to be collected and indexed to obtain reasonable statistics. The main advantage of the technique resides in the fact that it is a direct measure of texture. The full 3D orientation of the crystal is known at each point. As a consequence and as described previously, it can combine grain mapping and texture. In this sense it is also a very robust method for accessing texture information and less computation is needed to analyze the results.

Neutron (and possibly synchrotron X-ray) diffraction stands out for its possibility of measuring texture into the bulk of materials. It is an advantage because surface effects and surface preparation won't affect the measurement. It also gives a better statistical average of texture by adding a third and finite dimension to the gauge volume. This technique is however not readily available for any user as the access to a neutron (or synchrotron) facility must be granted, generally on the basis of the scientific quality of the proposal. For time of flight instruments with multiple panels (such as HIPPO), the texture information can be obtained relatively quickly (less than an hour). However the detector panels have a finite detection area (of the order of several degrees on a pole figure) over which the diffraction intensities are averaged. This tends to smooth textures, especially the sharp ones. On the other hand instruments with moving detectors (such as Stress-spec at FRM2, Germany) give a more accurate and less discretised measurement, but several hours are needed to collect the pole figures.

2.2.5 Representation of texture

As developed previously, texture is a synonym of preferred orientation. Because talking about orientations involves the use of three dimensions, it can be difficult to represent texture in an easily understandable format.

2.2.5.a ODF

Texture can be represented by a function that gives for each orientation of space the proportion of grains having this particular crystal orientation. To describe crystal orientations, it has been proposed to use the Euler transformation which is a way of linking two coordinate systems, namely the sample and the grain crystal coordinate systems in our case. The transformation consists of three consecutive rotations applied to the specimen coordinate system so that the resulting coordinate system matches with the crystal coordinate system. For a given sequence of rotations, there is a unique set of angles that

transforms one frame into another. Several conventions (or sequence of rotations) are commonly used in texture analysis for describing a crystal orientation in a sample coordinate system. The main ones which we will deal with are Bunge and Kocks conventions. They differ simply by the way the three rotations are defined. From one convention to the other, the Euler angles are linked by linear relationships (see Eq. 22).

An Orientation Distribution Function (ODF) is a function from $[0, 2\pi]^3$ to $\Re^+$ that associates an intensity (corresponding to a volumetric fraction for example) to a set of Euler angles (corresponding to a crystal orientation in the reference frame): $f(\varphi_1, \phi, \varphi_2)$. This function can be represented in terms of iso-intensity lines in a three dimensional Euler space (Figure 10). It is easier to observe and interpret the ODF in the form of 2D sections of the Euler space. It is common practice to slice the Euler space in φ_2 (or possibly φ_1) sections and plot the intensities as contours or in a colour coded format (Figure 11).

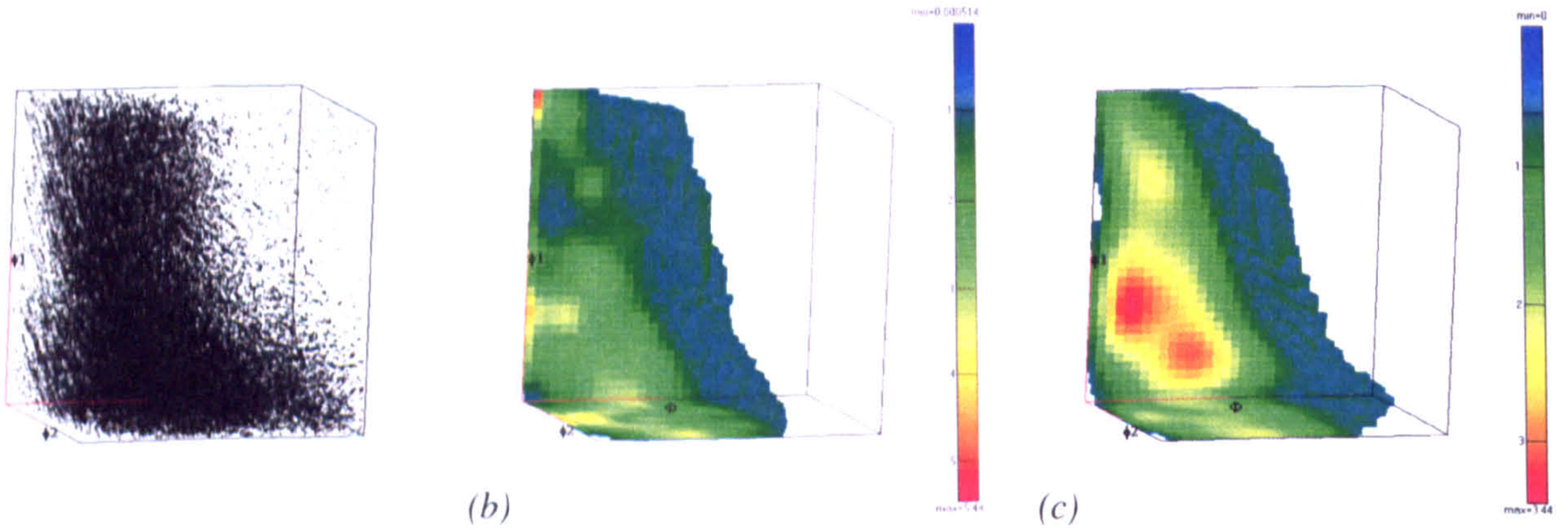

Figure 10 Representation of an EBSD ODF in the three dimensional Euler space. (a) cloud of points, (b) after contouring using a simple Gauss method, (c) after contouring using a series expansion method with 22 harmonics. (Zircaloy-4 rolled texture –representation made using HKL Salsa software)

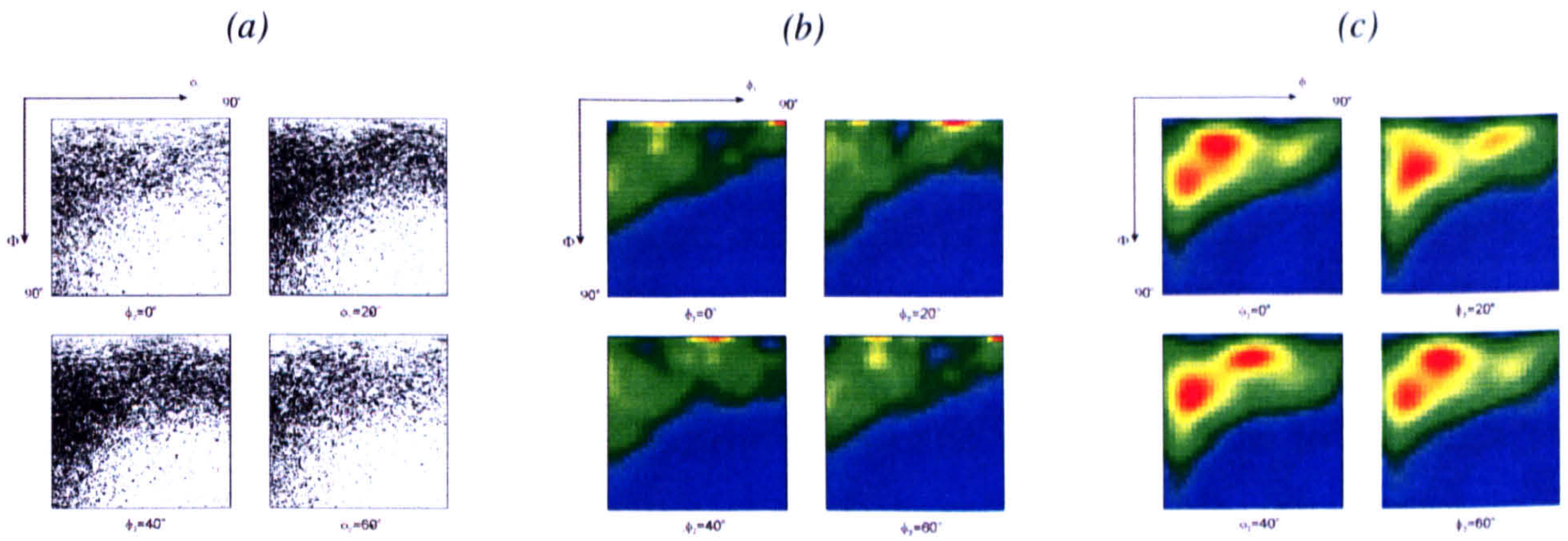

Figure 11 ODF sections through the previous plots.

The obtaining of an ODF or ODF plot is more or less straightforward depending on the measurement technique. The EBSD technique returns directly the orientation of each grain with reference to the sample coordinate system in terms of Euler angles. From a full set of measurements in a representative area it is possible to fill the Euler space with discrete points that represent each measurement point (Figure 10 (a)). The density of points (number of points contained inside elementary cells) can be used as the basis for deriving the ODF intensities (in Figure 10 (b) the cells – seen as pixels – have a 5^{o} spread). Although this cell method gives only a discrete representation of the ODF (as a table of values or a plot), it is usually sufficient for at least a qualitative understanding of the texture. Deriving an expression for the ODF is possible but somewhat more difficult as it usually involves the use of a series expansion method [26]. Figure 10 (c) shows the result of a series expansion of 22^{nd} order.

It is thus relatively straightforward to obtain an experimental and discrete plot of the ODF. One should however be cautious regarding the representativity of the data. A careful selection of the area should be made and maybe a combination of measurements on different surfaces of the sample can help reduce some sampling errors. The geometry of the grains can, for example, highly influence the texture results, especially if grain geometry and crystal orientation are not independent (the EBSD texture on a sample with

very elongated grains might give different results depending on the cross-section measurement plane).

It is also possible to get an ODF from diffraction measurements although it requires some rather complicated back calculations similar to calculations performed to retrieve 3D representations of an object from sets of 2D projections. Some details will be given in Chapter 7.

2.2.5.b Pole figures

Pole figures are projections of the three-dimensional texture information. They are performed along one of the crystal directions (typically the normal of a lattice plane) onto the sample coordinate system.

A {hkl} pole figure for a crystal is obtained by placing the unit cell at the centre of a unit reference sphere in the sample coordinate system. The intersection of the {hkl} plane normal with the sphere is called a pole. The position of these poles on the surface of the sphere gives some information about the orientation of the crystal. For an easier representation the poles are projected onto a plane usually by a stereographic or equal area projection. The result is a pole figure: a circle with spots where positions represents the orientation of the {hkl} planes.

A pole figure for a polycrystal is obtained by performing this operation for each crystalline volume. The density of poles on the surface of the sphere or on the pole figure gives information about the texture of the material: if the poles are uniformly distributed on the sphere, the material is said to have a random texture (there is no preferential orientation); if the distribution is not uniform, the material is textured. Some examples of pole figures are shown in Figure 21 in Section 4.1.3.

Diffraction techniques are actually directly measuring pole figure information: for a given {hkl} diffraction plane, the diffracted intensity in a direction of space is proportional to the

number of diffracting grains, i.e. grains oriented such that a {hkl} plane is facing that direction. Hence this intensity can be used as the basis for defining the densities on the pole figures.

2.3 Modelling

2.3.1 Background

As mentioned in the introduction, it can be difficult to understand the behaviour of inhomogeneous materials. One of the major difficulties resides in terms of how to link the microscopic and the macroscopic properties and how to predict the behaviours. In some relatively simple cases such as fibre composites for example, reasonable assumptions can be made. When the fibres of the composite are parallel to the loading direction, one can reasonably assume that there is uniform strain throughout the phases. Similarly if the phases of the composite are in series relative to the loading direction (i.e. the fibres are normal to the loading), uniform stress can be assumed. In those cases the knowledge of the phase properties can be used for determining the overall properties with a direct calculation.

The first models for dealing with more general cases of heterogeneous materials were based on similar assumptions. The Reuss and Sachs models, elastic and plastic respectively, use the proportional stress assumption to link the behaviour of the heterogeneous material and the properties of the individual phases. The elastic Voigt and plastic Taylor models on the other hand assume uniform strain in the material. The models are discussed in several books (see [5] for example). However outside of the cases of fibre symmetry depicted previously the uniform strain or stress assumptions are too simplistic to yield to satisfactory modelling. In the case of complex composite materials or polycrystal

aggregates these models don't account for all the phase interactions and heterogeneities, especially when plasticity is involved: either there is no force equilibrium between the grains or the grains don't fit together. Whereas neither assumption guarantees stress equilibrium, the assumption of uniform strain ensures at least compatibility. Therefore the Taylor model has been prefered over the Sachs model and used with reasonable success for aggregates with low crystal plastic anistotropy such as cubic materials, but the predictions are quite poor for highly anisotropic materials.

Several models have been developed to cope with the limitations of the Sachs and Taylor models. A main stream of development has been in self consistent models which account for intergranular heterogeneities.

2.3.1.a Principle of self consistent modelling

The main problem for modelling the behaviour of an aggregate from a microscopic perspective is that the response of each grain depends on the boundary conditions on the grain. These conditions are imposed by the aggregate and its mechanical state. However this state is itself defined by the average response of all grains. To resolve this interdependent problem, a self-consistent approach can be used.

A common ground for all self consistent schemes is the Eshelby ellipsoidal inclusion in an infinite homogeneous equivalent medium (HEM) [28]. Each grain is considered as an ellipsoid embedded in a matrix which represents the aggregate. Eshelby showed that if the inclusion is ellipsoidal, the stress and strain fields are uniform in the inclusion, and that an analytical relationship exists between the stress/strain of the matrix and that of the inclusion. The stress and strain fields in the matrix are taken as the average of those of all the grains and should be compatible with the macroscopically imposed ones, i.e. the boundary conditions. The self-consistent schemes try to establish this equilibrium by

alternatively updating the state of the HEM as the average of all inclusions, and the state of each grain-inclusion embedded in this new HEM until there is convergence, i.e. the systems {HEM+inclusions} reach mechanical equilibrium.

Self-consistent models can be classified in two categories: stiff response and incremental. Kroner [29] and Budianski and Wu [30] were the first to propose an elastic-plastic self-consistent model. The scheme was non-incremental. The response is quite stiff and close to that of Taylor model. An incremental scheme is discussed in the next Section.

Although they are more realistic than the Sachs or Taylor models, the self-consistent models have some limitations. For example the local grain to grain interactions are not considered in favour of a more general grain to matrix interaction. This has been partially improved in some models called multiple site self-consistent schemes [31].

2.3.2 Principle of EPSC

The Elasto-Plastic Self-Consistent (EPSC) approach as developed by Tomé et al. [32] is an example of a self-consistent scheme whose main features are that it is incremental, is rate independent and applies in the elasto-plastic regime. The scheme aim is to model the behaviour of an aggregate during uniaxial mechanical or thermal tests. The overall stress and strain evolutions are modeled along with the microscopic behaviours. The model outputs the elastic strain for chosen reflections in chosen directions in order to compare with experimentally measured diffraction strains.

2.3.2.a Basic equations

The basic equations used in Hutchinson's EPSC formulation are briefly described in this section. For a more detailed description see Ref. [33, 34]. In this section σ and ε represent the stress and strain tensors in a grain, and Σ and E the aggregate stress and strain tensors respectively.

- *Constitutive equations*

As an extension to Hooke's law, one can derive an instantaneous relationship between stress and strain for a volume undergoing plastic flow in the form of a pseudo-linear equation. The individual grain behaviour can be expressed by:

$$\dot{\sigma} = L^c : (\dot{\varepsilon} - \alpha.\dot{T}) \qquad \textit{Eq. 10}$$

where L^c is the incremental elasto-plastic stiffness tensor of the grain (or tangent modulus) and α is the thermal expansion coefficient of the crystal. L^c contains information about the elastic constants of the crystal and the activity and hardening of the potential slip systems in the grain at the given strain increment. If there is no plasticity in the grain, the elasto-plastic stiffness tensor equals the elastic stiffness tensor of the crystal and the equation is equivalent to Hooke's law. This formulation means that we consider that the mechanical behaviour is linear over the stress or strain increment. In the case of a uniaxial setup for example, the value of the slope (or modulus) at a given strain increment is equal to the tangent of the (not necessarily linear) flow curve at that point. This slope is imperatively equal to or smaller than the Young's modulus.

Similarly the constitutive law for the aggregate is:

$$\dot{\Sigma} = L : (\dot{\mathrm{E}} - \mathrm{A}.\dot{T}) \qquad \textit{Eq. 11}$$

where L is the incremental elasto-plastic stiffness tensor of the aggregate and A is the coefficient of thermal expansion of the aggregate. These two parameters are not directly available and are obtained by a self-consistent process (see Appendix B.1 and B.2 for more details).

- *Interaction law*

The interaction between the grains and the aggregate follows Eshelby's formulation for an ellipsoidal inclusion in a homogeneous medium [28]. It states that the macroscopic and microscopic stresses and strains are linearly related:

$$\dot{\sigma} - \dot{\Sigma} = -\tilde{L} : (\dot{\varepsilon} - \dot{\mathrm{E}}) \qquad \textit{Eq. 12}$$

where $\tilde{L}$ is the interaction matrix and is a function of L and the Eshelby tensor S. Although Eshelby's problem is elastic, it is kept valid in the plastic regime by considering the solutions in terms of rates (or increments) and by the use of the instantaneous moduli (Eq. 10 and Eq. 11).

- *Mixture law*

Finally the behaviour of the aggregate is the weighted average of that of all grains:

$$\dot{\mathrm{E}} = <\dot{\varepsilon}> \quad \textit{Or} \quad \dot{\Sigma} = <\dot{\sigma}> \qquad \textit{Eq. 13}$$

2.3.2.b Self-consistent Scheme

We assume that all the systems {HEM-grain} are under equilibrium under known conditions and in a known state. We then disturb the equilibrium by an increment of strain (or load) applied to the aggregate. The new stress and strain state in each grain is dependent on the state of the aggregate by means of the Eshelby's inclusion/HEM interaction equation (Eq. 12). On the other hand the new state of the aggregate is determined by the average state of all grains (Eq. 13). The resolution of this interdependence is done by means of a self-consistent formulation. A detailed description of the scheme can be found in Appendix B.2 in the form of flow charts.

2.3.2.c Inputs and Outputs

This section refers to Tomé's et al. implementation of Hutchinson's formulation which was used in this work. The main inputs for the model are the texture information and the single crystal properties. The texture information obtained from EBSD, X-ray or neutron measurements is entered in the form of a population grains file. The file contains a representative sample of grain orientations in terms of Euler angles and relative weight. In the model the crystal orientation of each inclusion is derived from this texture file. The relative weights are used for calculating the weighted averages that are present in Eq. 13.

Besides the structure properties such as the crystal arrangement, the single crystal information also includes the elastic, the thermal and the plastic properties. The elastic properties consist of a compliance matrix. The literature usually gives appropriate values for the crystal compliance matrix but it can be refined in order to fit the experimental results. The plastic properties are a list of slip planes and information relative to their hardening behaviour: the Voce law and the self and latent hardening parameters. For each slip system, the Voce law is defined by four parameters $\tau_0, \tau_1, \theta_0, \theta_1$ and the Voce threshold shear stress τ_{Voce} for a slip system evolves with regards to the total shear strain Γ accumulated in the grain by:

$$\tau_{Voce}(\Gamma) = \tau_0 + (\tau_1 + \theta_1.\Gamma).\left(1 - e^{\frac{-\theta_0.\Gamma}{\tau_1}}\right) \qquad \textit{Eq. 14}$$

This hardening law is represented in Figure 12.

This Voce threshold would appropriately represent the critical resolved shear stress of the slip systems if they were all independent. However in practice there are a lot of interactions between the systems. To represent these interactions, some empirical coupling coefficients are introduced in the form of self and latent hardening parameters. The former accounts for the obstacles generated by slip in the system considered. The latter represent the obstacles

from dislocations generated by other slip systems of the same or from a different deformation mode. The variation in the critical shear stress for slip system s is thus written as:

$$\dot{\tau}_s = \frac{d\tau_s^{Voce}}{d\Gamma} \sum_{s'} h_{ss'} \dot{\gamma}_{s'} \qquad \textit{Eq. 15}$$

where $h_{ss'}$ is an interaction parameter representing the hardening induced on s by the activation of s' and $\dot{\gamma}_{s'}$ is the increment of shear strain for the slip system s'.

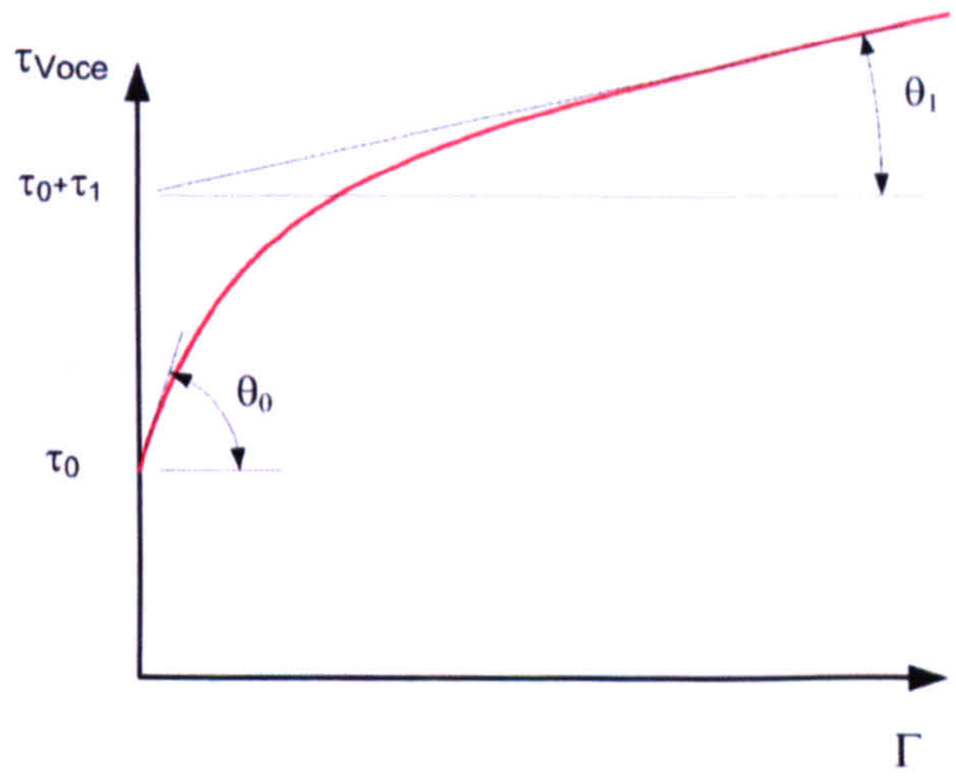

Figure 12 Graphical representation of Voce law

The parameters defining the Voce law and the coupling coefficients are the main parameters to adjust in order to fit the experimental data. Since they are used to derive the critical resolved shear stresses, these parameters determine whether a slip system in an inclusion is active or not. It is essential for the computation of the elasto-plastic tensor L_c of the inclusion.

Mechanical twinning is a deformation mechanism which accommodates strain by rotating part of the crystal. This mechanism is characterised by a nucleation phase, where the twin is formed, and a propagation phase, during which the twin grows. In this version of the model, twinning is treated in the same manner as slip with a CRSS based on Voce law and the interaction hardening parameters [34]. The modelled mechanism is therefore very

simplified and doesn't account for the nucleation phase, the stress relaxation associated and the grain reorientations.

The model also requires information regarding the applied process. The process is defined by the boundary conditions in stress and strain. For example for a uniaxial compession in stress control, the boundary stress conditions will be set to 0 except along the compression axis where the stress will be set to the value to reach at the end of the process. No strain boundary conditions will be set. The definition of the number of steps during the process is quite important: if not enough (i.e. too large) steps are defined, the model will yield incorrect results since the calculations are carried out in a forward integration scheme. Figure 13 shows how the too large strain increments can result in overshooting of the stress (the model overshoots because the flow curve is concave). The effect is particularly emphasised when there is a strong gradient in the evolution of the tangent modulus. While increasing the number of steps helps reduce errors, it also means increasing the computation time so a balance must be found.

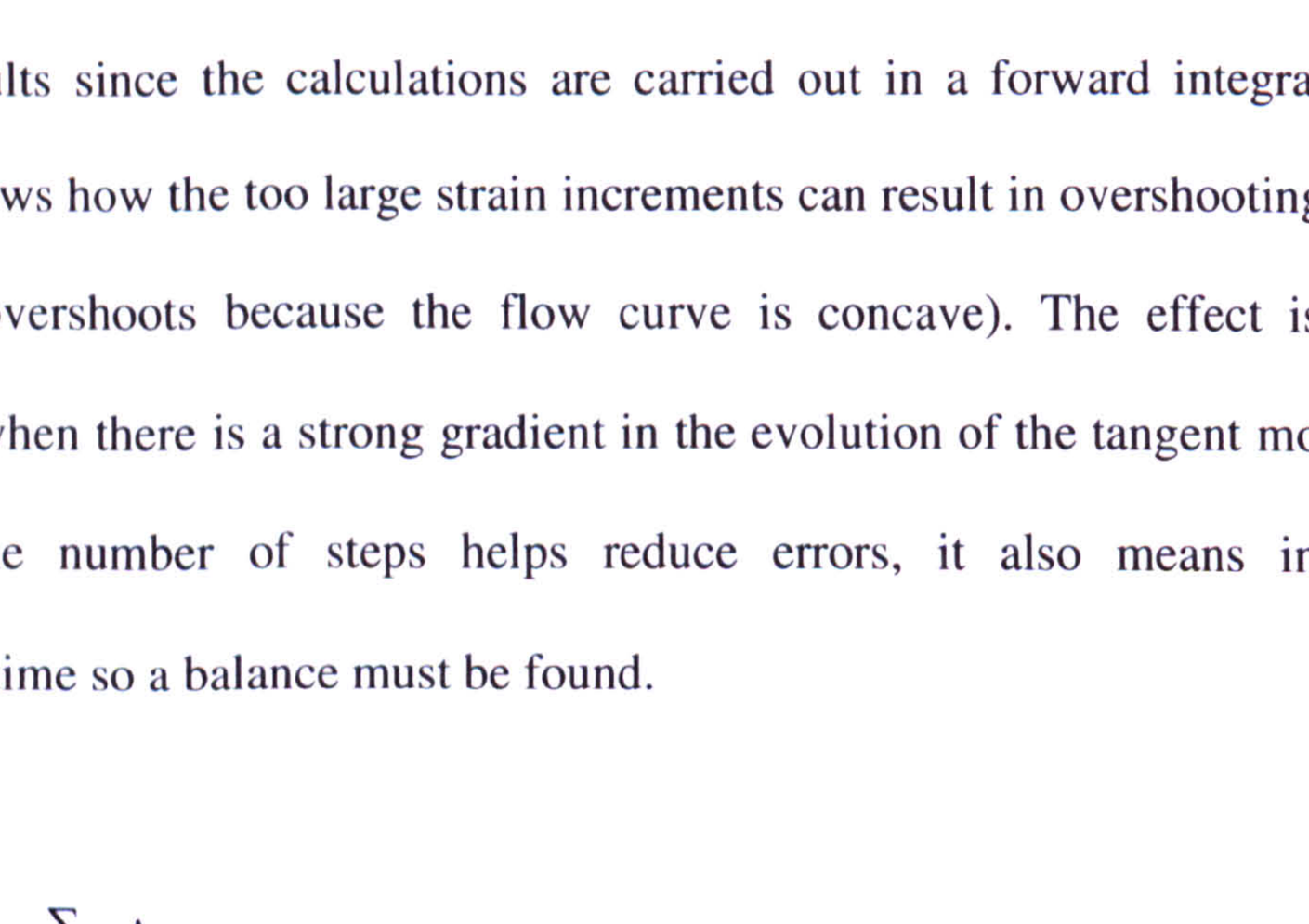

Figure 13 *Demonstration of the error induced by the forward calculation on the uniaxial tensile stress-strain curve*

The model provides several useful outputs for understanding the mechanisms at the level of the inclusions and the polycrystal: evolution of the aggregate and grain stress and strain states, of the overall activity of the different deformation modes, etc... For direct comparison with the diffraction experimental results the model also computes an equivalent elastic strain for each reflection needed: it determines which inclusions are oriented so as to diffract along the specified sample direction (accounting for detector angular span), and computes the elastic strain along this direction for each of these inclusions. The elastic strain for the reflection is the weighted average of these elastic strains over all the diffracting inclusions.

2.3.2.d Limitations

In its present form the EPSC scheme has several limitations. One of the most obvious is the way the interaction between a grain and its surroundings is dealt with: each grain is modeled as an inclusion in a uniform medium that is common for all grains. However this is not really representative of what happens in the material and the boundary conditions imposed on the grain by its neighbour grains might greatly differ from the homogeneous medium.

Some limitations associated with the code used in this work can be dealt with and some updates have actually been published to solve some of them. In the present version twinning is not modeled very well: it is considered as a unidirectional slip. So it doesn't account properly for the finite type nucleation and the relaxation associated, and for the crystal reorientation and texture changes. The approximation can be quite fraught with consequences for materials where twinning is a major deformation mode such as zirconium.

2.4 Conclusion

In this Chapter we explored the different experimental and modelling techniques used in the following Chapters. Diffraction (of neutrons, X-rays or electrons waves) was presented as a tool for probing elastic strains at a microscopic level and for evaluating the texture of materials. The concept of texture was also presented in depth, with considerations towards its representation and the mechanisms responsible for its formation. Finally the elasto-plastic self-consistent model was introduced as a tool for simulating the response of materials to thermo-mechanical loadings with a microscopic approach.

In the next Chapter we will review the state of the art concerning the deformation mechanisms in zirconium alloys.

Chapter 3 Review on the deformation of Zr alloys

3.1 Introduction

For several years now, people have been studying the deformation of zirconium and its alloys. A major review was published in the late 80's by Tenckhoff [18] which described the deformation mechanisms and the links between texture and anisotropy. Recently Linga Murty and Charit [24] wrote another review in the context of a global renewed interest in the subject, as nuclear energy is viewed by an increasing number of countries as playing a major role in the future energy balance. Part of this review was similar to Tenckhoff's but the authors introduced applications to new generations of alloys and focused on recent results on texture developments and anisotropy. These latter two concepts are intimately linked and it is difficult to dissociate them as one influences the other.

Although a lot of studies have been carried out over the past decades on deformation of zirconium alloys, there is still a lot to understand about the deformations at the microscopic level, and the link between micro- and macro- scale deformation. In recent years progress in neutron diffraction techniques has opened new opportunities for improving our understanding by probing information at the grain level.

In this chapter we will review some generalities about the deformation of zirconium alloys as well as the most recent publications on the topic. We will separate the cases of single phase (hcp) and dual phase (hcp/bcc) alloys and focus on their mechanical responses at both macroscopic and microscopic scales.

3.2 Deformation of single phase hcp alloys

3.2.1 The α (hcp) crystal

Zirconium atoms can arrange in two types of crystals. At room temperature, the stable phase of pure zirconium is hexagonal close packed (hcp). The structure starts to transform into body centred cubic (bcc) at around 860°C for the low alloying element content materials such as Zircaloys. The phase transformation is complete at approximately 980°C and the melting point is 1845°C. The addition of certain alloying elements, such as niobium, can stabilise the β bcc phase for temperatures below 860°C down to room temperature. However α hcp stays the majority phase for most zirconium alloys used in the nuclear industry.

In the hcp structure, the atoms are arranged in an ABAB stacking (Figure 14). The unit cell is defined by the vectors $\vec{a}$, $\vec{b}$ and $\vec{c}$ such that the angle $(\vec{a},\vec{b})=120°$, $\vec{c}$ is perpendicular to the plane defined by $\vec{a}$ and $\vec{b}$, and $a=b$. For pure Zirconium, the dimensions of the unit cell are $a=b=3.233$ Å and $c=5.149$ Å at 25°C (according to [35]).

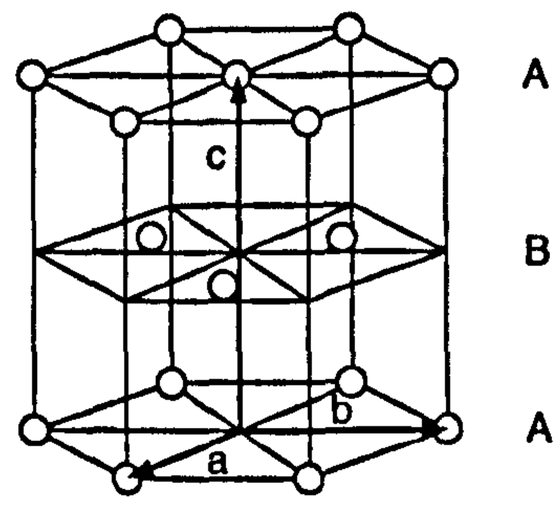

Figure 14 Hexagonal crystal structure

For hexagonal systems, the different atomic planes and directions are usually defined using the Miller-Bravais indices: h, k, i and l, where $i=-(h+k)$ (see Appendix C -). Some families of planes are also known by names in addition to indices: {10.1} and {11.1}

planes are called 1st order pyramidal planes and {11.2} are named 2nd order pyramidal planes. The prismatic planes are {10.0} and the basal planes are {00.2} (Figure 15).

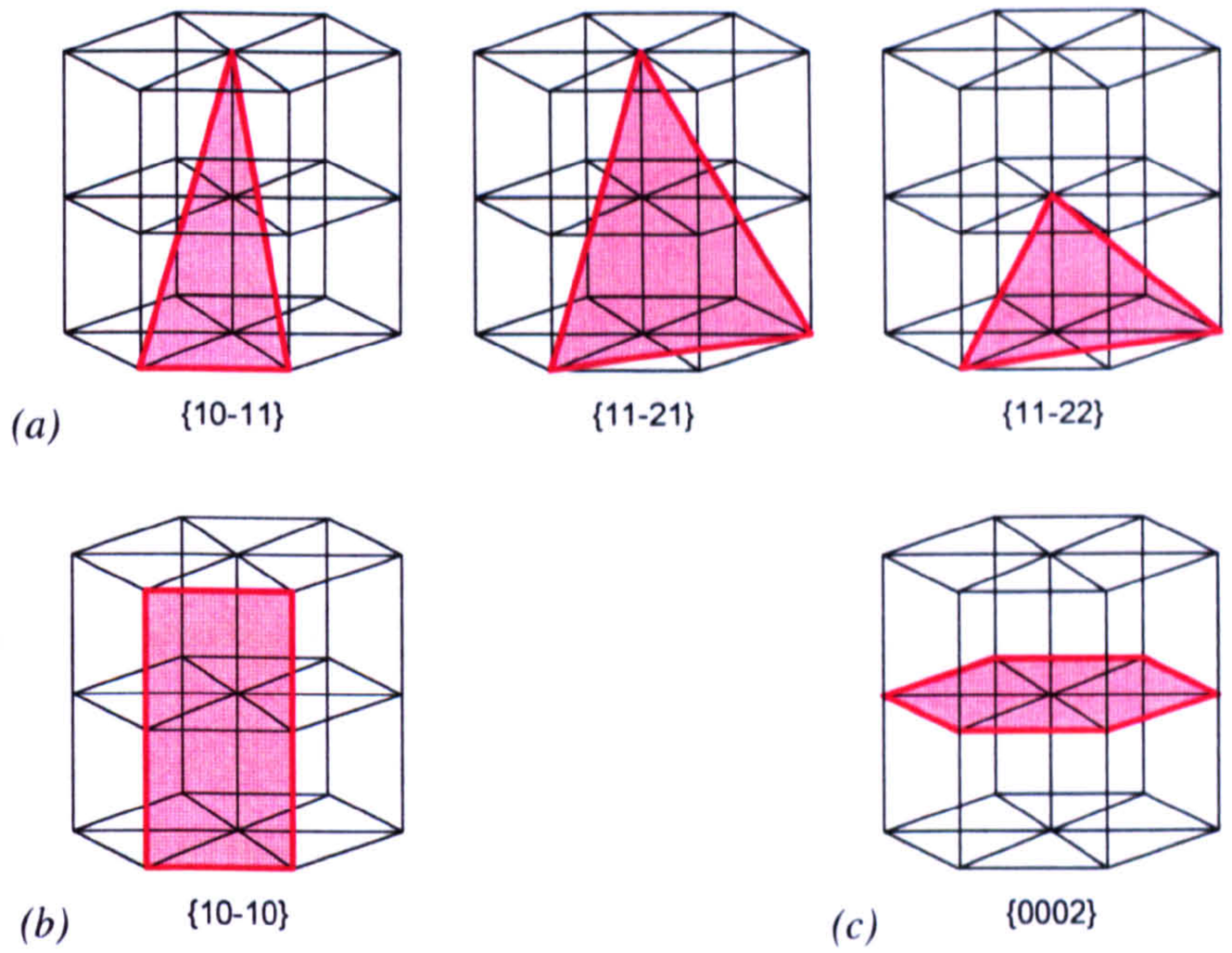

Figure 15 *The main planes in hcp (a) Pyramidal planes (b) Prismatic planes (c) Basal planes*

Two classes of hcp metals are distinguished, discriminated by the *c/a* ratio of the cell. The value of 1.63, corresponding to *c/a* value from the hard spheres packing model, serves as a threshold. Usually elements on the same side of this threshold show similar features in terms of deformation modes. Zirconium in its hexagonal form presents a *c/a* ratio of 1.59, lower than 1.63.

3.2.2 Elastic behaviour of the crystal

The hexagonal structure presents a slight elastic anisotropy. The Young's modulus is invariant by rotation around the <c> axis [5] but varies with the angular position relative to this axis. In Figure 16 the Young's moduli E are represented as the radii in spherical coordinate system referenced to the crystal coordinate system $\{a,b,c\}$. The elastic stiffness

tensor published by Fisher and Renken [36] was used to derive the Young's modulus as a function of the zenith and azimuth angles.

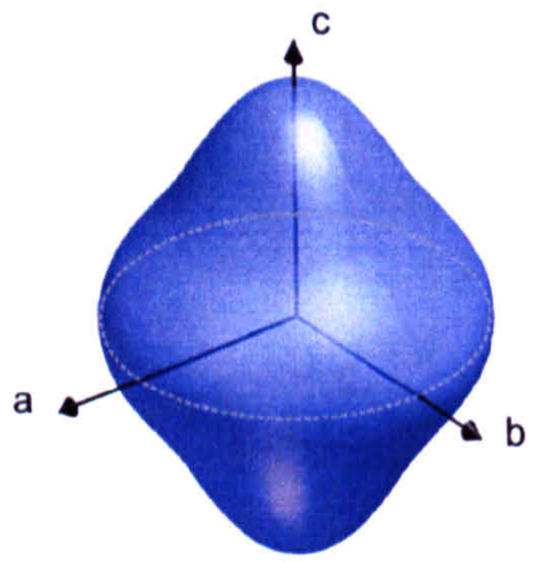

Figure 16 Variations of E (radius of the graph) with the direction considered in the crystal coordinate system

Another way of looking at the crystal elastic anisotropy is to derive the moduli of elasticity for some of the main crystallographic planes. Some values of modulus along typical lattice planes normals are given below:

$E_{10.0}$=99GPa

$E_{10.1}$=89GPa

$E_{00.2}$=125GPa

The extreme values are for the {10.1} and the {00.2} planes and the spread is of 35GPa, i.e. a variation of less than 30%. The elastic anisotropy is thus relatively small compared with some cubic materials (in austenite the variations of Young's modulus are of the order of 300%). The stiffest direction is the <c> axis of the cell.

3.2.3 Deformation modes

Plastic deformation in Zr hcp crystals happens both through slip and twinning.

3.2.3.a Slip modes

Slip is the most common mode of plastic deformation in crystalline materials at ambient conditions. The mechanism consists of the propagation of dislocations that are activated in the presence of shear stresses. Slip is defined by its 'slip plane', which is the plane of propagation, and the slip direction, defined by the Burgers vector.

In general, for a crystal under plastic loading, the selection of the most favourable slip system to activate (among all the potential systems) obeys three laws. The preferred system tends be the one for which:

- The difference is maximum between the applied resolved shear stress and the critical shear stress (threshold stress) of the system.
- The slip plane presents the highest density of atoms.
- The slip direction contains the shortest Burger's vector [18].

The best candidate slip mode for a given loading condition is usually the result of a compromise between these laws: if there is no shear on the most densely populated lattice plane, slip will not be possible on that plane and will happen on a plane less dense but for which the shear stress is high enough. The first criterion is related to Schmid's law which states that slip is only possible if the resolved shear stress applied on the slip plane overcomes the threshold critical resolved shear stress (CRSS).

It has been well established now that the easiest slip system in α zirconium is the prismatic <a> system (described in Figure 17). The prismatic planes in crystals with c/a ratio below 1.63 (as it is the case for α zirconium) are the most densely filled planes (on average). So the second of the criteria described above is fulfilled for this slip mode. Moreover <a> is the shortest available Burgers vector (third criterion). Finally it has been observed that the critical resolved shear stress is relatively low and hence easy to overcome (first criterion). Although some of these criteria are not always sufficient (for example basal slip is the easy slip mode in Mg whereas according to criterions 2 and 3 it should be prismatic slip),

prismatic <a> slip has also been effectively observed to be the easy mode in most Zr alloys. One might want to refer to [37] where it has been observed in single crystals and over a very wide range of temperatures.

The distinction of hcp structures compared to cubic ones is the lower level of symmetry. This particularity affects plastic flow in the hcp crystals. In cubic structures, because of the high level of symmetry, one family of slip systems contains a large number of systems distributed in an isotropic way around the reference cell. For example in Face Centred Cubic (FCC) metals, there are 12 possible slip systems in the $\{111\}<1\bar{1}0>$ family. In general one family suffices to satisfy the Von Mises criterion (which states that five independent deformation modes are necessary for ductility, i.e. arbitrary strain, in a polycrystal) in cubic polycrystals. In the case of Zr, the easy prism slip system only counts three modes which are available in a very anisotropic manner. They occurs on prismatic planes $\{10.0\}$ along $<1\bar{2}.0>$ directions (Figure 17), and according to Schmid's law, this slip can't take place when the cell is deformed along the <c> axis, as no shear loading is applied to the prismatic slip planes in this case. If this system were the only possible mode, the ductility of the material would thus be greatly impaired. Zr is relatively ductile and according to the Von Mises criterion, some other mechanisms are therefore necessary.

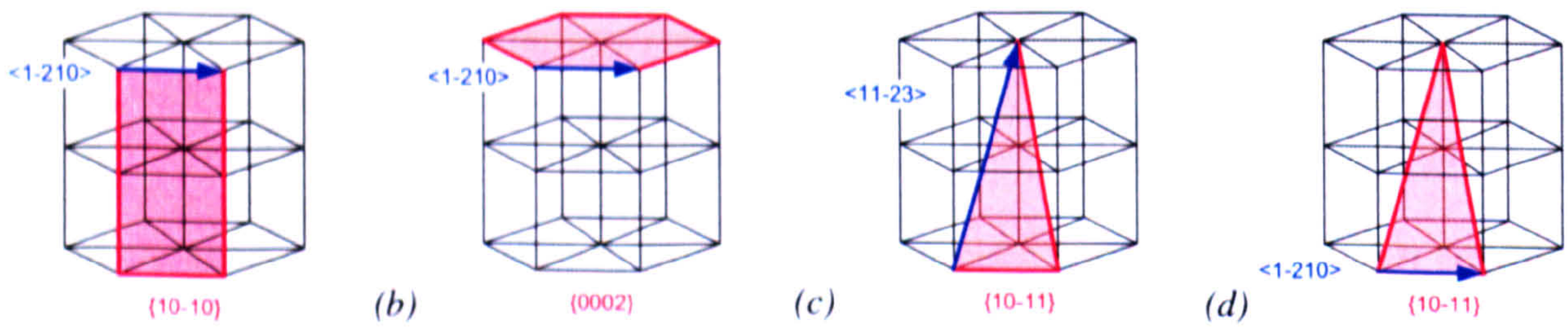

Figure 17 *Slip modes in Zr hcp: (a) prismatic <a>, (b) basal <a>, (c) pyramidal <c+a> and (d) <a> slip*

In theory there are a number of other possible slip systems available in hcp crystals: systems with a <a> Burger's vector slipping on prismatic, basal or pyramidal planes and systems with a <c+a> Burger's vector and prismatic or pyramidal slip planes. However,

not all slip systems are observed at room temperature. Moreover there has been a lot of controversy regarding some slip systems as to whether or not they are activated in zirconium. The reason for this controversy is that dislocations have never been observed directly to give evidence of the activity of these slip systems.

The traditional methods for direct observation of the existence of a slip mechanism call upon single-trace methods on single crystals or transmission electron microscopy. Akhtar observed by trace analysis some evidence of pyramidal slip during the deformation of single crystals of Zr at high temperatures [38]. He determined that <c+a> pyramidal slip happened on the {10.1} plane rather than {11.1} during compression on the <c> axis of the unit cell and identified the system as {10.1}<11.3>. Some published work also backs up this finding (see [39] for more references).

There has been more difficulty establishing whether basal <a> slip was activated at room temperature. Akhtar observed that during the uniaxial deformation of favourably oriented single crystals basal slip could be activated [37]. However he observed it only for deformations at temperatures above 850 K (577°C) and the ease of this mode increased with temperature. Tenkhoff gives some more references to early work suggesting dislocation motion on the basal planes [18]. Some authors claim that there is still no direct evidence for this to date [24]. Xu et al. have indirectly established that basal <a> slip is still a necessary deformation mode in polycrystalline zirconium alloys at room temperature [40]. Their conclusions are based on a back-calculation process: they showed that for their elasto-plastic self consistent model to fit with the results of the uniaxial deformation of a Zircaloy-2 polycrystal in-situ in a neutron beam, basal <a> slip had to be incorporated as a possible system. The model also showed that shortly after this slip mode kicks in, it become the most active mode and its activity represents around 60% of the total activity after 12% compression in the normal direction. This fact has thus been accepted by most

modellers and basal slip is usually included in self-consistent modelling of zirconium alloys.

The same paper concludes that the minimal set of slip systems for modelling uniaxial deformation of single phase zirconium alloys is prismatic $\{10.0\}<1\bar{2}.0>$, basal $\{00.2\}<1\bar{2}.0>$ and pyramidal $\{10.1\}<11.3>$. The pyramidal <a> slip is considered as a less important system.

3.2.3.b Twinning modes

Twinning is also a major deformation mode in most hcp structures. It has been described as being essential for ensuring ductility in some hcp polycrystals [41]: strain compatibility between neighbouring grains can only be obtained if a minimum number of independent deformation systems are available (five according to Von Mises criterion) and twinning mechanisms help compensate for the limited number of slip systems as described in the previous section. When the easily available slip systems can't accommodate loads in some specific directions of the crystal, some twinning systems can take over and ensure ductility. They are particularly important at low and room temperatures because the CRSS of most slip modes increases with lowering temperatures (see [38]), while twinning is relatively temperature independent.

The mechanism of twinning rotates the crystal by symmetry about a plane of atoms, called the twinning plane. For most hexagonal metals, the easiest system to activate is $\{10.2\}<\bar{1}0.1>$ (Figure 18 (a)). It is thus called the "normal twinning mode". This mode can be tensile or compressive on the <c> axis, depending on the c/a ratio. If $\left\|\vec{a}-\vec{b}\right\|=\sqrt{3}.a$ is smaller than c, the system is tensile [18]. So for zirconium this twinning mode is activated by a tensile stress on the <c> axis. Figure 18 (b) shows the result of the

activation of the $\{10.2\}<\bar{1}0.1>$ twins for a tensile load along <c> axis of a zirconium cell. The original and twinned cells, in red and blue respectively, are shown in the $(\bar{1}2.0)$ shear plane view.

From the geometry of the transformation in Figure 18 (c), the shear strain for the $\{10.2\}<\bar{1}0.1>$ twinning is defined by $s = AA'/OA'$ ([42]), so after some derivation, $s = c/(a\sqrt{3}) - a\sqrt{3}/c = 0.167$. Hence the strain gain achieved by twinning is quite small compared to that resulting from slip. Linga Murty et al. [24] mention that the effect of twinning on ductility overtakes largely a simple direct shear gain: twinning can put the crystal in a more favourable configuration for further slip activation where it was not possible before.

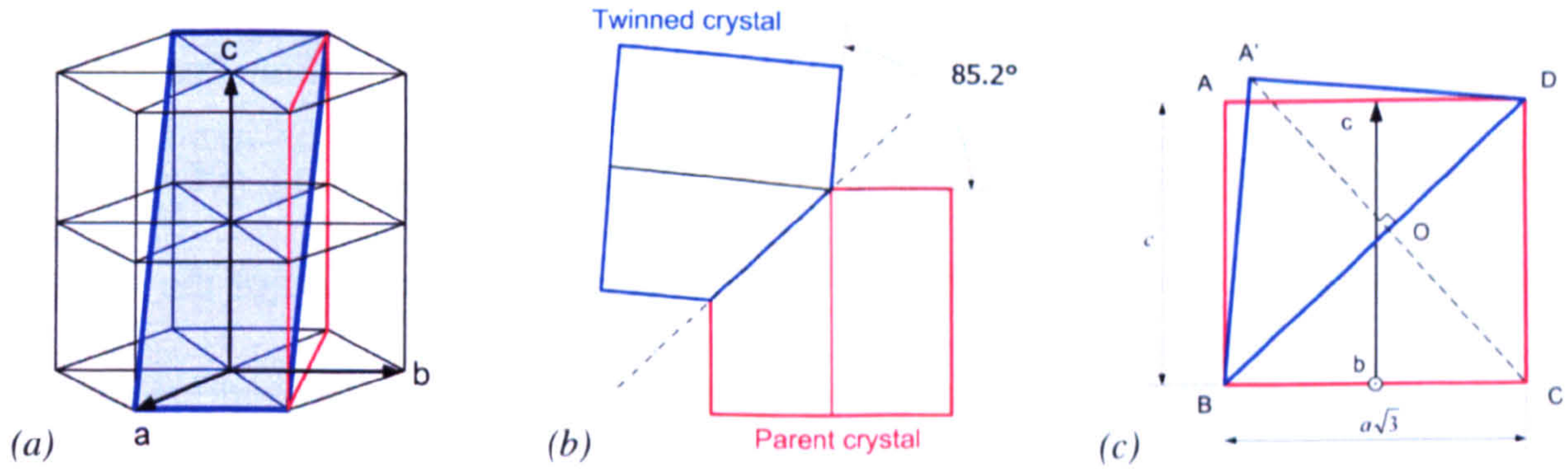

Figure 18 Main tensile twining mode {10-12}<-1011> for a loading along <c> axis; (a) twinning plane (blue) and shear plane (red) in the original cell; (b) original (red) and twinned (blue) cells viewed in projection in the shear plane;(c) Geometry of the transformation.

Other twinning modes are possible and a variety of twinning modes have been readily observed in zirconium especially at low temperatures [18, 43, 44]. Their activity depends on packing parameters and mainly on the c/a ratio. For zirconium the tensile $\{11.1\}<\bar{1}\,\bar{1}.6>$ and the compressive $\{11.2\}<\bar{1}\,\bar{1}.3>$ twins are quite readily seen to operate in addition to the normal mode.

3.2.3.c Particularities of twinning against slip

The process of twinning is substantially more complicated than that of slip. While slip is simply characterised by the propagation of dislocations, the mechanism of twinning must be divided in two phases: nucleation and propagation. Nucleation is extremely rapid. The suddenness of the relaxation associated with it is characterized by typical spikes (load drops) in the stress strain curves of single crystals. It is even believed that there is an overshoot [45]: nucleation is characterized by the abrupt apparition of a finite twin volume (Finite Initial Fraction) that is bigger than the necessary volume to accommodate the strain. Thus nucleation accommodates more strain than needed. The propagation phase corresponds to the expansion of this initial volume and is progressive with applied strain.

It is also not very clear how twinning is initially activated. A lot of authors use a Schmid's law by analogy to slip. For Brown et al. [46] for example, twinning in Mg is governed by a critical shear stress criterion. However the validity of this assumption has often been questioned (see [42] for example). Some authors suggested twinning activation could actually depend on both the hydrostatic pressure and the deviatoric part of the stress, thus rending a critical shear stress criterion unsuitable. Some studies performed by Lebensohn and Tomé [47] and more recently by Zhang et al. [48] showed that the influence of non-shear components had little effect on the CRSS so using a Schmid-like law seems to be a valid approximation for modeling twinning activation. Lebensohn and Tomé based their study on an Eshelby model of a double inclusion representing the twin and parent grains and found that the influence of non shear components is two orders of magnitude weaker than that of shear components of stress. Song et al. conclude that a critical shear stress is necessary for twinning but its value depends on many factors and it is unlikely that we can derive universal values for a particular material [49].

Another contrast between slip and twinning is that while in the case of slip the stress necessary to continue deformation increases with deformation (following a Voce law for example – see page 36), the propagation of twins is typically easier than the nucleation. Finally while slip modes can be activated in a reversible manner, twinning mechanisms are sensitive to the sign of the solicitation shear stress. The $\{10.2\}\langle\bar{1}0.1\rangle$ twinning mode for example is activated when tension is applied on the <c> axis but is not in compression.

3.2.3.d Thermo-mechanical effects on the deformation modes

Slip is very much affected by temperature: thermal activation at higher temperatures makes it easier for dislocations to propagate. Several papers show that the critical resolved shear stress of slip modes in Zr can reduce severely when the temperature increases [37, 38]. On the other hand the activation stress for twinning is only weakly affected by temperature [49]. Thus twinning is a dominant mechanism at low and ambient temperature but is virtually non-existent at high temperatures because slip is privileged.

3.2.4 Macroscopic behaviour of hcp alloys

As described throughout the previous section, some deformation modes in the Zr hcp crystal are easier to activate than others and because of the low symmetry of the crystal, each deformation mode is not available for any loading situation. As a result the plastic response of the crystal varies quite significantly depending on the loading direction. In non-randomly textured polycrystals, this anisotropy at the grains scale can be transferred to the macroscopic level.

The macroscopic behaviours of pure zirconium polycrystals and a large range of α alloys in a variety of processed forms have been extensively studied ([50-53] for example). All cases revealed a strong texture induced anisotropy. For example, when most of the grains are oriented with their basal planes towards a specific direction, this direction is plastically

harder than average. This is due to the lack of easy deformation modes when the <c> direction of the crystal is loaded mechanically: indeed prismatic slip is by far the easiest mode of deformation at room temperature and a <c> axis loading doesn't apply shear on any slip plane of the mode.

Another characteristic of the deformation of textured Zr alloys is the asymmetry of deformation: a difference of behaviour between tension and compression of textured polycrystals has been readily observed in many Zr alloys, especially in terms of yield strength [52, 53]. The unidirectionality of twinning is often a partial explanation of the phenomenon. If most grains are oriented with the <c> axis parallel to the loading direction twinning is likely to be activated at a large scale under tensile loading while the deformation mode will be seldom activated under compression. The result will be a much softer response of the polycrystal in tension. The initial intergranular stress state resulting from prior thermo-mechanical solicitations (manufacturing process, heat treatment...) can also contribute to an asymmetric aggregate response [52].

Some other particularities will be discussed in the experimental results Chapters.

3.3 Deformation of dual phase alloys

Generally, zirconium alloys containing sufficient β stabilising elements such as niobium,will be dual phase at room temperature. For most in-core nuclear structural applications the amount of alloying elements in Zr alloys must be kept to the minimum in order to preserve the low neutron cross section, so the proportion of β phase is generally quite low, typically below 15%. According to the Zr-Nb phase diagram, Zr-2.5%Nb contains theoretically 10% of β phase. However one should be aware that the second phase

is not always a pure β bcc phase, but rather a mixture of β with some intermediate and metastable phases.

The β phase of Zr is body centered cubic. As a consequence, the behaviour of this phase is much more isotropic in the plastic regime than that of the α phase, since the high symmetry of the crystal allows for a large number of uniformly spread systems inside a same slip family. The behaviour of dual phase alloys has been investigated by several research teams. However it is not yet fully understood: while some authors assumed that the second phase of Zr-2.5%Nb alloys was softer than the main hcp phase [54, 55], some results recently published tend to show that the β phase is actually the hard phase of the material [52].

3.4 Recent developments

In the recent years, there seems to be a renewed interest in understanding twinning in general, especially in hcp crystals. Some relatively modern techniques allow a different approach for studying the mechanism and complement more conventional TEM-based studies. There is also an increasing need to improve models by including an appropriate representation of the twinning mechanism for cases where it represents a significant proportion of the total plastic activity. Several experiments have been carried out on Zr or Mg alloys, to try and understand the effect of material properties (grain size, texture...) on the twinning mechanism. On the modeling side of things considerable efforts have been made to include a more realistic mechanism in the current self consistent models [45]. A numerical approach with an energetic point of view on the mechanism brought some insight on how nucleation proceeds [48].

Other recent papers, such as Xu et al. in 2008 [40], still try to establish the presence of some deformation mechanisms such as basal <a> slip during deformation of zirconium

alloys at room temperature. There is also uncertainty why twinning is more or less activated in some zirconium alloys than others: it has been observed during diffraction experiments on many Zircaloys but not in Zr-2.5%Nb so far [52].

3.5 Conclusion

The anisotropy of the α structure of Zr was evidenced in this review of the literature. It is particularly clear that the response of the crystal to plastic loading is very dependent upon the direction of loading. This results in direction-dependent heterogeneities in polycrystals, where the heterogeneities are the grains themselves. Also twinning seems to be a major deformation mode, and although its contribution to the strain is lower than that of slip, it has a strong effect on the texture of polycrystal aggregates.

In the next Chapter, we will describe and characterise the two materials used to carry out the experimental work: a rolled plate of Zircaloy-4 and a pressure tube of Zr-2.5%Nb.

Chapter 4 Materials and characterisation

4.1 Zircaloy-4

The first material used in this work is hot rolled Zircaloy-4. The 6mm thick plates were produced by Wah Chang, USA according to ASTM standards (ASTM B352, Grade R60804). The material was provided by INVAP, Argentina and consisted of a set of plain and welded plates. Such plates are used for the manufacture of reflector vessels in nuclear reactors such as OPAL, the open pool research reactor at ANSTO, Australia [56]. The reflector vessel is an essential part of the design of such reactors: it contains the heavy water that is used for moderating and reflecting the neutrons back to the core in order to maintain the reaction.

The samples are referenced by the principal processing directions: rolling direction (RD), transverse direction (TD) and normal direction (ND).

4.1.1 Composition

The composition of Zircaloy-4, usually abbreviated Zry-4, is shown in Table 1. This alloy was derived from Zry-2 by removing nickel as an alloying element, as Ni was found to increase hydrogen absorption and thus participate in hydride embrittlement [24].

Zirconium (Zr)	Tin (Sn)	Iron (Fe)	Chromium (Cr)	Oxygen
rest	1.20 – 1.70 wt%	0.18 – 0.24 wt%	0.07 – 0.13 wt%	1200 - 1300 ppm

Table 1 Chemical composition of Zry-4 according to ATI Wha Chang [57]

According to Grange [58], oxygen and tin are interstitial in the lattice. Oxygen atoms are naturally present in the zirconium matrix and occupy octahedral sites. They have a strong

effect of strengthening, by interacting with the dislocations. Tin might also participate in improving mechanical properties. Iron and chromium on the other hand have a lower solubility in α Zr and tend to precipitate as fine particles, mostly $Zr(Fe,Cr)_2$. Iron and chromium are mainly introduced to improve resistance to corrosion.

4.1.2 Microstructure

Figure 19 shows some micrographs from optical microscopy performed on the material in the three principal cross-section planes. The samples were mounted in Bakelite, ground and mechanically polished down to a 6 micron paste, and finally chemically polished by swabbing with a cotton cloth soaked with a solution of (45% H_2O, 45% HNO_3, 10% HF). The grain boundaries were difficult to see directly: the alloy is single phase α with a very low proportion of non soluble alloying elements that do not necessarily precipitate at the grain boundaries. Hence the micrographs were performed under polarised light in order to highlight the grain misorientations and reveal the microstructure. No comparative and quantitative conclusions should be made about the grains orientations from the micrographs though, as the polarisation set up was not calibrated and different polarisation settings have been used in each case.

The microstructures show a rather uniform and equiaxed grain shape. The grain size is quite uniform too and the diameters lie in the range 10 to 20 microns. The white intragranular particles visible in all the micrographs are suspected to be second phase precipitates. In rolled Zry-4, Kammenzind et al. [59] found similar intragranular particles and determined using Energy Dispersive X-ray Spectroscopy (EDS) that the particles were fine precipitates containing Zr, Fe and Cr. They measured an average precipitate size of 0.25 microns which seems to be consistent with what we observe.

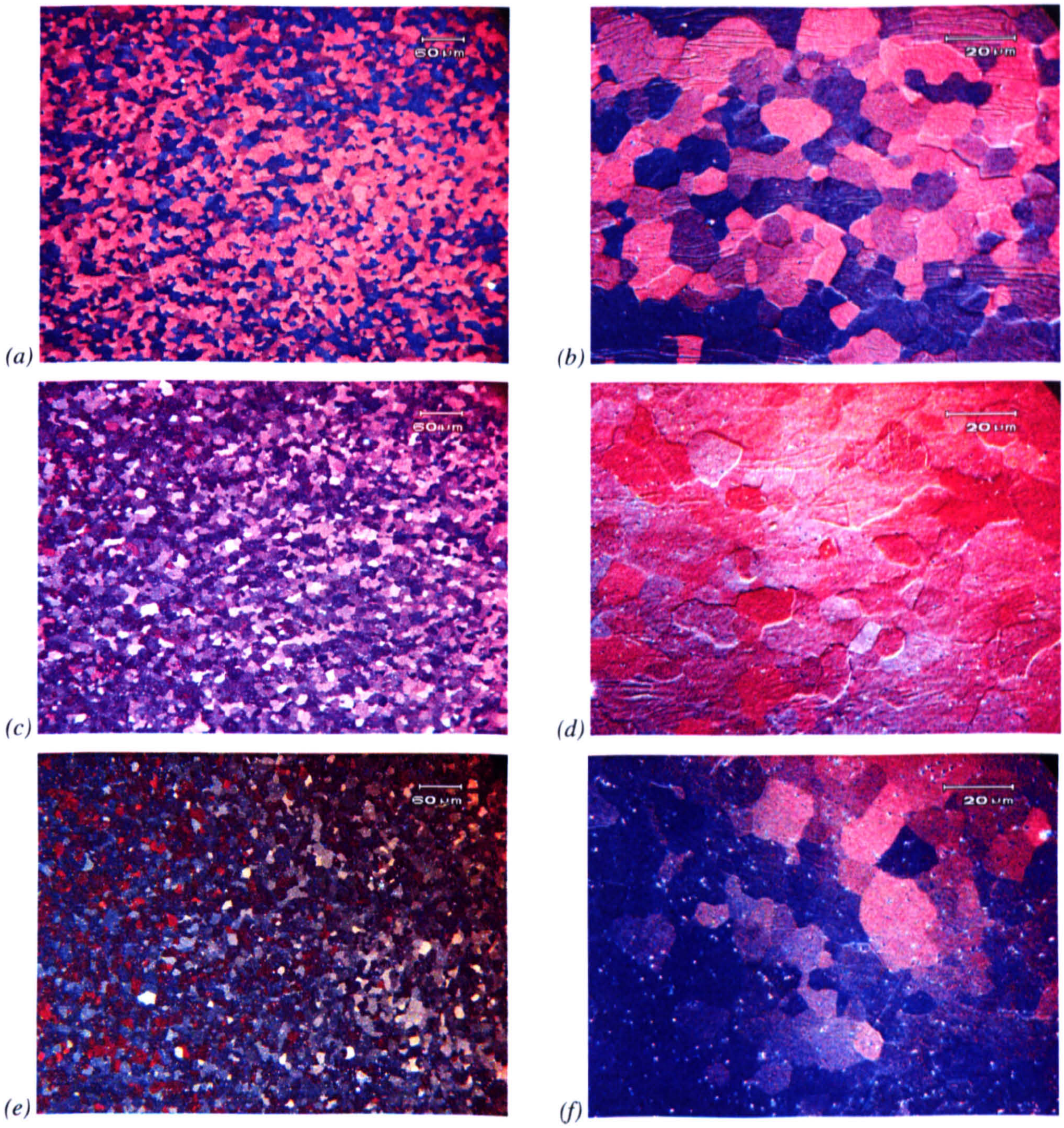

Figure 19 Microstructure in the Zry-4 plate in RD cross-section (a) and (b), TD cross-section (c) and (d), and ND cross-section (e) and (f) (objectives X20 and X100)

Some smear lines are consistently visible at higher magnification. Although these lines appear after polishing, they do not depend on the polishing or grinding directions. They are only visible in the RD and TD cross sections, and are generally oriented perpendicular to ND. It is not yet understood if these lines have a link with the processing history of the material.

An EBSD mapping was also performed on a RD-TD surface of an electropolished sample. The step size was 0.5 microns and the precipitates were not detectable. In Figure 20, the

colour of a pixel is defined by a RGB (Red-Green-Blue) colour coding such as $RGB = \left[255 \times \varphi_1 / 180;\ 255 \times \phi / 180;\ 255 \times \varphi_2 / 60 \right]$, with φ_1, ϕ and φ_2 being the Euler angles as measured at that point. Hence each colour corresponds to a crystal orientation, and the grains are visible as clusters of pixels with a similar colour. The indexing was successful with a rate above 80%. Most of the non indexed points were grain boundaries and were removed using the inbuilt extrapolation software in this figure.

Figure 20 EBSD mapping of Zry-4 on the ND cross-section

4.1.3 Texture

Several techniques have been used to evaluate the texture of this material. Figure 21 shows pole figures for the most common reflections using EBSD, X-rays and neutron diffraction. The different methods are described in Section 2.2.

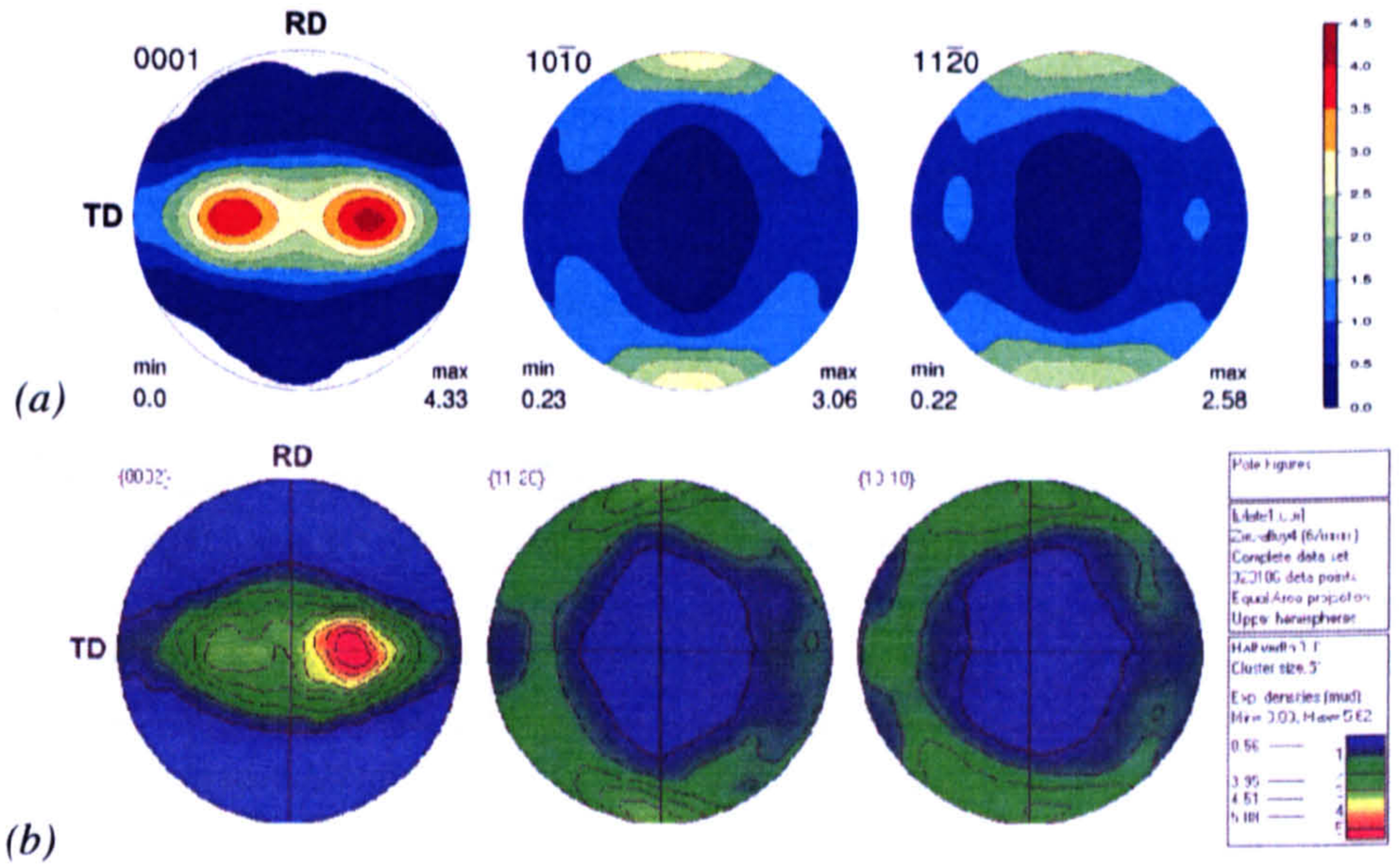

Figure 21 *Equal area projection pole figures (a) from a neutron texture measurement at HIPPO and (b) from an EBSD measurement in the mid section plane*

The main pole figures are represented in Figure 21 based on neutron and EBSD measurements, with RD, TD and ND being the vertical, horizontal and centre poles respectively. The texture commonly observed in rolled Zr alloys is also observed here, with the two characteristic 'eyes' in the basal pole figures: a large proportion of the grains are oriented such that the <c> axis is tilted by around 30° to 35° from ND towards TD. There are virtually no basal pole aligned towards RD.

From the neutron data, the {10.0} and {11.0} pole figures are qualitatively very similar with strong poles in RD. Part of the intensity of these poles is a result of the double pole in the {00.2} pole figure: even if the crystals represented in the basal poles were randomly distributed by rotation around the <c> axis, both the {10.0} and {11.0} pole figures would show high intensities in the RD because both the basal maxima (at +/- 30°) would contribute to the {10.0} and {11.1} intensity. However along RD the {10.0} intensity is slightly higher than the {11.0} intensity, at 3 and 2.6 multiples of random respectively and the {11.0} pole figure reveals some intensity peaks in the ND-TD plane. Hence it seems there is a slight preferred orientation for the prismatic planes too, with {10.0} planes towards RD. Figure 22 is a schematic of the two preferred orientations in the plate.

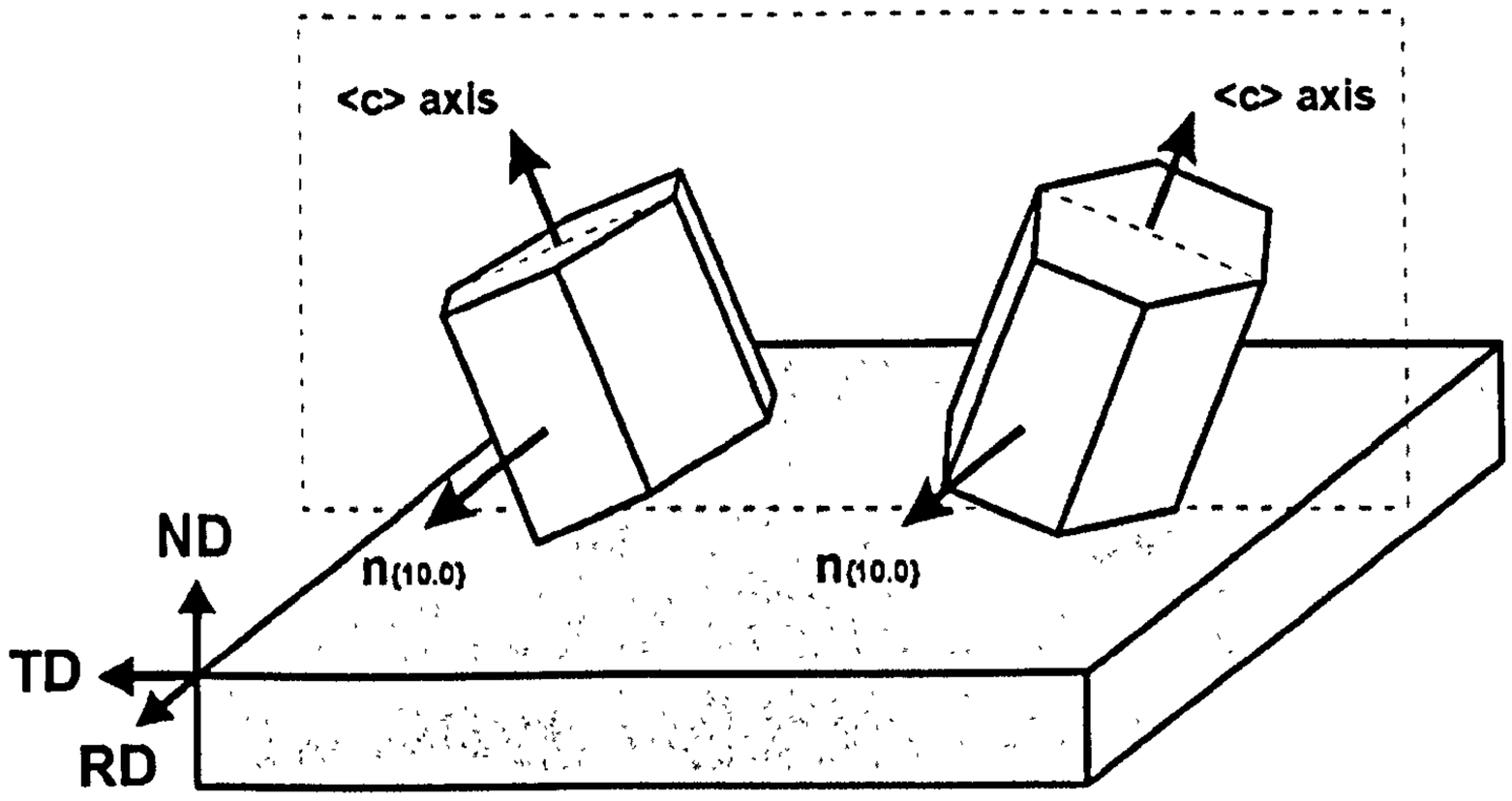

Figure 22 Schematic representation of the preferred orientation in the Zry-4 rolled plate

The measured {00.2} pole figures are not perfectly symmetric. Although the phenomenon is more pronounced in the EBSD data, the asymmetry is also present in the neutron diffraction data and it was consistently observed through several EBSD measurements. Hence it is quite unlikely to be resulting from measurement issues. The initial EBSD measurements were performed on the top surface of the plate so the first conclusion was that there could be some through thickness texture gradients and that the texture of the plate presents some shear on the surfaces that balances out over the whole thickness. Such things have already been observed and reported on some mechanically processed materials [18, 60]. However in our case, the same asymmetry was observed in the neutron measurement which is a bulk averaged measurement and in EBSD measurements executed in the mid-section plane. It could be a result of some asymmetry in the rolling process itself: a practical sheet rolling process has less symmetry than in the ideal case [60]. This would imply a texture gradient along TD and if the texture is measured far from the RD/ND mirror plane and close to the edge of the sheet, one would observe such asymmetry in the pole figures. However several EBSD tests have been performed in different parts of the available piece of material and showed only small texture variations. Hence it is not very clear why the texture should present this asymmetry.

The maximum intensities in the basal pole figures are 4.3 and 5.6 m.r.d. (multiples of random) for the neutron and EBSD measurements respectively. Even allowing for sample to sample variations and the fact that the techniques are not sampling over the same volume, it seems that EBSD yields much sharper textures. Actually the neutron data is likely to be smoothed due to the measurement technique: HIPPO is an instrument with a limited number of detection banks each representing a large solid angle (around 10^{o} to 15^{o} [61]) and the whole orientation space is not fully covered (see Chapter 7 for more details). As a result sharp poles can escape the coverage or be smoothed by the averaging over the detector banks. Moreover the data fitting by varying spherical harmonics might not capture strong textures perfectly. On the other hand the EBSD data results from direct orientation measurements and the pole figures can be obtained by descretisation over smaller clusters (5^{o} in Figure 21 (b)).

4.2 Zr-2.5%Nb

The second material used for the experiments in this thesis was a CANDU pressure tube. These tubes are used as pressure vessels in which the fuel element bundles are fitted (Figure 23). Jovanovic et al. describe the process of obtaining the tubes in [62]: the material is extruded in the (α+β) region prior to being cold worked and heat treated. The diameter of the tube is 104 mm and the wall thickness is 4.4 mm.

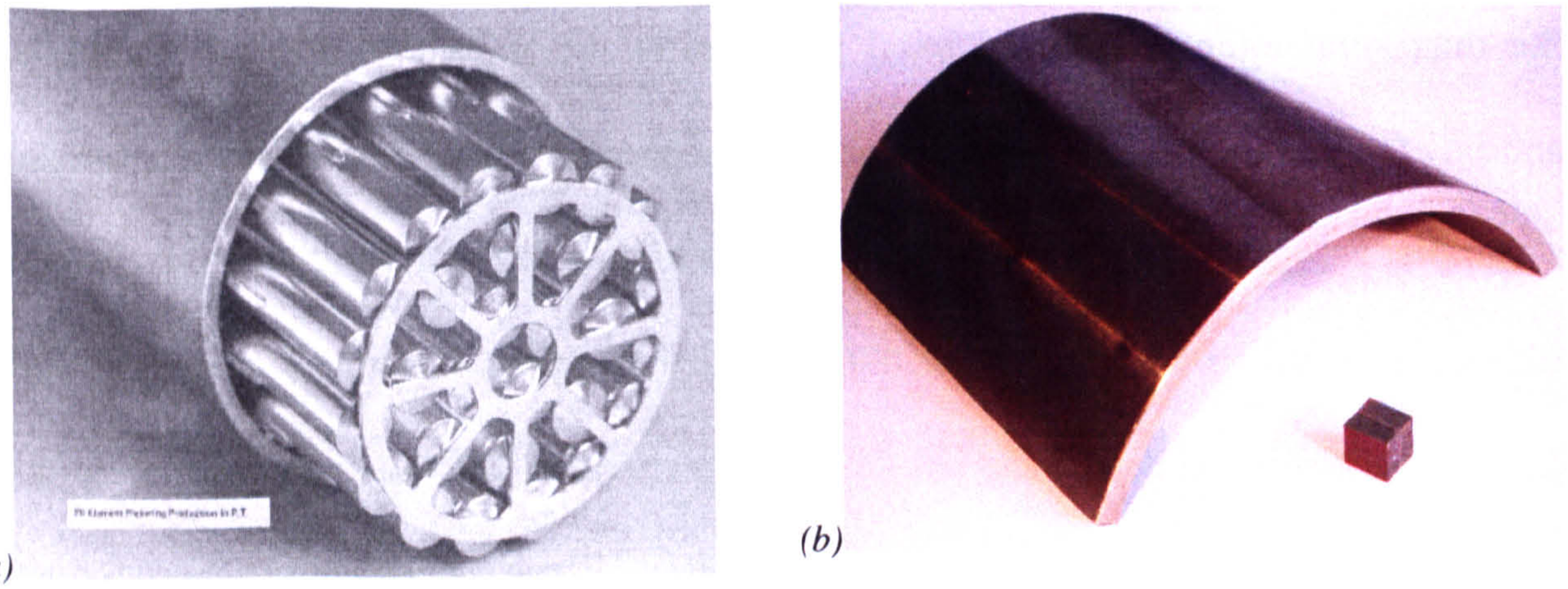

Figure 23 (a) Pressure tube with bundle [63] and (b) piece of pressure tube and sample as used in Chapter 5

4.2.1 Composition and Microstructure

Zr-2.5Nb is a binary alloy with 2.5% by weight of niobium to increase strength. The β-stabilising property of Nb is responsible for the second phase being present, in addition to the α (hcp) phase. After extrusion and autoclaving, the material contains approximately 10% of β_{Zr} (bcc) at room temperature [62]. This phase is only metastable and can further change into β_{Nb} via some intermediate ω phase.

Some optical microscopy has been performed on the piece of material using similar grinding and polishing techniques as described in Section 4.1.2. Figure 24 shows micrographs of the material taken in two of the principal planes. The α grains appear flat and elongated with the approximate dimensions: 1 μm in the radial (RaD), 10 μm in the hoop (HD), and 20-30 μm in the axial (AD) direction. The second β-phase (in black on the micrographs) is intergranular around the α phase grains. This microstructure is typical for pressure tubes [64].

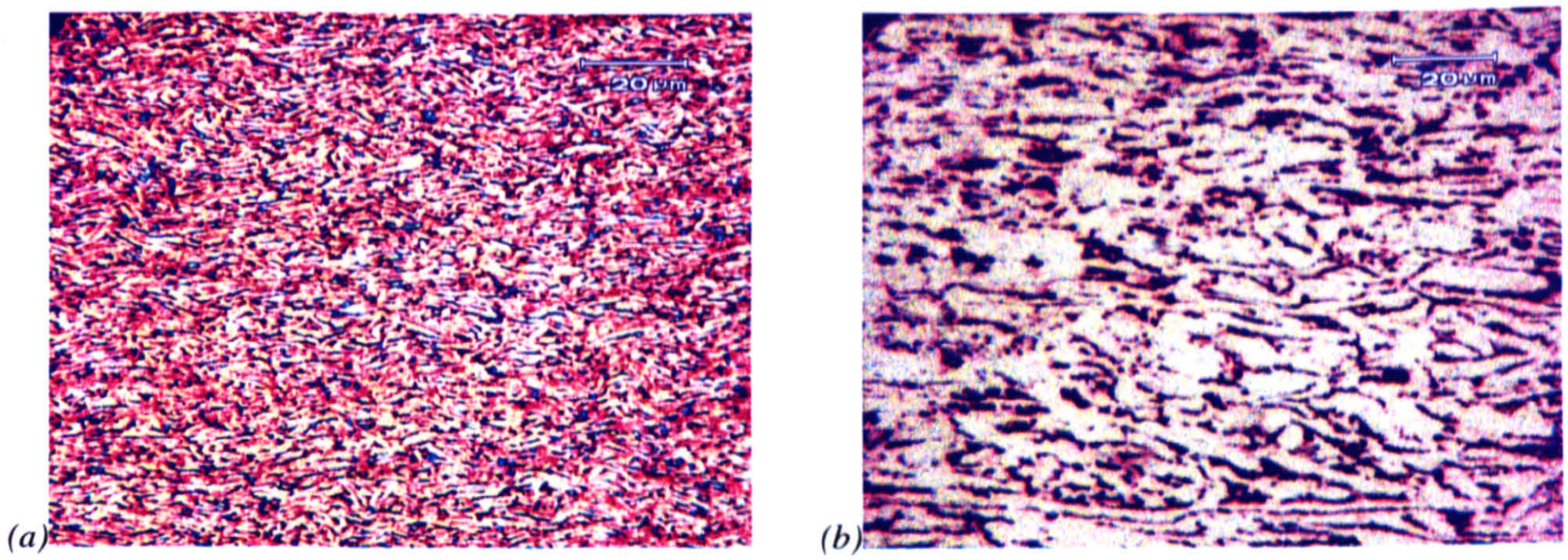

(a) (b)

Figure 24 (a) Axial cross section (b) Radial cross section

4.2.2 Texture

Similar to Zry-4, some neutron diffraction and EBSD texture measurements were performed on the Zr-2.5Nb material and the pole figures are shown on Figure 25 and Figure 26. The α phase is strongly textured with a high proportion of basal planes in the hoop/radial plane. There is a strong basal pole in the hoop direction with an intensity above 7.5 times random according to the neutron results (Figure 25). On the other hand the maximum intensity in the EBSD results is above 18 m.r.d. (Figure 26 (a)). As discussed previously, the measurement and analysis methods with the HIPPO instrument tend to smooth sharp textures which can lower the maximum intensity and explain the difference. However here, the EBSD measurement cannot be trusted fully: the sample preparation was not very satisfactory and only 30% of the points on the map could be indexed. Although the number of grains sampled is certainly enough to ensure statistical accuracy, there is no guarantee that the indexing effectively is random. We can imagine that the quality of the surface locally and of the Kikuchi patterns could depend on the grain orientations (due to different levels of deformation in different grains for example). If such is the case some orientations are privileged in the indexing and thus over represented in the texture, yielding biased results. Also the β indexed points represents only 0.5% of the number of the total

indexed points, where the second phase is in theory 10% of the volume. So there is more difficulty at indexing the β phase than the α phase.

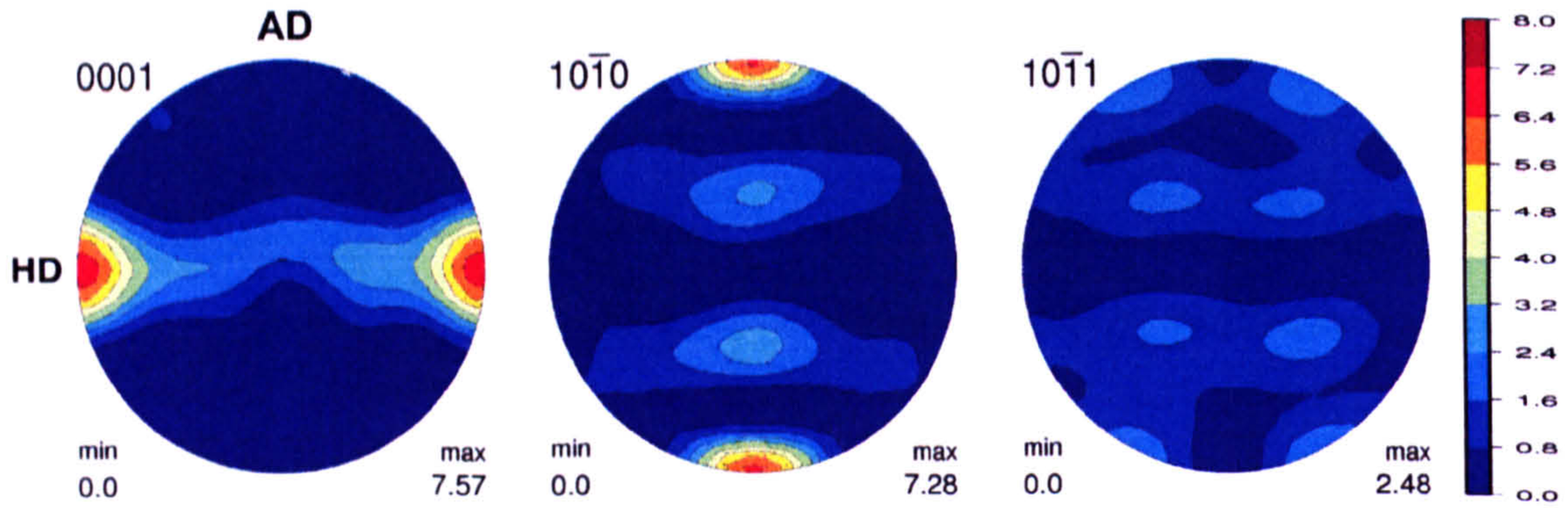

Figure 25 Pole figures from neutron diffraction for the α phase in Zr2.5%Nb

The texture of the β phase could not be measured on the neutron instrument because the diffraction peaks were not visible on the spectra. Some diffraction measurements subsequently performed at ENGIN-X confirm that the second phase peaks are present but are very low and broad (see Section 5.3.2). However they were not all visible in all sample directions, which suggests that there is also a preferred orientation for the β phase. On the other hand some points on the EBSD map could be indexed as β phase and they were used to build the pole figures on Figure 26 (b). It seems to confirm that the beta phase is textured with a cube texture, the {100} planes being oriented along the axial and at 45° between the hoop and radial directions. Once again one should be cautious with these EBSD results with such a low indexing. Moreover the amount of data points indexed (short of a thousand) as β phase is in itself not satisfying for statistics.

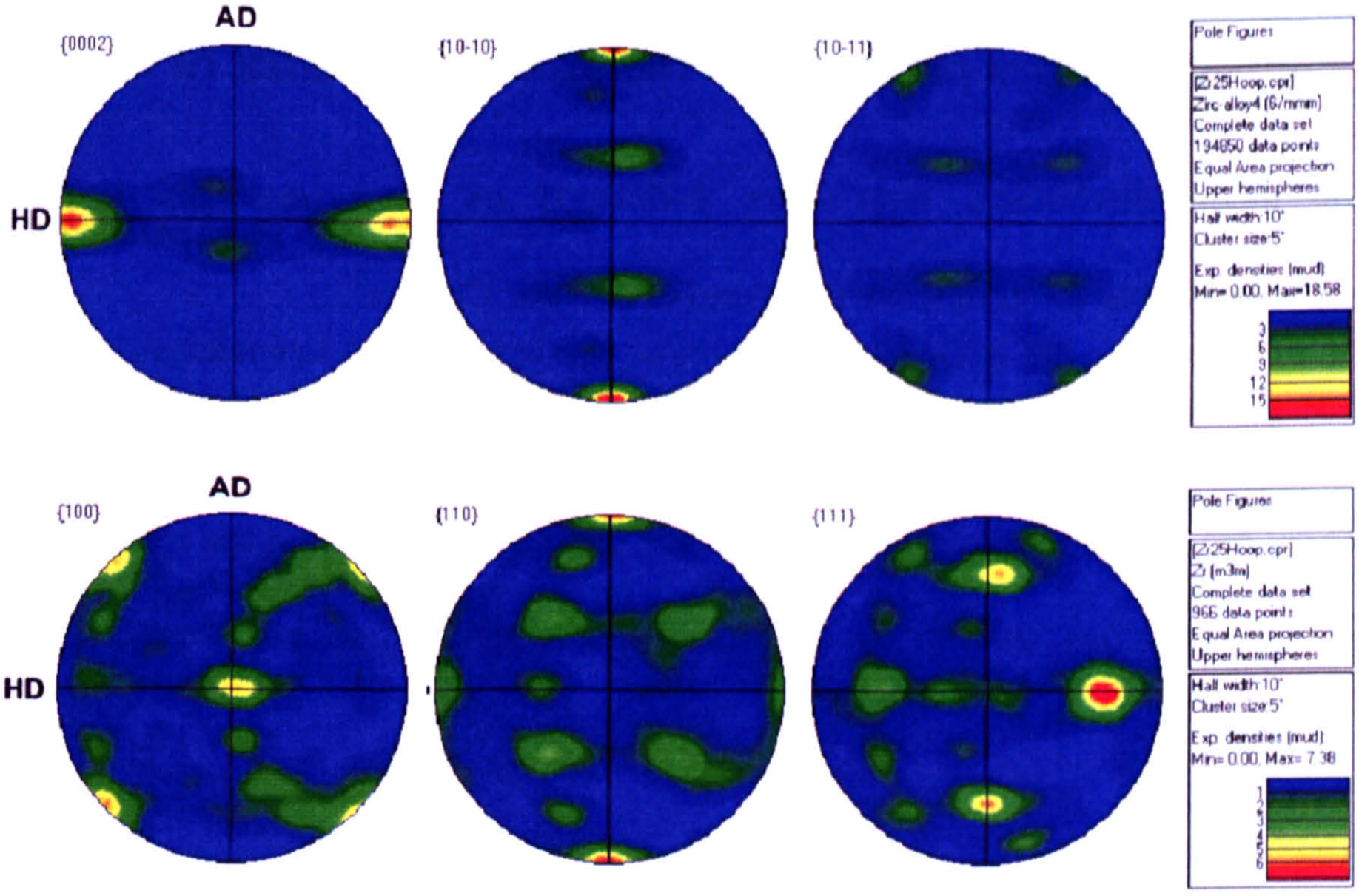

Figure 26 Pole figures from EBSD in Zr2.5%Nb for (a) the α phase and (b) the β phase

There seems to be a Burgers-like relationship between the α and β phases as some $\{110\}_\beta$ are aligned with the $\{00.2\}_\alpha$ [21] (see also Section 2.2.3.b on transformation textures). This would suggest that most of the α texture observed is a transformation texture rather than a deformation texture developed during cooling after the hot extrusion stage and that was mostly retained even after the cold working following extrusion. Supporting this hypothesis, Kapoor et al. [55] and Kiran Kumar et al. [65] also found that the cold working step had little effect and didn't change the main features in the texture of Zr-2.5%Nb.

4.3 Conclusion

The two alloys were introduced and characterised. The microstructures of Zircaloy-4 revealed equiaxed grains with an average diameter of around 20 microns. In Zr-2.5%Nb, the α grains are very flat in the {AD;HD} plane with a thickness of 1 μm along RaD; the β grains take the form of thin laths surrounding the a grains. Both materials are highly

textured with a low proportion of basal orientations towards RD and AD for Zry-4 and Zr-2.5%Nb respectively.

Some thermo-mechanical tests were performed on these materials in-situ in a diffractometer, and the results are discussed in the next Chapter.

Chapter 5 In situ compression diffraction experiments

5.1 Introduction

In-situ thermomechanical tests carried out within a neutron beam are very valuable tools for investigating material behaviour at the microscopic level. In this chapter the results of such experiments are presented for the two zirconium alloys characterised in the previous chapter, Zircaloy-4 and Zr-2.5%Nb in the form of a rolled plate and a pressure tube respectively.

5.2 In-situ compression of Zircaloy-4

5.2.1 Samples

Six coupons were produced, each consisting of two 6mm cubes glued together. This was necessary in order to provide a sufficiently large gauge volume to obtain diffraction data in a reasonable time and avoid obscuring of the centre of the samples by the grips. The cubes were extracted by electro-discharge machining (EDM) from the parent material, a plasma welded Zircaloy-4 hot rolled plate. The plate, supplied by Wah Chang, USA had been annealed to 450°C over a total period of nine hours to remove residual stresses induced by the processing. The samples were taken at least 17mm from the centre of the weld. Because the heat affected zones are very narrow for plasma welds, it is assumed that the sampled material has not been affected by the process. The cubes were assembled two by two such as to form 6 x 6 x 12 mm^3 coupons for compression along each of the parent plate processing directions (see Figure 27). Three sets of two samples were produced for compression along the rolling (RD), transverse (TD) and normal (ND) directions. Details of the sample directions are given in Table 2.

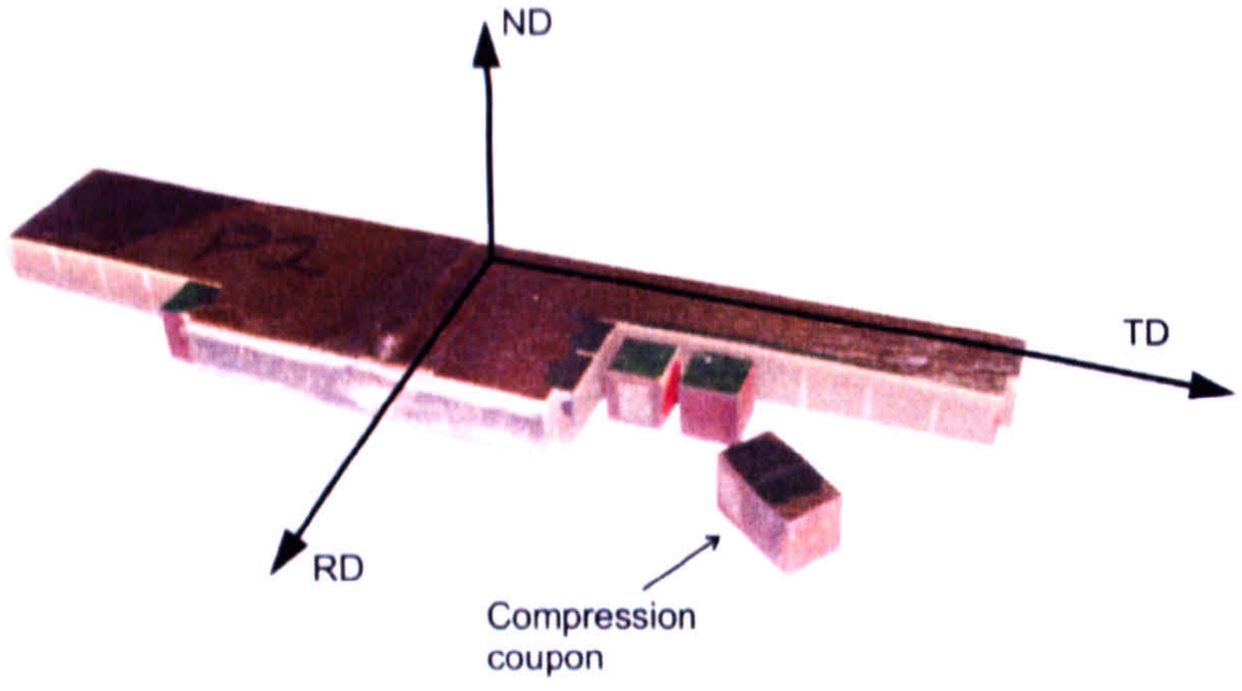

Figure 27 Zircaloy-4 plate and compression coupon

Sample	1	2	3	4	5	6
Compression direction	RD	TD	ND	RD	TD	ND
Measurement direction 1	RD	TD	ND	RD	TD	ND
Measurement direction 2	TD	RD	TD	ND	ND	RD

Table 2 Table of samples

5.2.2 Experimental procedure

The compression tests were carried out in-situ at ENGIN-X, the engineering instrument at ISIS [9, 66]. ISIS is a spallation source where the neutrons are emitted as pulses and directed toward the experimental chamber. The beam is 'chopped' so as to have a well defined range of wavelength (see Section 2.1.5.a). The sample for study is placed in the way of the beam and suitably-oriented grains diffract provided Bragg's law is fulfilled. Two detectors collect the neutrons diffracted at + and – 90° from the incoming beam and their Time of Flight (TOF) is computed. The TOF is directly proportional to the wavelength and the d-spacing of the diffracting reflections can then be derived from Bragg's equation (the d-spacing is used as a gauge of the elastic strain at the grain level). The neutron gauge volume, defined by the incoming slits and the detection collimators, was $4 \times 4 \times 6$ mm^3 and was completely immersed in the samples. For each data point, the neutrons were collected during 6mn.

The samples were compressed using an Instron servohydraulic load frame capable of providing up to 100kN. The rig was in stress control in the elastic region and in position control in the plastic zone. Each single test consisted of a series of strain increments. For each increment of stress or position the actuator was held constant while the neutron measurement was being made. The samples were compressed to approximately 10% total deformation. During the process, three unloadings were also done at 3%, 6% and 10% deformation. These were performed in stress control with neutron measurements at regular intervals.

Thanks to the two detectors the behaviour of the atomic planes could be followed both in the compression direction and one of the Poisson directions. To enable such a measurement the stress rig was placed at 45° with respect to the incoming beam (Figure 28). Thus for compression along one direction, only two tests were necessary to get neutron data in each of the three processing directions, with a duplicated measurement along the compression direction. It is worth also noting that the detectors have an angular span of 30° in terms of 2θ, which means that the strains measured are actually an average of the strains in the reflections oriented towards the processing directions ±7.5° within the sample. The main advantage of a TOF instrument is the wide window of wavelength of the beam. It can generally encompass a large number of diffraction reflections. In our case, to investigate the strong anisotropy in alpha zirconium, it is important to record as many peaks as possible. With a range of wavelength of 2.3 to 5.7 Å, the spectrum of a single measurement covered 12 peaks, which is beneficial in studying zirconium as its hexagonal lattice presents a very strong plastic anisotropy. Most of the first order and some second order crystal planes were recorded (see Table 3). The peaks were fitted individually using Open Genie and the GSAS fitting routine and the TOF profile function 3 which is a convolution of a pair of exponentials and a pseudo-Voigt function as defined in [11].

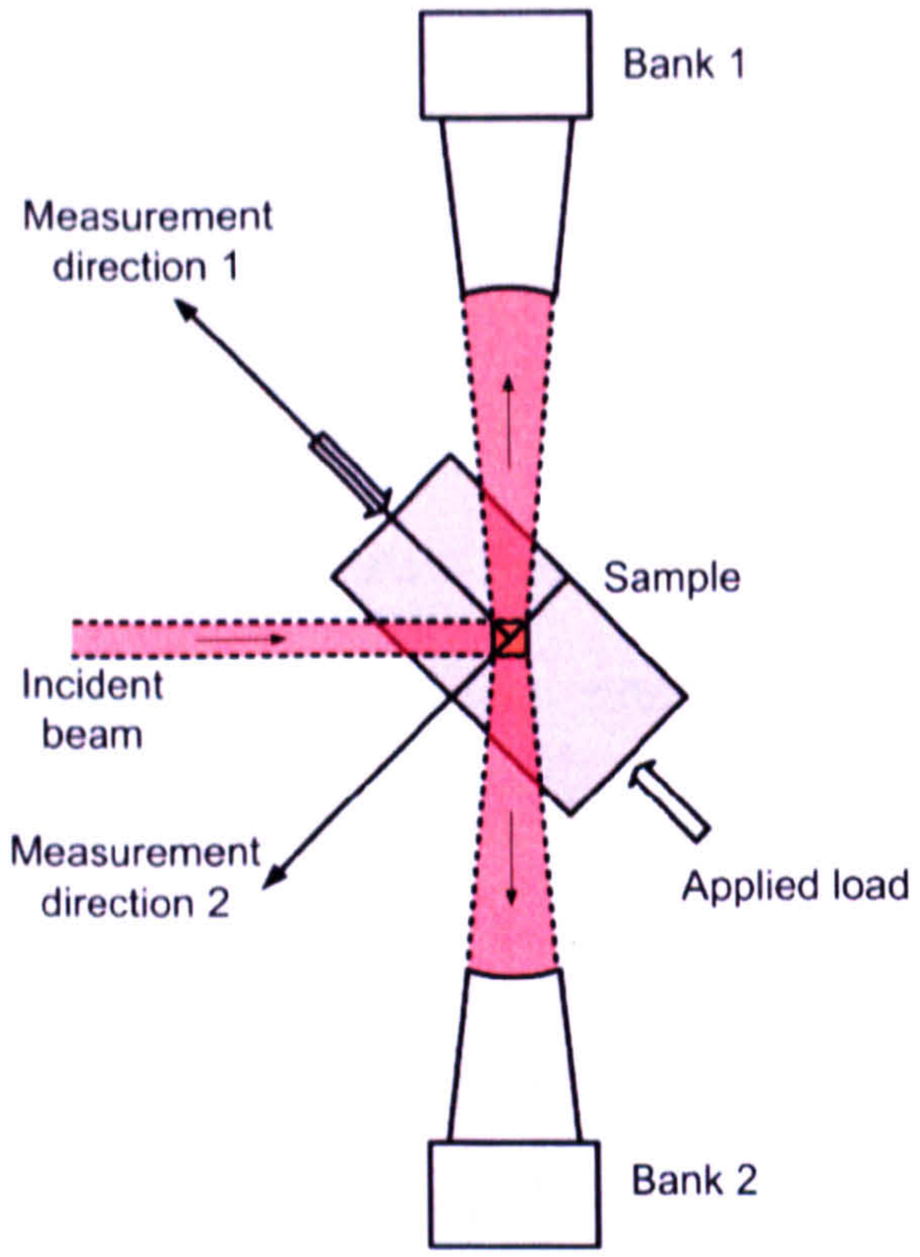

Figure 28 *Set up of the experiment*

	1st Bragg order	2nd Bragg order
Prismatic reflections	{10.0} {11.0}	{20.0}
Pyramidal reflections	{10.1} {10.2} {11.2} {10.3} {20.1}	{20.2}
Basal reflections	{00.2}	{00.4}

Table 3 *List of Zr-α reflections observed in the spectra at ENGIN-X*

5.2.3 Results

5.2.3.a Macroscopic response

The stress was derived from the force applied by the actuator on the coupons and recorded by the load cell. The strain was computed from the position of the actuator piston. As a result the strain is overestimated, as this position-derived strain is not only the sample strain but also incorporates the compliance of the rig. To deconvolute these effects, the rig has been subjected to a compression test with no sample, and the strain calculated from the

position has been corrected: for each level of stress, the position of the actuator without sample was substracted from that measured with sample; this new position was then the one converted into strain.

Figure 29(a) shows the loading curves obtained for five different coupons in terms of true stress and strain. In the elastic part the responses show quite significant differences from sample to sample but these are more artefacts due to uncertainty in the derivation of strain rather than real features. The yield strains of 1% are unrealistically high and suggest that the strain is still overestimated even after the correction. The contribution of the compliance of the rig might not have been completely removed. There may also be some 'settling' (of the grease, the glue, the sample itself...) in the early stage of compression which contributes to the over compliant response. Thus it is difficult to draw conclusions about any difference in the elastic macroscopic response (for compression in TD for example, two tests give dissimilar elastic responses).

The dips in the stress response evident on the flow curves correspond to the holds for the neutron diffraction measurements: where the position is kept constant to allow time for the measurement, the material relaxes and consequently less stress is required. The amplitude of these dips increases with deformation, as there is more plastic flow and more relaxation for higher applied stress. From the response of the five samples tested, three behaviours emerge corresponding to compression along the three processing directions. The differences are mainly observable in the plastic zone. For compression along RD, the material deforms more easily than when compressed in the other directions. The yield strengths for the RD, TD and ND are approximately 350MPa, 380MPa and 420MPa respectively. Not only the yield point but also the rate of hardening varies noticeably depending on the direction considered. For compression in RD, the response exhibits a sharp knee-like yield point, which means that the material flows quite significantly as soon as the yield point is reached. The rate of work hardening seems to increase after 2%

compression. On the other hand, for the other directions the hardening is high at yielding and the rate of hardening tends to decrease with deformation.

To aid visualisation, the stress and strain data were averaged over the time taken for each diffraction measurement. This way the dips are removed from the stress-strain curves and relaxation is included in the average value of stress. Figure 29 (b) shows the time averaged responses for three typical samples. The trends previously described are more evident.

At the end of the test, the loads applied to reach a total strain of 10% were 500MPa, 600MPa and 670MPa for the RD, TD and ND respectively.

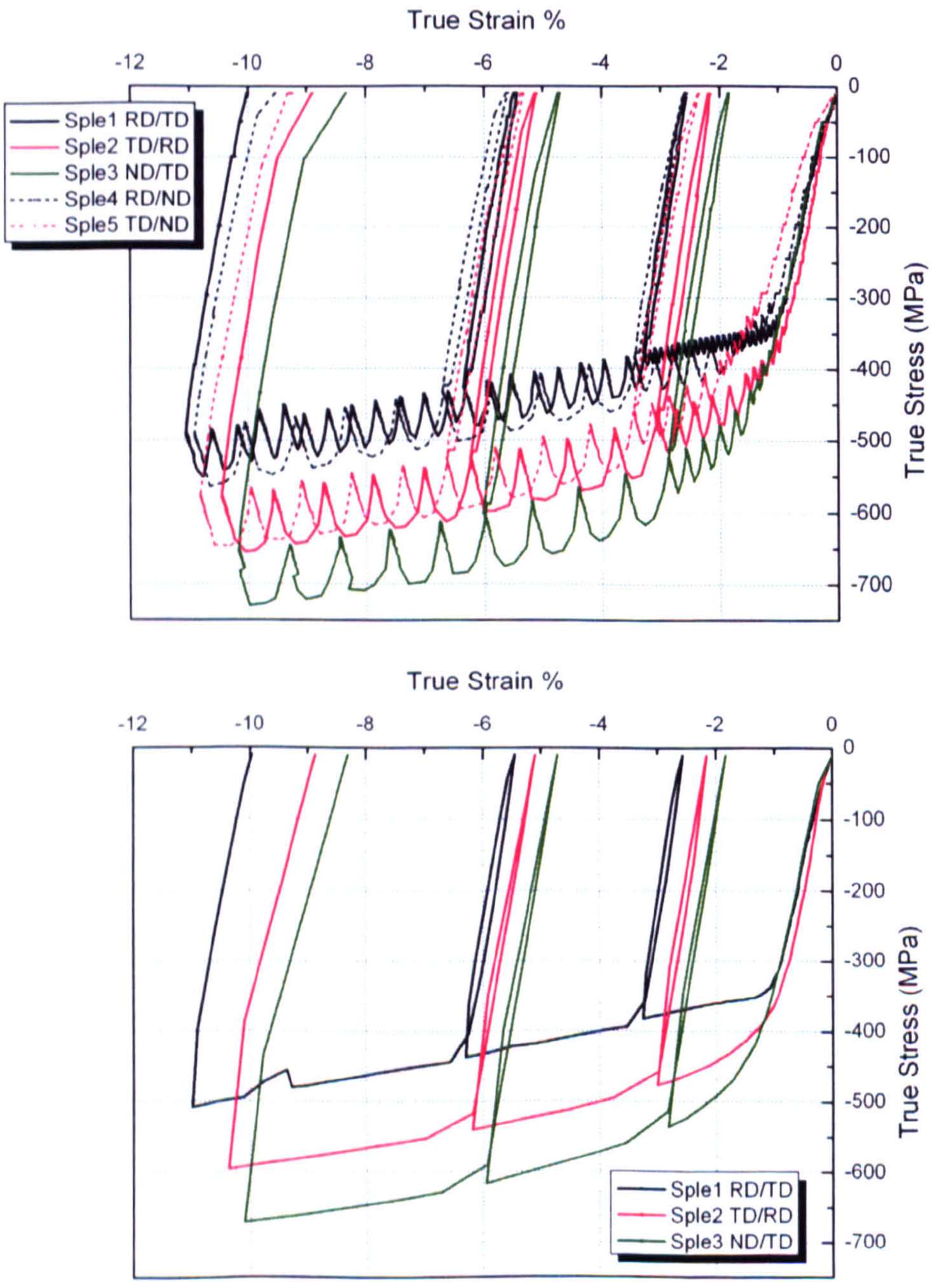

Figure 29 *Macroscopic response for compression along different directions. (a) complete log, (b) averaged data.*

This plastic anisotropy at the macroscopic level reflects the combination of single crystal anisotropy and strong texture of the polycrystal. The EBSD and neutron measurements reported in Chapter 4 reveal that the material has an "eye" texture, typical for rolled zirconium alloys [18]. Most grains are oriented such that the c-axis, not easily deformed in compression, is close to the ND. Hence this direction shows a higher yield stress and more significant work hardening in compression. On the other hand, many grains are oriented {10.0} towards the RD. The easy prismatic slip mode is thus largely activated for compression along RD, which explains the low yielding stress in this direction.

The hardening behaviour for the sample compressed along RD is in agreement with the micromechanical behaviour (described in the next section). Twinning is highly activated and reorients the basal planes from the ND towards the RD. The population of grains changes with less (soft) prismatic and more (hard) basal reflections oriented towards the RD, which explains why the hardening rate increases with deformation after the sharp yield. This result is quite common, and Song and Gray [43] for example, found and studied similar stress-strain curves for pure zirconium. The phenomenon can also partly be attributed to a Hall-Petch strengthening: twinning divides the grains in smaller entities and these new boundaries create an obstacle for further slip as discussed in [44].

5.2.3.b Microscopic response

This section of the chapter deals with neutron diffraction results. Before going into the details, I will present some lexical and notation definitions:

- The term 'reflection' will refer to the set of grains that contribute to a particular diffraction peak in the pattern.

- The notation $\{hkil\}_X$ describes {hkil} planes or reflections aligned towards the direction X (RD is the rolling direction; TD is the transverse direction; ND is the

normal direction; ‖ represents the direction of compression, i.e. bank 1; P represents the Poisson direction, i.e. bank 2).

- $Q_{\|}$ refers to the measurement direction parallel to the compression axis and Q_P to the transverse measurement direction (Poisson direction).

Typical diffraction spectra for the initial state material are shown in Figure 30 for each direction. The texture is evidenced here by the variation in relative peak intensities between the different directions. For instance, in the RD, there is no intensity at all for d-spacings corresponding to basal {00.2} reflections. During compression the spectra will evolve: the peaks will shift, broaden and change in intensity. This will help estimate (qualitatively or quantitatively) the changes in strain state, mosaicity (dislocation density and strain distribution), and texture respectively as detailed in the following subsections.

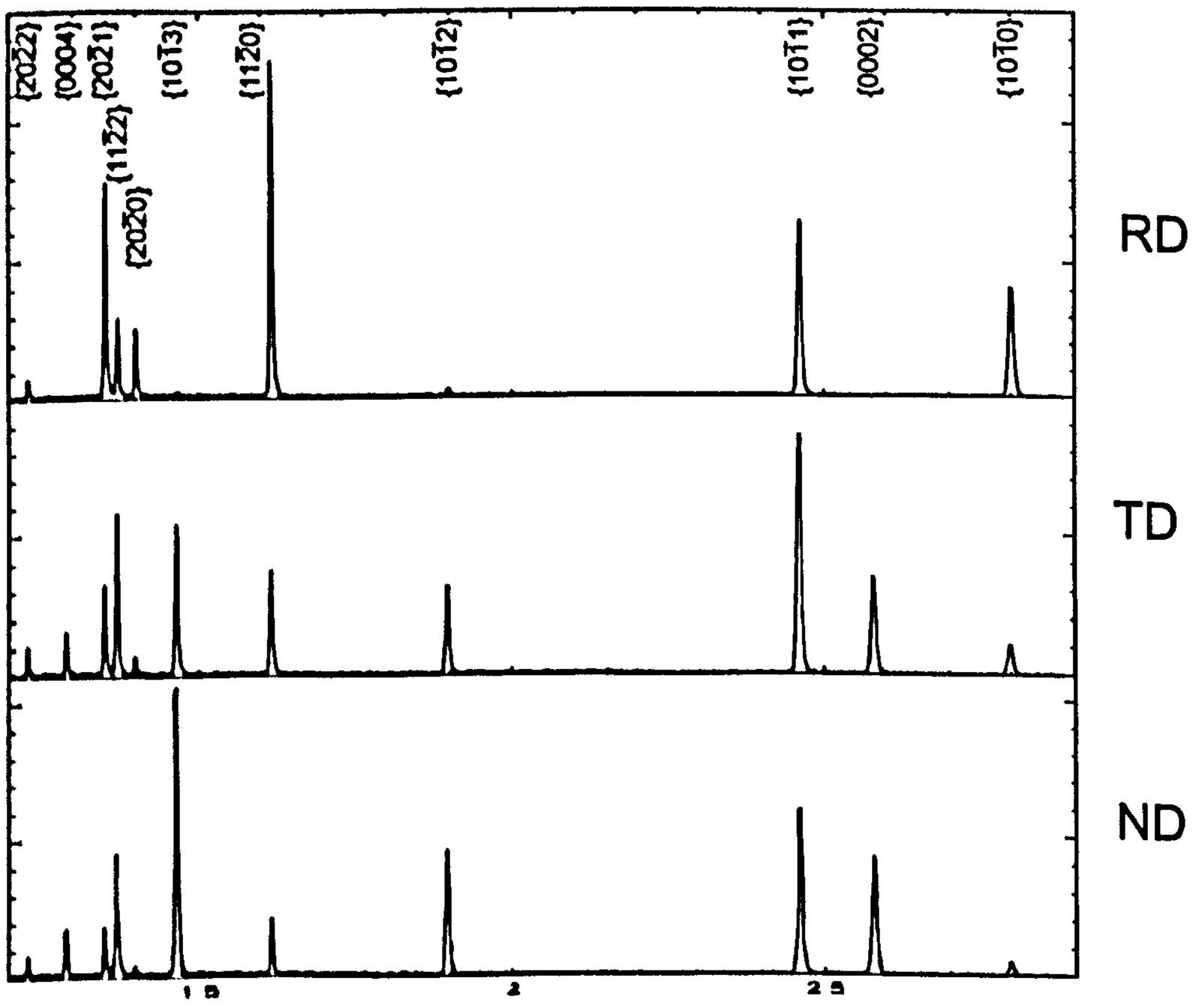

Figure 30 Diffraction spectra in the as received Zry-4 plate

- *Intensity changes*

During compression along the RD, the diffraction spectra in $Q_{\parallel}$ changed noticeably. Figure 31 shows the evolution of the profiles (intensity versus d-spacing) as a function of the applied stress in this direction. The initial spectrum does not contain any {00.2}, {00.4} or {10.3} peaks. After 400 MPa, the intensities for these planes rise and increase significantly and the {10.0} intensity decreases correspondingly.

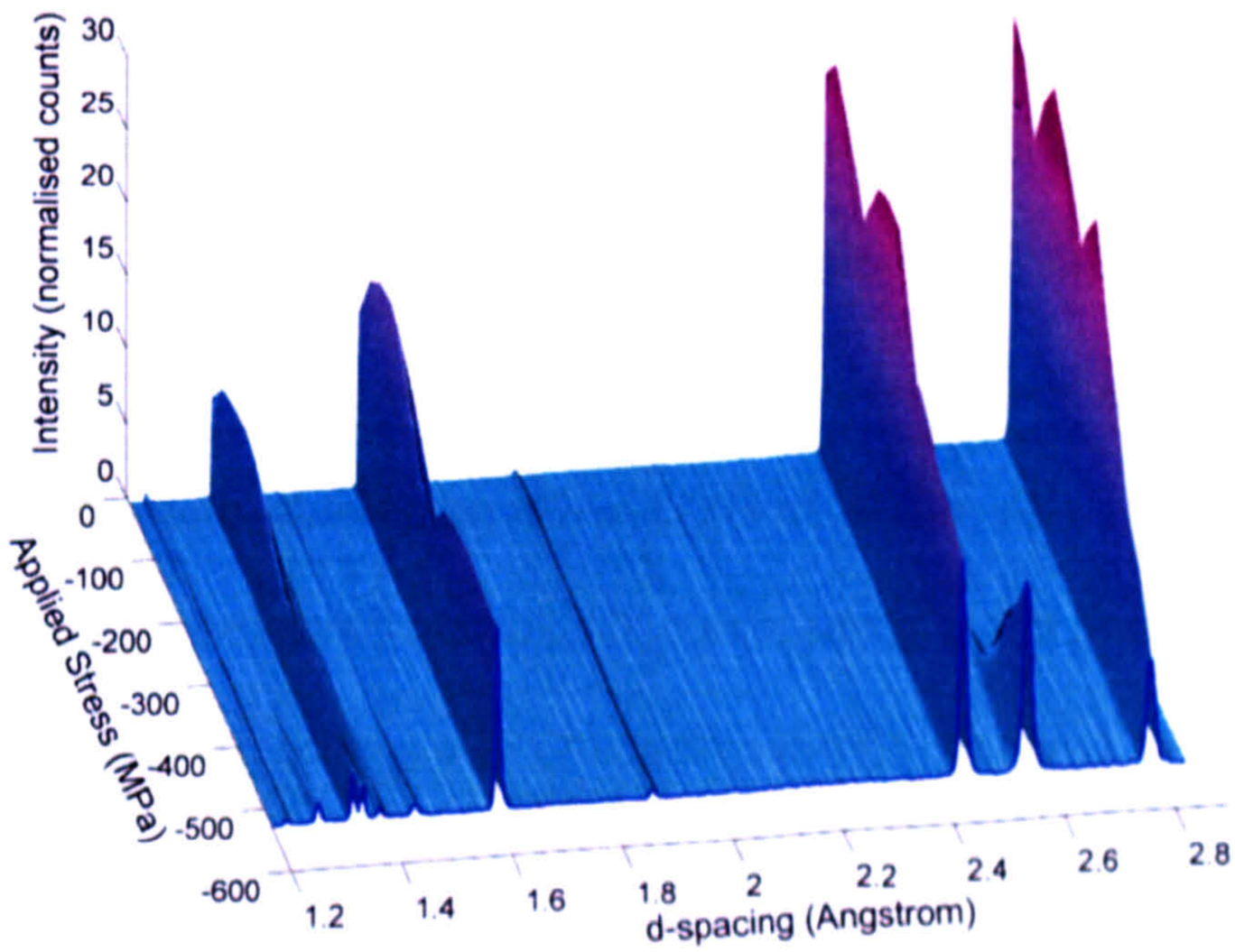

Figure 31 *Evolution of the $Q_{\parallel}$ spectrum during RD compression*

The peak intensities, when normalised by the incident intensity, are a function of the diffraction properties of the reflection considered and the texture of the material. One common way of addressing intensity is through the use of a 'reduced intensity'. For example, Carr et al. [25] define a reduced intensity that is not dependent on the reflection and which would be directly proportional to the volume of diffracting grains. To simplify, the peak intensities have been normalised by dividing them by the sum of all the intensities in the spectrum:

Eq. 16
$$I_{reduced} = \frac{1}{d_{hk.l}^{4} \cdot j.F_{hk.l}^{2}} \cdot \frac{I_{hk.l}}{\sum_{hk.l} I_{hk.l}}$$

where $j_{hk.l}$ and $F_{hk.l}$ are respectively the multiplicity and the structure factor for reflection {hk.l}.

By the means of those reduced intensities, it is possible to determine the proportion of grains having a particular diffracting orientation. Figure 32 (a) shows the evolution of the reduced intensities in $Q_{\parallel}$ when compressing along the RD. The initial population was such that most of the grains were oriented {10.0}, {11.0} and {20.1} in the RD. At the end of the test, most of the diffracting crystals are oriented $\{00.2\}_{\parallel}$ and $\{11.0\}_{\parallel}$. On the other hand the proportion of $\{00.2\}_{ND}$ (Figure 32 (b)) and $\{00.2\}_{TD}$ decreases with deformation. Severe and sudden crystal rotation seems to have occurred which cannot be explained by slip rotation only. Tensile $\{11.1\}<\bar{1}\,\bar{1}.6>$ twinning is likely to be the deformation mode responsible for the phenomenon as it rotates the crystal by nearly 90° [18] and transforms $\{00.2\}_{ND}$ and $\{00.2\}_{TD}$ reflections into $\{00.2\}_{RD}$. Further results presented in this Chapter and in Chapter 7 confirm this. For this reason, the point at which the intensities change will be called the 'onset of twinning'. For the range of stress applied, this texture change is not observed for compression along TD and ND. In those cases the texture is such that most of the crystals are not oriented to easily allow activation of the twinning mode.

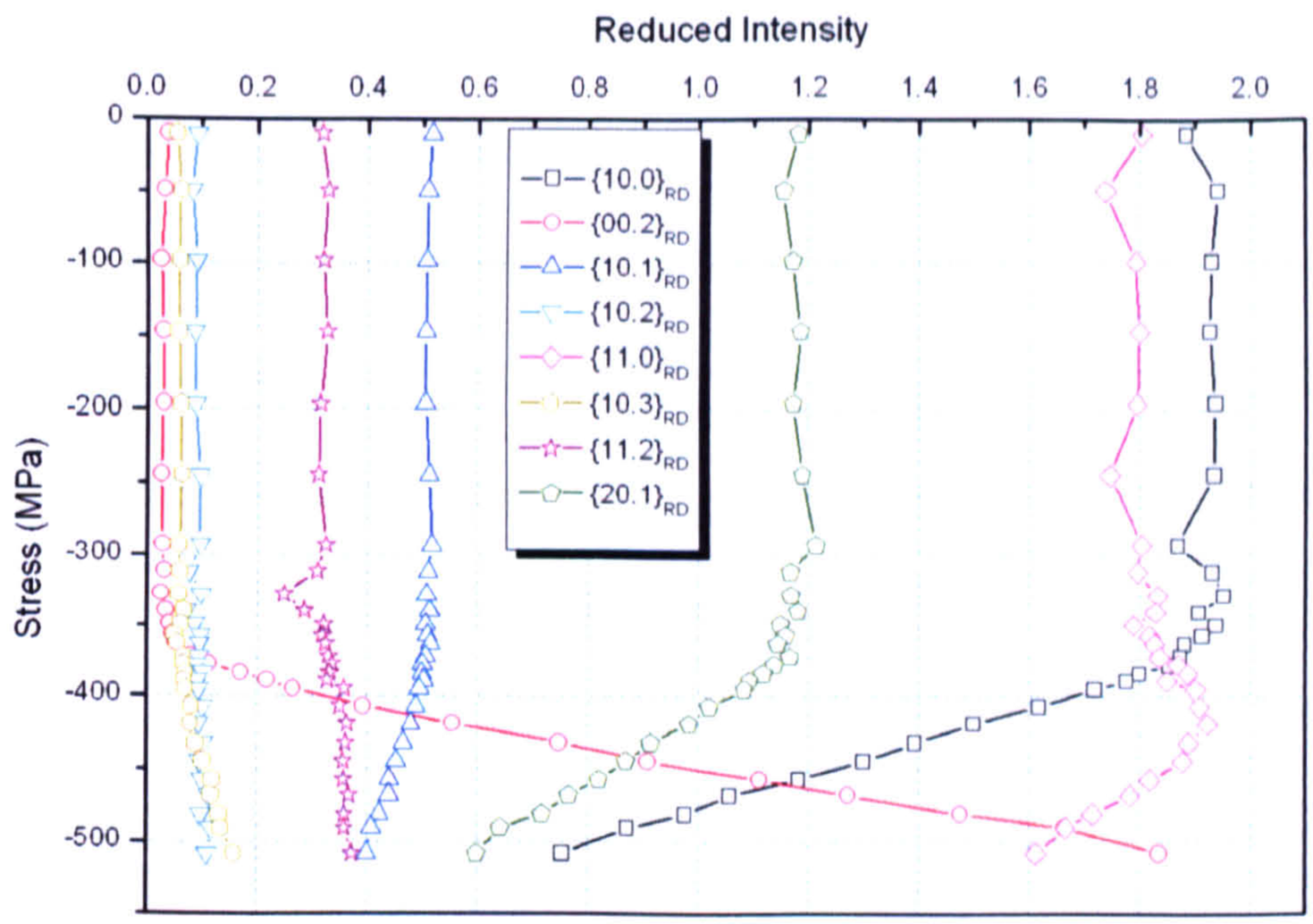

(a)

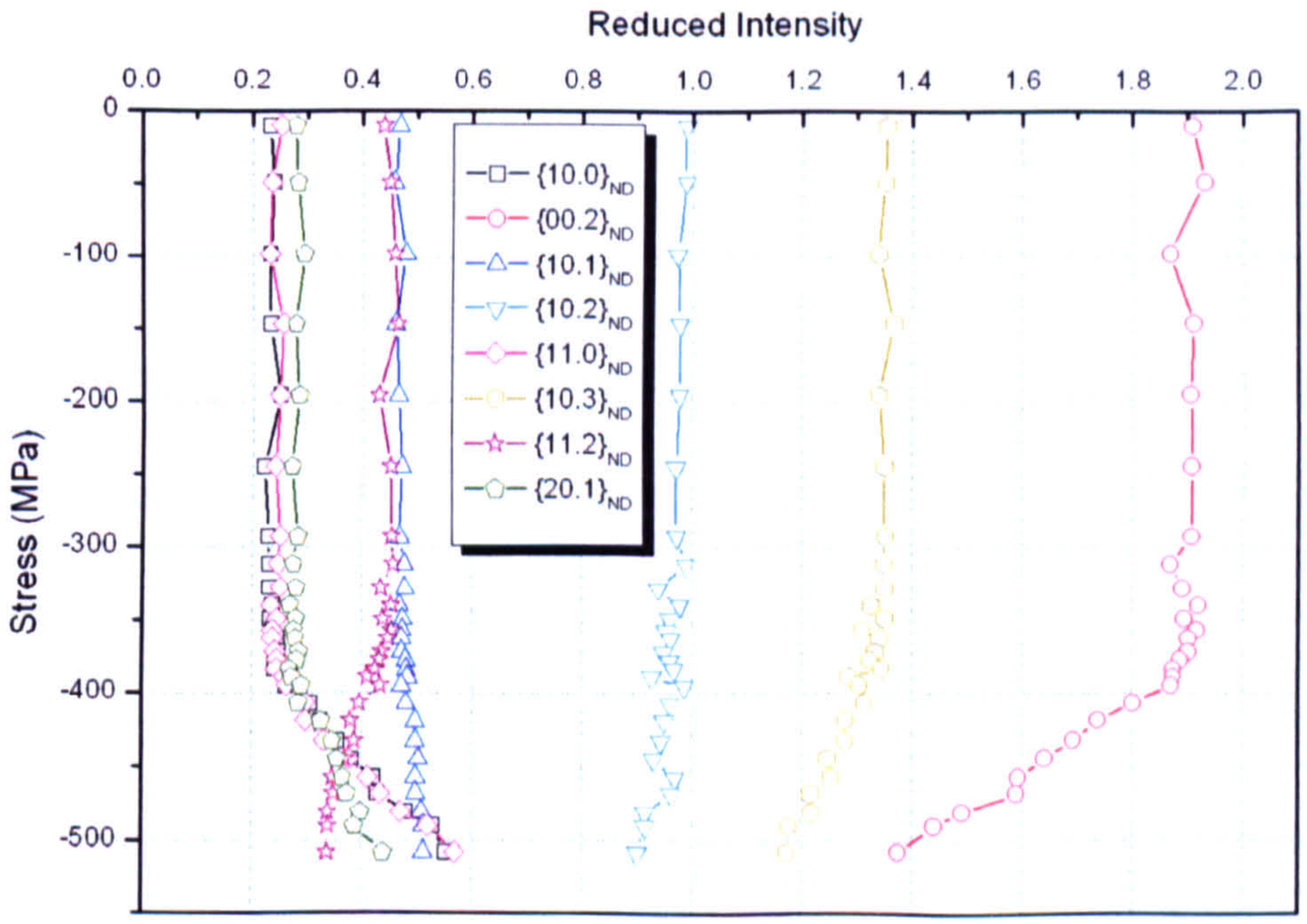

(b)

Figure 32 *Evolution of the (a) Q_{RD} and (b) Q_{ND} peak intensities during RD compression*

- *Lattice strain evolution*

The strains for each reflection were deduced from the peak shifts relative to the first measurement at –10MPa of applied stress (the necessary load to hold the coupons):

$$\varepsilon_{hk.l} = \frac{d_{hk.l} - d^0_{hk.l}}{d^0_{hk.l}} \qquad \textit{Eq. 17}$$

where $d_{hk.l}$ and $d^0_{hk.l}$ are the values of d-spacing of the reflection {hk.l} at the given applied stress and at –10MPa respectively. From now onwards, the strain will be expressed in

terms of μstrain (or microstrain): 1μstrain is equivalent to $1x10^{-6}$. It is important to notice that the strains calculated are only the strains generated during the uniaxial loading process and do not account for previous intergranular residual stresses. Indeed the grains are very likely to be pre-strained after the post processing annealing: the crystal thermal anisotropy leads to intergranular misfits and residual stresses between crystal misorientations. It is important to keep in mind this pre-strain history though, as the initial state superimposes to the loading strains and can influence the grain response.

A problem with this definition of lattice strain rises for reflections for which there is no peak available in the spectrum prior to compression: the $d^0_{hk.l}$ is not available directly and must be defined in another way. A solution proposed by Brown et al. [67] in their study of Mg is to use the d-spacing for the same reflection in the other bank. However this approach ignores the presence of initial thermal stresses which can be neglected in Mg alloys as the thermal anisotropy is very small [68]. Another approach was used by Muransky et al. [69]. They derived the reference d-spacing from a Rietveld fit on the diffraction spectrum for the unstressed material. These solutions are really only valid in the case of powders but can be applied to polycrystals if we decide to neglect the initial intergranular residual strains and make an appropriate evaluation of the error in the determination of d_0. In the present case the Rietveld fitting attempts with spherical harmonics were not successful at capturing the variation in peak intensities in the reference spectra. Another method was applied which consisted of deducing the *a* and *c* cell parameters from the reference d-spacing of the {10.0} and {10.1} reflections using the relationship:

Eq. 18

$$d^0_{hk.l} = \frac{a_0}{\sqrt{\frac{4}{3}\left(h^2 + h.k + k^2\right) + \left(\frac{l.a_0}{c_0}\right)^2}}$$

The resolution of the system of two equations with two variables gives expressions of a_0 and c_0 in terms of $d^0_{10.0}$ and $d^0_{10.1}$. In turn Eq. 18 can be used to derive the d_0 for the other reflections in terms of $d^0_{10.0}$ and $d^0_{10.1}$:

Eq. 19

$$d^0_{hk.l} = \frac{d^0_{10.0}}{\sqrt{\left(h^2 + h.k + k^2\right) + l^2 . \left(\left(\frac{d^0_{10.0}}{d^0_{10.1}}\right)^2 - 1\right)}}$$

The method is better than Brown's approach because it accounts for some of the initial intergranular strains during the calculation of a_0 and c_0. Indeed the {10.0} and {10.1} d-spacings used for the calculation deviate from a powder measurement as a result of the grain misfits. The c_0/a_0 ratio is different from the ideal c/a ratio (of a single crystal) because of the intergranular strains (the pseudo cell is distorted). However in the second step of the calculation (Eq. 19) the material is again assumed to be a powder which does introduce some potential error in the calculated c lattice parameter.

The recalculated d_0 from Eq. 19 can be compared to the measured initial d-spacing for reflections that present a diffraction peak in the spectrum. Table 4 shows the relative difference in unit of microstrain for reflections in the RD spectrum. This difference indicates what is the error induced by the calculation of d_0 with the above method. However it does not represent the initial state of intergranular stresses: firstly because some intergranular strains are accounted for in the calculation (as explained above); secondly because {10.0} and {10.1} have been chosen as reference reflections so the misfits represented by these errors are relative to the residual strains in these reflections. For all the peaks in the RD spectrum, the error in the determination of d_0 is less than 220με. We can assume that the error would be of the same order for each peak. Although this value is much bigger than the fitting error for most of the diffraction measurements, it is still one order of magnitude smaller than the strains at which the peaks appear (around —

2000με). Hence this method will be considered satisfactory for the determination of the d_0 of reflections initially absent of the diffraction spectrum.

Reflection		{10.2}	{11.0}	{20.0}	{11.2}	{20.1}	{20.2}
$\left\lvert \frac{d_{hk.l}^{0,calculated} - d_{hk.l}^{0,measured}}{d_{hk.l}^{0,measured}} \right\rvert$	$\times 10^6$	160	58	181	188	130	218

Table 4 *Difference between the measured and the computed d_0 expressed in microstrain*

For the three types of compression tests, Figure 33 shows the evolution of the measured strains for some atomic planes normal to $Q_{\parallel}$ and Q_P. The neutron strains for reflections {10.0}, {00.2} and {10.1} are plotted against the applied stress. The uncertainties in strain are derived from the peak fitting errors using error propagation methods:

Eq. 20
$$\Delta\varepsilon = |\varepsilon| \cdot \sqrt{\frac{\Delta d_{hk.l}{}^2 + \Delta d_{hk.l}^0{}^2}{\left(d_{hk.l} - d_{hk.l}^0\right)^2} + \left(\frac{\Delta d_{hk.l}^0}{d_{hk.l}^0}\right)^2}$$

These fitting uncertainties are represented by error bars on the graph, except when the error is smaller than the size of the markers.

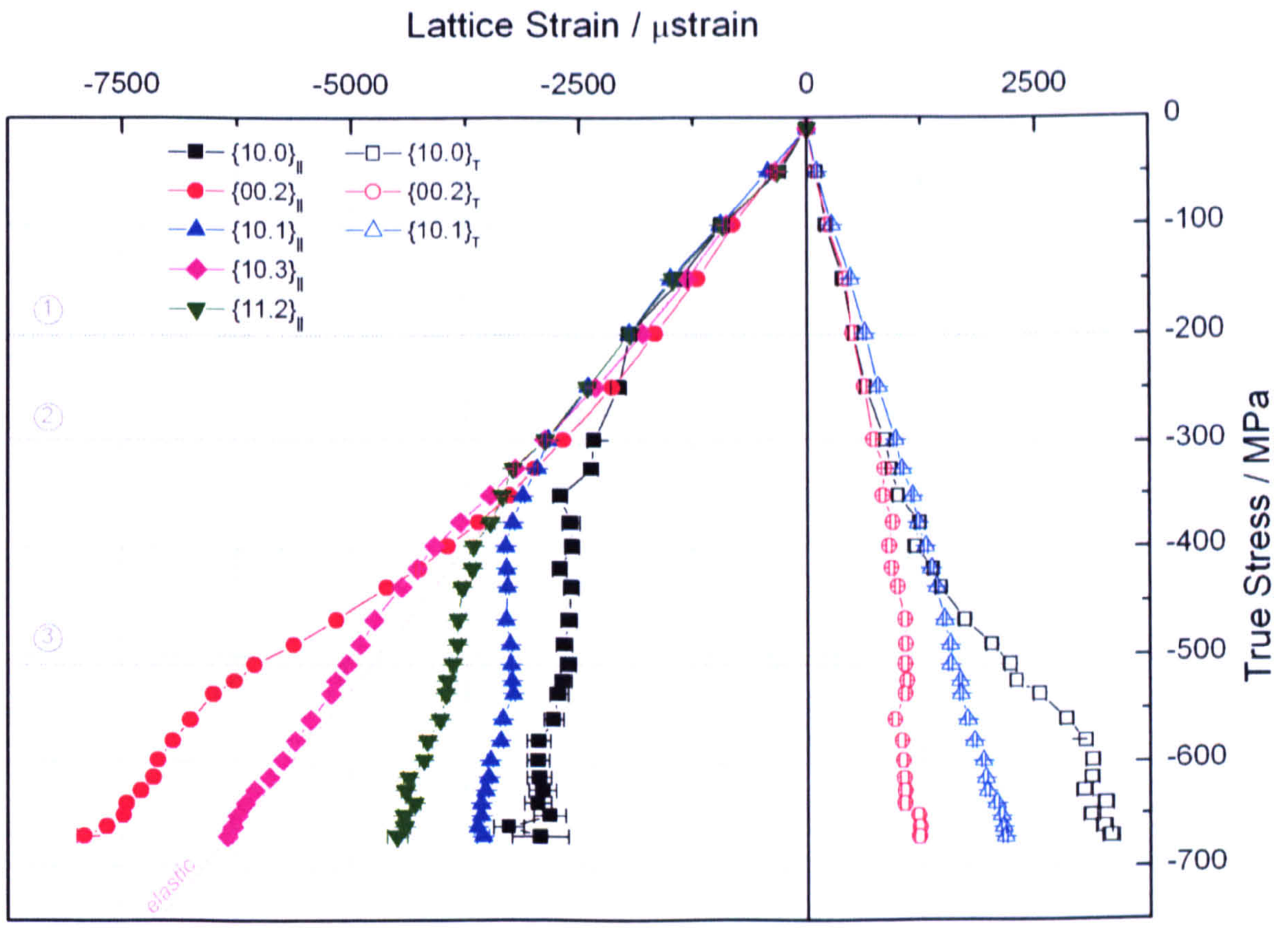

(a)

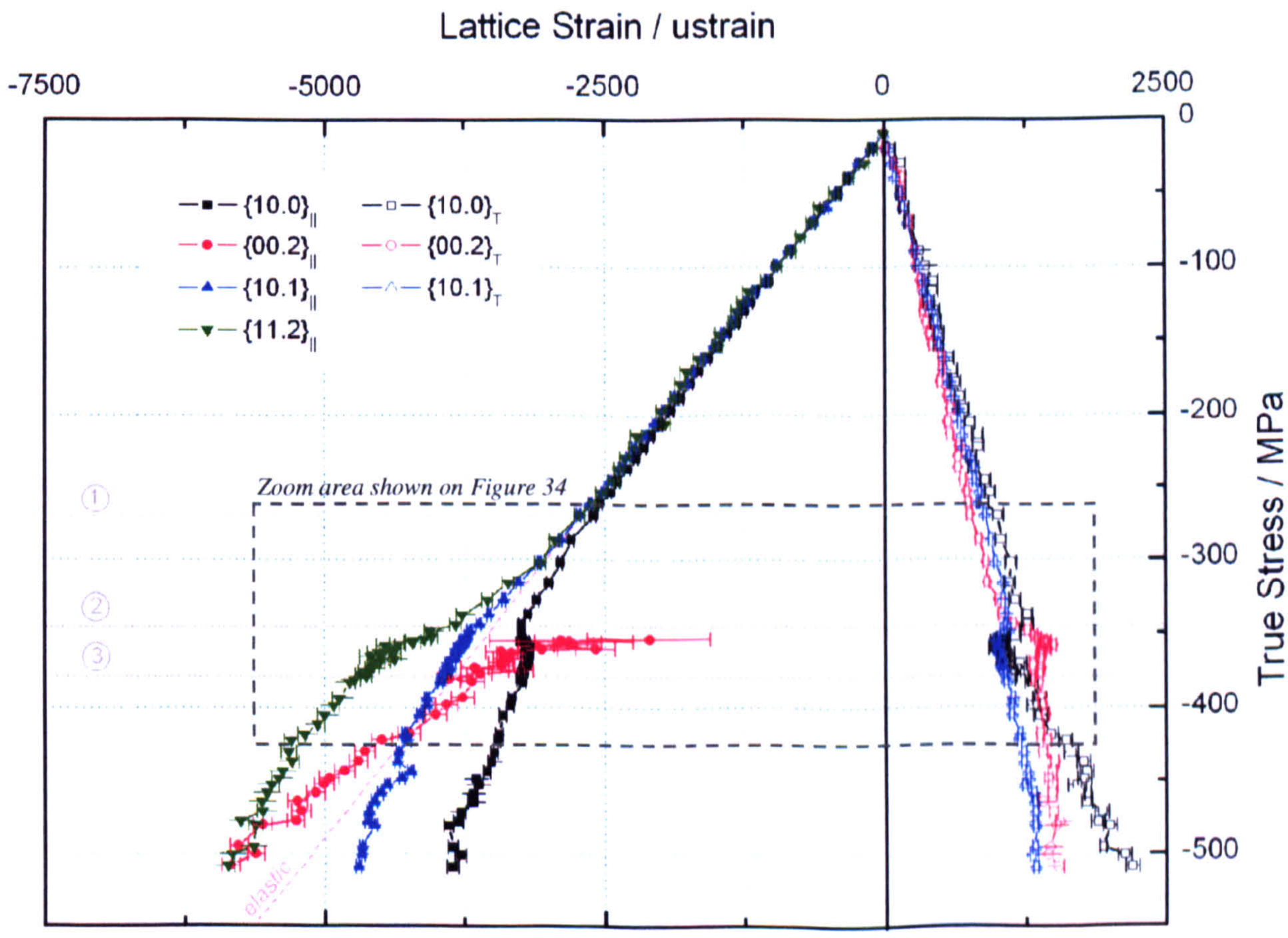

(b)

Figure 33 Elastic strain evolution during (a) ND/TD, (b) RD/TD tests (Continued…)

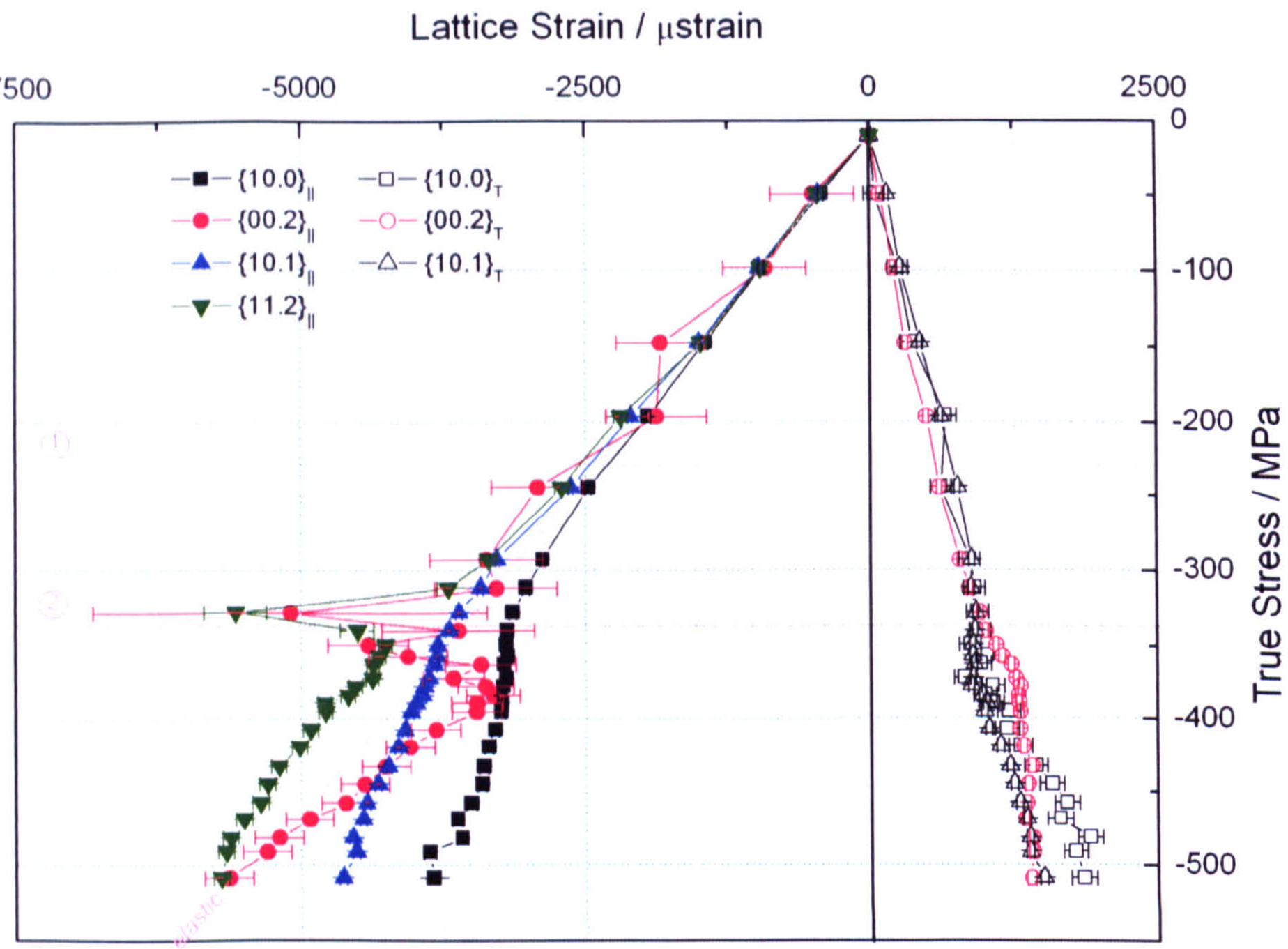

(c)

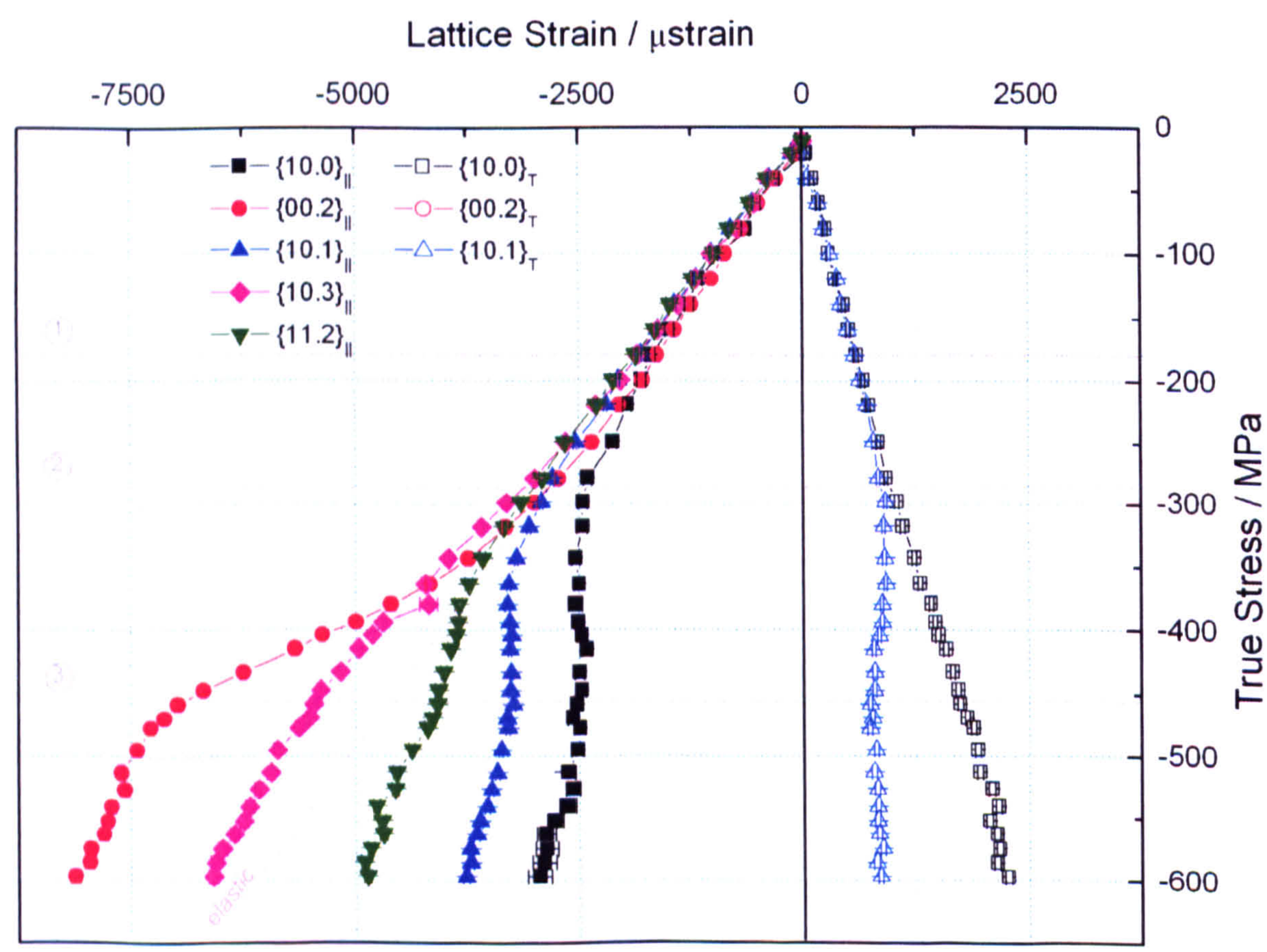

(d)

Figure 33 Elastic strain evolution during (c) RD/ND, (d) TD/RD tests (Continued...)

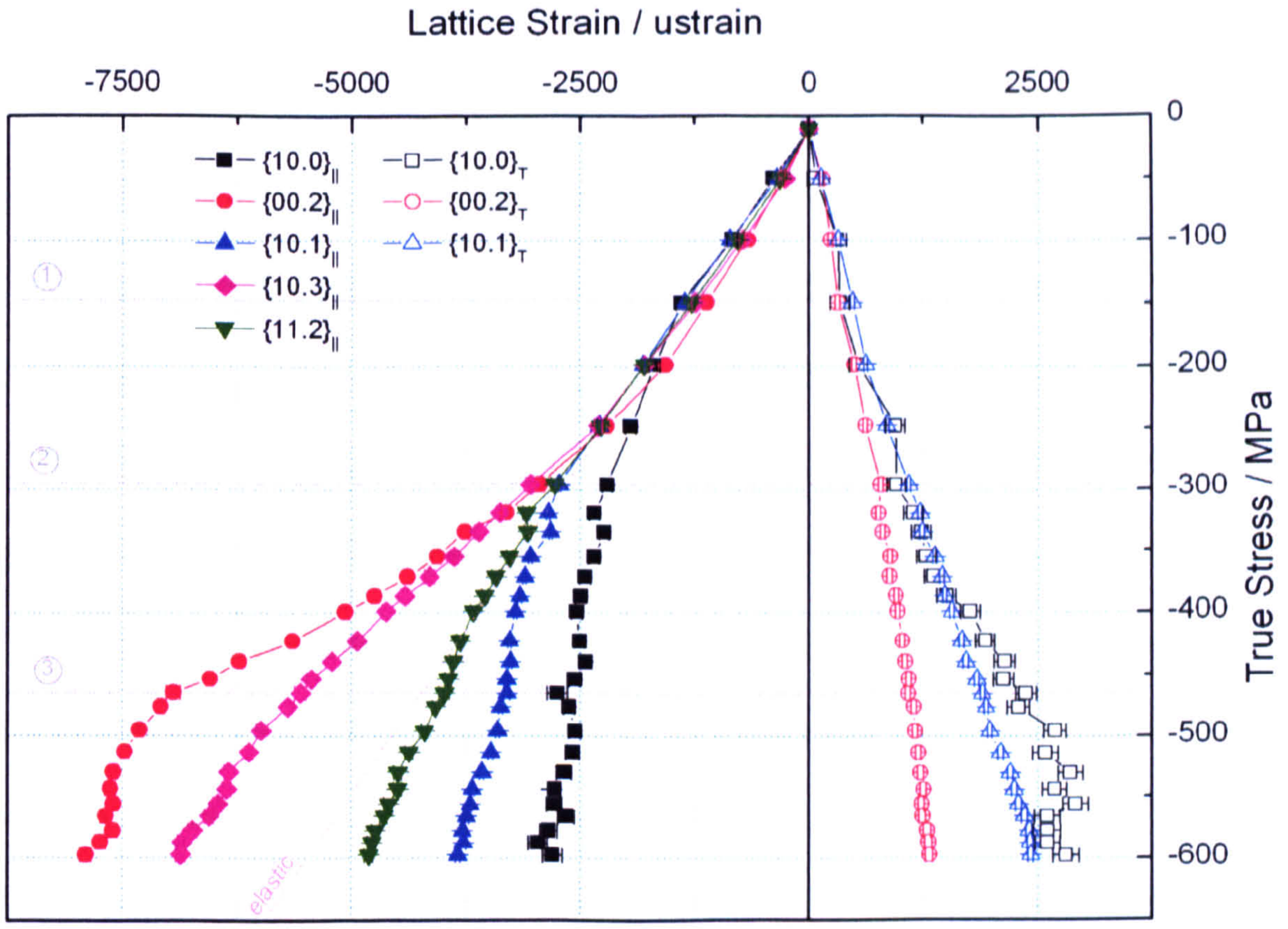

(e)

Figure 33 Elastic strain evolution during (e) TD/ND test (the dotted line marked 'elastic' represents the average elastic response over all the reflections; lines 1, 2 and 3 identify the major inflections)

Some features in these graphs are common regardless of the direction of compression and can give rise to generalised interpretations. In the elastic region (above line 1), the relationship between elastic strain $\varepsilon^{e}_{hk.l}$ along $Q_{\parallel}$ and macro-stress Σ is quasi-linear and is governed by the diffraction elastic constants $E^{diff}_{hk.l}$:

$$E^{diff}_{hk.l} = \frac{\Sigma}{\varepsilon^{e}_{hk.l}} = E_{hk.l}\frac{\Sigma}{\sigma_{hk.l}} = E_{hk.l}\frac{\Sigma}{(\Sigma + \Delta\sigma_{hk.l})} \qquad \textit{Eq. 21}$$

where $\sigma_{hk.l}$ is the stress in the {hk.l} reflection along $Q_{\parallel}$, $\Delta\sigma_{hk.l}$ is the deviation of $\sigma_{hk.l}$ from Σ and $E_{hk.l}$ is the crystal Young's modulus along the normal to the {hk.l} plane. The elastic anisotropy is quite small as showed by the small divergence between the {hk.l} responses in the elastic regime. Typically the spread of diffraction elastic constants is around 25% (see below) and so is the spread in stress. From Eq. 21 we can thus consider that the diffraction elastic constants $E^{diff}_{hk.l}$ represent the Young moduli $E_{hk.l}$ for the

corresponding planes with an uncertainty smaller than 20% (based on $\Delta\sigma_{hk.l} = 25\%$). With this assumption, the measured elasticity moduli are between 95 and 100 GPa for the prismatic planes, 90 and 105 GPa for the pyramidal planes (the 3rd orders pyramidal planes are stiffer than the 2nd and 1st order ones) and 105 and 115 GPa for the basal planes, which are the stiffest. These values are in good agreement with the single crystal constants determined by Fisher and Renken [36] (although perfect agreement is not expected between measurements on a single crystal and on a polycrystal). They found that the elastic anisotropy in a single crystal of zirconium was characterised by a range of Young's moduli from 89 to 125GPa for the {10.1} and {00.2} directions respectively (see also Chapter 3). Linearity is also observed in the Q_P directions.

On Figure 33, after the elastic regime, the responses of the reflections depart significantly from linearity in different directions: towards smaller or higher elastic strains depending on the reflection. The qualitative evolution is rather consistent between the different compression tests: at a given applied stress $\{00.2\}_{\parallel}$ are under higher elastic strains than average while $\{10.0\}_{\parallel}$ are the reflections with the smallest strain below the elastic response. All the $Q_{\parallel}$ reflections show a negative inflection (towards lower strains) at some point during the deformation, which indicates a saturation in the lattice strain the reflections can bear. Hence these inflections will be considered as indicative of plastic yielding.

On the graphs the lines 1, 2 and 3 identify the major inflections. These lattice strain saturations occur successively in $\{10.0\}_{\parallel}$, $\{10.1\}_{\parallel}$ and then in $\{00.2\}_{\parallel}$. They correspond to the yielding of the respective grain families. When the prismatic reflections start yielding, some of the load they should be bearing if still in the elastic regime is transferred to the other reflections, which are still responding elastically. As more reflections yield, there are fewer and fewer grains in the elastic regime. These remaining grains, which are more suitable for bearing load, take a higher share of load than they would if all the grains were

still in the elastic regime (or if yielding was uniform) and thus their response departs from the elastic linearity towards higher strains. This is particularly visible for reflections $\{10.3\}_{\|}$ and $\{00.2\}_{\|}$ as they are the last to yield: in Figure 33(a) for example, after –350MPa, the two responses depart from the elastic behaviour (dotted line) towards higher elastic strains. After –480MPa and –550MPa of stress applied in the TD and ND respectively, there is a change in response for the $\{00.2\}_{\|}$ reflection as the grains deform plastically in their turn. At the end of the 10% total deformation, the same family bears more than twice as much elastic strain as $\{10.1\}_{\|}$ and $\{10.0\}_{\|}$ and reaches –8000 μstrain.

For the different types of compression, Table 5 summarizes the mechanical state in which the four main reflections are when they show a negative inflection. While for ND and TD compression the strains in the prismatic $\{10.0\}_{\|}$ and pyramidal $\{10.1\}_{\|}$ reflections saturate at less than –2000 and –2900 μstrain respectively, these grains yield under higher elastic strain for compression in the RD (around –2500 and –3800 μstrain approximately).

	RD		TD		ND	
	True stress MPa	Lattice strain μstrain	True stress MPa	Lattice strain μstrain	True stress MPa	Lattice strain μstrain
$\{10.0\}_{\|}$	–270 / –240	–2600 / –2500	–180 / –170	–1700 / –1550	–200	–2000
$\{10.1\}_{\|}$	–355 / –350	–3770 / –3800	–280 / –300	–2800 / –2750	–300	–2850
$\{11.2\}_{\|}$	–380 / –390	–4780 / –4800	–380 / –410	–3840 / –3700	–400	–3660
$\{00.2\}_{\|}$			–450 / –465	–6950 / –6930	–510	–6060

Table 5 *Yielding points for various reflections*

- *Compression in RD*

The microscopic response during compression along the RD is quite different to that observed for compression along TD and ND. The fact that some reflections are missing in the initial spectrum seems to affect the behaviour.

The RD/TD experiment is particularly detailed with around 80 measurement points. Figure 34 is a zoomed in picture of the region [–260; –420] MPa. As seen before, we have a good evidence that the appearance of {00.2} peaks and the simultaneous reduction in the intensity of the {10.0} peaks in the $Q_{\parallel}$ spectrum are a result of tensile twinning. The $\{00.2\}_{\parallel}$ peaks appear for –350MPa of applied stress and the intensity increases consistently until the end of the test (Figure 32), which would suggest that twinning is taking place from –350MPa onwards. The graph shows clearly an interesting feature: the initial stage, i.e. for stresses between –350 and –370MPa, is accompanied by a sudden relaxation of nearly 100 microstrain in the $\{10.0\}_{\parallel}$ family. This is very unlikely to be a measurement artefact because the fitting error is very small (around 20 microstrain), and given the resolution and smoothness of the curve.

The unloading of this reflection (which represents a large proportion of the grains present) must be compensated by other grains. The response of the $\{10.1\}_{\parallel}$ reflection is not obviously affected, and it actually seems to yield progressively at the same time. On the other hand, there is a concurrent positive inflection towards higher elastic strains for $\{11.2\}_{\parallel}$ which suggests that it bears the extra load. The elastic strain in the $\{00.2\}_{\parallel}$ reflection is approximately –2600 microstrain at the onset of twinning, and the corresponding grains are in a very relaxed state as compared the aggregate (below the linear response). The response is however very steep and the lattice strain increases rapidly as the test goes on.

The reflections along Q_P are also affected by the twinning. However the interpretation is quite difficult as these reflections average the strain of a set of grains undergoing very different levels of loading.

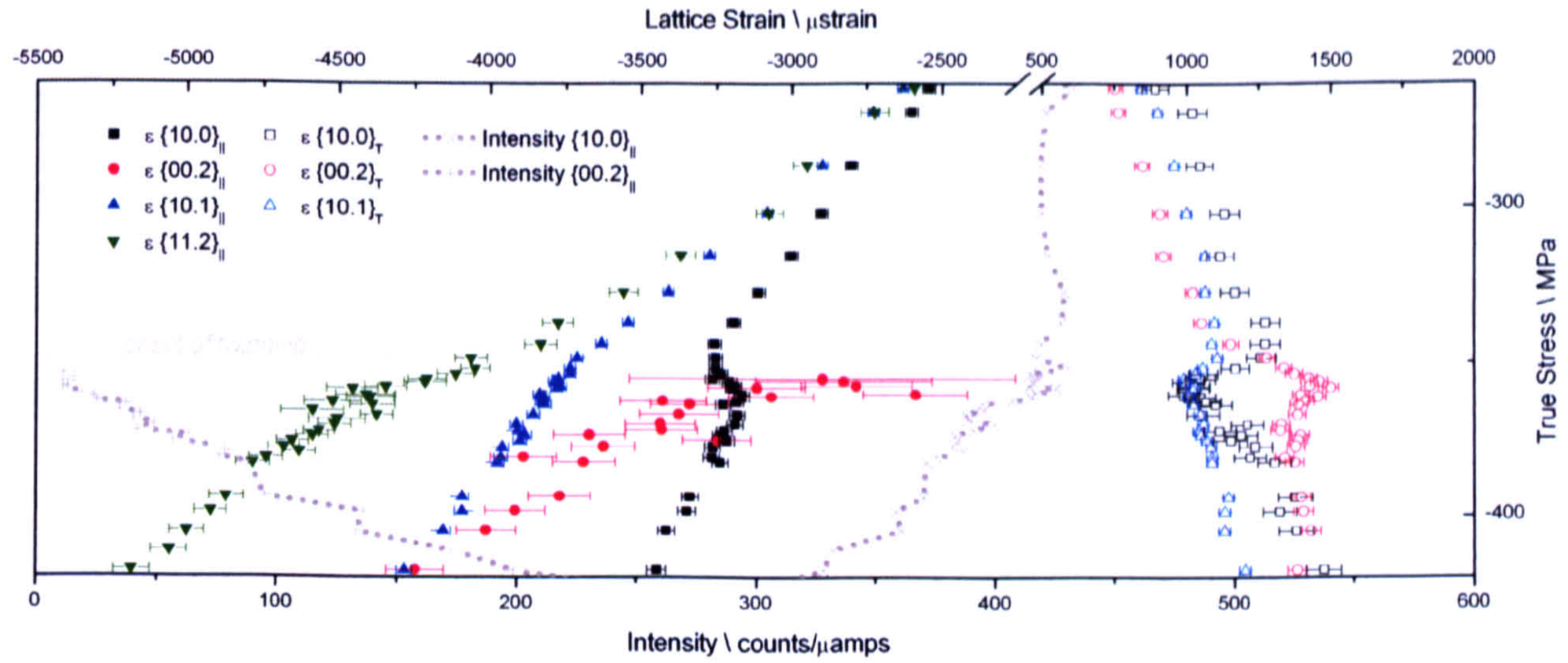

Figure 34 *Elastic strains and peak intensities evolution at the onset of twinning for RD/TD test (zoom area shown on Figure 33(b))*

The grains that activate twinning are called parent grains. Tensile twinning is activated when tension is applied on the basal planes of the crystal (i.e. along the <*c*> axis of the cell). By a Poisson equivalent it is also activated in grains with the prismatic planes in compression. Hence the grains in which twinning is most likely to take place, i.e. the most likely parent grains, are those for which prism planes are oriented along the compression direction $Q_{\|}$. Some of these grains are represented by the $\{10.0\}_{\|}$ reflection, which interestingly enough undergoes the elastic strain relaxation described previously at the start of twinning. It seems quite clear now that twinning is responsible for the phenomenon.

At this stage it is difficult to draw conclusions about what happens at the onset of twinning in the compression direction (Figure 34). Two effects can contribute to a relaxation of the $\{10.0\}_{\|}$ overall lattice strain. The most stressed grains in the family tend to twin and be relieved first. The spread of lattice strain and the average measured lattice strain in the family are thus reduced. One expects also that the parent prism planes get relaxed by the twinning because of the transfer from elastic strain to plastic strain. It is however difficult to explain the suddenness and the amplitude of the relaxation. Muransky and al. observed on the contrary a temporary burst of load in the {10.0} reflections when twinning was activated in magnesium. It was explained that the lowering in strain in the $\{10.0\}_{\|}$

reflections that twin is compensated by an increase of load in the other $\{10.0\}_{\|}$ reflections. In our case, the load relaxation in parent $\{10.0\}_{\|}$ reflections is balanced by the second order pyramidal planes. But this doesn't justify why the phenomenon is not characterised by an inflection similar to slip activity rather than by the observed doubling back in the curve. An explanation could be that twinning is activated in virtually all the $\{10.0\}_{\|}$ between –345 MPa and –370 MPa (Figure 35). The formation of twins in single crystals usually causes load drops [42]. Lebensohn and Tomé [47] propose that twinning overshoots at nucleation which contributes to relaxing the stress in the parent grain. A large scale twin birth would justify the relaxation observed at the scale of the whole reflection. As twinning starts, the overall $\{10.0\}_{\|}$ lattice strain is the average of the strain in stressed untwinned grains and relieved twin grains. As more and more grains twin, the measured strain tends to the behaviour of the relieved grains until all have twinned at –370 MPa. The evolution of peak intensities indicates that reorientation continues during the whole compression test (Figure 32 and Figure 34), but this could be due to twin growth only.

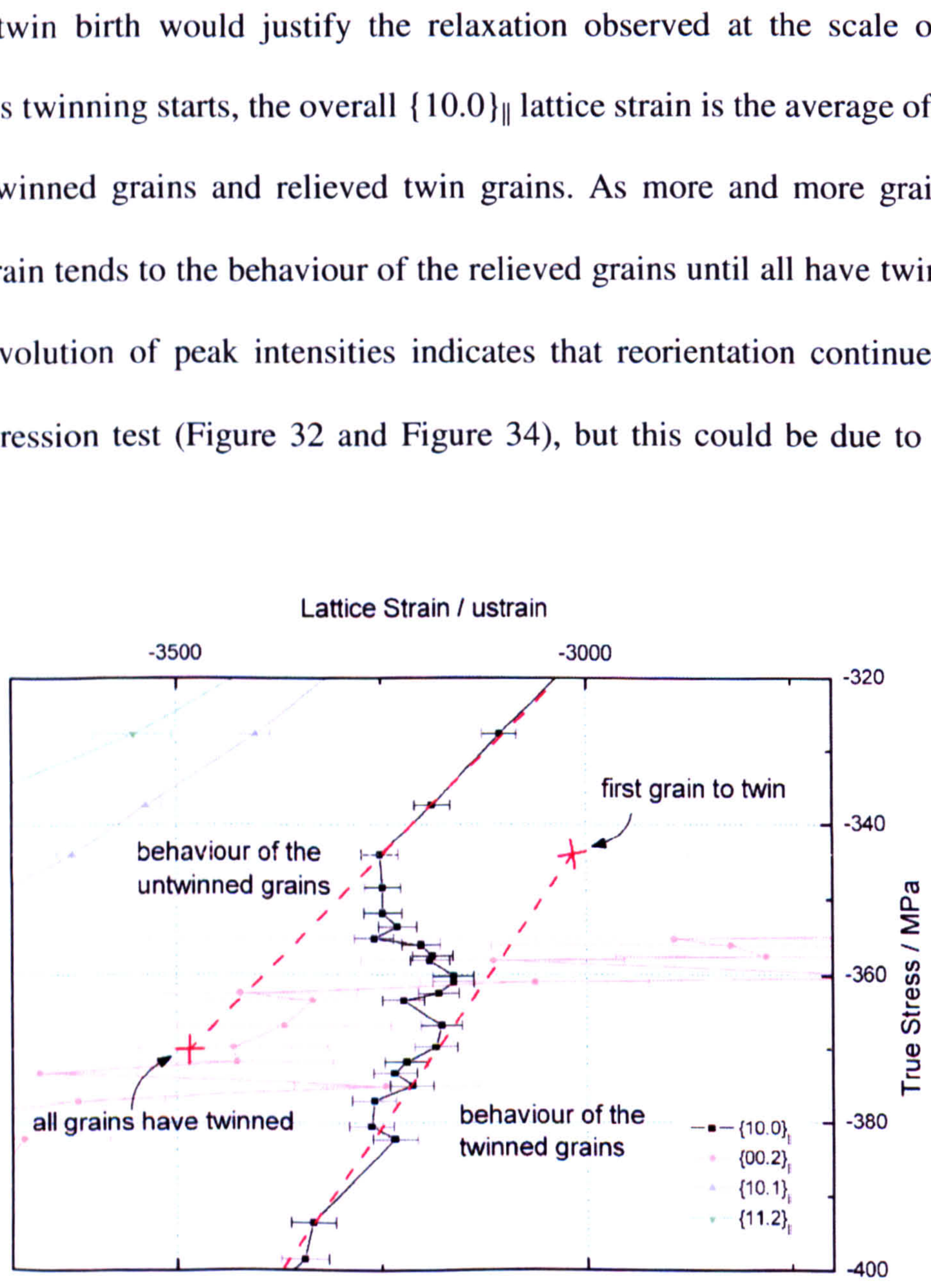

Figure 35 The $\{10.0\}_{\|}$ relaxation during RD/TD test in Zry-4

If this hypothesis is correct, twinning nucleation would happen at a large scale in the material between 1.3% and 2% of applied total strain (Figure 36) but with small twins which would justify the slow initial rise of $\{00.2\}_{\|}$ intensity. After 2% total strain, the main mechanism would be the propagation of twinning, i.e. the expansion of the twin nuclei, responsible for a steady increase of the $\{00.2\}_{\|}$ intensity.

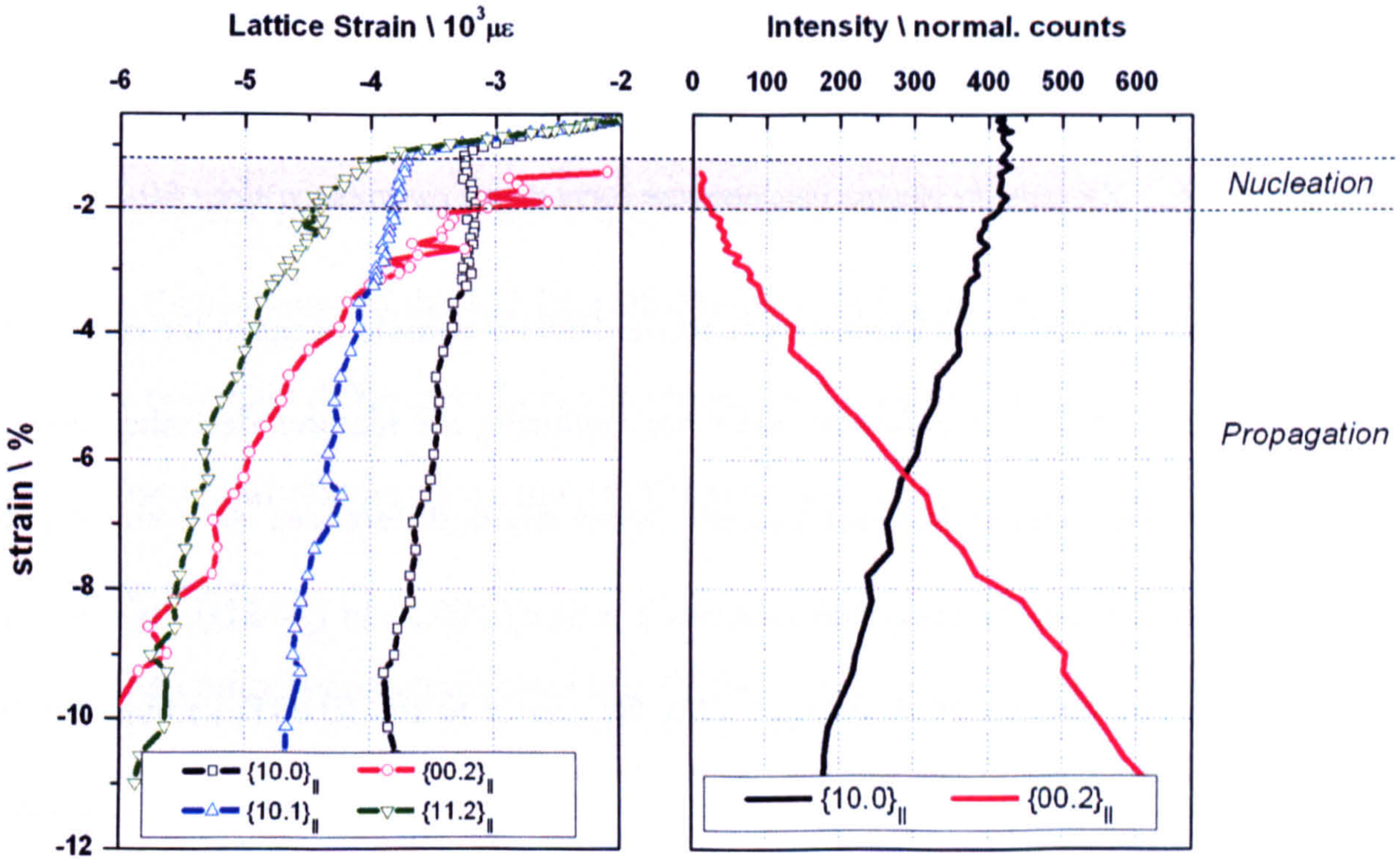

Figure 36 *Elastic strains and peak intensities evolution as a function of the macroscopic total strain for the RD/TD test*

Tenckhoff describes twinning as a mechanism essential to ductility, not by the magnitude of strain it generates (which is generally fairly low compared to slip), but as it re-orients the crystals favourably for further slip activation. However we have seen that in the present case, tensile twinning orients the basal poles towards the compression direction, which is not a favourable configuration for the activation of the two easy prism <*a*> and basal <*c*> slip modes. As a consequence, tensile twinning is rather an indirect contributor to hardening. This effect is easily visible on the stress/strain curve in Figure 37 for compression along RD, as the hardening rate increases after the sharp yielding point.

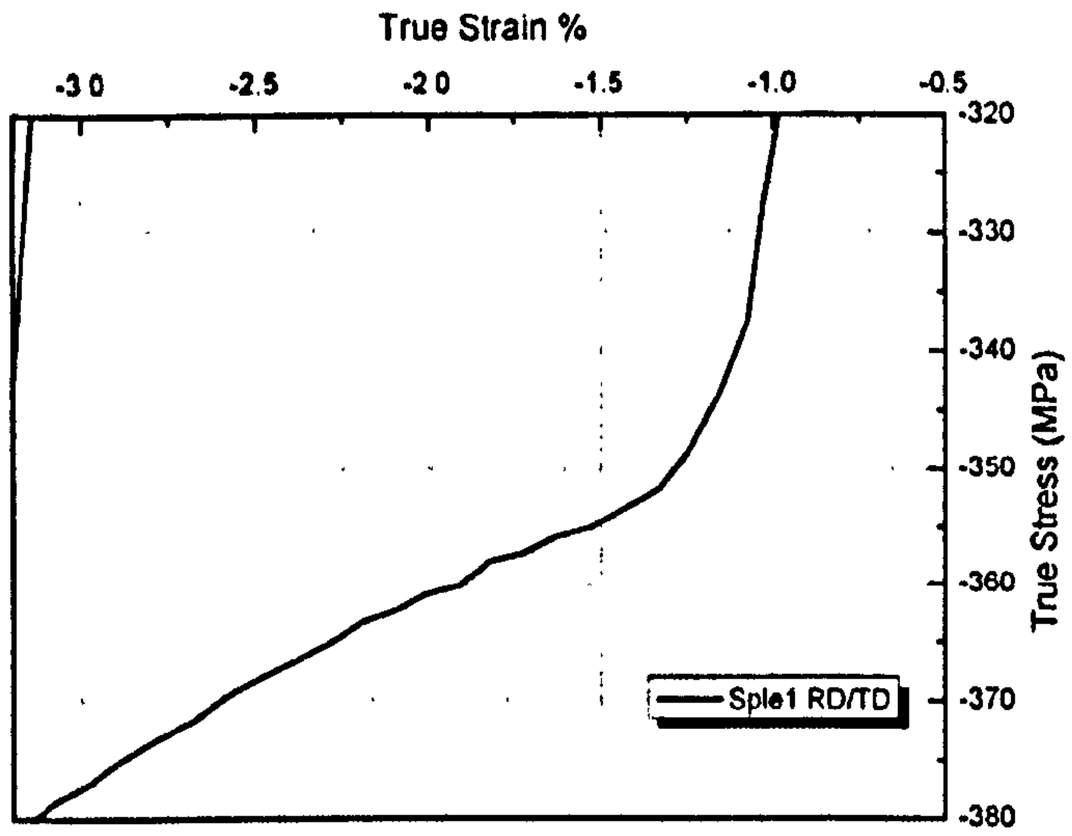

Figure 37 *Zoom on the macroscopic response curve during compression along RD*

So far we have been focusing on the response of the RD/TD sample because the resolution of the experiment is very high which is useful for capturing the features described above. The responses in the sample RD/ND present some slight differences as compared to RD/TD. In the initial state, the spectrum contains a peak of {00.2} in $Q_{\parallel}$ (RD). Its intensity is very low but is enough to allow fitting. This difference to the RD/TD sample can be attributed to the small texture variations across the rolled plate. The presence of the peak from the start allows direct determination of a $d^0_{00.2}$ (although it has a large fitting error associated) which is convenient for the computation of strain rather than using the indirect method (Eq. 19, p.79). Because the reflection is present from the start, it is also possible to follow the evolution of the microstrain in this population of grains before twinning occurs. The response is initially linear on average (Figure 33 (c)), and the reflection deforms elastically. At the onset of twinning, at around –350MPa of applied stress, and until –380MPa, the plot shows a strong relaxation of $\{00.2\}_{\parallel}$ elastic strain of around 1000 μstrain. This drop is not instantaneous but takes the form of a 'S shape'. As previously mentioned, the $\{00.2\}_{\parallel}$ grains that just twinned appear in a relaxed state as compared to the aggregate and a fortiori have a much lower stress state than the pre-twinning $\{00.2\}_{\parallel}$ population of

grains. The new-born twins thus tend to lower the average $\{00.2\}_{\|}$ strain. When the proportion of newly twinned grains is higher than the proportion of pre-twinning grains, the $\{00.2\}_{\|}$ reflection mostly captures the behaviour of the twinned grains. As observed in the RD/TD sample, the reflection (now mostly represented by twinning child grains) rapidly bears most of the load. No further yielding is observed for $\{00.2\}_{\|}$ in the range of macroscopic stress applied. It is worth noting that the strain in $\{00.2\}_{\|}$ after twinning is of the same order in the RD/TD and RD/ND samples, which validates the method of determination of $d^0_{00.2}$ in the case of RD/TD.

The RD/ND test presents another feature not observed in the other test: at the onset of twinning, the response of the $\{11.2\}_{\|}$ reflection shows a spike of higher strains.

There are two main differences between the two RD compression tests:

- The initial textures are slightly different and are probably caused by variations in the plate.
- The compression strain rates are different: whereas the RD/TD test was monitored with around 80 measurements points (meaning a hold for 7 min) the RD/ND test counted only 40, and the latter was thus approximately twice as fast as the former.

So far no investigation has been carried out to determine why the reflections behave differently at the onset of twinning, but it is thought that strain rate could have an effect on the micromechanical behaviours.

- *Residual strains*

As mentioned earlier, three unloadings were performed for each compression test. The diffraction measurements at –10 MPa for each unloading give an idea of the level of residual misfits. For all the tests the unloading elastic strains (relative to the initial state) are compared in Figure 38. For clarity only three reflections are presented: the two extreme

reflections $\{10.0\}_{\|}$ and $\{00.2\}_{\|}$, and an intermediate $\{10.2\}_{\|}$ reflection. In all cases, the basal reflections are in compression while the prism reflections are in tension. Depending on the compression direction, $\{10.2\}_{\|}$ grains are either in compression or in tension.

For compression in the rolling direction, $\{10.0\}_{\|}$ are initially in tension but to a much smaller extent than for other tests. On the other hand, $\{00.2\}_{\|}$ is in a less compressive state for ND than for TD compression. This evidences the effect of texture on the intergranular residual stresses: for compression along directions with strong texture coefficients, the grains that are most represented experience smaller residual stresses. Indeed, because of their higher volume fraction, these grains have a strong influence on the macroscopic response, hence there are on average less misfits between them and their environment.

At the end of the compression tests, there can be large spread of strains: for the ND/TD sample, the basal reflections are in compression at –2000 μstrain while the prismatic ones are tensile at 3000 μstrain. A rough approximation, applying the uniaxial Hooke's law with a Young's modulus of 100 GPa, gives that the corresponding type II residual stresses are –200 MPa and 300 MPa respectively.

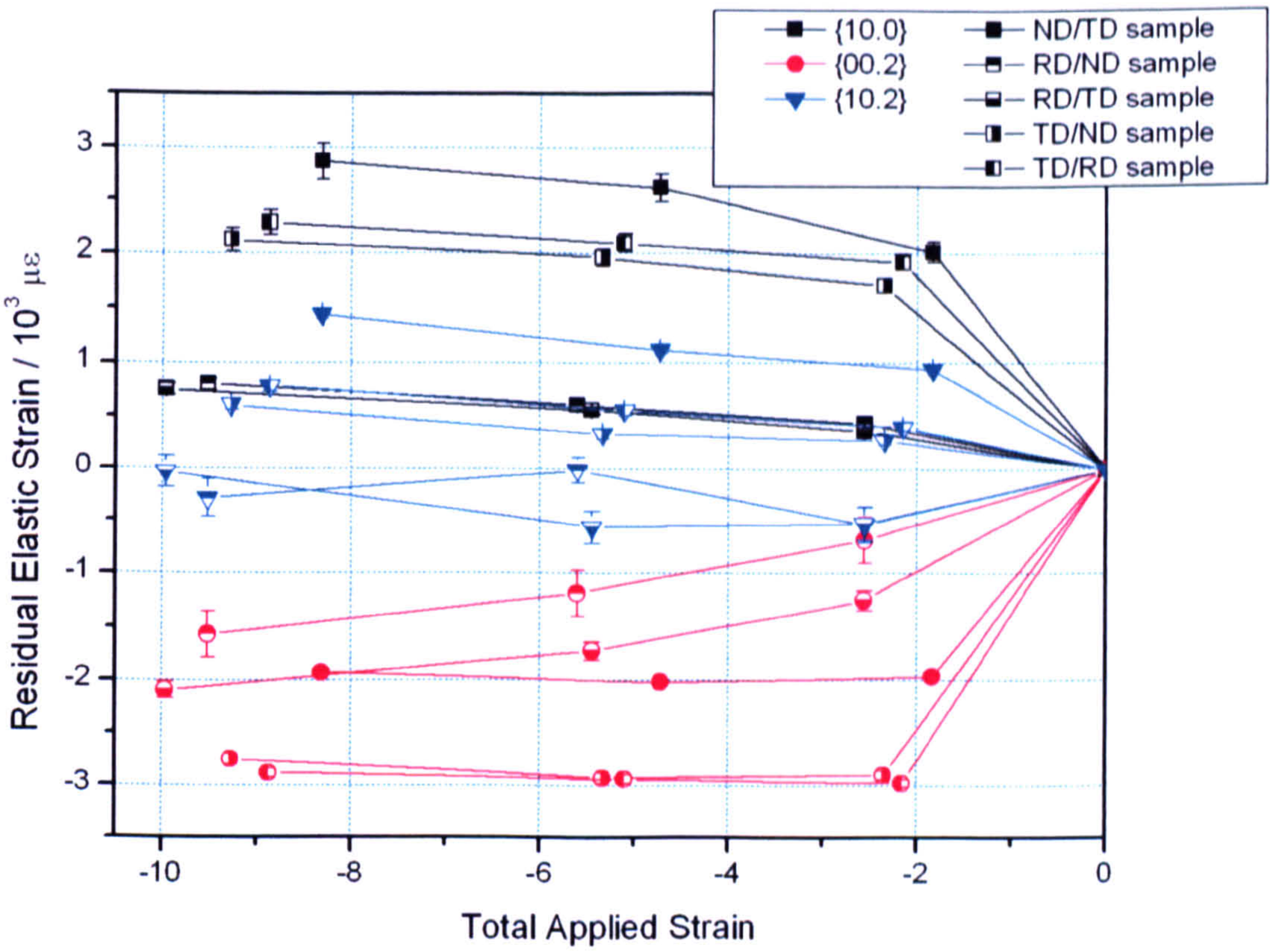

Figure 38 Residual strains after the unloadings relative to the initial state

- *Peak width*

The width of a diffraction peak contains a lot of valuable information. Hutchinson [33] lists the most important reasons for peak broadening. Beside the instrumental resolution, the width of the peak depends on material characteristics: the grain size, the density of dislocations and the level of microstrain.

Slip and the consequent increase in the number of dislocations bring some mosaicity in the material that is usually characterised by slight intragranular misorientations. The incident beam is not perfectly parallel and each of these misoriented subset might still diffract, although with a slightly different Q direction. In a monochromatic instrument, this mosaicity contributes to the peak width. To show this let us consider two subsets of a grain with the same d-spacing, but with a different diffraction direction, respectively Q_1 and Q_2. Although the subsets diffract with the same 2θ (wavelength fixed), the detector will see the neutrons at two different angular positions corresponding to twice the angle between Q_1

and Q_2. In theory this geometric effect should not play a role in a 'perfect' TOF instrument. Indeed the 2θ being fixed by the detector position, only the subsets with a perfectly aligned Q vector would diffract. For other subsets, the angle of the incident beam would have to be offset and the diffracted beam would miss the detector. However in practice detectors cover a wide angular range in 2θ (30° on ENGIN-X) and the same phenomenon is observed as for angle dispersive methods: the rays diffracted by subsets with same d-spacings but with a slightly different Q direction can still be collected by the detector. The wavelength will then show a distribution (which is function of the 2θ range of the detector). Although the large detection coverage contributes to increasing the peak width, it also allows more volume to diffract into the detector and saves counting time.

Each subset might also have a different level of stress and thus different d-spacings. They would then each diffract rays of different wavelengths (or 2θ for angle dispersive methods) which would result in the broadening of the peak. It is also seldom that all the grains contributing to the same reflection bear the same load and by the same effect this distribution of intergranular microstrain contributes to the peak broadening. These contributions are very dependent upon the amount of plasticity in the material: if there is more plasticity, there is more mosaicity and more intergranular strains. It is difficult to separate all the contributions to the peak width, but assuming that the experimental conditions are exactly the same between measurements, the instrumental contribution to peak broadening is constant, and it is possible to extract some qualitative information about the relative amount of plasticity between the measurements.

In this work, the width w is the width at half maximum of the Voigt component of the diffraction peak and is expressed in terms of microstrains. To eliminate the instrument contribution, one can express the relative width with reference to the first run by a

quadrature subtraction (inspired from [6]): $W = \pm\sqrt{\left|w^2 - w_0^2\right|}$, with w_0 the peak width for the first run. The sign of W is given by the sign of $(w - w_0)$.

Figure 39 shows side by side the evolution of the peak width and 'Δ lattice strain' for $\{10.0\}_{\parallel}$ during the compression of RD/TD. What we call 'Δ lattice strain' are expressed by $\Delta\varepsilon^{e}_{hk.l} = \varepsilon^{e}_{hk.l} - E^{diff}_{hk.l} \times \Sigma$ where $\varepsilon^{e}_{hk.l}$ and $E^{diff}_{hk.l}$ are the total elastic strain and the diffraction elastic constant for the {hk.l} reflection respectively, and Σ is the macroscopic applied stress. Hence $\Delta\varepsilon^{e}$ is the divergence of the lattice strain from the elastic behaviour of that reflection. It is very close to what can be found in the literature under the name 'incompatibility strains', with the difference that incompatibility strains are usually defined as the difference between the elastic strain in the grain and the elastic strain in the aggregate. They thus include strains that arise from both the elastic and plastic anisotropy of the crystal. The advantage of 'Δ lattice strains' is that they represent only the incompatibilities that arise from plastic anisotropy. Thus the 'Δ lattice strains' are nil (or virtually in practice) in the elastic part and take positive or negative values as deformation mechanisms take place.

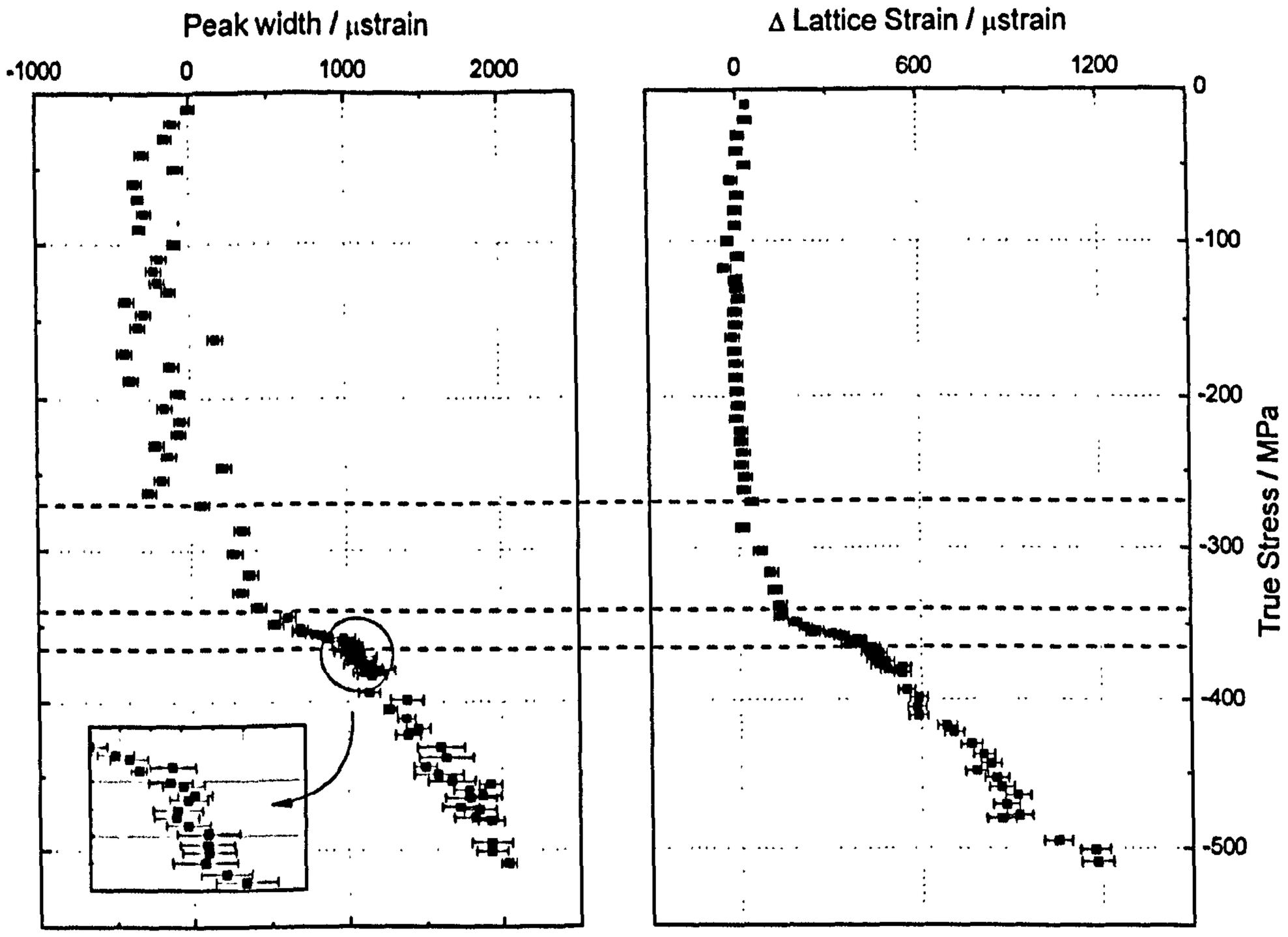

Figure 39 Evolution of the peak width and the Δ lattice strain for $\{10.0\}_{\|}$ during compression along RD in Zry-4

On Figure 39, both curves show identical inflections at the same levels of stress. At –270 MPa as the reflection starts to yield, the peak width increases. At the onset of twinning and up to –360 MPa, the peak broadens significantly. This sharp increase could be due to the difference of strain between the untwinned grains and the relieved twinned grains. After this stage, there seems to be a stabilisation of the broadening (subplot in Figure 39) before a slow increase again. An explanation could be that at –370 MPa, most grains of the $\{10.0\}_{\|}$ have twinned and have undergone the same strain relief. Some other plasticity mechanisms and twin growth then contribute to the peak broadening.

The two mechanisms previously described as responsible for the relaxation of the measured lattice strain in $\{10.0\}_{\|}$ at twin nucleation, have competing effects on the peak width. Twinning contributes to peak broadening by introducing a lattice strain difference between twinned and untwined {10.0}. On the other hand it can contribute to a reduction

in peak width as the most stressed grains twin and relax first, which tends to reduce the spread of stresses in the reflection. However since there is sudden peak broadening in conjunction to the $\{10.0\}_{\|}$ relaxation, the former appears to be predominant. If it is the case it could be that the relaxation experienced by the parent grains is greater than the spread of elastic strain in the {10.0} reflection before twinning.

5.3 In situ deformation and annealing of Zr-2.5%Nb

For this experiment, the material was extracted from a pressure tube (see Section 4.2). The first part of the experiment consisted of a set of in-situ compression on the raw material, very similar to what was done on zircaloy-4. Another set of samples were annealed in situ in the neutron beam, and compressed in-situ thereafter at room temperature. In this section the following designations will be used:

- AD: Axial direction
- RaD: Radial direction
- HD: Hoop direction

5.3.1 Samples and set up

5.3.1.a Compression on as received samples

The pressure tube wall is 4.35mm thick. This dimension is a limitation for the design of the compression coupons: we need a sufficient gauge length to run the compression test properly and avoid too much beam shadowing from the stress rig components (grips); moreover the diffracting volume must be large enough to ensure a good diffraction peak quality with a reasonable counting time. It was decided that the coupons would consist of an assembly of elementary coupons glued together with a cyanoacrylate adhesive. To reduce the amount of gluing, the elementary coupons were cut oblong in the axial direction with the dimensions 4 x 4 x 8 mm^3.

Four coupons were designed for in-situ compressions on the material as received, measuring the strain component pairs AD/RaD, AD/HD, RaD/HD, HD/RaD. For the AD/RaD and AD/HD, four elementary parallelepipeds were combined into 8 x 8 x 8 mm^3 coupons (Figure 40). For compression along RaD and HD, only two were glued together

into 4 x 8 x 8 mm^3 samples in order to reduce the cross section area and the load to apply. Indeed some preliminary tests showed that these directions are very hard and the necessary load to reach 10% deformation might have surpassed the capacity of the 100kN stress rig.

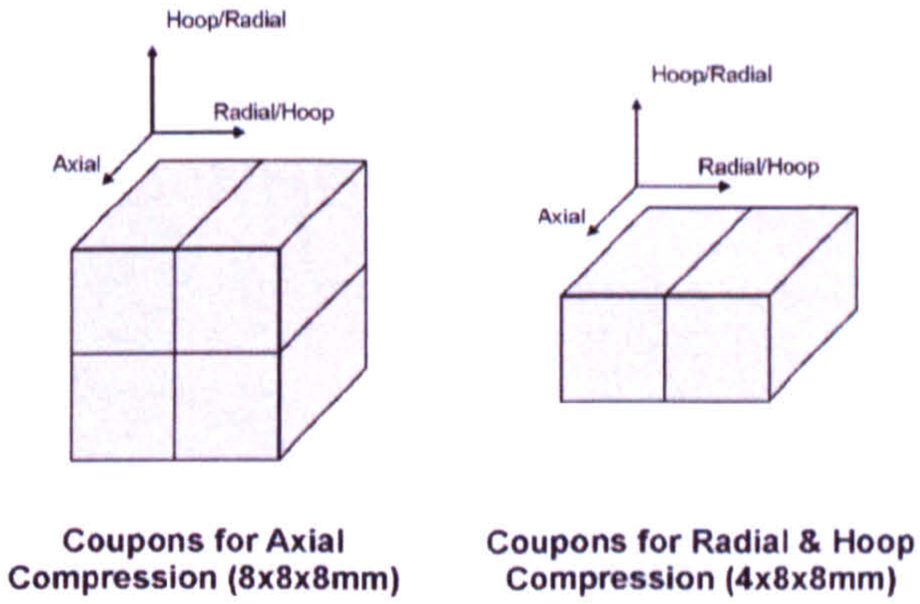

Figure 40 *Description of the compression coupons*

The same set up was used as for compression of Zircaloy-4 (Figure 28 and Figure 41), with the difference that an extensometer was placed on the alumina platens of the grips (alumina was used because of its high strength and stiffness and transparency to neutrons to reduce beam shadowing). However the extensometer was used only for a better strain recording (though not ideal because not on the sample itself) and the process was still run in alternatively stress or position control.

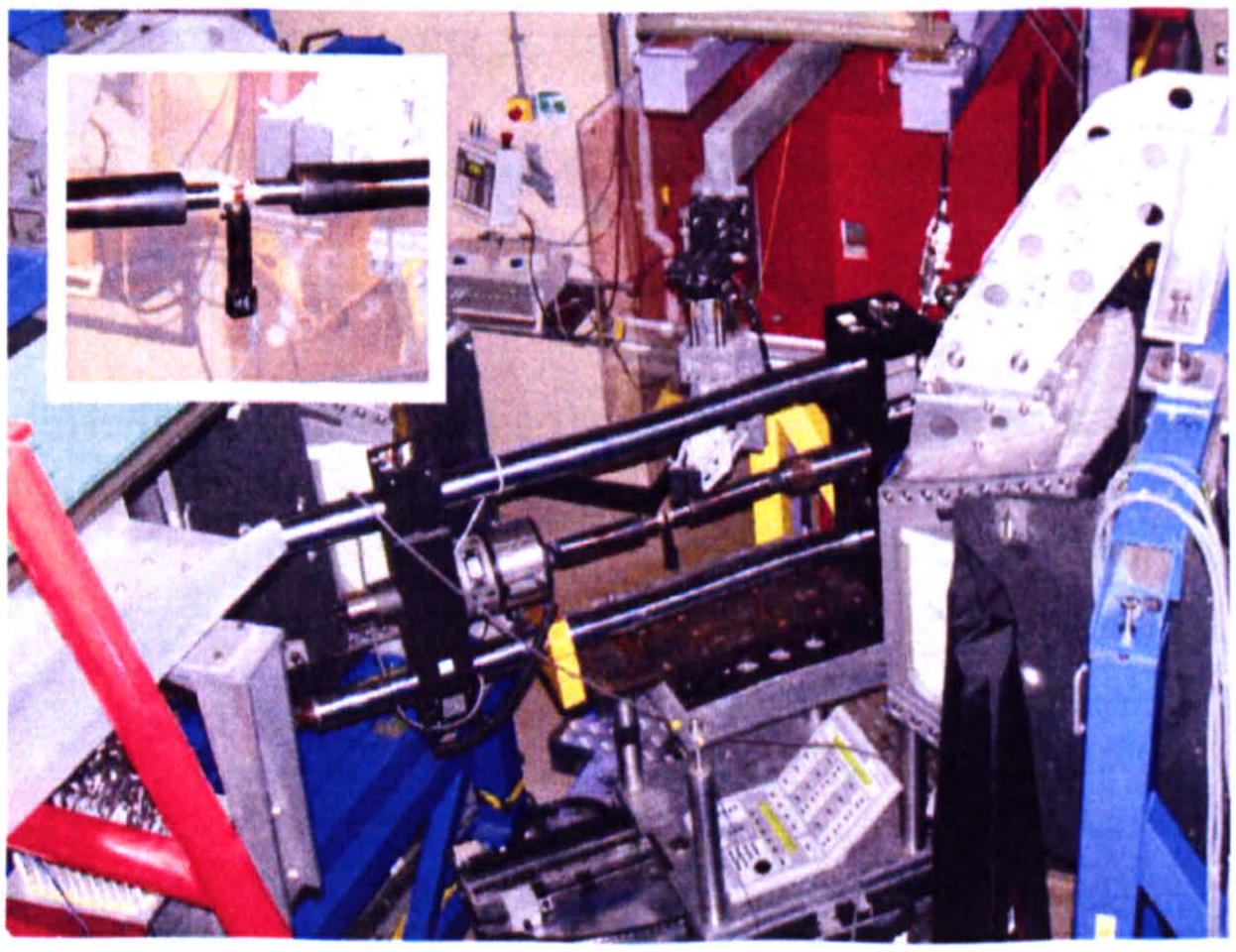

Figure 41 *Set up for in-situ compression on the as received material*

The gauge volume used was 4x4x6mm^3, and it is not fully immersed in the samples RaD/HD and HD/RaD (Figure 42). Partially filled gauge volumes are generally a problem in strain measurement and can introduce an error in the measured d-spacing. In our case, the lattice strains are relative to the first run and as long as the centre of gravity of the gauge volume is the same throughout the test, this does not impair the results. The diffracting volume is also slightly reduced by approximately 20%. To compensate for this loss, the counting time was increased correspondingly from 16mn to 23mn for the RaD/HD and HD/RaD tests.

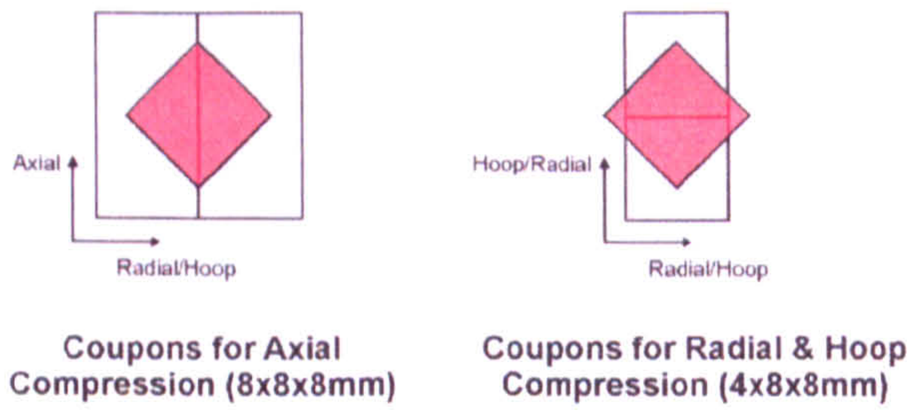

Figure 42 Top view of the compression coupons and gauge volume

5.3.1.b Annealing

Two 8 x 8 x 8 mm^3 coupons were heated up to 620°C (HT1) and 560°C (HT2) respectively. They were placed in the rig with a small constant load of approximately –4MPa to hold them in an AD/RaD and AD/HD setup respectively. They were heated by a radiant furnace under a continuous flow of argon in order to reduce oxidation (Figure 43). The temperature was controlled based on the measurements of a thermocouple in contact with the samples through a hole in the grips.

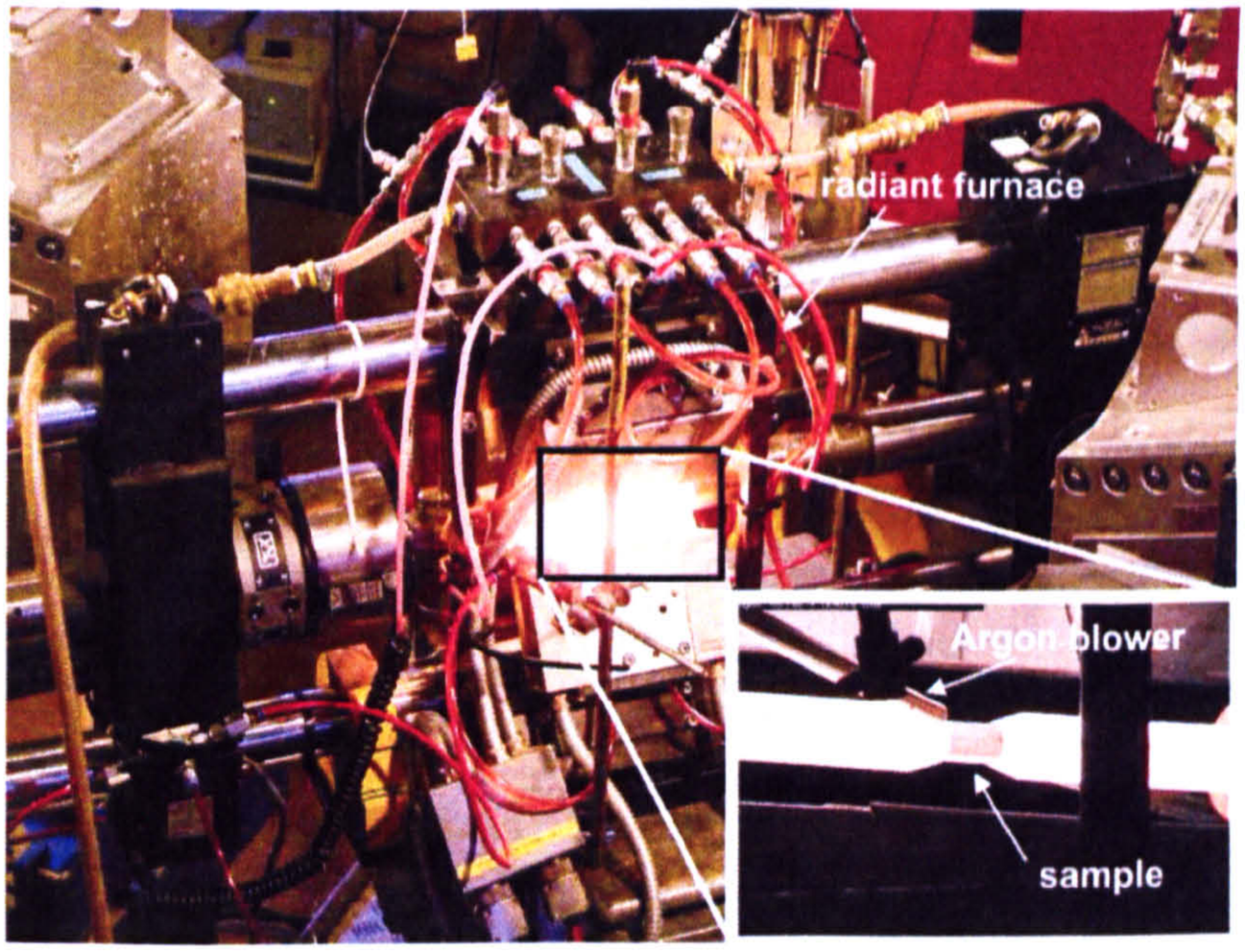

Figure 43 Set up for heat treatment

The full annealing processes for heat treatments HT1 and HT2 are described in Figure 44. The heating of the samples was done at a rate of approximately 40°C/min. The maximum temperature was held for 20min. Three neutron strain measurements were performed during the steady increase in temperature. During the cooling phase, holds in temperature allowed several neutron measurements to be performed and also effectively reduced the cooling rate. The heat treatment itself was over a period of time of around 3 to 3.5 hours. Room temperature diffraction spectra were acquired prior to and post the heat treatment. The measurements are indicated by the markers on the curves.

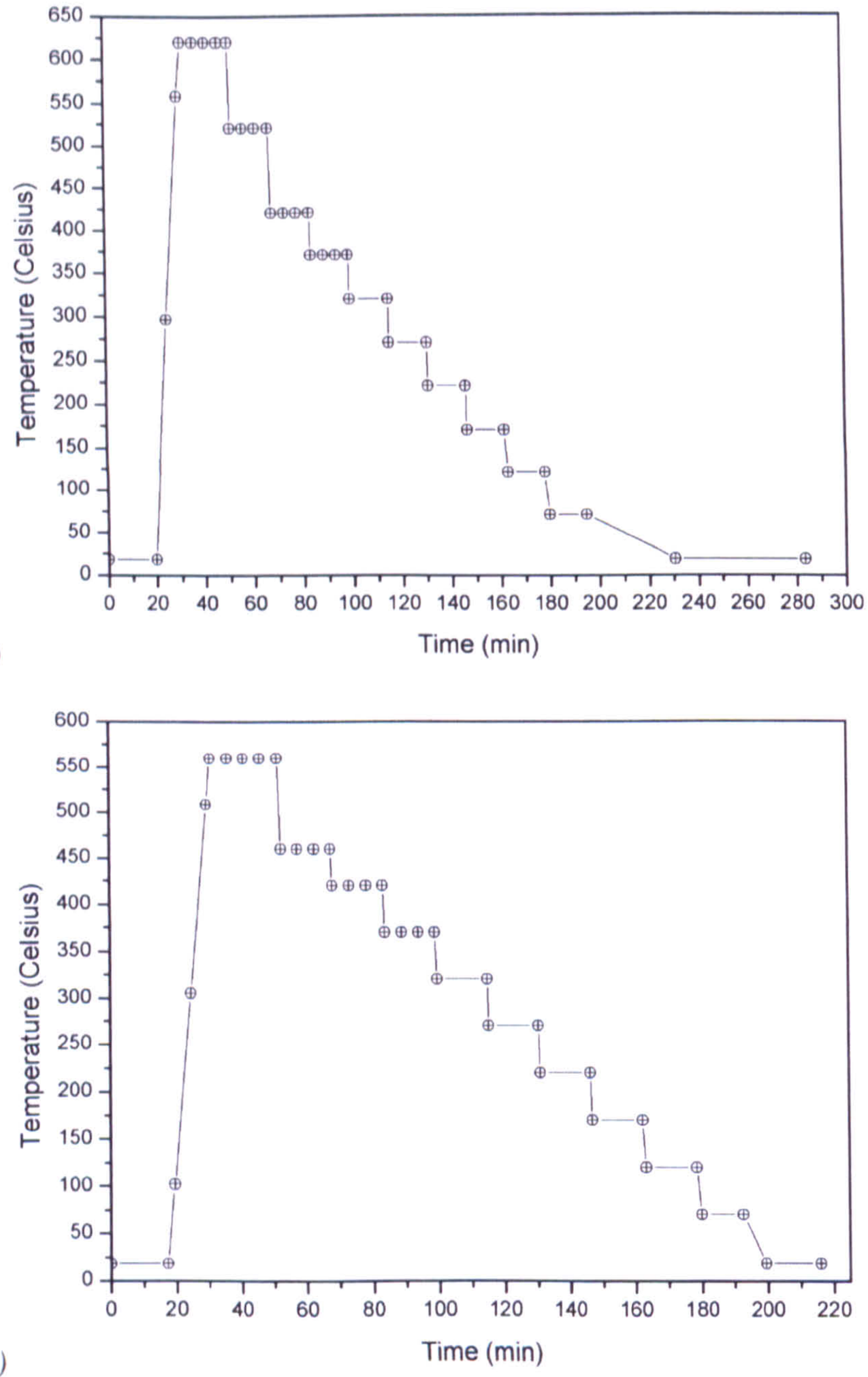

Figure 44 Temperature vs time for (a) heat treatment HT1 and (b) heat treatment HT2

5.3.1.c Post-Annealing compression

The sample annealed to 560°C was then compressed AD/HD at room temperature in the way described previously. A picture of the setup is shown in Figure 45.

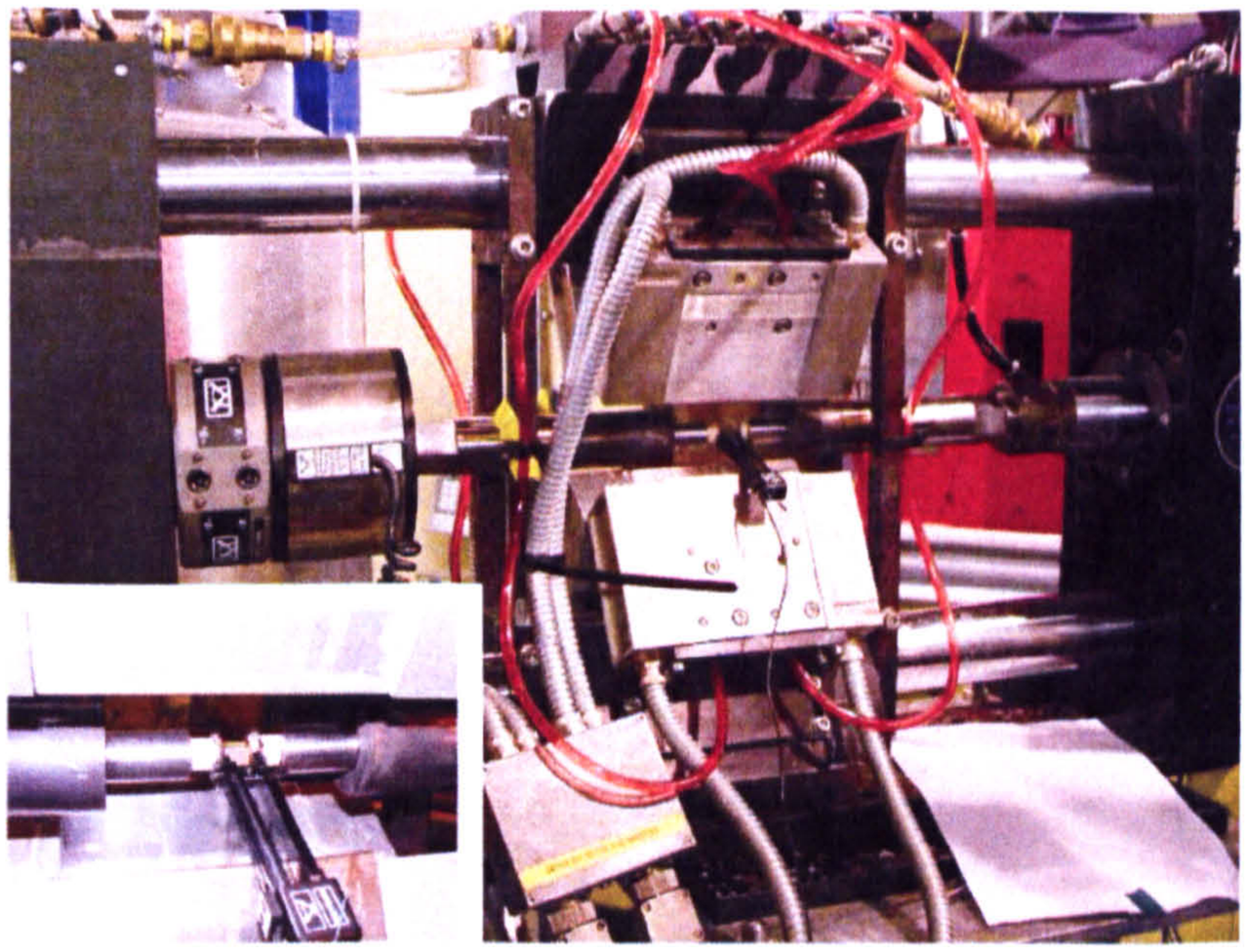

Figure 45 Experimental set up for compression after heat treatment of Zr2.5Nb

5.3.2 Results

5.3.2.a Diffraction Spectra

As described in section 4.2 the material contains two phases: α hexagonal close packed (hcp) and a small proportion of second phase. The two phases are expected to leave a trace in the diffraction spectra. Figure 46 shows the spectra in the principal directions. Beside the very well identifiable hcp peaks, some small and broad peaks are visible in some directions particularly for a d-spacing of around 2.5Å. Figure 47 is a zoom of the spectrum around this area. A Rietveld fit has been applied to the spectrum using 3 templates corresponding to the α, the metastable β-Zr and the intermediate ω phases. The later is hcp with a *c/a* ratio lower than 1 [70, 71]. To account for the texture, the intensities of the α peaks have been weighted by a spherical harmonics function. The fit suggests that the second phase is actually a mixture of several phases, probably including β-Zr and ω.

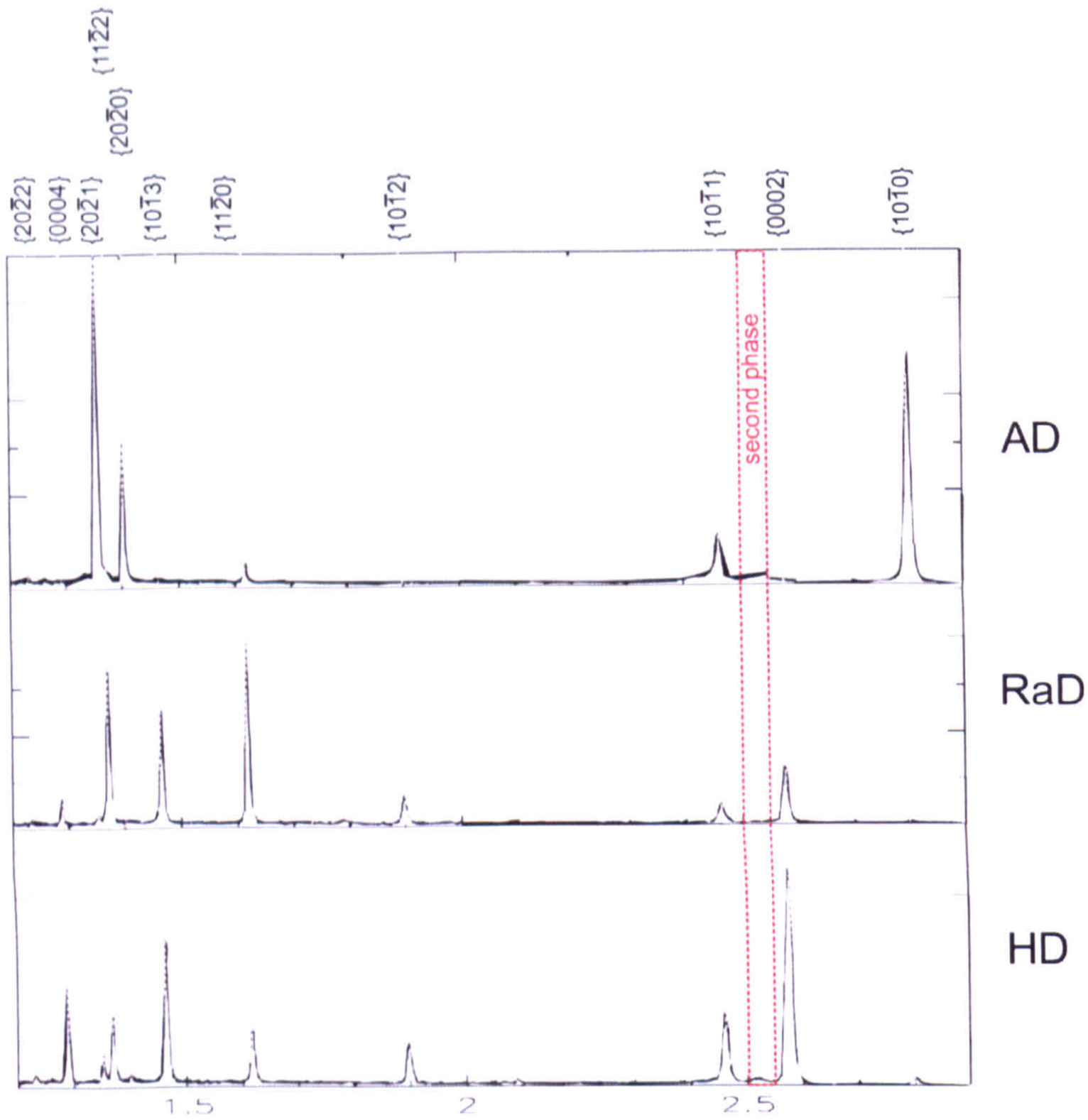

Figure 46 *Diffraction spectra in the 3 processing directions for Zr2.5Nb as received*

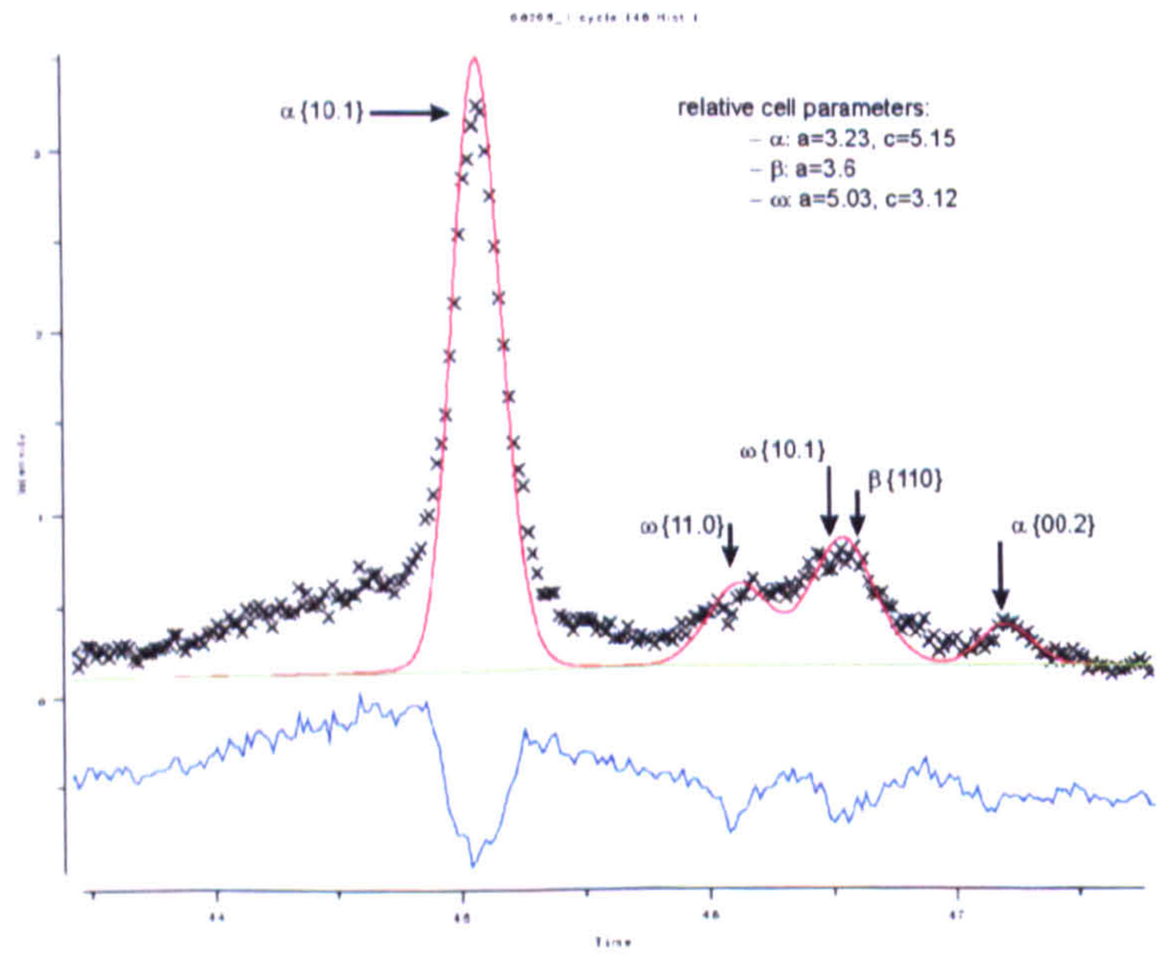

Figure 47 *Rietveld fit with 3 templates for α, β and ω phases.*

5.3.2.b Heat treatment

The aim of the heat treatment was to relieve the intergranular stresses in the α phase caused by cold work without changing the microstructure. Heat treatment HT1 reached temperatures above the monotectoid temperature of 610°C [62] while the temperatures in HT2 stayed below this threshold. As seen previously, the second phases are best visible in the spectrum between the peaks $\{10.1\}_\alpha$ and $\{00.2\}_\alpha$. Figure 48 shows the peak evolutions in this region of the AD spectrum during the two heat treatments. In both cases, some peak shifts are clearly visible in the α peaks. They are induced by the thermal variations: as the temperature changes, the crystal expands or contracts, and the interplanar spacings increase or decrease. For the second phases the interpretation is not as straightforward: some peaks seem to appear and others disappear during the heating and early cooling stages, suggesting some structural changes. The most probable secondary phases to be present during the process are β and ω. The β phase is stable as β_{Nb}, but is often seen in the form of the metastable β_{Zr} [62, 64] under the pressure tube fabrication conditions. In its metastable form this bcc phase has a bigger cell parameter, which means that the diffraction peaks are shifted to the higher d-spacings as compared to the stable form. The transformation from β_{Zr} to β_{Nb} usually happens during heat treatment and involves the hcp ω as an intermediate phase. A by-product of this decomposition is α. In the range of d-spacing we are focusing on (i.e. 2.4 to 2.6 A), the second phase reflections expected are $\{110\}_\beta$ and $\{11.0\}_\omega$ and $\{10.1\}_\omega$.

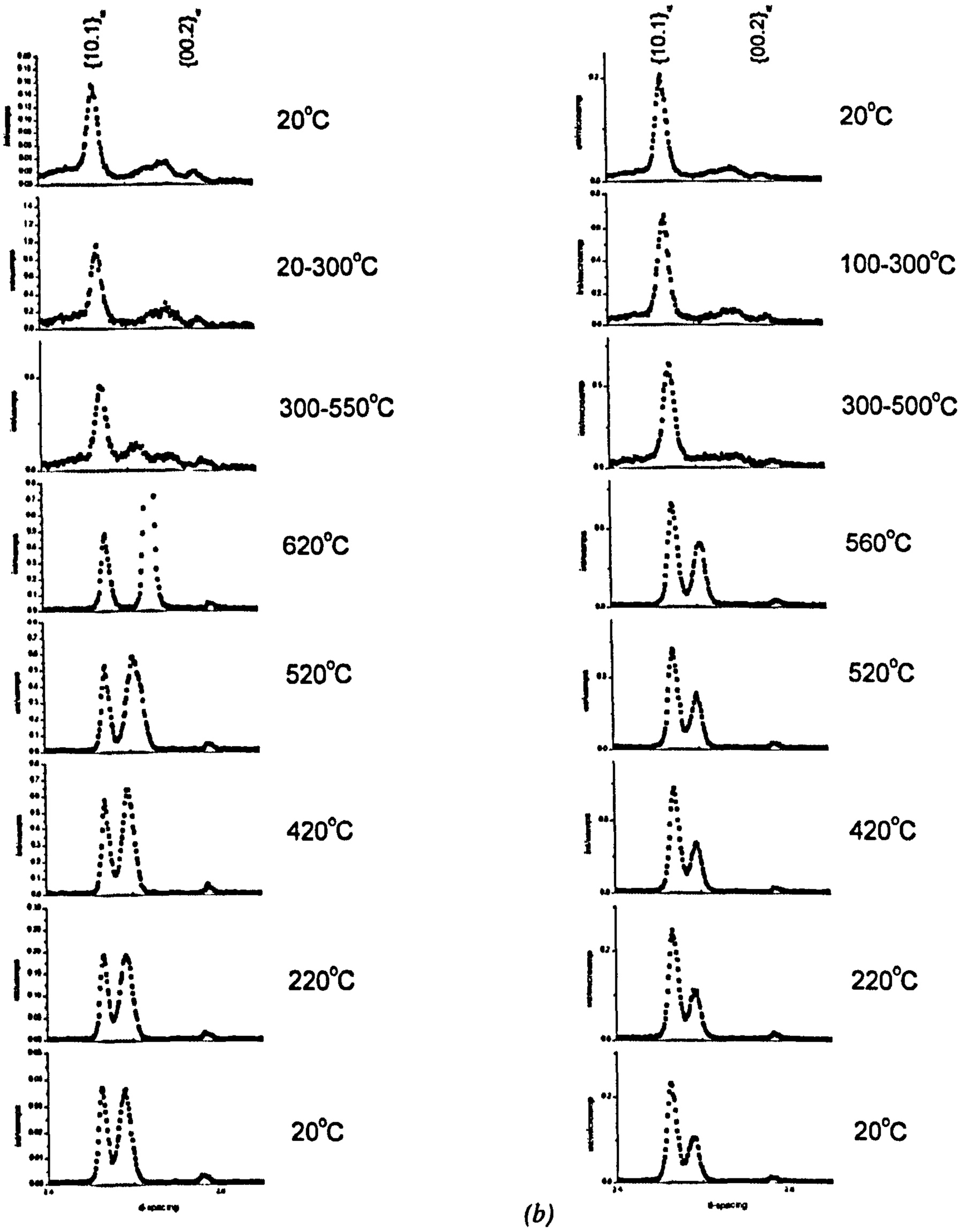

Figure 48 *Diffraction peak evolution during (a) heat treatment HT1 and (b) heat treatment HT2*

During the heating process of HT1, some secondary phase transformation seems to happen between 300°C and 550°C, where a doublet of peaks is clearly visible. These could be the two peaks that characterise ω in this region. However one needs to be cautious as the measurement is a time-averaged collection of neutrons and thus gives no indication of the history (it could be averaging some other phenomenon that happens during that range of temperature such as a transformation to β_{Nb}). At 620°C, above the eutectoid, the material is

α and β_{Zr}. The sharp peak corresponds to $\{110\}_{\beta Zr}$. At the end of the plateau at 520°C, the peak is highly shifted to a lower d-spacing by around 10,000 microstrain. Such a shift can't be a result of thermal contraction alone but it would correspond quite well to a phase transformation. Hence it seems that at the early stage of cooling, between 620°C and 520°C the second phase transforms back to the stable β_{Nb} During further cooling down the peak shift corresponds to the thermal shrinkage. The reduction in the proportion of β phase associated with the cooling down seems to affect the ratio of intensities between the $\{10.1\}_{\alpha}$ and $\{110\}_{\beta}$ peaks.

During HT2 things are slightly different. First, in the HT2 300-500°C spectrum, the peak doublet is not present when comparing to the HT1 300-550°C spectrum. This encourages us to think that the extra peak is a β_{Nb} peak that appears after 500°C rather than a ω phase peak. As such it is an indicator of the stabilisation of the second phase. Secondly, the peak observed at 620°C in HT1 is not visible during HT2, which tends to confirm that the peak corresponds to $\{110\}_{\beta Nb}$ and that HT2 remained below the $\alpha+\beta_{Zr}$ two phase region.

Interestingly the second phase peaks are much sharper after heat treatment. An explanation could be that in the as-received sample there is a mixture of ω and β_{Zr} phases with overlapping diffraction peaks. Moreover these metastable phases might contain a high level of mosaicity and dislocations contributing to the peak broadening. The heat treatment has both the effect of stabilising the second phase and reducing the dislocation density.

In Figure 49, the AD spectra are compared before and after HT1 and HT2. For clarity, the spectra recorded at room temperature after HT are shifted by +1ms. Apart from the differences in the second phase, the peaks of the α phase are very similar and show very little intensity variation, which suggests that the texture has not been affected too much by the heat treatment. Moreover the intensity variations are slightly less after HT2 than HT1.

The fact that during HT1 the temperature reached above the eutectoid threshold might have had an effect on the resulting texture. The local texture variations in the as received material are also clearly visible: although the initial spectra for HT1 and HT2 are qualitatively similar, the relative peak intensities are different.

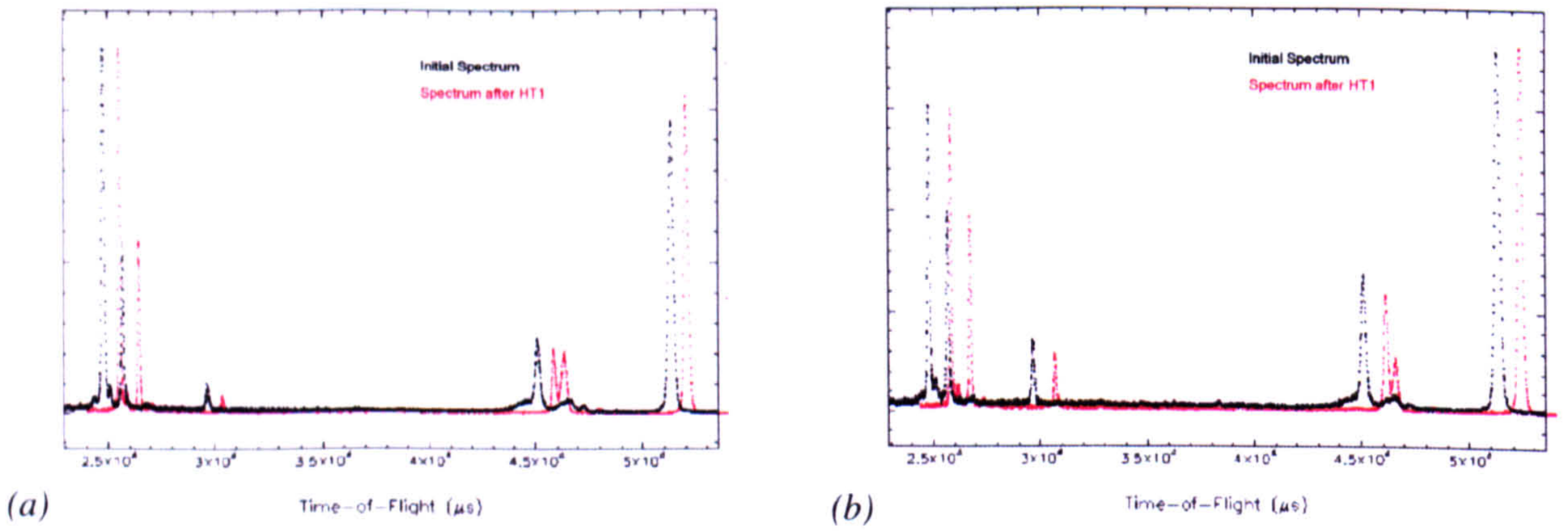

Figure 49 *Comparison between the pre and post HT spectra, (a) for HT1 and (b) for HT2 (to ease the comparison of intensities, the post HT spectrum is shifted by +1ms)*

5.3.2.c Macroscopic responses

Figure 50 shows the macroscopic behaviour before and after heat treatment. The strain was recorded by the extensometer placed on the alumina platens. For the as received materials, HD is the stiffest direction but at the same time the least ductile as the sample failed at ~ 8% of total strain applied. RaD can bear more load than AD. For all of the directions, the hardening is quite strong at lower plastic strains and has a very small rate after 4% deformation. The tests were stress controlled at low deformations and position controlled at higher deformations. When the rig was driven in stress control for stresses far above the yield point, the samples could creep quite significantly during the diffraction measurements, which explains the plateaux in some stress-strain curves. The heat treatment seems to reduce the strength of the material by 50 to 100 MPa.

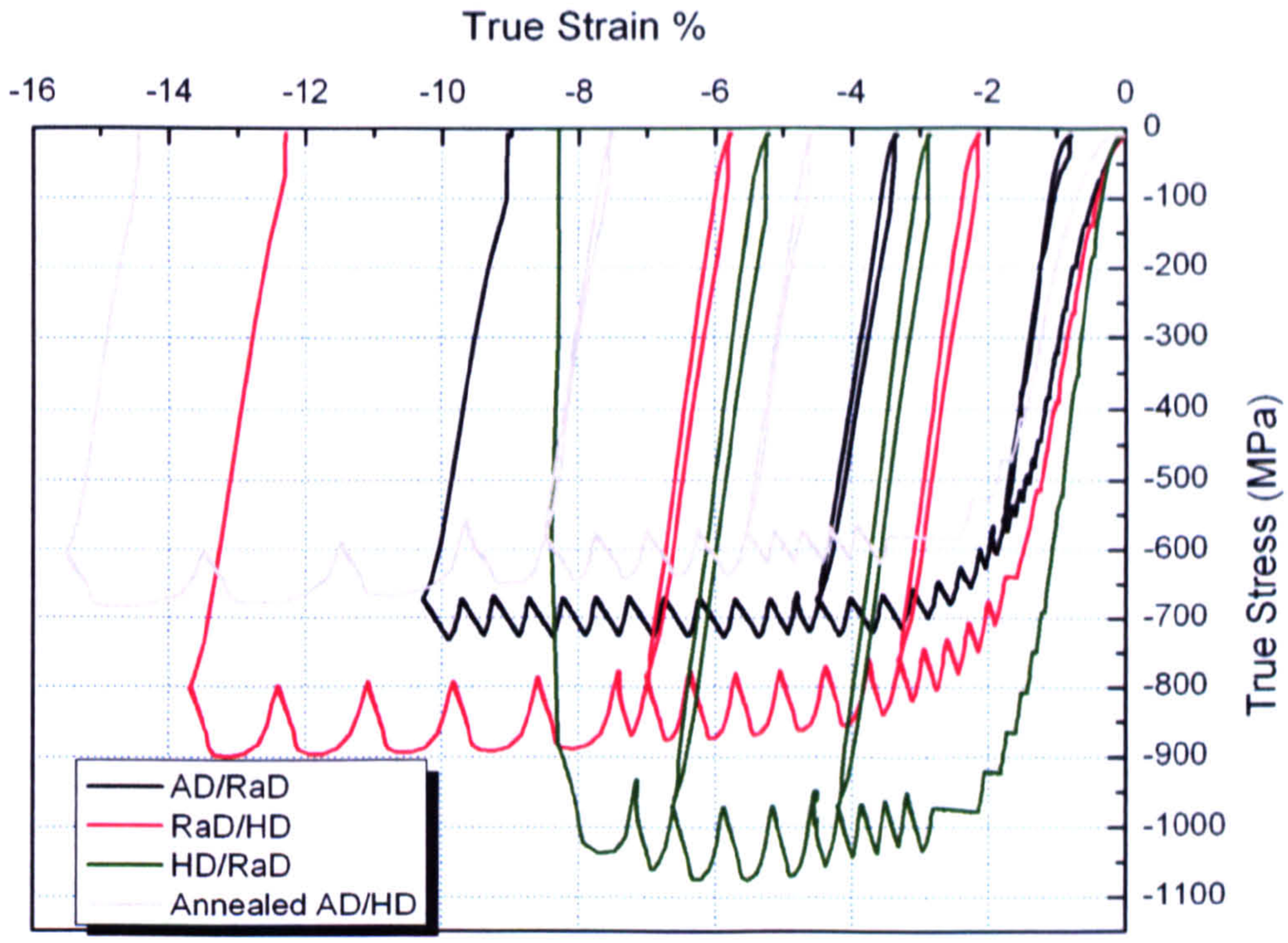

Figure 50 *Macroscopic response of Zr2.5%Nb along each processing direction and before and after heat treatment*

5.3.2.d Elastic strain response during compression

For the α phase, the peaks were fitted individually using OpenGenie (with the same profile function as for Zry-4) and the elastic strains derived from the peak shift in the same way as described in Section 5.2. The three overlapping second phase peaks in the as received material were fitted as one single peak wherever possible. However for compression along HD and after heat treatment, the β {110} peak tends to overlap with the $\{10.1\}_\alpha$ or the $\{00.2\}_\alpha$ peaks, and single peak fitting is made difficult. In these cases a Rietveld fit was performed. The templates used were hcp for the α phase and bcc for the secondary phases.

To account for the texture-induced peak variations in α, spherical harmonics have been introduced up to the 8^{th} order. The elastic strain in the β phase is deduced from the cell parameter (i.e. from the d-spacing of {100}).

For compression after HT1, a Rietveld fit was used to extract the lattice parameter of β because the strongest β peak, {110}, and the α {10.1} peak were overlapping, which

rendered single peak fitting difficult. Figure 51 shows the Rietveld fitted AD spectrum after heat treatment HT1 and before compression. During compression, the second phase peak was shifting faster than the α peaks and eventually merged completely with $\{10.0\}_{\alpha}$. Hence it was not possible to fit the second phase for the entire compression tests.

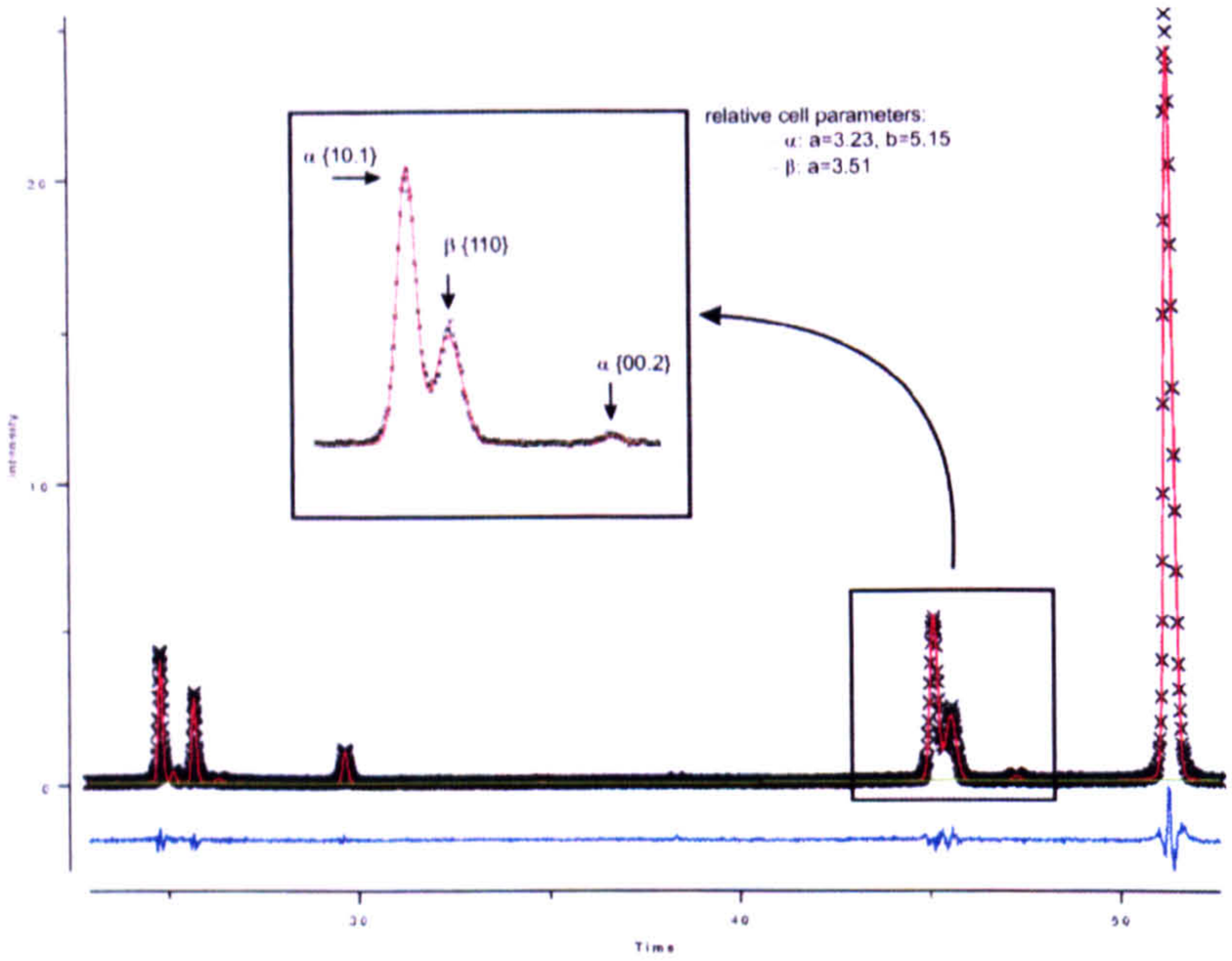

Figure 51 Rietveld fit of the AD spectrum after heat treatment.

From the different plots in Figure 52, it is clear that the overall behaviour of the α phase reflections is similar to that for Zry-4: the prism $\{10.0\}_{\|}$ reflection yields first, followed by the first and second order pyramidal $\{10.1\}_{\|}$ and $\{11.2\}_{\|}$, while the basal $\{00.2\}_{\|}$ bears the load. During compression along AD, the $\{00.2\}_{\|}$ shows a similar S-shape as was observed during compression of the Zry-4 along the rolling direction. Before this relaxation, the elastic strain increases suddenly to –17000 μstrain before dropping to –2000 μstrain. We can also assume with a good level of confidence that the relaxation is due to twinning as demonstrated for Zry-4. This is an interesting result: given the fine grain size of the α phase, twinning might not at first thought be considered as a major deformation mechanism. Twinning has rarely been observed in Zr-2.5%Nb and only one reference has been found in the literature that mentions it [72]. The author optically observed twinning in

coarse grained Zr-2.5%Nb but did not in fine grained material with an average grain size of 5microns. He attributed this to a Hall-Petch type effect on twinning activation. In a warm-rolled plate of Zr-2.5Nb, with grains in the form of platelets 30 x 30 x 3μm^3, Cai et al. also observed a {00.2} elastic strain relaxation during compression along RD which is the direction less populated by basal planes. However the consideration of several other elements like peak intensity evolution and extensive TEM investigation drew them to the conclusion that this strain 'doubling back' was not due to twinning but was most probably induced by the dislocation evolution. We are on the other hand rather confident that the relaxation observed in our results is due to tensile twinning. This is supported by the peak intensity evolution and the evolution of texture (as described in a following Chapter). To explain this difference we ought to consider the differences between the two materials. In the case of Cai et al., the material is a rolled plate whereas in the present case it is an extruded tube. Despite some globally similar features, the resulting textures are quite dissimilar in terms of sharpness: while the maximum {00.2} pole intensity is less than 2 times random in the rolled plate, it reaches 7.5 in the tube. The respective {00.2} deprived directions (RD for the plate and AD for the tube) contain a different proportion of basal grains, which affects the compression behaviours along these directions. In Cai's case there are enough other grains which can yield even with the few very 'hard' {00.2} grains around. In the case of our material there is so much {00.2} planes parallel to the load that these grains have to twin. Despite these considerations, there is still some inconsistency: the grains in Zr-2.5%Nb pressure tube are platelets of dimensions 25 x 10 x 1 μm^3, much smaller than in the rolled plate. Hence it seems that the grain size is not the only aspect that determines twinning activation, but some other factors like texture could also have a strong influence.

The second phase is also represented on the plots. It appears that it is behaving as a hard phase, bearing high elastic strains. Both during AD and RaD compression, the lattice strain

evolution of this phase doesn't show an inflection characteristic of yielding but the phase seems to bear much higher elastic strains than the α phase. This result contradicts the assumptions made by Kapoor et al. [55] and Kiran Kumar et al. [54] who consider the β phase as being softer but is in agreement with the findings of Holt et al. and Cai et al. [52, 73]. The latter suggest that this stiff behaviour is not inherent to the phase but rather is a result of a Hall Petch effect associated with the fine grains. Because most of the Nb is segregated in the β phase, there is probably also a solution hardening effect. Such unexpected behaviours of normally soft β phases have been observed in Titanium alloys too [74, 75].

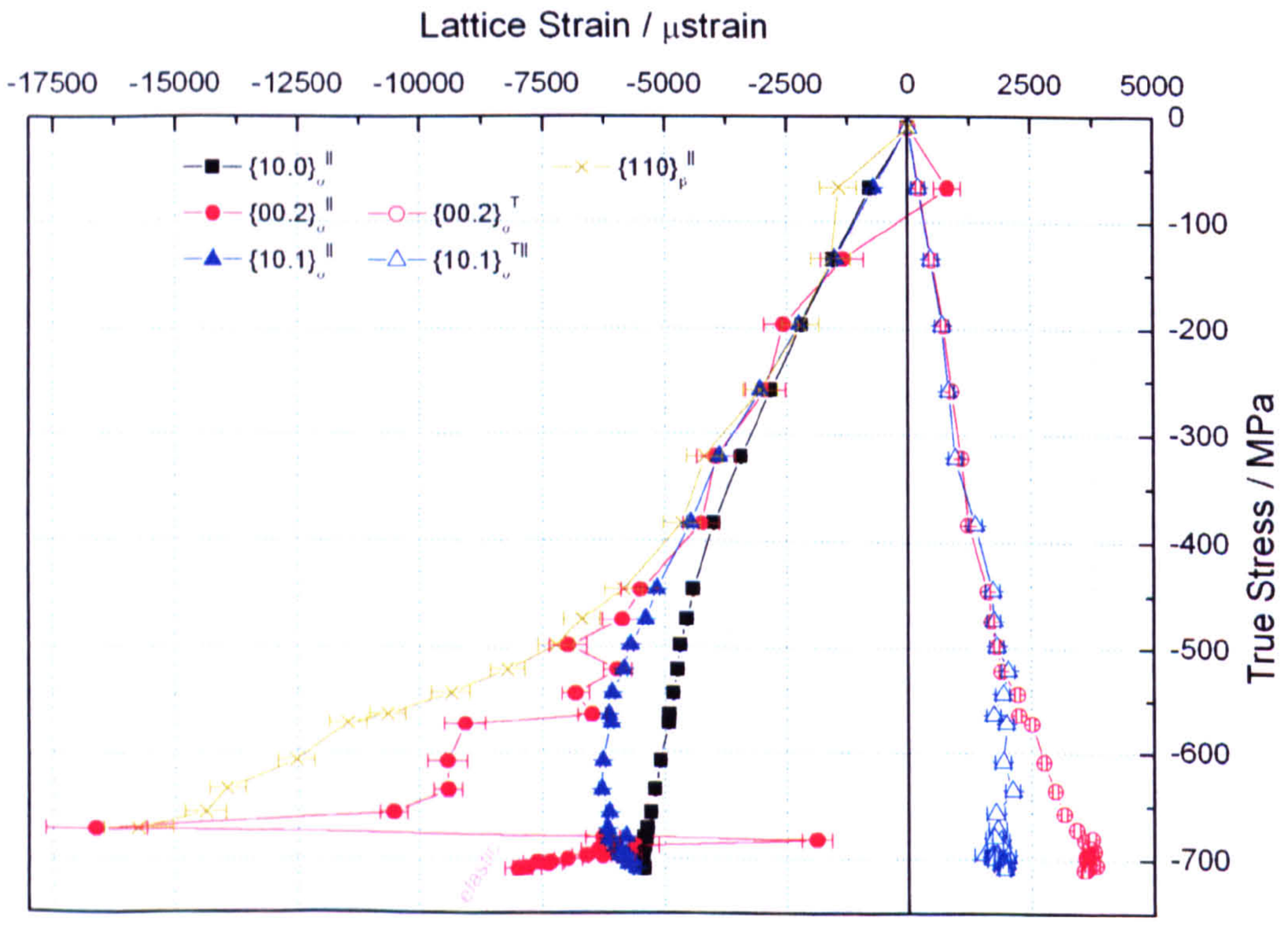

(a)

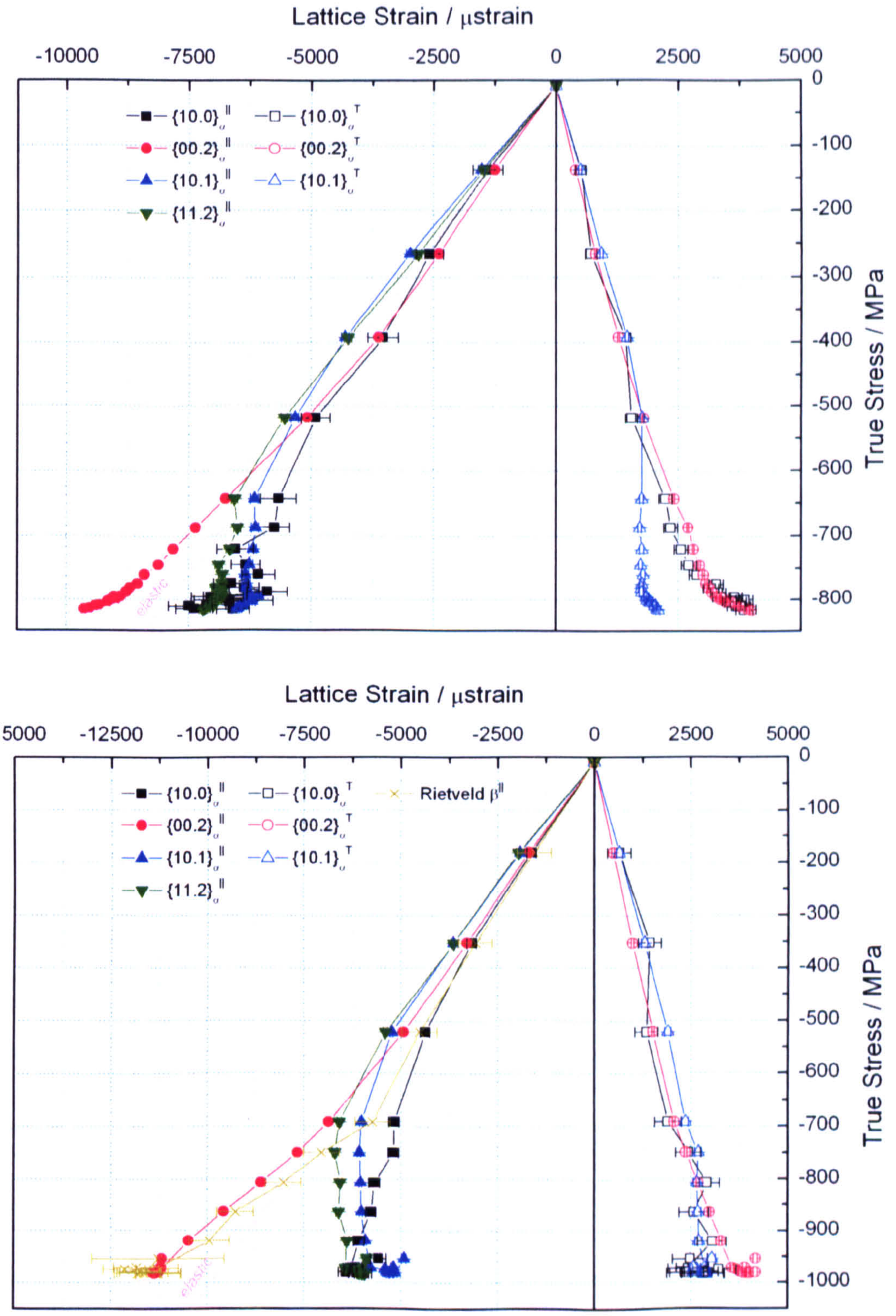

Figure 52 *Elastic strain responses for Zr-2.5Nb for (a) compression AD, measurement AD and RaD, (b) compression RaD, measurement RaD and HD, (c) compression HD, measurement HD and RaD.*

After heat treatment, although the second phase stabilised into β_{Nb}, this phase is still behaving similarly to the β_{Zr} during AD compression (Figure 53): it is under much higher stress than the hcp phase. Twinning is also visibly activated in the α phase as evidenced by the sharp relaxation of the basal reflection. It is however happening at lower macroscopic stresses than before HT: around –570 MPa instead of –650 MPa. Another remarkable

feature is visible in the Poisson direction (which is the Hoop Direction in this case): there is a doubling back of the strain in the Poisson reflections. Interestingly this doubling back occurs simultaneously with twinning. It is however difficult to establish a direct correlation with twinning at this stage, and similar phenomenon have been observed in materials where twinning is not a major deformation mode (see [76] for example). It is interesting to notice that the Poisson strains show a larger spread in this test than observed in the other tests. The $\{10.0\}_{TD}$ reflection is even briefly in compression, and were it not for the doubling back, it would probably be in a significant state of compression at the end of the test.

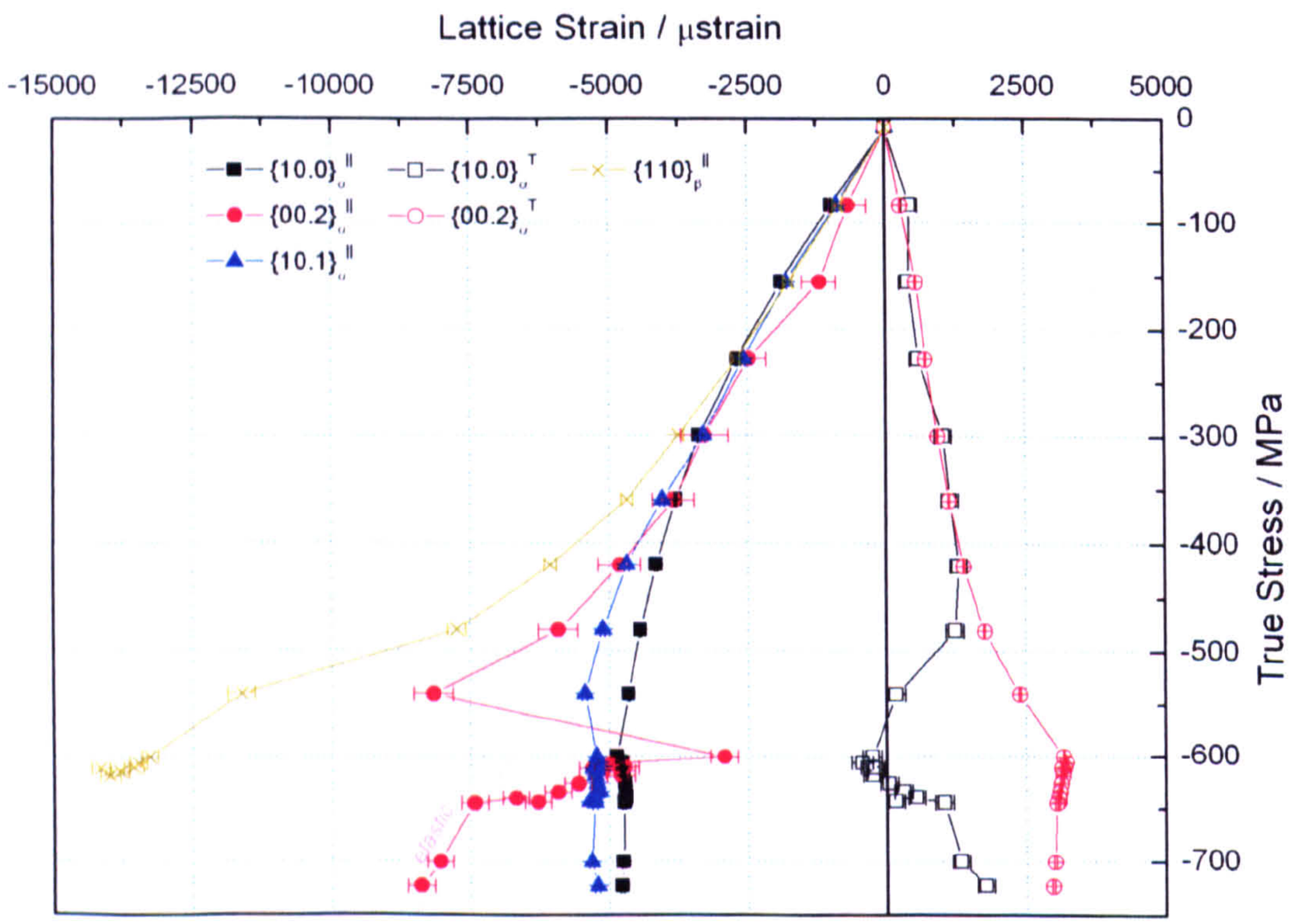

Figure 53 *Elastic strain response for compression AD and measurement AD and HD after heat treatment*

5.4 Conclusion

The results presented in this Chapter show that in-situ compression is a useful tool for understanding the deformation mechanisms in the two zirconium alloys. By following the evolution of the elastic strain during compression it was evidenced that there are strong orientation-dependent heterogeneities in the materials. Both alloys showed similar qualitative microscopic responses: along the compression directions, the prismatic reflections yield first and the basal reflections yield last. At the end of the tests, the intergranular misfits reach several thousand microstrain. As suggested by the lattice strains and peak intensity evolution, tensile twinning seems to be a major twinning mode especially for RD and AD compression of Zircaloy-4 and Zr-2.5%Nb respectively. For RD compression of Zry-4, the well known relaxation in the parent grains at the onset of twinning has been observed at the mesoscopic length scale in the $\{10.0\}_{\|}$ reflection. This result could be indicative that twinning activates in a large proportion of grains at once.

For both alloys, the macroscopic responses were very different depending on the compression direction. The crystal anisotropy has been brought to a macroscopic level by the texture.

The results performed on Zr-2.5%Nb evidenced that the β phase behaves like a hard phase, both before and after heat treatment.

In the next Chapter, an elasto-plastic self consistent scheme will be used to try to simulate the mechanical response of Zry-4 during compression tests. The computed results will be compared with the experimental results presented in Section 5.2.

Chapter 6 Modelling

In this section I use the Elasto Plastic Self Consistent (EPSC) scheme to model the response of Zircaloy-4 depicted in Chapter 5. The main objective is to use the EPSC for solving an inverse problem where we are trying to determine the crystal properties (specially the hardening properties of the deformation mechanisms). This can help understand the mechanisms more precisely, make predictions for other types of deformation etc.

The model was also used to study the scale transfer for the determination of macroscopic (residual) stresses from the measurement of lattice strains, and how the assumptions generally made in the literature can affect the result.

6.1 Inputs

The generalities about the model and its input are addressed in Section 2.3. This Section focuses on defining the specific inputs used and the practical issues met in the case of Zircaloy-4 compression.

6.1.1 Texture information

As mentioned in Section 2.3, it is necessary to provide the model with information about the fraction of grains with given orientations. This texture information is the main component for a transfer of properties from the microscopic to the macroscopic level. It should be in the format of a weight file: for each possible set of Euler angles, a weight is assigned corresponding to the volume fraction of grains with this orientation. The Euler angles are a set of three angles that describe a crystal orientation in the sample reference: they are associated with three rotations which when performed in sequence transform the sample coordinate system into the crystal coordinate system. Using the 'weights' function

in PopLa, we were able to convert the pole figures output by GSAS into such files. Figure 54 details the whole process.

The histograms from neutron diffraction measurements at Hippo were fitted by a Rietveld fit, using spherical harmonics to weight the peak intensities. The GSAS function Polfplot was used to obtain the six pole figures ({00.2}, {10.0}, {11.0}, {10.1}, {10.2} and {11.2}) from the spherical harmonic coefficients. The pole figures were further corrected for sample misalignment through successive rotations and tilts with the help of the PopLA program. These correction steps are necessary because the principal directions of the sample were not necessary aligned with the HIPPO coordinate system. The rolling process presents some symmetry and so should the texture. The corrections were thus performed so that the main features in the pole figures show some symmetry with regard to the pole directions. PopLA can also automatically determine some of the correction factors to apply by symmetry considerations.

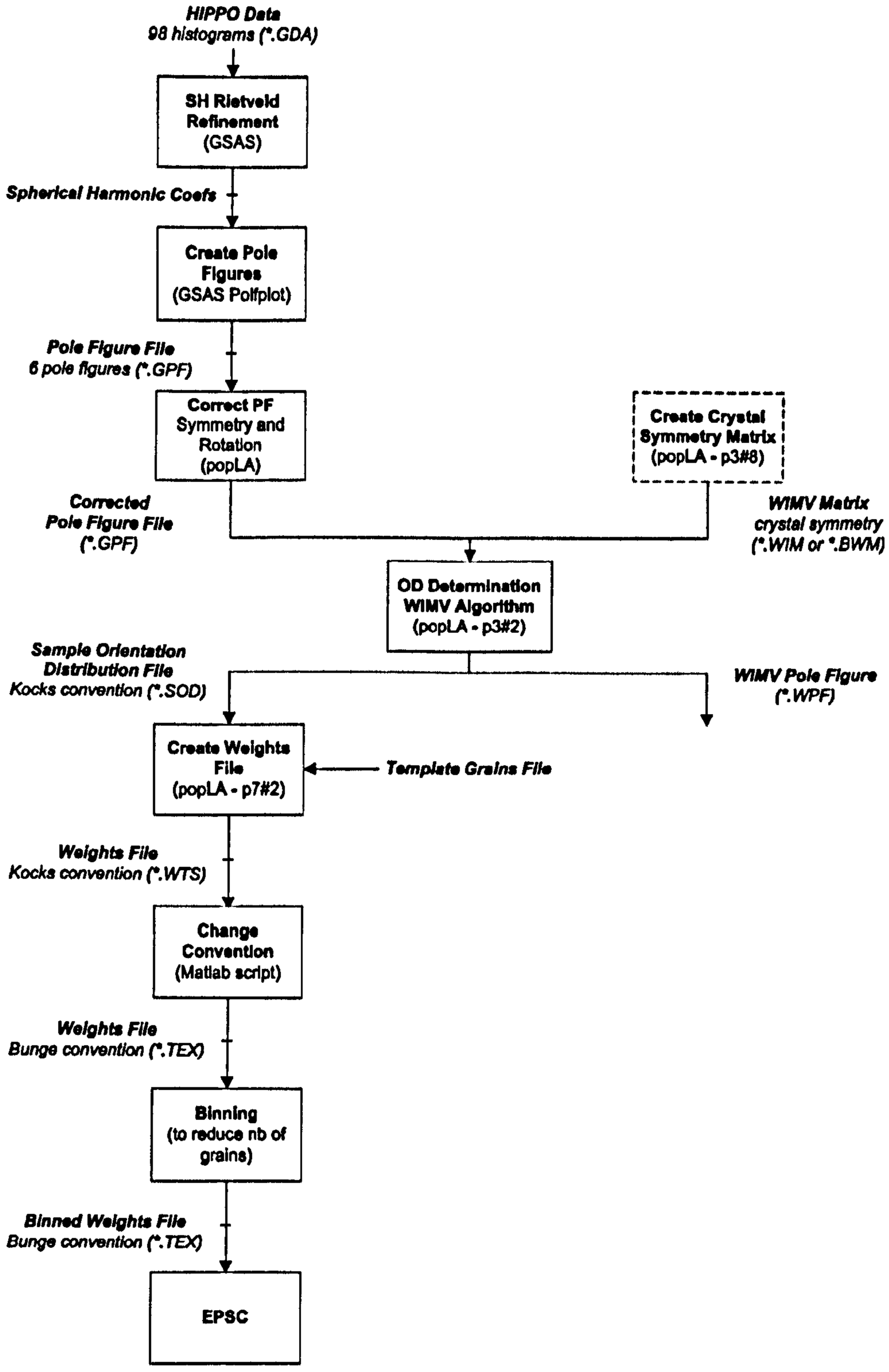

Figure 54 Flowchart showing how to obtain grains weight files for input in EPSC

The WIMV (Williams - Imhof - Matthies - Vinel) algorithm was then used [77]. This has two purposes: the main objective is to produce an orientation distribution, which is a three dimensional matrix of values of the orientation distribution (OD) function over part or all Euler space. The other advantage of applying the WIMV is to renormalize the pole figures. The negative densities produced in the data after SH were truncated by Polfplot as PopLa doesn't accept negative densities in pole figures (besides these are not real). As a result of

this truncation, the pole figures are no longer normalized. The WIMV algorithm is iterative: from an estimated OD, it calculates the pole figures to be compared to the experimental ones; if the comparison is unsatisfactory, some correction factors are applied to the OD and the process is repeated until it yields a good agreement. As explained in Section 2.2.5.a, the orientation distribution function associates an intensity to each set of Euler angles in the 3D Euler space. For simplicity it can be expressed as a set of 2D matrices with one of the Euler angles constant. If this slicing of the 3D Euler space is done with regards to the first angle, the OD is called the sample OD (SOD) as it corresponds to a distribution of sample orientations with respect to the crystal coordinate system. In this work we tend to use this formalism. On the other hand if the slicing is performed with regards to the last Euler angle, we talk about the crystal OD (COD). The original Euler space is defined for a range of 2π, π and 2π for the angles Ψ, Θ and ϕ respectively (in Kocks convention). By means of crystal symmetry, in the case of a hexagonal crystal, the Euler space can be reduced to a range of $\pi/2$ in Θ and $\pi/3$ in ϕ [26]. As there seems to be some asymmetry in the real texture (see pole figures in 4.1.3), we decided to consider the sample as triclinic and not reduce further the Euler space, and the SOD covers $0 \leq \Psi \leq 2\pi$, $0 \leq \Theta \leq \pi/2$ and $0 \leq \phi \leq \pi/3$ for our texture with hexagonal-triclinic symmetry.

Using the 'weights function' in PopLA, the SOD was converted to a weight file, a list of Euler angles and associated weights that represent the number of grains with that orientation in terms of multiples of random. The SOD and the weight files are expressed in Kocks convention of Euler angles as required by the function. However, to input in the model, the more conventional Bunge's φ_1, Φ, φ_2 angles must be used. The relationships used to convert from the former to the latter are:

$$\text{Eq. 22} \qquad \begin{cases} \varphi_1 = \Psi + \pi/2 \\ \Phi = \Theta \\ \varphi_2 = \pi/2 - \phi \end{cases}$$

Figure 55 represents the SOD over the reduced Euler space in Kocks convention and Figure 56 is the first slice of the SOD. It is clear from those plots that at the edges and corners of the reduced Euler space, the cells are not whole: they are respectively ½, ¼ and 1/8 of a cell. As a result, to avoid over counting at the boundaries, the weight file is defined for sets of Euler angles such that $\Psi \in [0,2\pi[$, $\Theta \in [0,\pi/2[$ and $\phi \in [0,\pi/3[$.

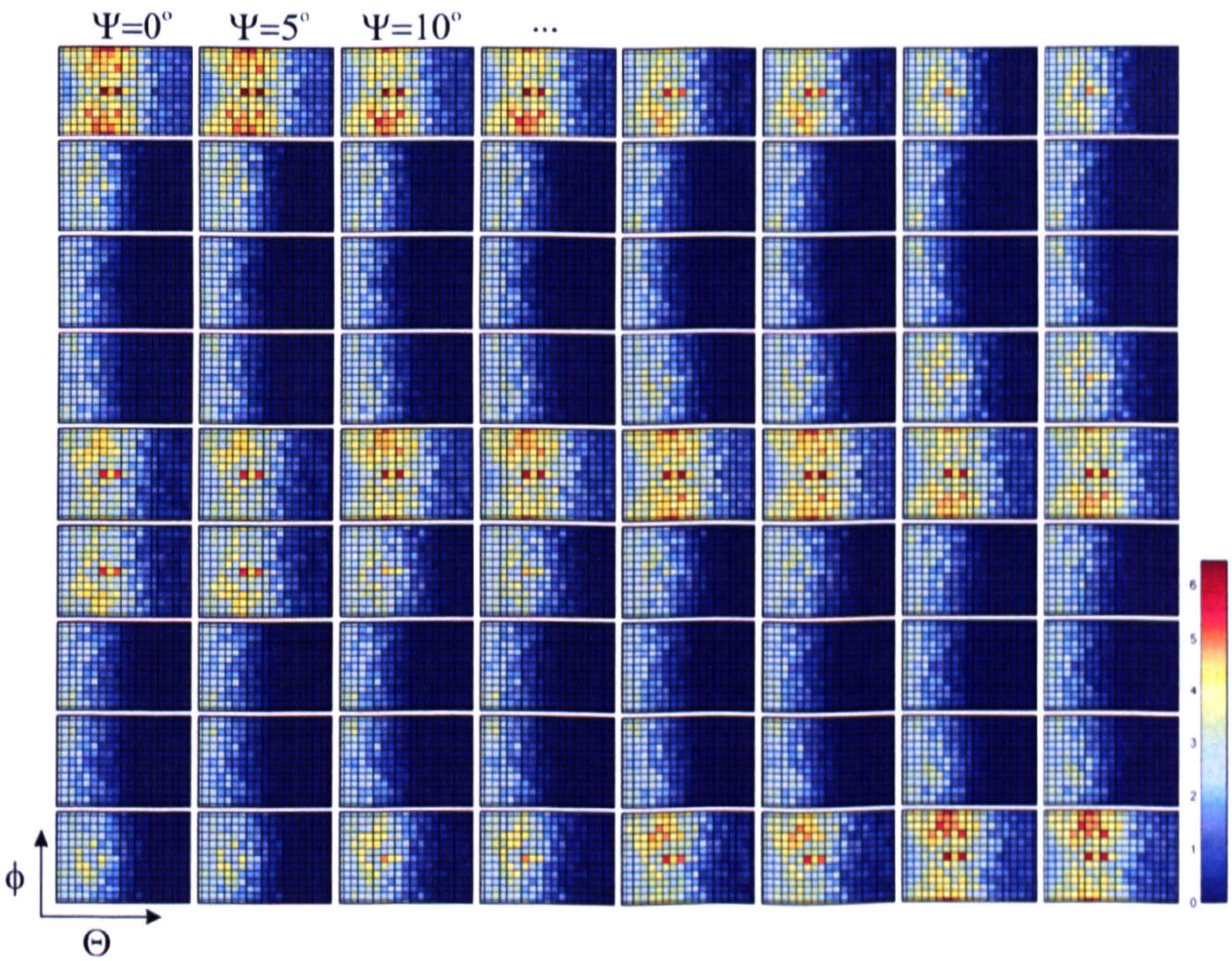

Figure 55 Representation of the whole SOD in Kocks convention: sections of Ψ from top right (0°) to bottom left (355°) in increments of 5°; for each section, Θ ranges from 0° to 90° and ϕ from 0° to 60°

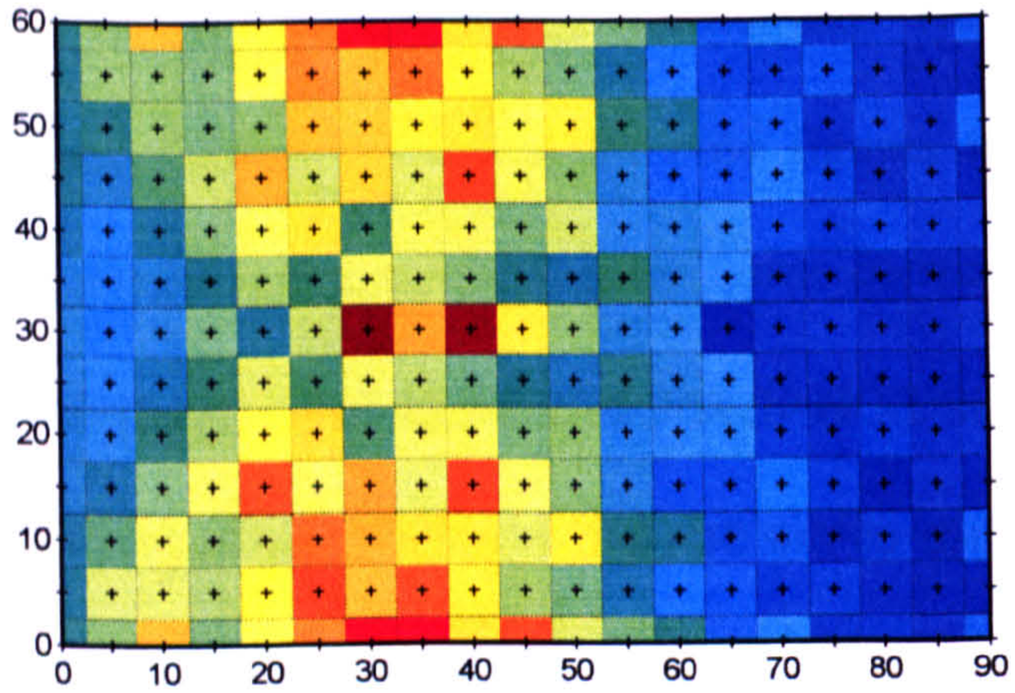

Figure 56 First section of the SOD; abscissa is Θ and ordinate is ϕ; the centre of each $5^o x5^o$ cell is represented by a cross

In the texture input file, the more grains, the longer the processing time to run the EPSC. It is thus better to keep the number as low as possible while still maintaining statistical accuracy. When considering Figure 55 and Figure 56, there seem to be large gradients of intensity with regards to Θ and ϕ, whereas the changes are more gradual in Ψ. Thus the increment size was taken of 5° and 10° respectively: $\Psi \in [0^\circ : 10^\circ : 350^\circ]$, $\Theta \in [0^\circ : 5^\circ : 85^\circ]$ and $\phi \in [0^\circ : 5^\circ : 55^\circ]$. Moreover orientations with intensities lower than 0.2 were discarded. The number of grains in the file was consequently reduced from over 13,000 to approximately 5,600. It was verified that this approximation on the texture information didn't affect the response by more than a few percent. The EPSC model renormalises the multiples of random intensities into fractions of the sum of all the weights, which are approximations of the volume fraction of each orientation.

Because the orientations with very low m.r.d. (multiple of random densities) were discarded, there are no grains with their basal planes aligned towards RD in the weight file. Although the approximation does not affect the response of the model, this means however that it is not possible to see how the elastic strain evolves for these reflections during the tests. It was thus decided to artificially re-introduce a $\{00.2\}_{RD}$ orientation with a very low associated weight.

6.1.2 Initial stress/strain state

As we have seen in Chapter 4, the Zry-4 plate was annealed after cold rolling. As a result of annealing there are some thermal residual stresses in the material which act as pre-strains for the compression test and might affect the results. Hence we need to implement this initial state in the model prior to simulating deformation.

These strains were not measured so we can only estimate them by running the EPSC model. Assuming that the stresses are totally relieved at 450°C, the model will compute the stresses that arise after going back to room temperature from an unstressed state at the annealing temperature. The calculation is solely based on the thermal expansion coefficients. These coefficients were defined for the single crystal of Zr in the crystal coordinate system by:

$$\alpha = \begin{bmatrix} 5.3 & 0 & 0 \\ 0 & 5.3 & 0 \\ 0 & 0 & 10.1 \end{bmatrix} 10^{-6} K^{-1}$$

These values were determined by Xu et al. [78] during an in-situ heating and cooling experiment on Zircaloy-2 in a neutron beam. These values differ slightly from the pure zirconium single crystal values determined by Goldak et al. [35]. For the annealing process, the model was run in temperature control with the free surface boundary conditions from 723K to 298K in 100 steps. The file containing the final stress strain state for each grain served as an input for the further simulation of the compression tests.

In order to avoid erroneous results it is important that the annealing simulation has been performed with the same deformation modes and texture as used for the compression (this is actually more of a file compatibility problem because it is unlikely that a lot of deformation modes activate during the cool down).

6.1.3 Crystal properties

One of the necessary inputs to the model is the crystal properties information: elastic, thermal and plastic. The thermal expansion coefficients have been defined in the previous section. The elastic and thermal coefficients can be obtained from the literature or could be refined based on some experimental results. Because for most tests only a few points were measured in the elastic zone it was not possible to refine the elastic constant with the EPSC model with a resolution smaller than the elastic anisotropy. Hence the elastic stiffness tensor was taken from the literature [36], with

$$C = \begin{bmatrix} 143.5 & 72.5 & 65.4 & 0 & 0 & 0 \\ & 143.5 & 65.4 & 0 & 0 & 0 \\ & & 164.9 & 0 & 0 & 0 \\ & & & 32.1 & 0 & 0 \\ & & & & 32.1 & 0 \\ & & & & & 35.5 \end{bmatrix} GPa$$

The parameters that define plastic flow in the crystals have to be refined by comparing the EPSC results with the experimental data and that is where the inverse problem lies. Refining these hardening parameters is more complicated than it seems. A set of deformation modes must be chosen out of the seven most probable systems (prism slip, basal slip, pyramidal <a> slip, pyramidal <c+a> slip of first and second order, tensile and compression twinning). Once this decision is made, there are nine parameters to refine for each slip mode and thirteen for the twinning modes (although the four extra parameters can be reasonably fixed to some literature value). This means that with the four modes chosen here (prismatic slip, basal slip, pyramidal <c+a> slip and tensile twinning) there is a minimum of 36 parameters to refine. Although, as we will discuss later, there are some possibilities of understanding the effects of different parameters on the EPSC response, the

system seems quite chaotic / stochastic as the parameters' effects on the predicted strains are not fully independent.

A method based on visual comparison ('by eye') was used to determine what the best set of parameters is. A graphical interface was developed from which the parameters could be adjusted, the EPSC run and the results plotted and compared against the experimental data. The interface is detailed in Appendix B.4.

6.2 Results

6.2.1 Annealing

The first step consisted of modelling the annealing process. Some information about the pre-deformation state of the material can be deduced from this simulation.

The Von Mises stresses experienced by the grains after annealing range from 25 to 125MPa. These extrema stresses are found in grains that are $\{00.2\}_{ND}$ and $\{00.2\}_{RD}$ respectively, as shown in Table 6. Only the stresses along the macroscopic processing directions are presented because for these grains they are very close to the principal directions of stress (the shear stresses are smaller than 0.1MPa).

	σ_{RD} *(MPa)*	σ_{TD} *(MPa)*	σ_{ND} *(MPa)*	$\sigma_{VonMises}$ *(MPa)*
Grain 1 $\{00.2\}_{ND}/\{10.0\}_{TD}$	–3	–13	17	25
Grain 2 $\{00.2\}_{RD}/\{10.0\}_{TD}$	77	–21	–61	125

Table 6 Residual thermal stresses in two grains after annealing

In both cases there is tension along the <c> axis of the crystal (parallel to ND and RD for grain 1 and 2 respectively) and the prismatic planes are under compression. This is a result of the higher coefficient of thermal expansion along the c-axis: during the cool down the

grains shrink more along the c-axis than along other crystal directions and the lower average coefficient of thermal expansion tends to keep these orientations in tension.

However the magnitude of the stress is quite different between the two grain orientations. This is at first not intuitive because with temperature loading, there is no directionality (which is different to uniaxial mechanical loading). So the <c> axis residual thermal stress should be the same regardless of the crystal orientation. This would actually be true only in the case of a uniform distribution of orientations in the aggregate. The difference observed here is caused by a larger or smaller misfit with the surrounding medium. Because of the texture, the macroscopic thermal response is hugely (though not exclusively) influenced by the response of $\{00.2\}_{ND}$ grains. Thus grain 1, which has such an orientation, doesn't show a very different response to its surrounding, hence the small residual stresses. On the other hand, grain 2 belongs to a family of grain orientations that is largely underrepresented and shows a very different response to thermal variations with the average medium: the residual stresses are high.

6.2.2 Compression along ND

As a first approach, we tried to resolve the inverse problem on the deformation mechanisms (described in Section 6.1.3) by applying the model to each compression test separately in order to get an approximation of the values for the plastic flow parameters. The resolution of the problem caused less problem for compression along ND. As mentioned previously, the parameters were adjusted until the modelled and measured flow curves and lattice strain/stress curves were in reasonable agreement. It was found that looking at the lattice strains vs. the applied plastic strain was also helpful for the refinement. The model itself was run in stress control up to the maximum macroscopic stress at the end of the experiments. It was checked that 200 steps are sufficient for

avoiding the errors introduced by the forward calculation (see Section 2.3.2.c). This is a strong advantage of stress control over strain control: at the early stage of plasticity, the tangent modulus varies significantly over a small range of strain; hence in strain control the increments have to be very fine in order to avoid overshooting at the yield point. It is quite critical because the error is propagated throughout the calculation. It was observed that in strain control, 200 increments are not enough and around 500 are necessary to get rid of this error (corresponding roughly to a step size of 0.02%). Moreover it was found that it is more common to have a very stiff response than a very soft response. So by controlling in stress we are less likely to crash the model.

The refined parameters are shown in Table 7. These values are lower than those proposed by Xu for Zircaloy-2 [78]. In Figure 57 the Voce laws for each deformation mode are represented for both studies. Although the initial CRSS of basal and pyramidal slip are lower in the present study, the rate of hardening is much higher until 3% shear strain. After that the steady behaviour is similar in both cases. The other slip and twinning modes also have a much softer response in the present study. At this stage it is also important to recall that the Voce law represents the general evolution of the threshold shear stress for a system and is a function of the total shear strain accumulated in the grain. However the effective threshold will depend on interactions with other slip systems (of the same mode or of a different mode). These interactions are represented by the hardening parameters h^{self} and $h^{s'/s}$ which account for the obstacles that new dislocations in the system s' introduce to harden the system s. The effective CRSS will follow the Voce law only if the self and latent parameters are indistinguishable (equal to 1).

	Voce law parameters (GPa)				Hardening interaction parameters				
	τ_0	τ_1	θ_0	θ_1	h^{self}	$h^{pri/s}$	$h^{bas/s}$	$h^{pyr/s}$	$h^{ttw/s}$
Prismatic slip	0.06	0.01	10	0.01	5	5	5	1	1
Basal slip	0.08	0.08	10	0.01	5	1	5	1	1
Pyr <c+a> slip	0.23	0.08	10	0.5	1	1	1	1	1
Tensile twinning	0.2	0.01	10	0.01	1	5	1	1	1

Table 7 *Hardening parameters used for modelling compression along ND*

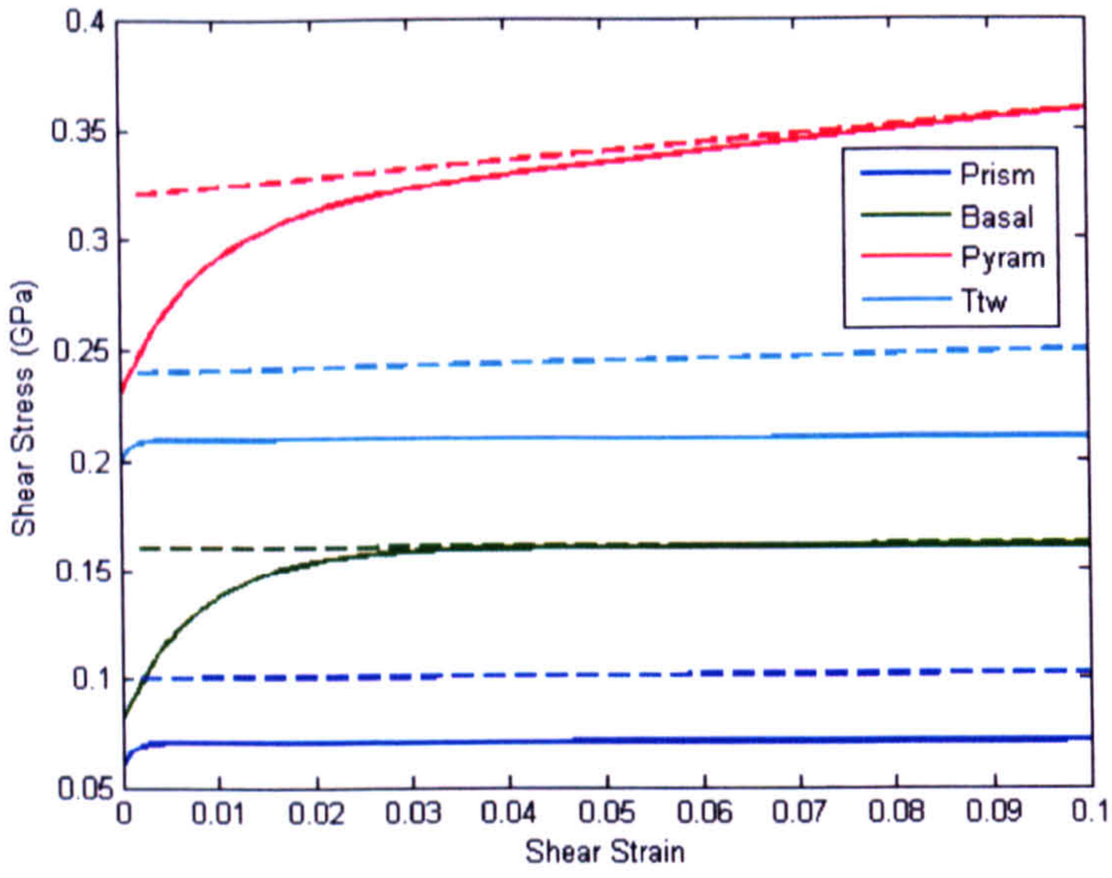

Figure 57 *Voce laws as refined by Xu (dotted lines) and in the present work (full lines)*

Figure 58 and Figure 59 show the results of the EPSC simulation compared to the experimental results. In the experimental flow curve, the markers represent the average stress-strain state during each diffraction measurement. The modelled macroscopic response follows the same trend as the experimental curve, although slightly under estimating the strain. The lattice strain response of both the $\{10.0\}_{\|}$ and $\{10.1\}_{\|}$ are very well modelled: the features are well captured and the values are very close. The response of the basal reflection is slightly softer than the experimental result. Also the $\{10.3\}_{\|}$ and $\{11.2\}_{\|}$ families yield much earlier than measured. A simple correction would be to increase the hardening of the pyramidal <c+a> slip system, by adjusting the Voce law for a higher CRSS. When applied, the correction was successful at stiffening these reflections but it also resulted in a significant hardening of the macroscopic response and moved it further away from the experimental flow curve.

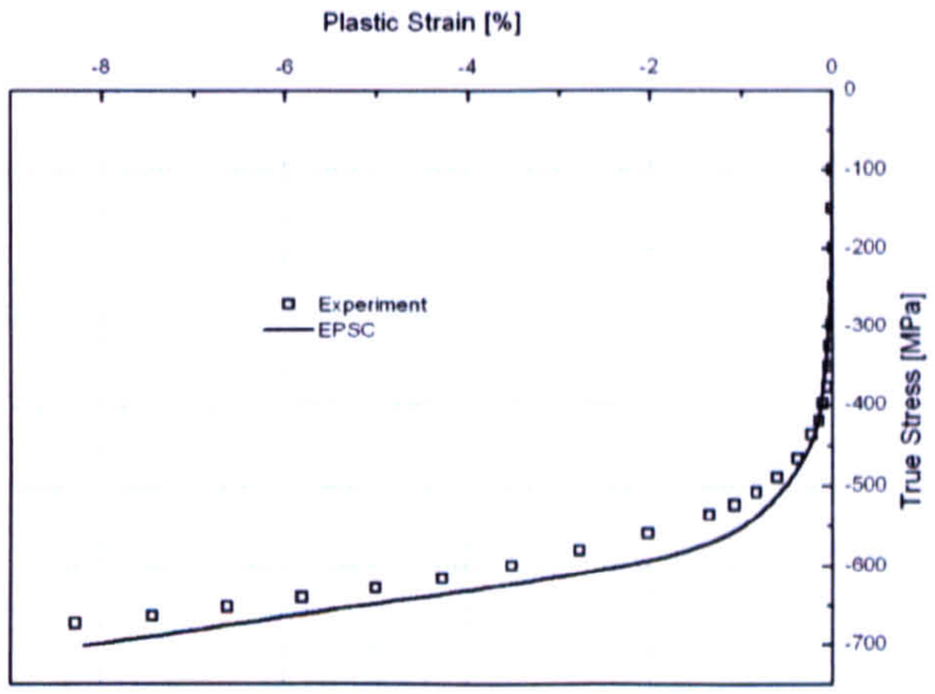

Figure 58 Macroscopic response of Zry-4 in compression along ND – Comparing experiment and model

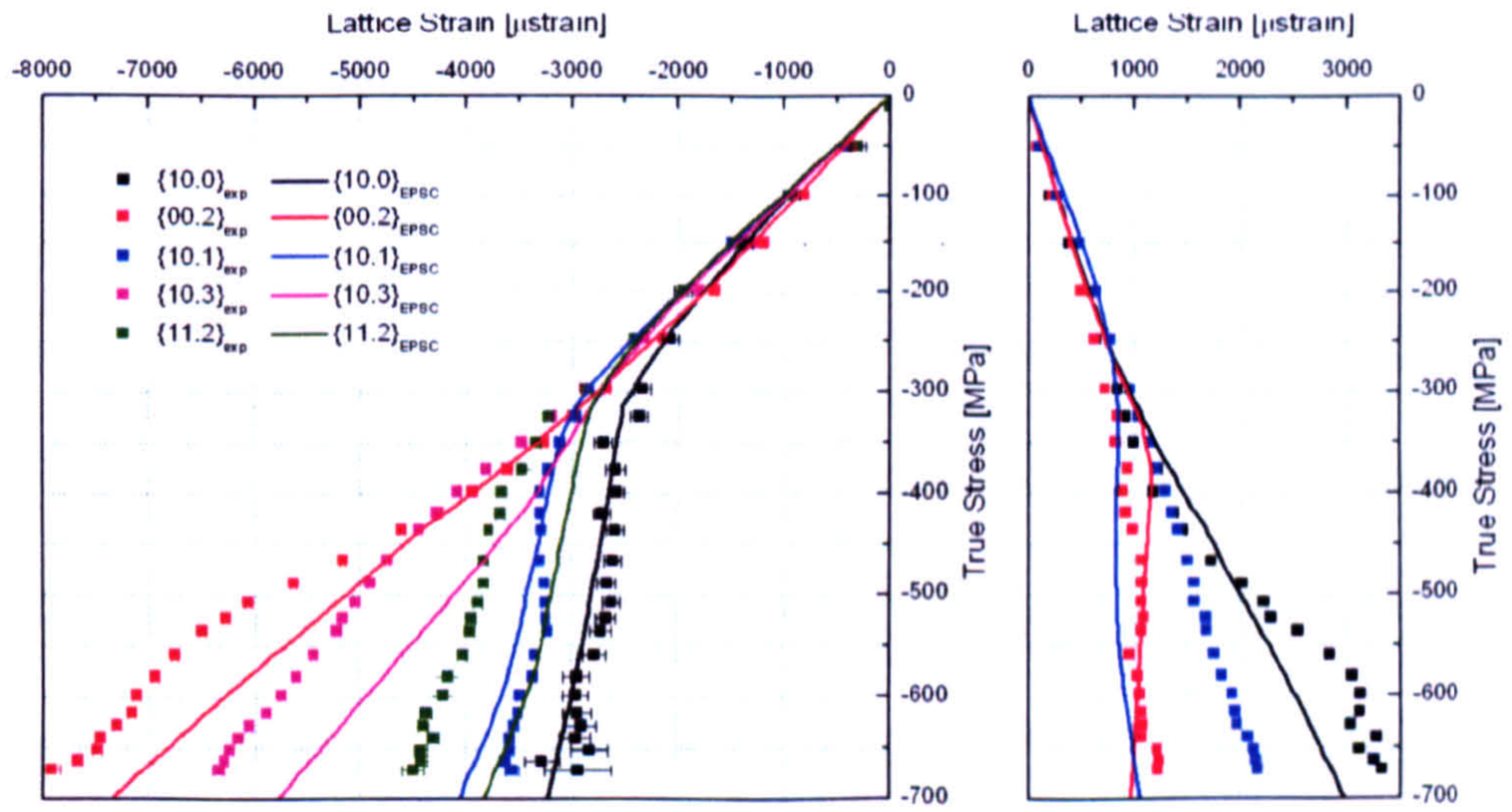

Figure 59 Lattice strain response in ND (left) and TD (right) for ND/TD compression– Comparing experiment and model

In the Poisson direction TD, the behaviours of $\{10.0\}_{TD}$ and $\{00.2\}_{TD}$ are relatively well captured. On the other hand, the response of $\{10.1\}_{TD}$ is not well simulated by the model. However the information in the Poisson direction is in itself more complicated because the reflections encompass grains with a large variety of responses.

The relative activity of the different deformation modes is represented in Figure 60. The first system to activate is prismatic slip at around –80MPa until basal slip kicks in at –120MPa and quickly takes over and represents 90% of the total activity. Twinning is activated at around –300MPa but never represents more than 4% of the total activity. At –400MPa, some grains start to undergo pyramidal slip; it represents roughly 30% of the total activity at the end of the compression test.

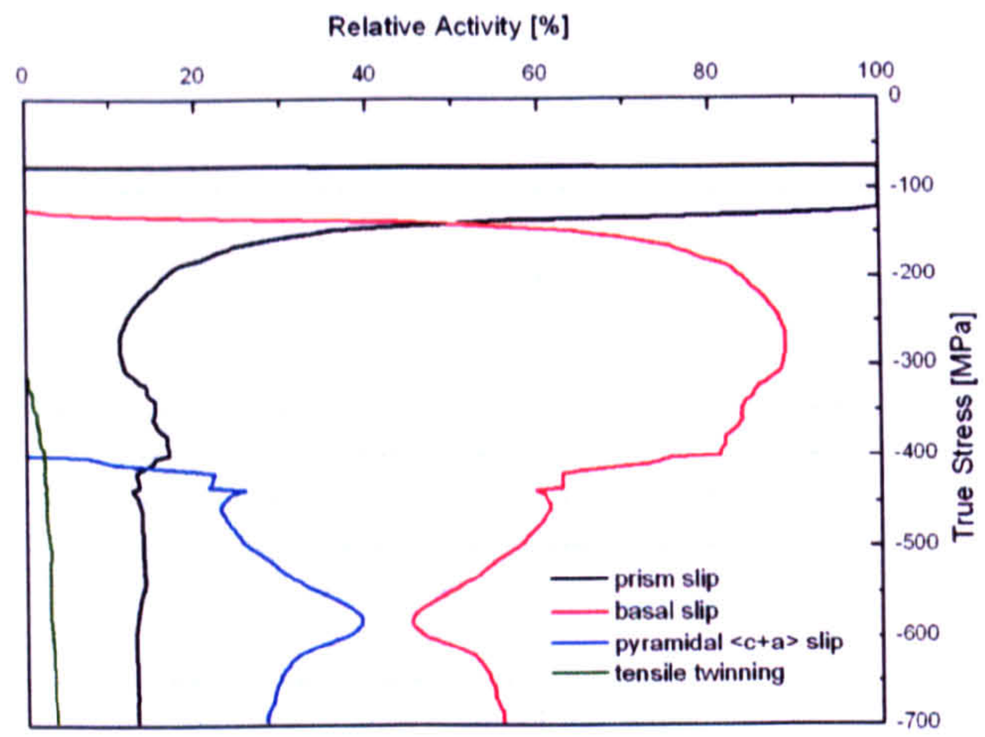

Figure 60 Relative activity for the deformation modes during EPSC compression along ND

Figure 61 shows the evolution of the average number of active systems (avacs) per grain with regards to the applied stress. Beyond –600MPa (roughly 4% total strain), the system is steady: the total avacs is constant at around 3.3 active systems per grain and the number of active systems per mode is relatively constant too. Prismatic slip mainly activates in $\{10.0\}_{\parallel}$ grains which form a poorly represented family for ND compression. Thus although this system is easy to activate, it can only represent a small proportion of the total activity when some systems are activated in very populated families of orientations. Hence it represents only 15% of the total activity, i.e. on average each grain activates 3.3 x 0.15=0.5 prismatic slip system.

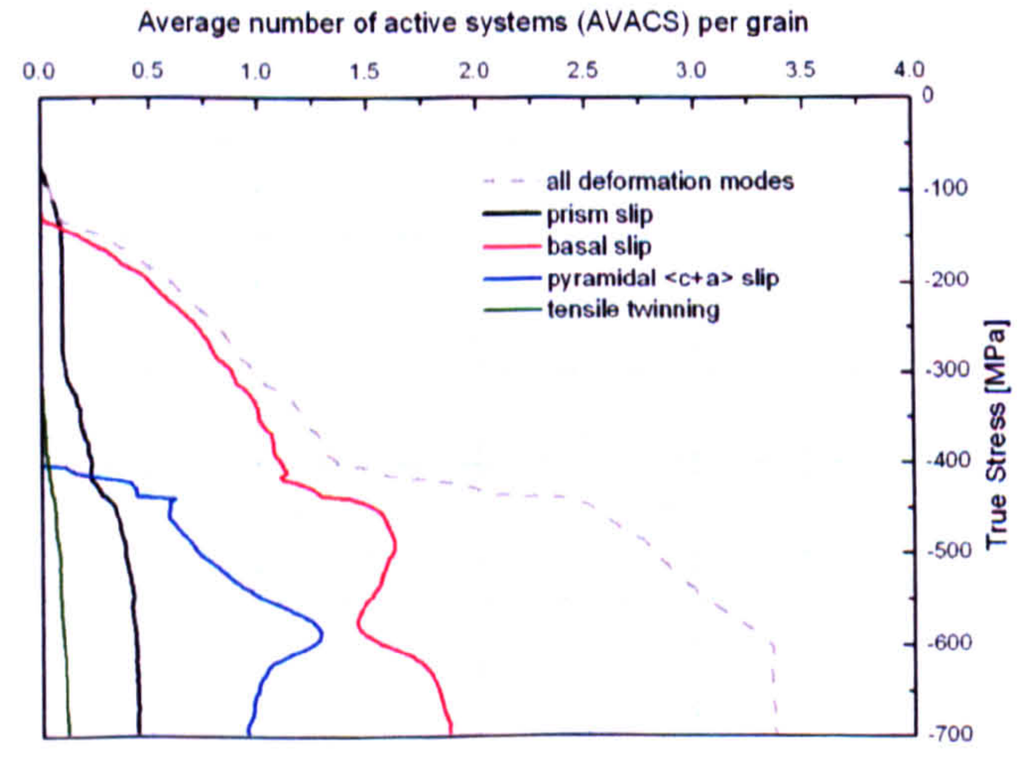

Figure 61 Average number of active systems per grain during ND compression

6.2.3 Compression along TD

For compression along the transverse direction the parameters used previously do not seem to lead to a satisfactory simulation. As shown on Figure 62 the macroscopic response is too soft compared to the experiment.

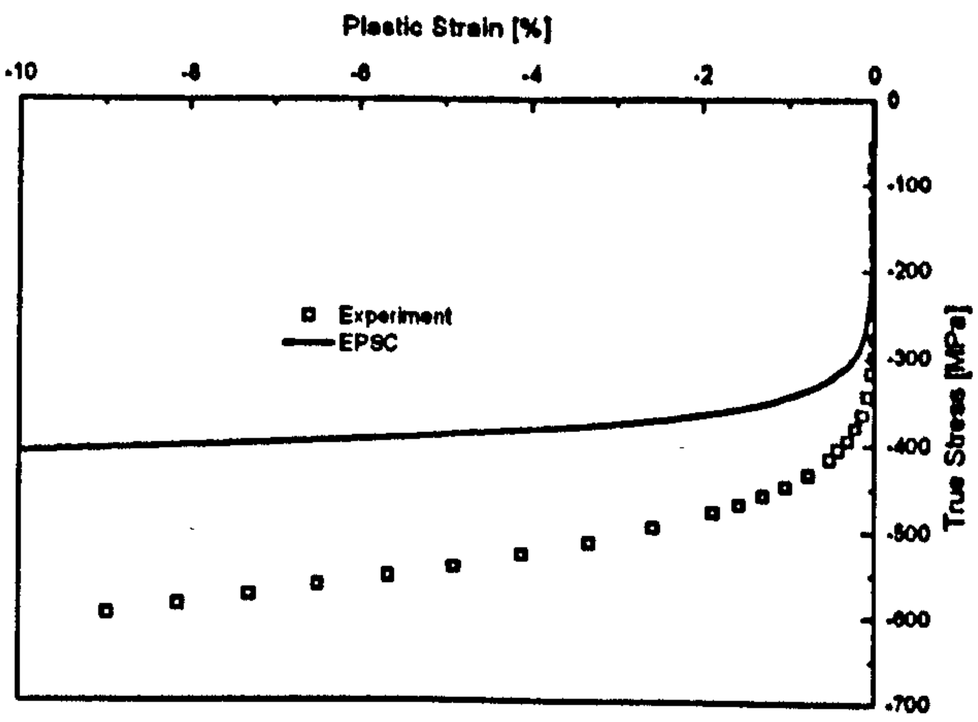

Figure 62 Comparison between the model and experiment for TD compression using the hardening parameters refined for ND compression

For refining the parameters that give the best fit, the same method as for ND compression was used: the parameters were adjusted manually. However this refinement was not successful and parameters could not be found that give a simulation in agreement with the experimental results. The results for one of the best fits achieved are shown in Figure 63. There the macroscopic response is in reasonable agreement with the experimental data, but the reflections behave somewhat differently. One of the main issues was that according to the experiment the $\{10.0\}_{\parallel}$ and $\{11.0\}_{\parallel}$ reflections bear a constant load (lattice strain) from around –250MPa of applied stress. As they represent a large proportion of the grains (~14.5% of the volume), the macroscopic response is very much influenced by the behaviour of those planes. It was thus difficult to refine the parameters such as to capture this early yielding without over-softening the macroscopic response. It was found that the self and latent hardening parameters had a major role in this matter. Some more details are given in the discussion on why the refinement was more difficult for the compression tests along RD and TD.

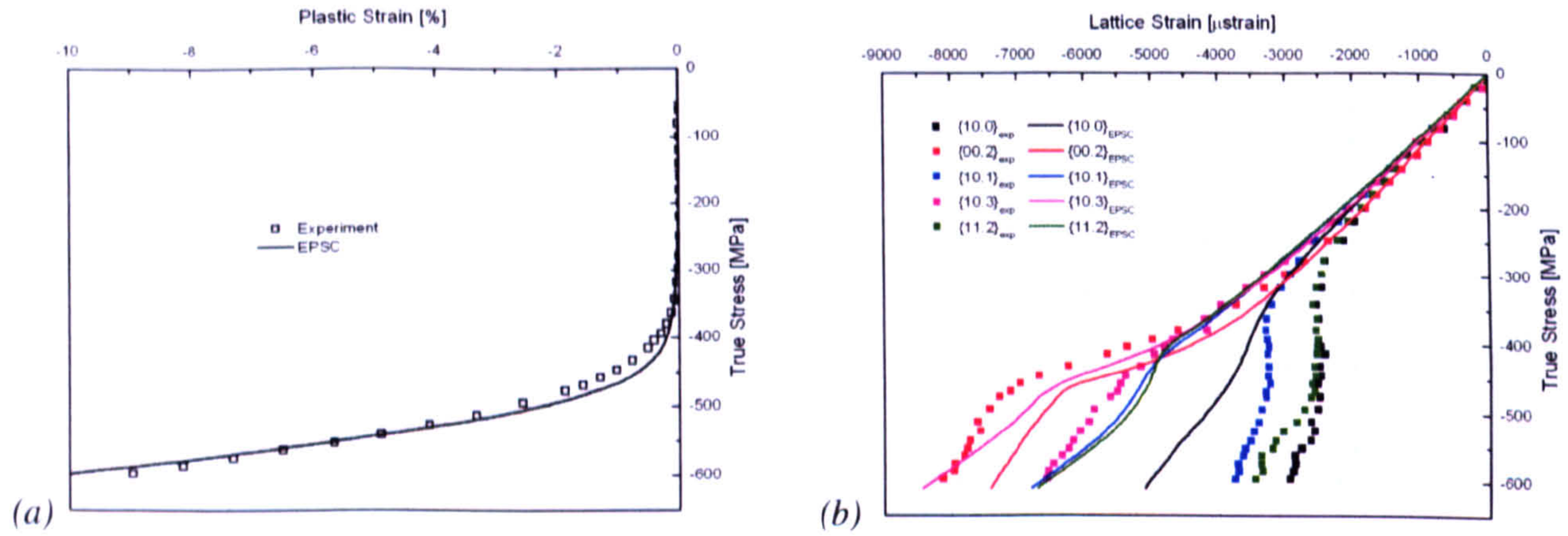

Figure 63 Comparison between experiment and the best simulation for TD compression: (a) flow curves, (b) lattice strain response in TD

6.3 Discussion

6.3.1 Influence of the hardening parameters on the behaviour

The modelling confirms that the behaviour of some reflections is closely related to the activity of specific slip systems. The activation of the prismatic slip system for example is responsible for the yielding of the prismatic {10.0} reflections in the compression direction. This yielding is evidenced by the strong inflection towards vertical in the elastic strain vs. stress curve at around –300MPa, as shown in Figure 59. Figure 61 shows that there is an increase in the activity of prism slip at the same time. The results presented here don't show a similar correlation between the response of a reflection and the activity of a particular slip system, but it was observed during the parameter refinement that the $\{10.1\}_{\|}$ and $\{00.2\}_{\|}$ were more influenced by changes in the hardening laws of basal and pyramidal slip respectively than of other deformation modes. As we will develop later, this is only a general trend and the responses are very sensitive to all the input variables.

6.3.2 Reasons for difficulty to fit RD and TD compared to ND

It was very difficult to find parameters that provide satisfactory modelling of each compression test independently, let alone to refine a global set of parameters for all the tests. This was particularly true for the simulation of compression along TD and RD. The contributions to this poor correlation can be divided into three categories: contributions that arise from the complexity of the model and the method of exploration of the parameter space, from the limitations of the model itself, and from the uncertainties in the other model inputs.

6.3.2.a Sensitivity of the model

The response of the model can be very sensitive to changes in hardening parameters. As described earlier, these parameters describe both the hardening of a system as a result of the global accumulated shear strain in the grain (the Voce law constants) and the hardening introduced by each of the other systems (the coupling coefficients $h^{s'/s}$). In grains that can geometrically activate several systems, there can be strong interactions between the systems and the parameters can't be treated separately. Hence refinement is complicated and the model is often sensitive to changes in the hardening parameters of interaction $h^{s'/s}$. Figure 64 shows the Schmid factors for the different slip planes as a function of the α angle between the applied force and the <c> axis of the zirconium crystal. There is actually a band of Schmid factor values for a given α angle: the factor varies slightly when the applied force is rotated around the <c> axis. The Schmid factor is required for the determination of the resolved shear stress and as such is an indication of the geometrical 'easiness' of slip, with higher values indicating easier slip. The plot shows that depending on the direction of the applied force, the configuration is more or less favourable for the activation of a specific slip mode. For each configuration and given slip mode, only the

system with the highest Schmid factor is plotted. It is clear that the easiest configurations vary greatly with the slip mode considered. On the other hand for a given load direction, some modes are more likely to be activated than others. Hence for a <c> axis loading (angle=0), only pyramidal slip is geometrically possible. In other words, $\{00.2\}_{\|}$ can only accommodate plastic strain through pyramidal slip.

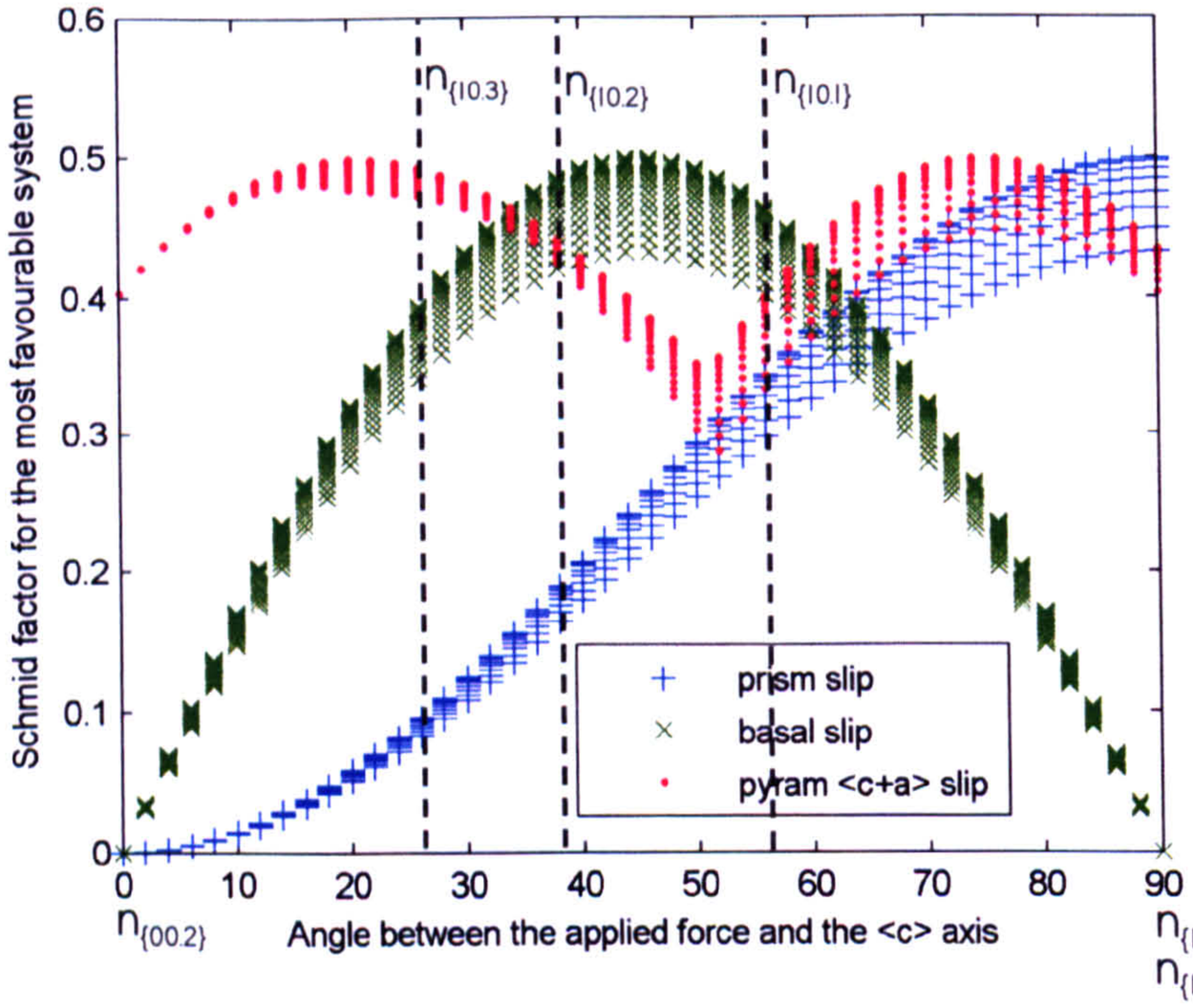

Figure 64 Schmid factors for the main three slip systems

Table 8 recaps the Schmid factors for some common grain orientations. In $\{10.1\}_{\|}$ grains, any of the three slip systems is potentially geometrically active. Grains oriented such that the loading is normal to one of their prismatic planes can't activate basal slip but can flow through prismatic or pyramidal slip.

	Prism slip	**Basal slip**	**Pyramidal slip**
$\{00.2\}_{\|}$	0	0	0.40
$\{10.0\}_{\|}$	0.43	0	0.40
$\{11.0\}_{\|}$	0.43	0	0.40
$\{10.1\}_{\|}$	0.33	0.36	0.44
$\{10.2\}_{\|}$	0.20	0.43	0.40
$\{10.3\}_{\|}$	0.12	0.39	0.46

Table 8 Schmid factors for some reflections normal to the loading direction

The above considerations help explain why the refinement of the hardening parameters is easier for compression along ND than the other directions: ND contains a large proportion of $\{00.2\}_{\|}$, so the behaviour is mainly governed by the behaviour of these grains. As only one slip mode is geometrically favourable in these grains, the hardening parameters are globally more independent and easier to refine. So unless it is feasible to explore the whole parameter space, it can be difficult to find the set of parameters that best fit experimental data in some cases.

6.3.2.b Limitations of the model

It was found in this study and others that a major difficulty was to obtain from the model a total absence of hardening in the response of the $\{10.0\}_{\|}$ reflections, without softening the macroscopic response too much in return.

In the EPSC code used, twinning is considered as a 'unidirectional slip mode' which is a rather crude approximation. Although as such it can accommodate the strain, it doesn't account for the stress relaxation usually observed experimentally when twinning activates. Moreover, twinning induces significant grain reorientations. These texture changes affect the mechanical response but are not considered in the model. Since twinning is mostly activated during RD and TD compressions, these limitations in the modelling of the mechanism make it difficult to properly correlate EPSC and experimental results.

There might be also some time-dependent effects that are not captured by the model. Indeed the model is rate independent, so effects such as creep are not incorporated.

6.3.2.c Uncertainties

On Zircaloy-2, a material with a similar composition as Zircaloy-4, Xu et al. were able to find a global set of hardening parameters that yielded a much better model to experiment

correlation [78]. It seems the texture information input in the model could be a problem in our case. Indeed looking at the EPSC results for ND compression, the model overestimates the macroscopic stress response whereas the lattice strain of nearly all reflections of the compression direction (and certainly the over-represented $\{00.2\}_{\|}$ and $\{10.3\}_{\|}$ families) are underestimated. So there seems to be a flaw in the passage from micro to macro indicating that the texture used for the model doesn't represent exactly that of the material compressed experimentally. This could be down to the measurement technique or sample-to-sample variations. It is also possible that the initial strains were not properly assessed and that all the rolling residual strains were not fully annealed.

6.3.3 Two phase material

It was not possible to run the model to fit the Zr2.5%Nb results because of the presence of the second phase. The first reason is that the texture of the second phase was not measured with a good accuracy: the peaks were not visible on the diffraction spectra at HIPPO, and EBSD gave too little indexing in this phase to get quantitative information with a satisfactory statistical accuracy. Also the model in the version available to us was not capable of treating two phases. It could have been upgraded to a two phase model, and some people have been using such models [75]. One of the most obvious approaches would have been to introduce the new phase grains as a new set of inclusions with different crystal properties. Dye et al used a more sophisticated approach where the fact that grains of one phase are surrounded by the other phase is mimicked by a double inclusion scheme [79]. Cai et al. used a combination of Finite Element Modelling (FEM) and single phase EPSC: the FEM was used to simulate the average phase responses which were in turn implemented as boundary conditions in the EPSC model [80]. However any of these

approaches would have required a lot of additional work and it was beyond the scope of this work to develop a double phase extension to the model.

6.3.4 Refinement of the hardening parameters

As mentioned earlier, for the parameter refinement, the main criterion used to judge the goodness of a fit was based on observation: the parameters were adjusted manually until model and data are in good agreement visually. The exploration of the parameter space was performed based on considerations regarding the effect that each parameter has on the response. Most authors seem to use a similar ways of resolving the inverse problem. Xu explored part of the variables space through a multidimensional grid [78]. However all these methods have limitations: they lack automation and do not guarantee the best solution. It would thus be useful to develop a robust procedure to refine the EPSC coefficients.

6.3.4.a Discrete grid search method

There are a large number of physically possible combinations of the plastic flow parameters. The typical ranges of values are:

- $0 < \tau_0 \leq 1$ and $0 \leq \tau_1 \leq 1$ GPa and changes of the order of 0.01GPa can have an effect on the response.
- $0 \leq \theta_0, \theta_1 < 100$ GPa and changes of the order of 0.05GPa can affect the response (100GPa roughly corresponds to the Youngs modulus in zirconium).
- $0 \leq h^{s/s'} < 10$ and changes of 0.5 affect the response.

The corresponding parameter space grid, for four deformation modes, includes over 10^{73} nodes, which means as many parameter combinations to test. It is possible to reduce the parameter space based on some physical considerations. For example, we must have

$\theta_1 \leq \theta_0$ for a representative Voce law. The space can also be reduced by discretising the θ_0 and θ_1 axis in a logarithmic scale for example such as $\log_{10}(\theta_0, \theta_1) \in [-2:0.01:2]$ (which corresponds to 80% fewer points for each dimension, without altering the quality). The grid could then be reduced to around $7x10^{66}$.

However it is still practically impossible to test the whole grid by hand, hence the necessity of developing an automated method of refinement. An algorithm such as the one described in [81] could be used in order to reduce the number of points to test in the grid. For such an automated method proper criterions must be defined to represent the goodness of fit.

6.3.4.b Optimisation attempt

An attempt was made to develop an optimisation routine to solve the inverse problem. The algorithm used was based on the simplex search method and the Matlab function called fminsearch was chosen to perform the task. The data to fit consisted of the microscopic responses. The objective function to minimise was the least-squares difference between the experimental and the EPSC elastic strains for the {10.0}, {10.1} and {00.2} reflections both in the compression and Poisson directions. Two least-squares criteria were used: one on the strains themselves, the other was on the gradients (slopes between two successive points). The latter is quite appropriate since the deformation modes have a strong effect on the inflections in the microscopic response. Trying to capture these inflections can be as appropriate as fitting the values themselves given that the model and the data are rather unlikely to correlate perfectly due to the model limitations and the experimental errors.

This optimization scheme was not very successful though and the process tended to get stuck in local minima. Moreover the computing time was huge. Although, for a first refinement, only the most influential parameters were optimized (the others being fixed to reasonable values), a strict minimum of eight parameters must be kept. This means that the optimisation usually requires several hundred steps and the EPSC model must be run as

many times. For future work a good approach would be to first try and fit the macroscopic responses using several initial estimates. For this purpose one should make use of the strong texture in order to run this pre-refinement: some systems are more likely to be activated in grains with a certain orientation with regards to the loading direction than others (a consequence of the Schmidt law). For example prism slip and tensile twinning are relatively easy in $\{10.0\}_{\|}$ grains whereas pyramidal slip tends to activate primarily in $\{00.2\}_{\|}$. If there is a higher than random proportion of one particular reflection along the loading direction (which usually happens in textured materials), the macroscopic behaviour will tend towards the behaviour of this reflection. So the deformation mechanisms taking place in these reflections will govern the macroscopic hardening as compared to other mechanisms. As discussed preciously, for compression along ND (containing nearly 20% of the basal reflections), the macroscopic hardening response of the model is very sensitive to changes in the pyramidal slip hardening parameters and not so much to other deformation modes. It is then possible to refine independently the parameters of the systems based on the macroscopic responses during loading in different directions. After having set a number of parameters values that fit the macroscopic curves, one can use them as initial estimates for further refinement of the lattice responses. The use of a super computer with parallel computation is probably required to reduce running time.

The definition of convergence criteria for the optimisation is critical. The model does not perfectly represent what happens in the real sample (for reasons described earlier) and what is measured with neutron diffraction, so it is important to allow for reasonable margins of error.

The simplex method might not actually be the best scheme to carry out optimisation in this case since it is not very adaptive. A better option might be to use a genetic algorithm to refine the parameters. Dr. C. Mareau is currently working on such a solution and has been able to apply it successfully for fitting macroscopic responses by minimising the absolute

area between experimental and computed responses (*Personal Communication, May 2009*).

6.3.4.c A clever search method?

If one can find some correlation between the parameters and an output of the model that can be compared to the experimental data, one could develop a clever optimization method. Xu attempted to define the sensitivity of the results to the hardening parameters by testing them individually [82]. It can be difficult to segregate these effects as often they are intertwined and the response of the model can be quite chaotic relative to the input parameters. However it appeared clearly that the activity of prismatic slip was mainly driving the response of the $\{10.0\}_{\|}$ reflection, whereas basal slip and pyramidal <c+a> slip were responsible for the yielding of $\{10.1\}_{\|}$ and $\{00.2\}_{\|}$ respectively. So to a certain extent, the behaviour of these particular reflections can be altered by tuning the respective slip system parameters.

6.3.5 Determination of macroscopic stresses

This Section is a slight digression to show how the model can be used for a very practical problem.

6.3.5.a Introduction

As mentioned in Section 2.1.4, one of the main applications of neutron diffraction in engineering is the determination of type I stresses and particularly residual stresses. The current and most popular techniques to convert lattice strains into macroscopic stresses all have limitations for materials with a crystal structure showing anisotropic properties. The main issue with the transformation concerns the deconvolution of type I and type II

stresses in the diffraction data. The purpose of the present Section is to investigate the error generated by the techniques.

Daymond [8] has proposed a list of methods for the derivation of macroscopic stresses and has tested them on simple cases of uniaxial tests on cubic and hexagonal symmetry polycrstals. However by working on experimental data, experimental errors add to errors in the method. We propose to study the validity of some of the methods by working on simulated rather than experimental data.

The method that makes more sense physically and referred to as 'method A' in Daymond's paper implies the individual fitting of diffraction peaks and the macroscopic state is deduced by a weighted averaging similar to the one used in the EPSC scheme. The main difference is that not all grains are represented in the spectrum as the number of reflections is limited by the range of TOF of the instrument. In other terms the spectrum is only representative of part of the aggregate and hence will the deduced macroscopic stresses. This is where lies the most obvious limitation that we plan to investigate. We will call this assumption the assumption of representativity. Moreover we should note that some care should be taken: some grains might be represented twice in very close reflections (in terms of lattice plane orientation) and because of the angular span of the detection area. For the same reason second order reflections must be discarded for the calculation of the weighted average.

'Method A' is summarized by the diagram in Figure 65. A physical problem attached to the technique is that the elastic strain tensor is computed for each reflection from the hkl elastic strains in the principal directions, but the grains sampled by one reflection in one direction are not the same as the one sampled by the same reflection in another direction.

We propose a different approach where the macroscopic elastic strains are computed by the law of mixtures and the macroscopic stresses are then deduced using Hooke's law (Figure 66).

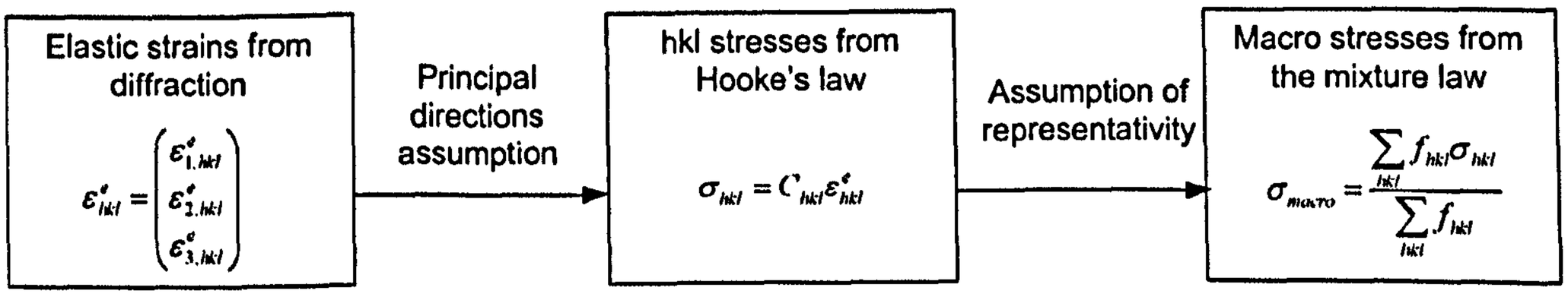

Figure 65 Schematic of method A [8]

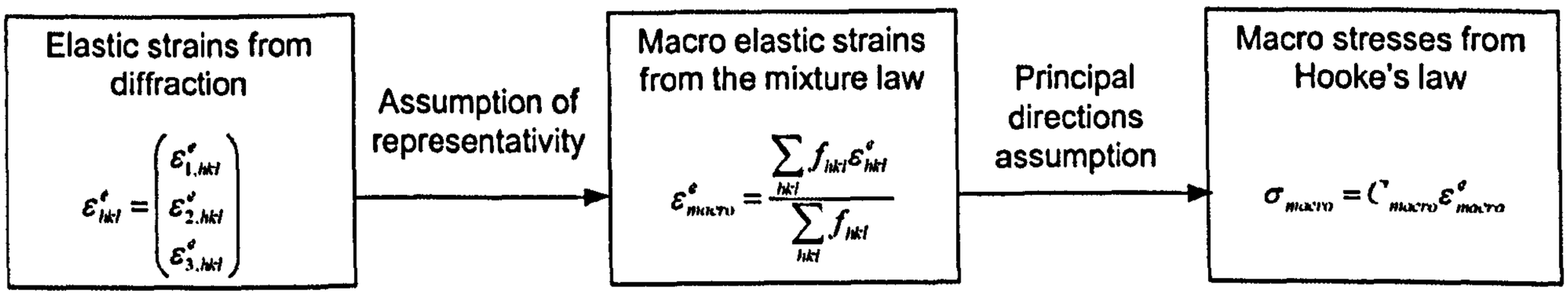

Figure 66 Schematic of the proposed method

6.3.5.b Case of uniaxial loading

For a first approach, let's consider the case of compression of Zircaloy-4 along the normal direction. For the simulation we used the EPSC with the same input used previously and the parameters refined in Section 6.2.2.We are not testing the EPSC model here but the validity of the length scale transfer method so the EPSC parameters are not of crucial importance here.

A typical Zr spectrum at ENGIN-X contains 11 peaks so the model was programmed to output the elastic strains for the corresponding reflections in each of the macroscopic principal directions (RD, TD and ND).

- *Derivation of the macroscopic elastic strains*

Making the assumption that the grains sampled by the first order reflections in the spectrum are representative of the whole aggregate the macroscopic elastic strains in the principal directions were derived by a weighted average of the {hk.l} elastic strains. The volume fractions of grains represented by each reflection were taken as the weighting coefficients $f_{hk.l}$ (information provided by the EPSC model from the texture information).

By summing all the f_{hkl} we have an idea that the grains represented in the ENGIN-X spectrums only correspond to approximately 30% of the total number of grains in the gauge volume (31%, 30.7% and 33.7% respectively in RD, TD and ND). Hence the assumption made for the scale transfer is quite large since the Euler space is partially sampled and the reflections don't necessarily represent a good statistical coverage of the Euler space.

- *Derivation of the macroscopic stresses*

The stresses in the principal direction were derived from the macroscopic elastic strains using Hooke's law and assuming that there are no shear components. The stiffness tensor used was derived from the EPSC modelling for the whole aggregate. The non-orthotropic components in the EPSC tensor didn't reach 30MPa so it was simplified to an orthotropic case:

$$C = \begin{bmatrix} 123 & 59.6 & 58 & 0 & 0 & 0 \\ & 123 & 58 & 0 & 0 & 0 \\ & & 131 & 0 & 0 & 0 \\ & & & 31.5 & 0 & 0 \\ & & & & 31.5 & 0 \\ & & & & & 31 \end{bmatrix} GPa$$

The results in terms of a uniaxial flow curve are represented in Figure 67 and compared with the 'true' flow curve from the EPSC scheme. It shows that the calculated stress is underestimated by nearly 15%. It is very likely that most of this error is a result of the representativity assumption. One should also be aware that this error might be larger in the case of a triaxial stress state.

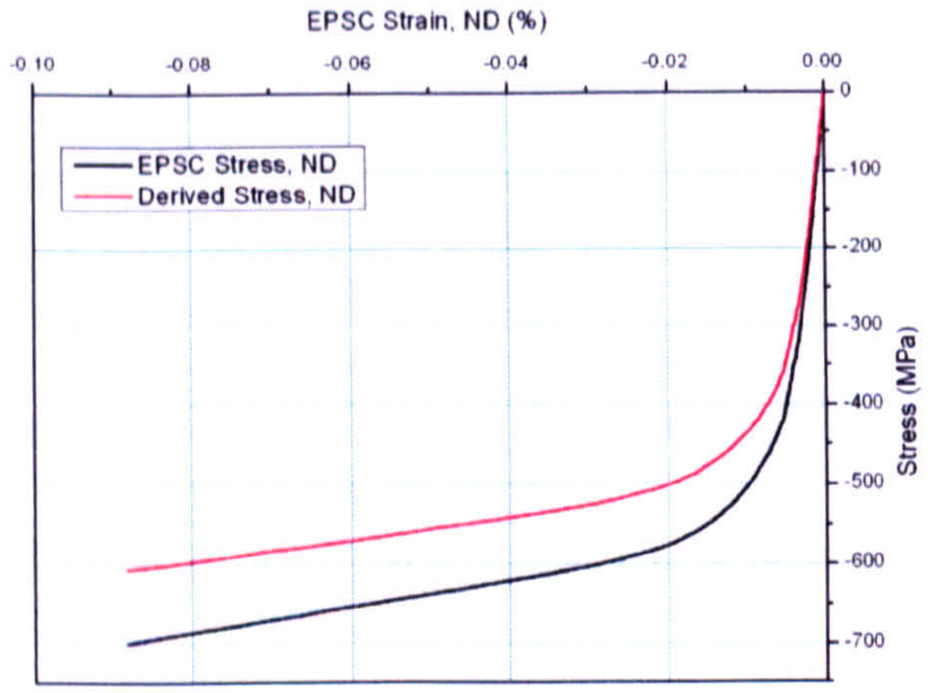

Figure 67 Comparison between the 'real' stress in the ND and the stress derived from the diffraction reflections strains by the proposed method.

6.3.5.c Discussion on the Rietveld method

Another method which can be used for macroscopic stress determination is based on a Rietveld fit of the diffraction spectrum. It presents the advantage of fitting all the reflections at once via a template of the spectrum. The a and c parameters returned by the refinement scheme can be converted into strains ε_a and ε_c. The macroscopic strain in the measurement direction is then derived by $E = f_a\varepsilon_a + f_c\varepsilon_c$, where f_a and f_c are weighting factors to account for texture. Santisteban et al. for example used $f_a = \Delta\varepsilon_c/(\Delta\varepsilon_c + \Delta\varepsilon_a)$ and $f_c = \Delta\varepsilon_a/(\Delta\varepsilon_c + \Delta\varepsilon_a)$, where the $\Delta\varepsilon$ are the uncertainties from the a and c strains [83]. Because the Rietveld fits are performed over the whole range of reflections, the results are average a and c spacings. So part of the length scale transfer is done. Since the regression tends to favour high intensity peaks in order to reduce the least-square difference, the results will be more influenced by highly populated reflections, which is what happens in reality: the state of the aggregate is dependent on texture. On the other hand peak intensities are also determined by other factors which can bias the Rietveld fit. Some of the anisotropy in the microscopic response is considered because the a and c spacings of the cell can be refined independently.

This method can't be tested using the EPSC model because the model only returns values of diffraction strains rather than a diffraction spectrum.

6.4 Conclusion

Several methods were used to refine the hardening parameters in order to get agreement between the simulated and the experimental data.

As a first approach, an initial guess was made for the crystal plasticity parameters based on literature values and a simplex search method was applied to refine them. Another approach consisted of manually adjusting the parameters so as to improve the simulation by considering the effects of some parameters on the response.

However global parameters that would give a good correlation for all tests could not be found, and it was even difficult to simulate the response of compression along TD and RD in an independent way. Explanations for this lie in three areas: the size of the parameter space, the limitations of the model, the inaccuracy in the input. Considering the number of parameters to refine it was not possible to cover the whole parameter space, and the best combination might have been left out. For compression along the transverse and rolling directions the model is very sensitive to parameter changes and the refinement is thus more difficult. The model itself has also some limitations that can reduce the realism of the simulation: twinning induced relaxation and reorientation for example are not included in the model. One of the main inputs to the model is texture information. However this texture may differ slightly from the texture of the compression coupons: it was measured at a different place in the plate. Moreover there are some uncertainties from the mean of measurement (neutron measurements preformed on a multiple detector instrument tend to smoothen sharp textures) and the texture information might have been altered during the data treatment.

Finally we have also shown that the model can be used for other applications such as the development of techniques to appropriately convert diffraction information into macroscopic stresses.

In the next Chapter, we will see how texture measurements can help understanding better the mechanisms of deformation.

Chapter 7 Texture evolution

We have noticed from the results of in-situ compression that some intensity changes happen in the spectra during compression (p.75 onwards). They reflect a change in the texture. Some large changes have been described as being the result of twinning. In this chapter we will have a closer look at the texture evolution during the compression of the two materials along the different directions.

7.1 Set up

Several cubes were extracted from the Zry-4 plate and the Zr-2.5%Nb tube and compressed along each processing direction and at different levels of plastic deformation. The cube dimensions prior to deformation were 6 x 6 x 6 mm^3 and 4 x 4 x 4 mm^3 for Zry-4 and Zr-2.5Nb respectively. A 200kN (100kN dynamic) Instron load frame was used for compressing the samples and the stress was derived from the load cell measurements. Because of the small sample size the strain could not be directly measured on the samples and the experiment was controlled from the strain recorded by an extensometer placed on the compression platens. The sample plastic strain was derived by subtracting the elastic strain in the {sample + grips} assembly to the total strain measured. This elastic strain was derived from the measured stress via Hooke's law. For this purpose, the Young's modulus of the assembly was derived from the slope during elastic loading.

The cubes were then measured at HIPPO, the neutron powder diffractometer at Lansce, USA. Figure 68 is a schematic of the instrument. It is composed of several detectors clustered into panels. The panels are gathered in banks set at diffraction angles 10°, 20°, 40°, 90° and 150°. The 10° and 20° banks have a very low resolution compared to the other banks: if it is expressed in terms of peak width relative to the peak position, the d-range

resolution is 4.6% and 9.2% respectively, whereas it is only 0.37% for the 150° panels [84]. The peaks collected on the small angle detectors are too broad so only the 40°, 90° and 150° banks are used for texture measurements [85]. There are thus 30 available panels for a single measurement. The coverage of a pole figure by the detectors at Hippo is shown Figure 69(a). Because of the access hole to the chamber, there is a gap of detectors in the 90° bank. For a better coverage the samples were measured at rotations around the vertical axis of 0°, 45°, 67.5° and 90° relative to the incoming beam (Figure 69(b)). The measurements are thus made with 120 points on the pole figure.

Each detector panel covers an angle range of around 10° to 15° (see [61]) and Figure 69 (c) shows their coverage on a pole figure.

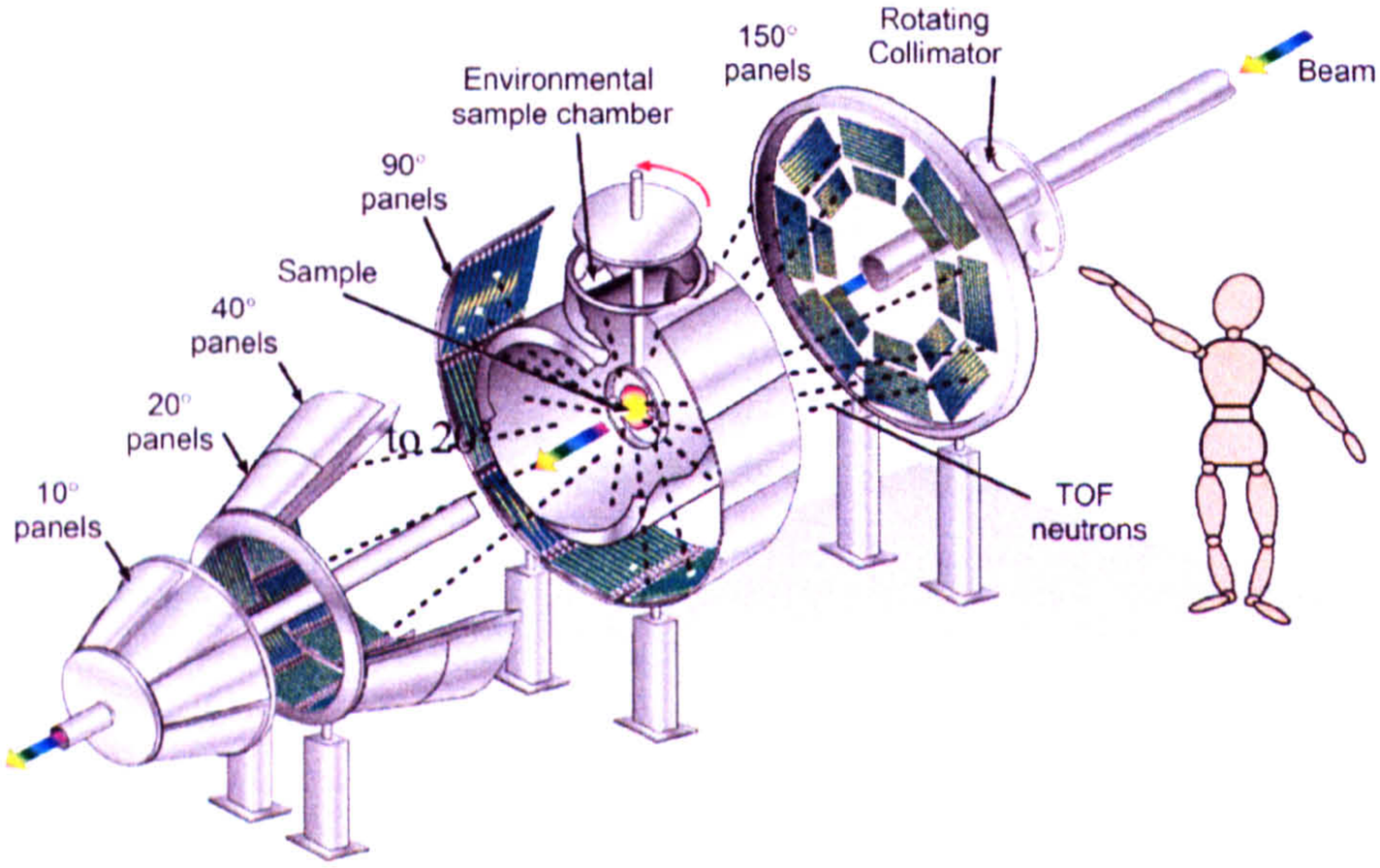

Figure 68 Hippo diffractometer at Lansce, USA (from [84])

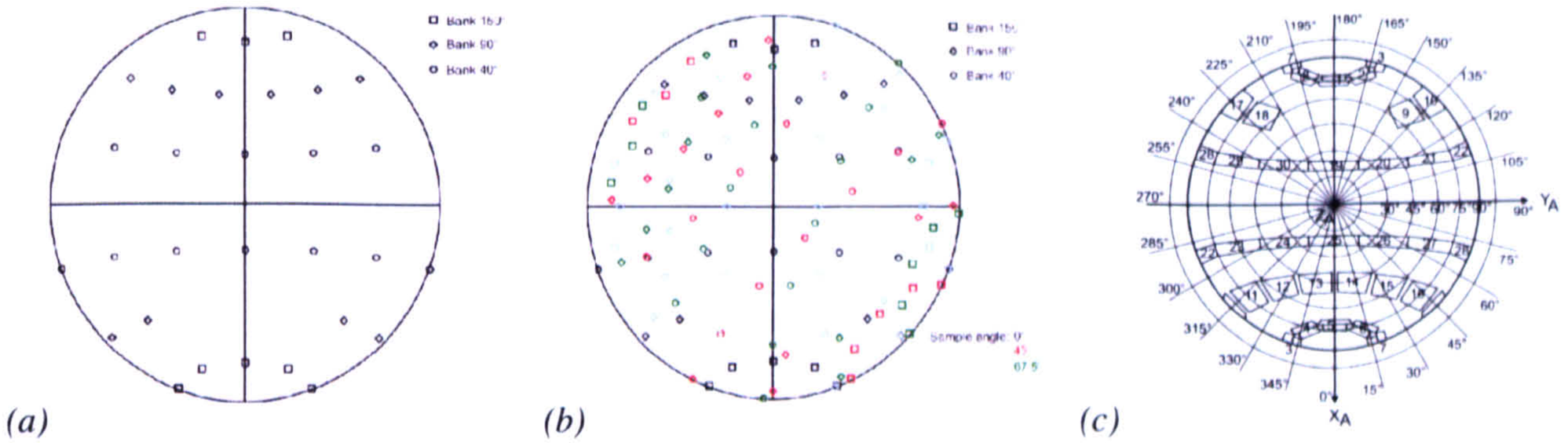

(a) (b) (c)

Figure 69 Position of the Hippo panels on a pole figure (a) for one sample orientation and (b) for the 4 sample orientations (diagram inspired from [85]); (c) is the representation of the detector bank coverage (from [84])

Hippo is a TOF instrument and so each panel collects a full diffraction spectrum. Typical diffraction spectra from zirconium alloys on Hippo are shown in Figure 70. The quality of the spectra varies greatly with the diffraction angles. The lower the diffraction angle the broader the peaks.

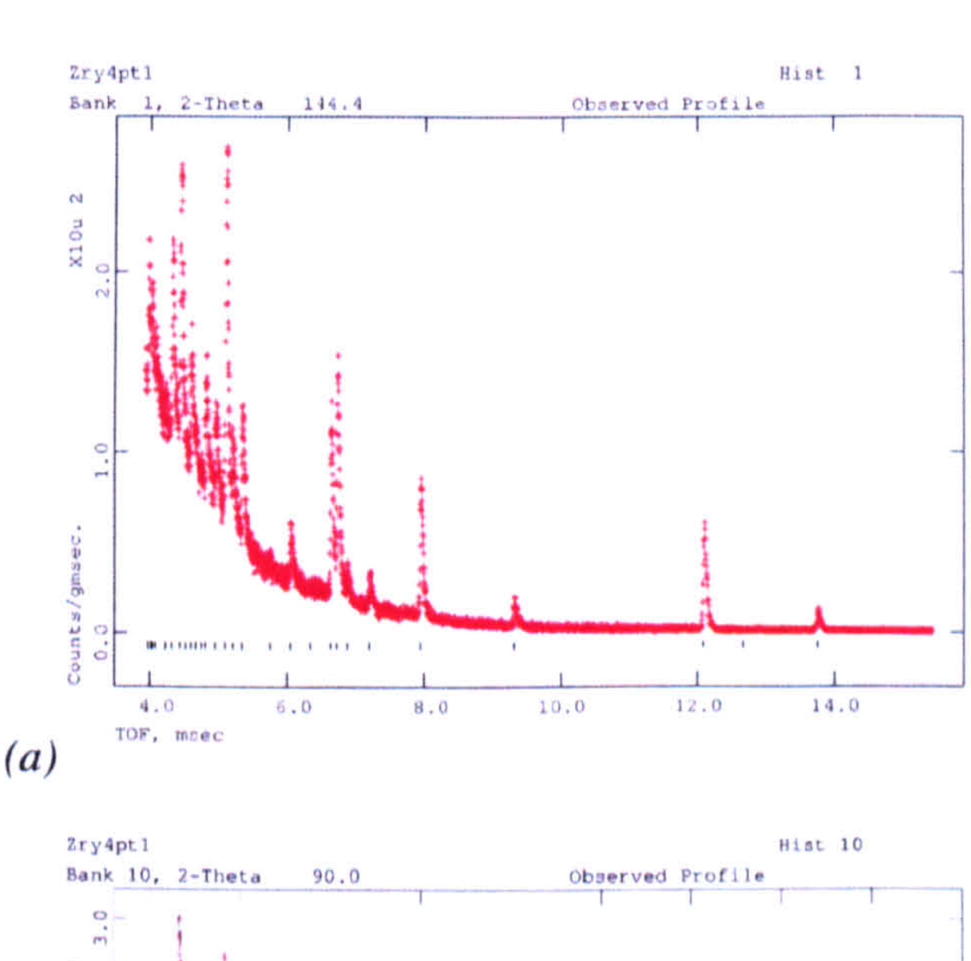

(a)

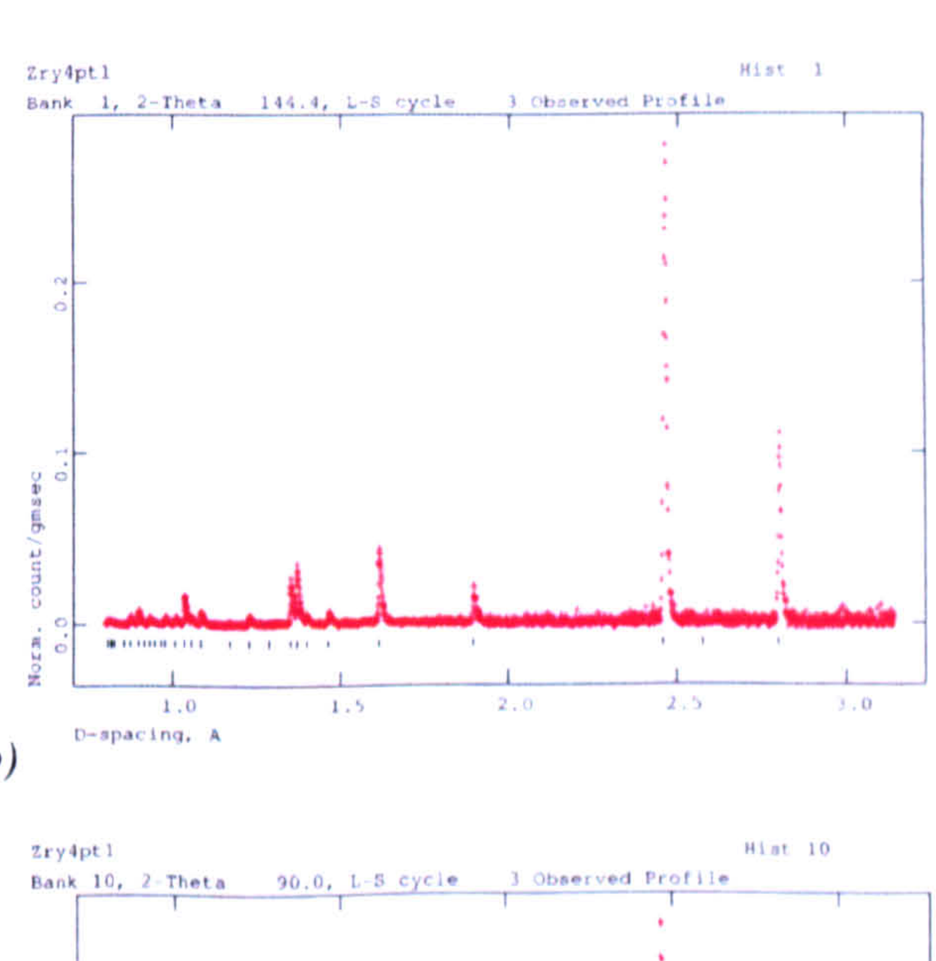

(b)

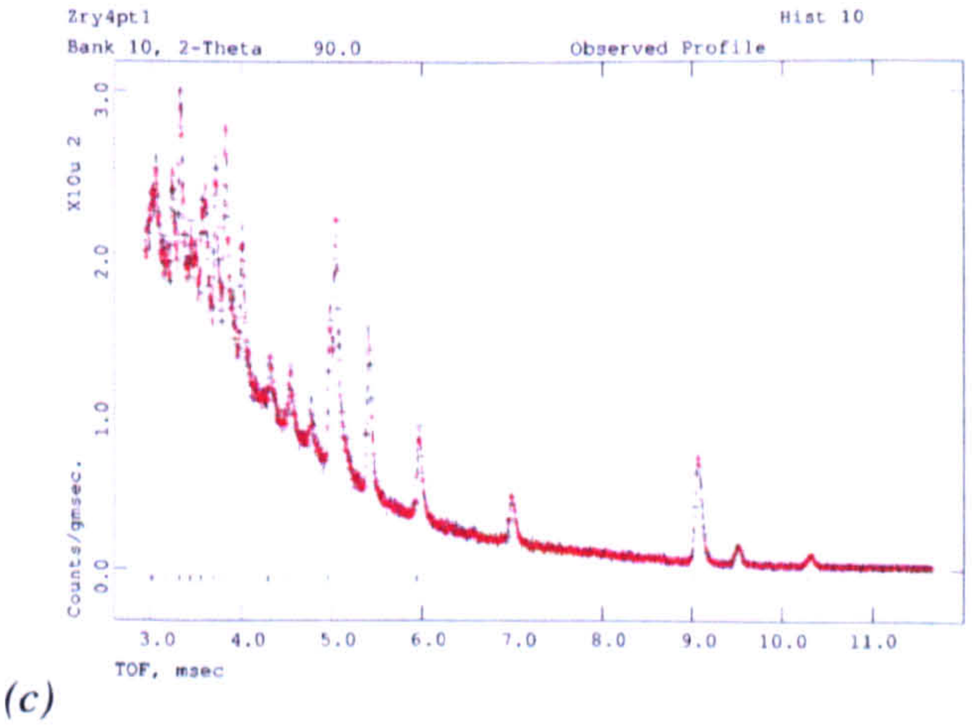

(c)

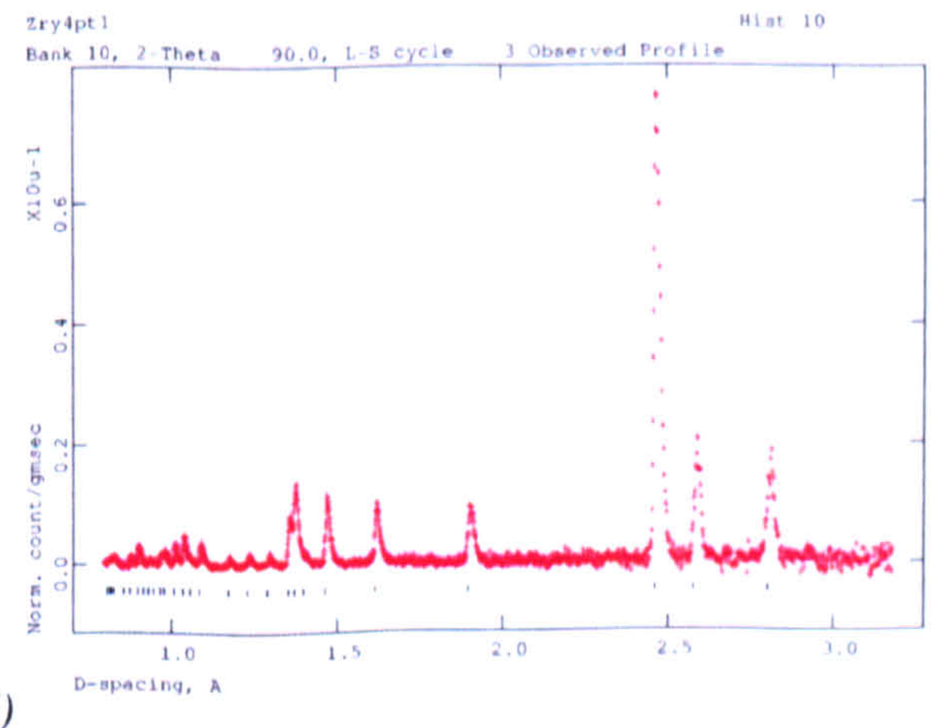

(d)

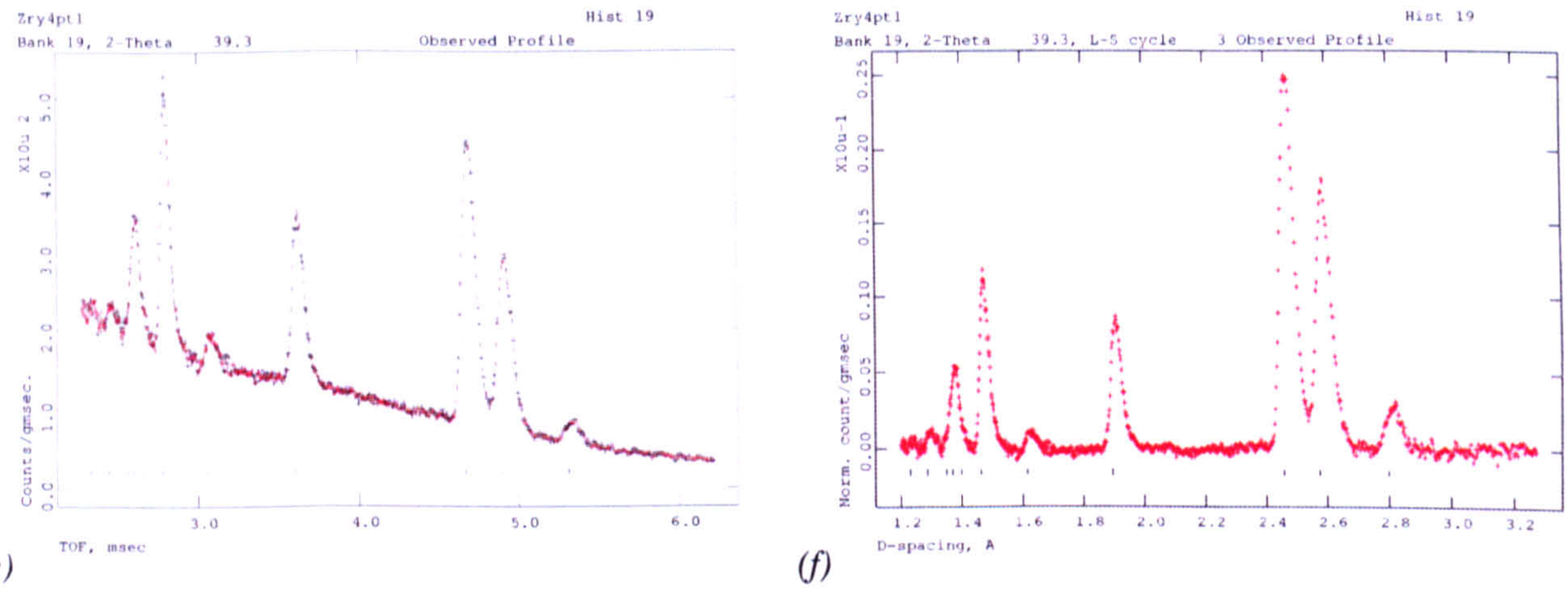

Figure 70 Spectra from the Zry-4 collected at hippo on (a) a 150° (c) a 90° and (e) a 40° panel. (b), (d) and (f) are respectively the same spectra expressed in terms of d-spacing and after background correction

The spectra are fitted with GSAS using the Rietveld method with spherical harmonics (SH). GSAS only accepts 98 histograms so a choice had to be made to reduce the number from the 120 available. For each sample orientation, the patterns from 5 banks were discarded and for two of these orientations a sixth bank was not considered. Bank 9 collected only background so for each sample orientation, the spectra from this bank was discarded from the selection. Figure 71 shows the resulting reduced pole figure coverage as inputted in GSAS.

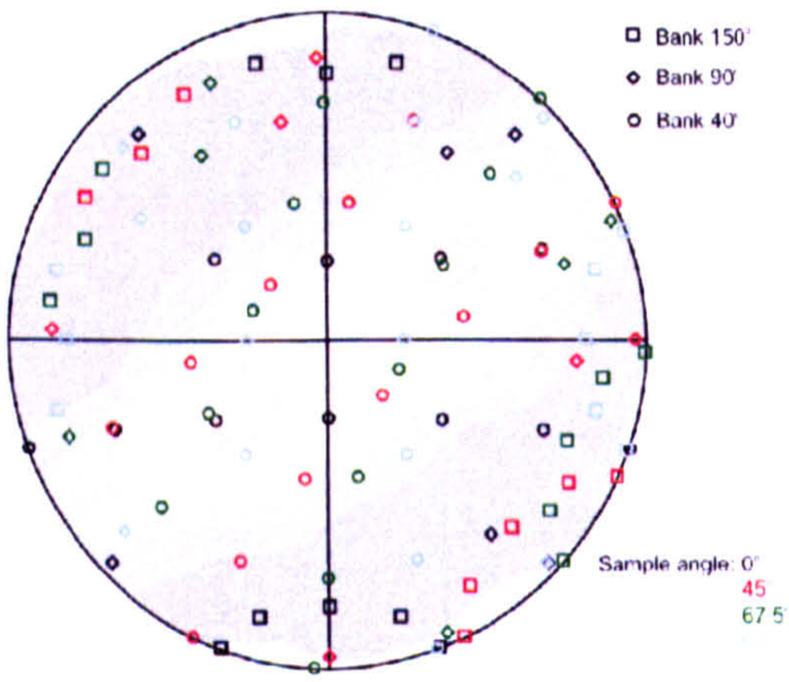

Figure 71 Pole figure coverage from the 98 histograms inputted in GSAS with an example of basal pole figure in the background.

It is worth noting here that GSAS can actually handle up to 99 patterns. However to limit the occurrence of negative densities on the pole figures, a 'zero pole figure' has been

introduced. The implementation of 'zero pole figures' consumes one of the available histograms for each phase considered; hence the 98 available remaining histogram slots. Even with this restraint, negative densities are an artefact of SH fitting which it is difficult to get rid of, especially for very sharp textures. The points with negative intensities are then usually assigned the value 0. In the present work, the areas of truncation are represented by a white colour on the pole figures. The truncation slightly changes the average intensity (no longer exactly 1) and the pole figures are not perfectly normalized. However, since the error seems to be less than 5%, and for the purpose of representation, we neglected the renormalization.

Given the number of fitting parameters the refinement has to be done in several steps. The sequence of operations followed a similar principle as the one described in [84]. It shows some minor differences and the detailed procedure is depicted in Appendix A.1. The background is refined first followed by a cell refinement in LeBail mode. The profile parameters are adjusted before a Rietveld refinement. The Spherical Harmonics (SH) coefficients are then allowed to vary and their number gradually increased.

One has to know how many SH coefficients are necessary to capture the texture at best. We chose to run the refinements with several cases to determine the optimum order. Figure 72 shows sets of pole figures obtained after refinements with 6^{th}, 8^{th} and 12^{th} order SH for the Zry-4 as-received texture. The higher the order, the better the high intensity poles are captured. However for 12^{th} order SH, the pole figures are a bit noisier and the contours are not smooth. Similar oscillations have been found by Matthies et al. [84] when fitting HIPPO data with degrees of harmonics expansions above 12 and they identified them as artefacts. We thus decided to refine up to the 8^{th} order of SH for the Zry-4 measurements. Although there might be a chance of flattening out the wiggles by introducing a 'unit pole figure' restraint before the SH fitting this option was not investigated as increasing the

order of SH didn't seem to make a significant difference to the pole figures and the fitting to peak maxima.

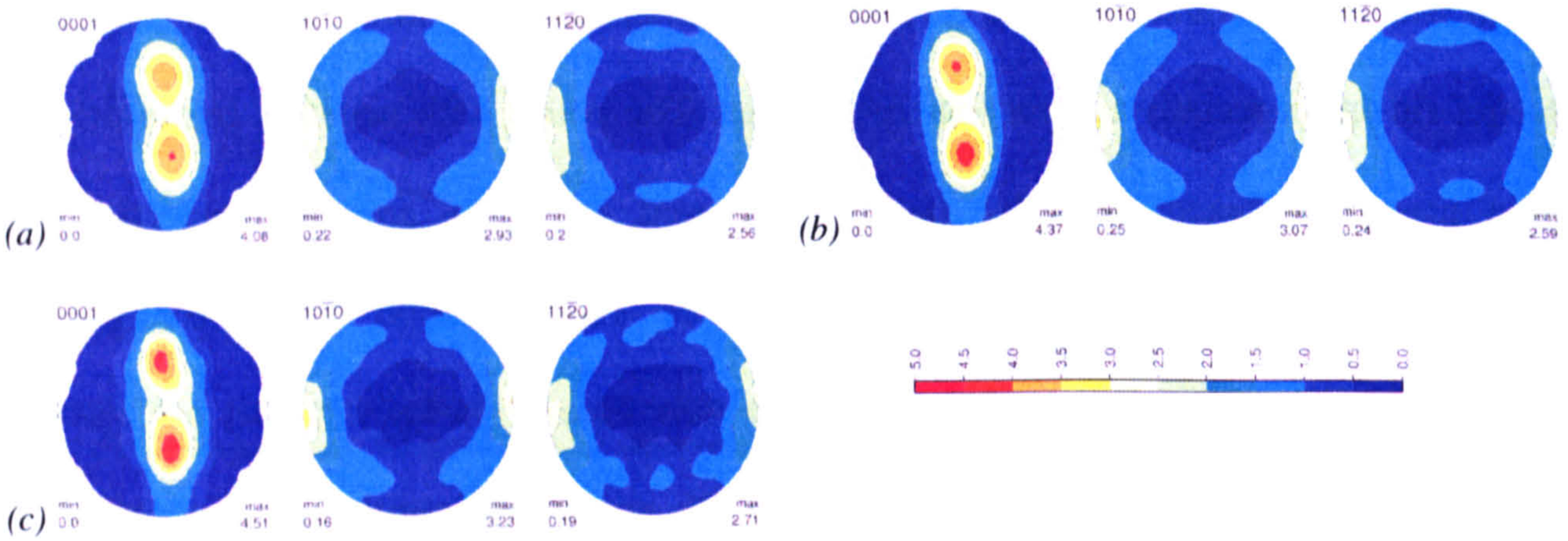

Figure 72 Pole figures for Zry-4 after (a) 6th, (b) 8th and (c) 12th order SH refinement

To determine the number of spherical harmonics needed to extract the texture from the histograms, we can also look at the evolution of the reduced χ^2 value with the SH order. The reduced χ^2 is an overall measurement of the goodness of the fitting of all the histograms used. It is an output of the GSAS software after the least squares refinement of all the spectra. For an optimum fit, the reduced χ^2 should equal 1. For details about how it is derived the reader is referred to the section on Least Squares Theory in the GSAS Manual [11]. Figure 73 shows the evolution of the reduced χ^2 with the order of spherical harmonics in the case of Zr-2.5Nb in its initial state. The quality of the fitting clearly increases when the number of harmonics is high (the reduced χ^2 tends to 1). However after the 12^{th} order the improvement is marginal.

As a final point about determining the best order of spherical harmonics, the reader is referred to Matthies et al. [84] who defined a more quantitative method using a negativity index.

Although part of the ODF has been determined by the spherical harmonics method, only the even coefficients are available. It is therefore necessary to export the data in terms of pole figures. For this purpose the GSAS routine Polfplot was used.

The sample positioning and alignment in HIPPO lacks of precision so some arbitrary rotations need to be applied to get a more symmetrical set of pole figures [84]. Using the PopLA package, the pole figures were tilted and rotated by means of symmetry.

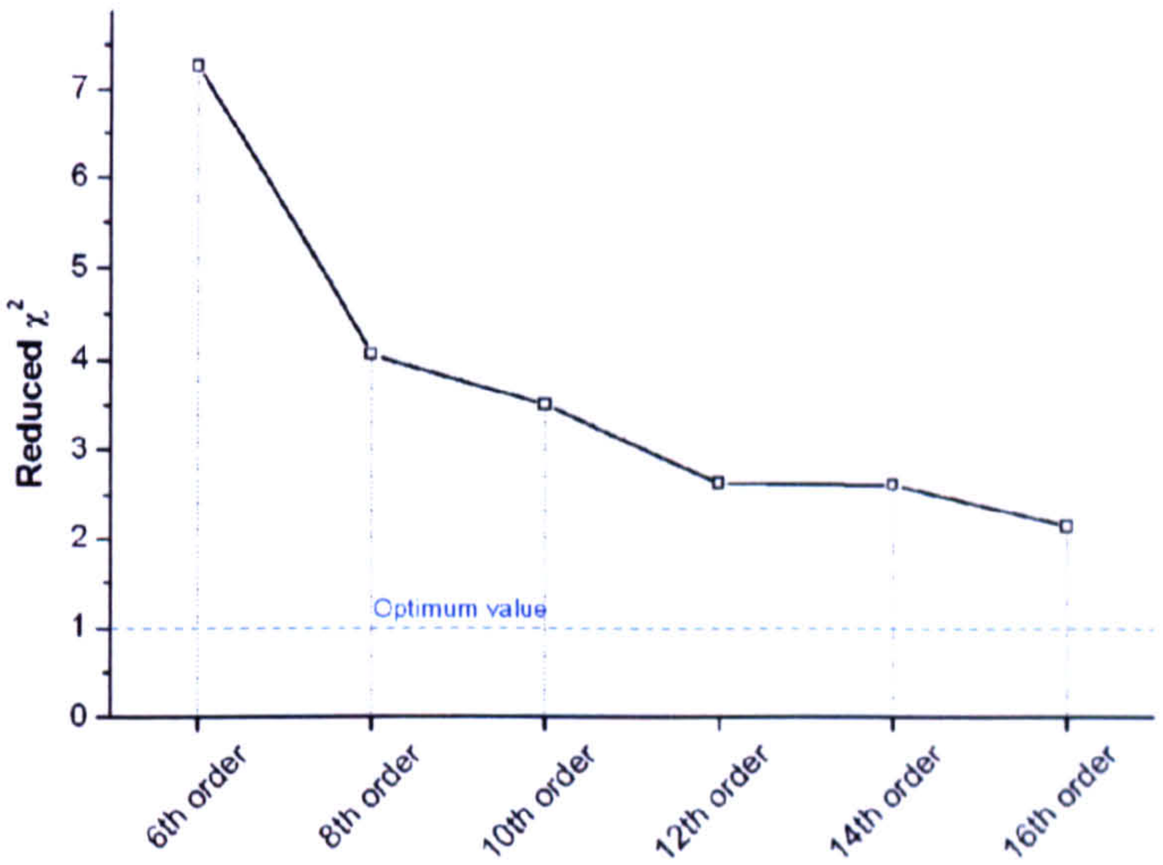

Figure 73 Reduced χ^2 after refinements at different SH order for Zr2.5%Nb

7.2 Results

7.2.1 Zircaloy-4

The neutron texture of the as-received Zry-4 plate is described in Section 4.1.3. In this section the textures of the coupons compressed at different strain levels are discussed.

7.2.1.a Compression along ND

The macroscopic responses of the two samples that have been compressed along the ND are shown in Figure 74. The samples were deformed to 6.3% and 15% of plastic strain with strain rates of 0.6×10^{-3} and 1.4×10^{-3} s^{-1} respectively.

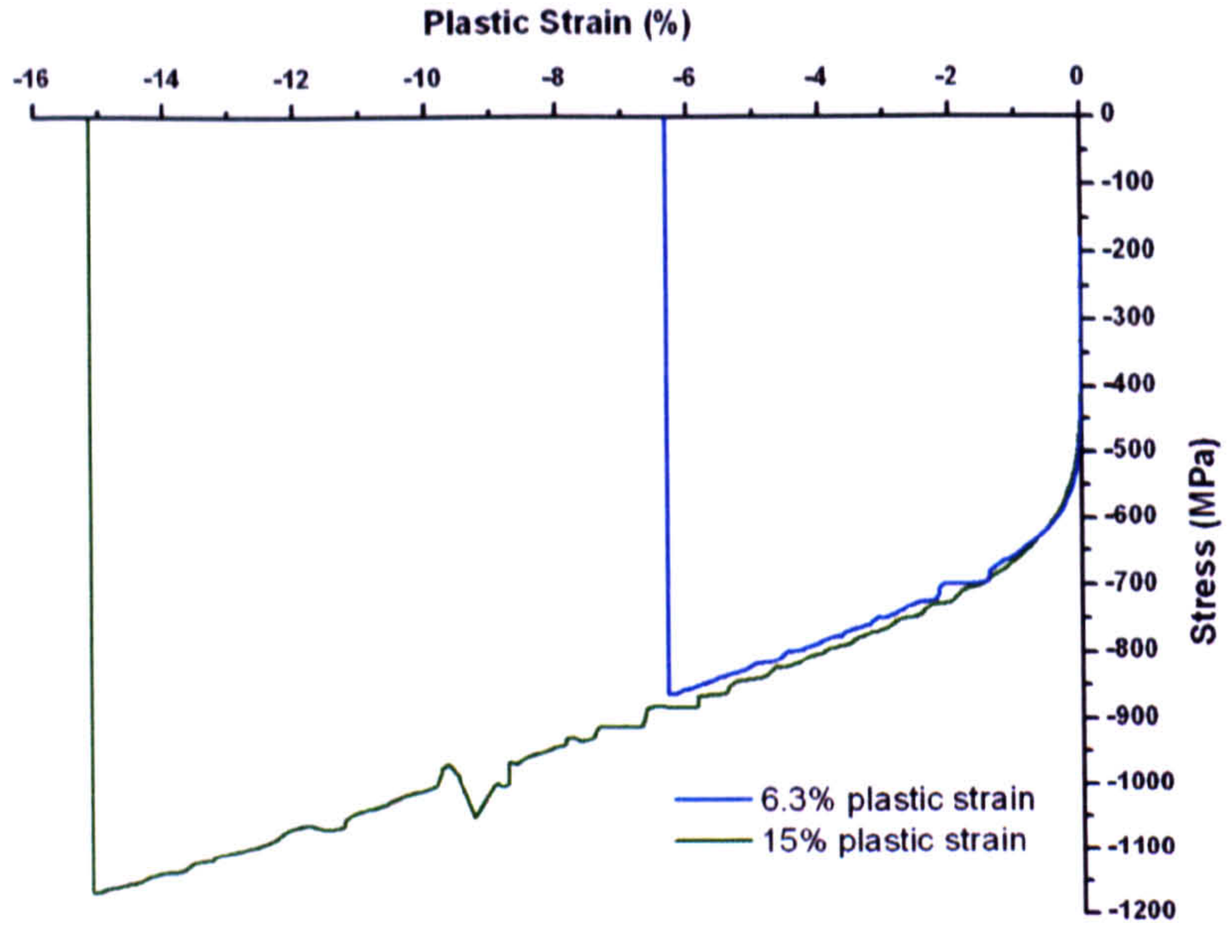

Figure 74 Macroscopic response for the Zry-4 coupons compressed along ND

The corresponding textures are shown in Figure 75 in the form of pole figures. Similarly to the as-received material (Figure 21), the central, horizontal and vertical poles are ND, TD and RD respectively. When compared to the initial texture, the pole figures apparently sharpen as the deformation rate increases. The maximum pole intensity for basal reflections increases from 4.37 to 5.76 times random before deformation and after 15% deformation respectively. In addition, the two eyes of the basal pole figure move towards the centre of the pole figure. This is clear when a zenith angle plot is taken from the basal pole figures as shown in Figure 76.

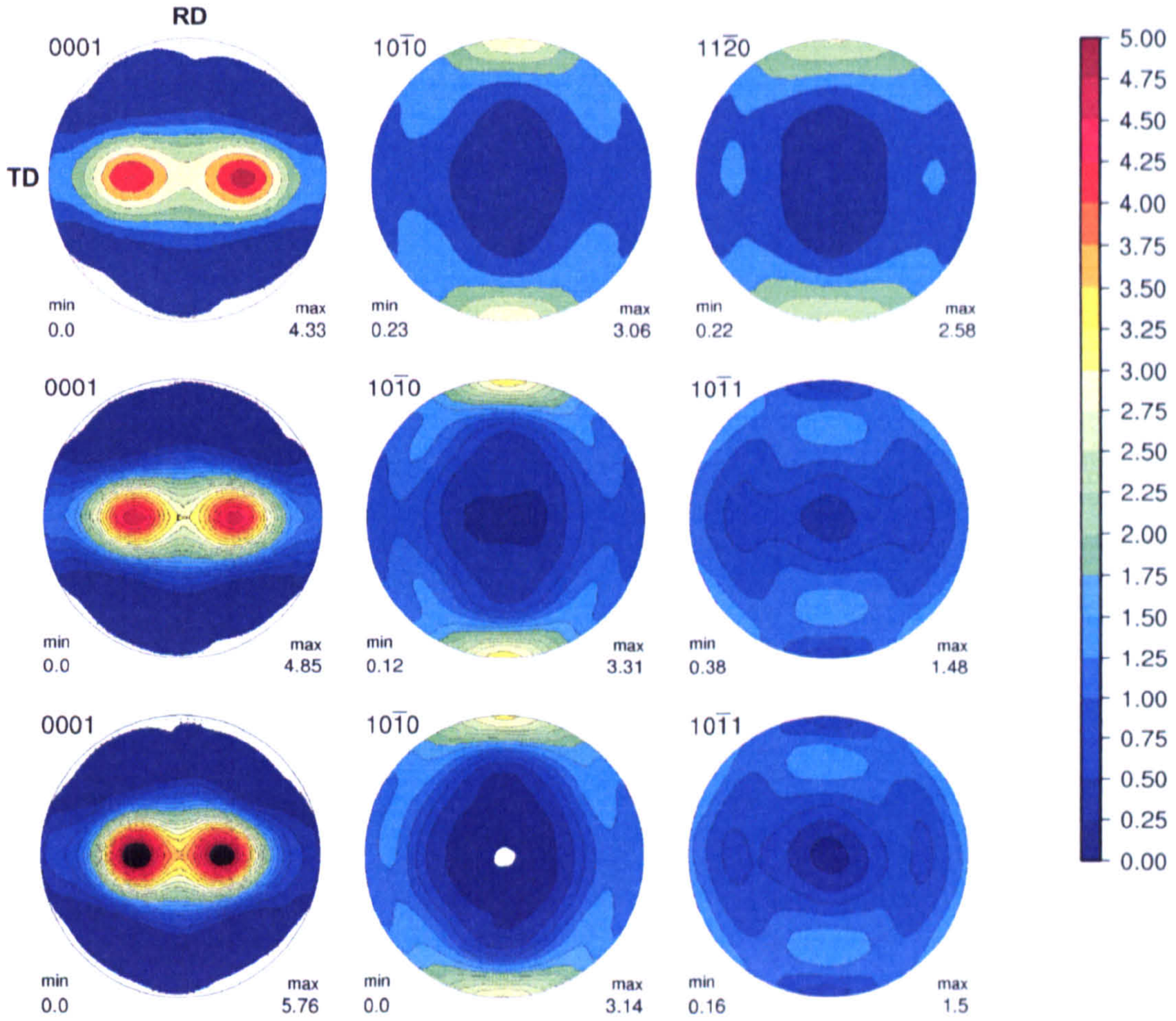

Figure 75 Basal, prismatic and pyramidal pole figures (a) as received, (b) after 6.3% and (c) 15% plastic deformation for ND compression (the top/bottom poles, left/right poles and centre are aligned with RD, TD and ND respectively)

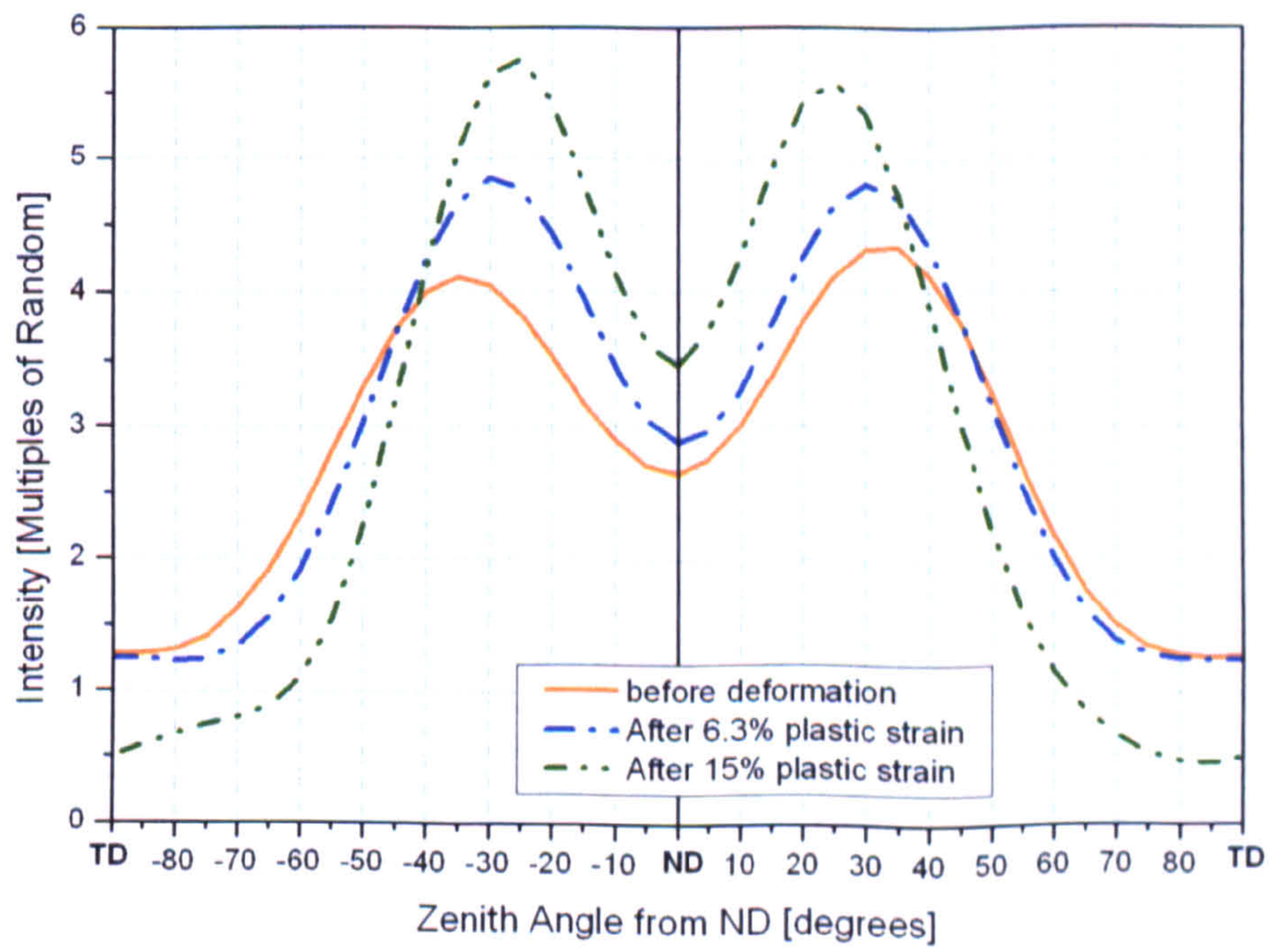

Figure 76 Evolution of the basal intensity for a TD-ND-TD scan during ND compression

7.2.1.b Compression along TD

Two samples were compressed along TD up to 6.5% and 15.9% plastic strain with the same rates as for ND compression. The corresponding stress-strain curves are plotted Figure 77.

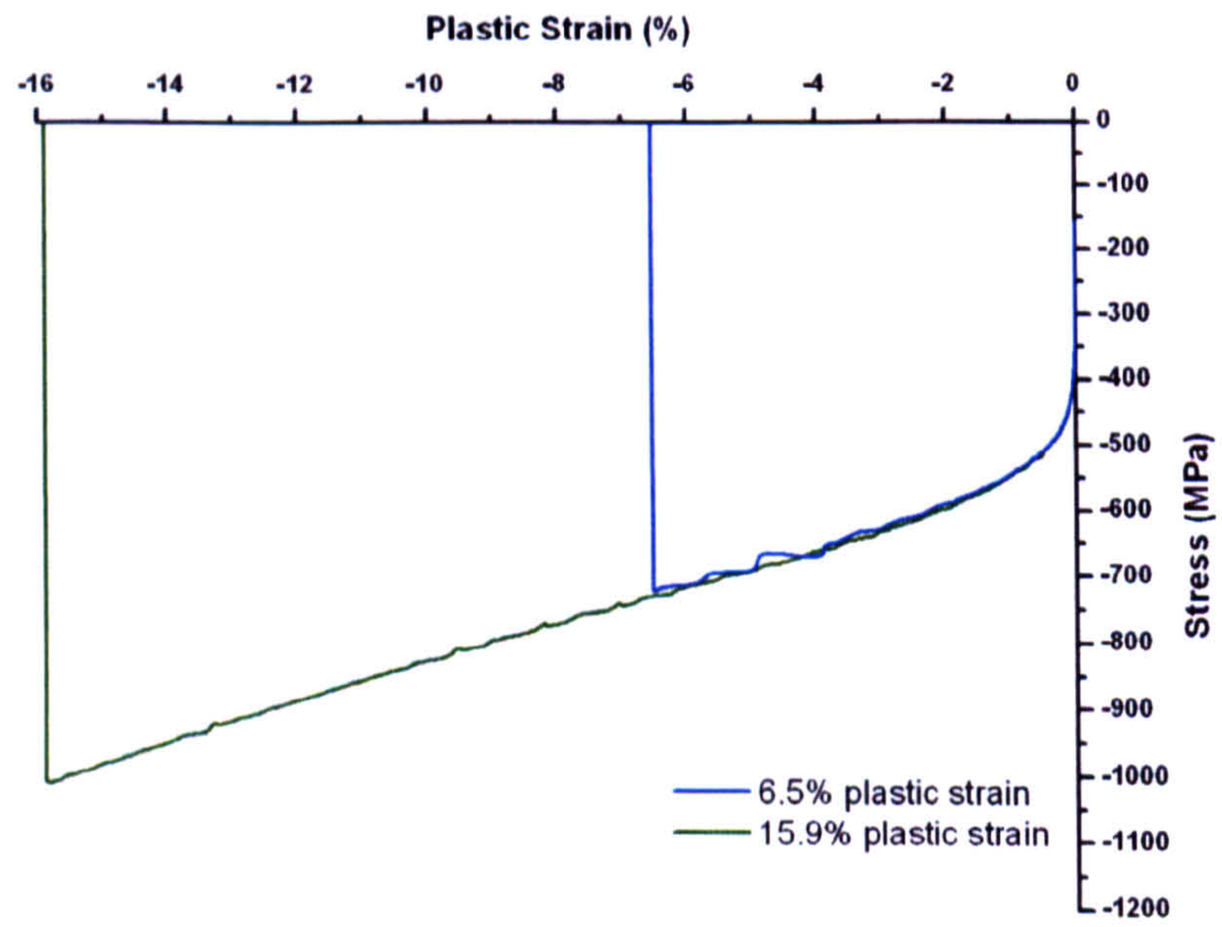

Figure 77 Stress-Strain curves for compression along TD

The pole figures for the main reflections are represented in Figure 78. Similarly to the ND compression case we have plotted a TD-ND-TD zenith angle scan of the {00.2} pole figure (Figure 79).

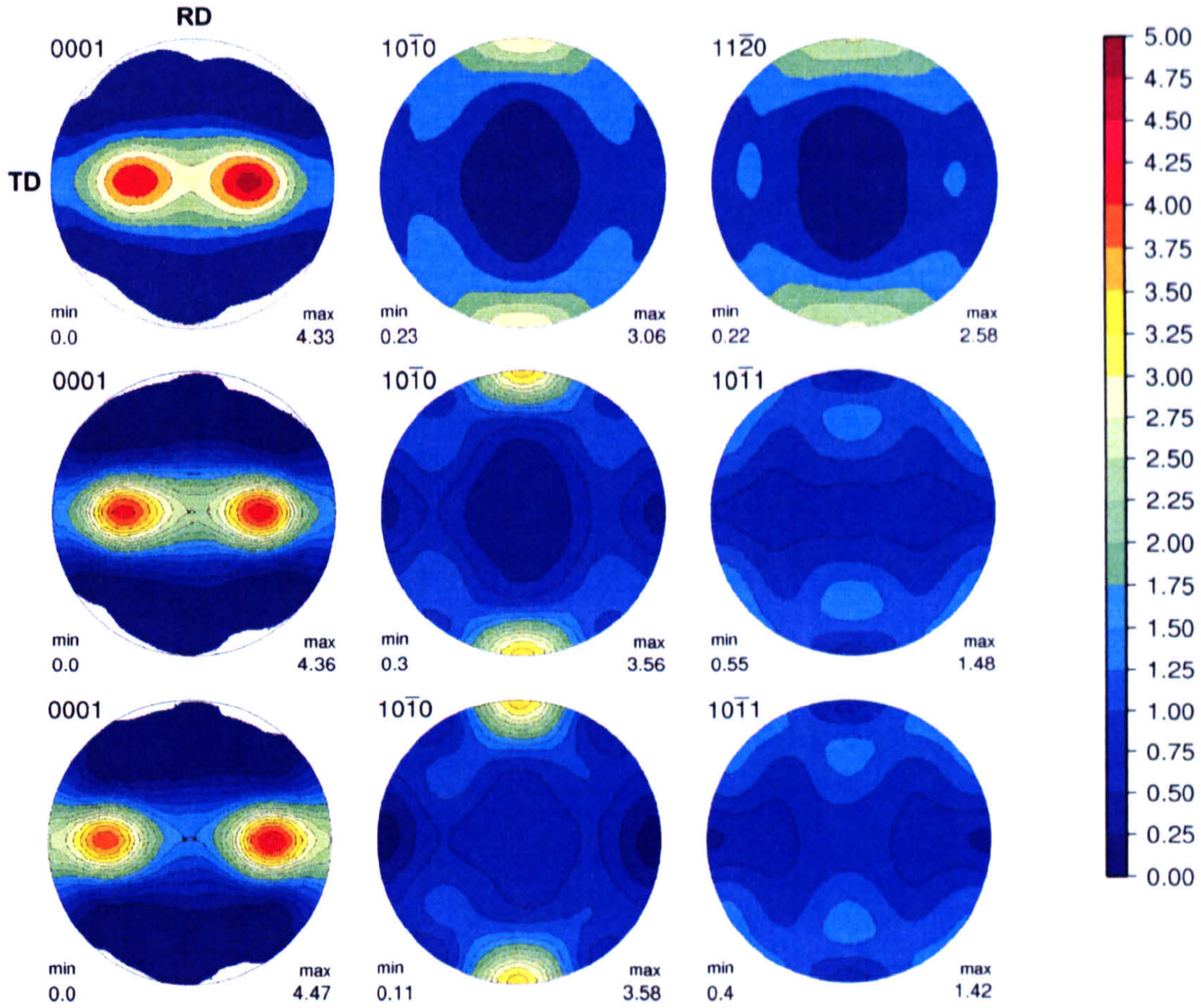

Figure 78 *Basal, prismatic and pyramidal pole figures (a) as received, (b) after 6.5% and (c) 15.9% plastic strain for TD compression (the top/bottom poles, left/right poles and centre are aligned with RD, TD and ND respectively)*

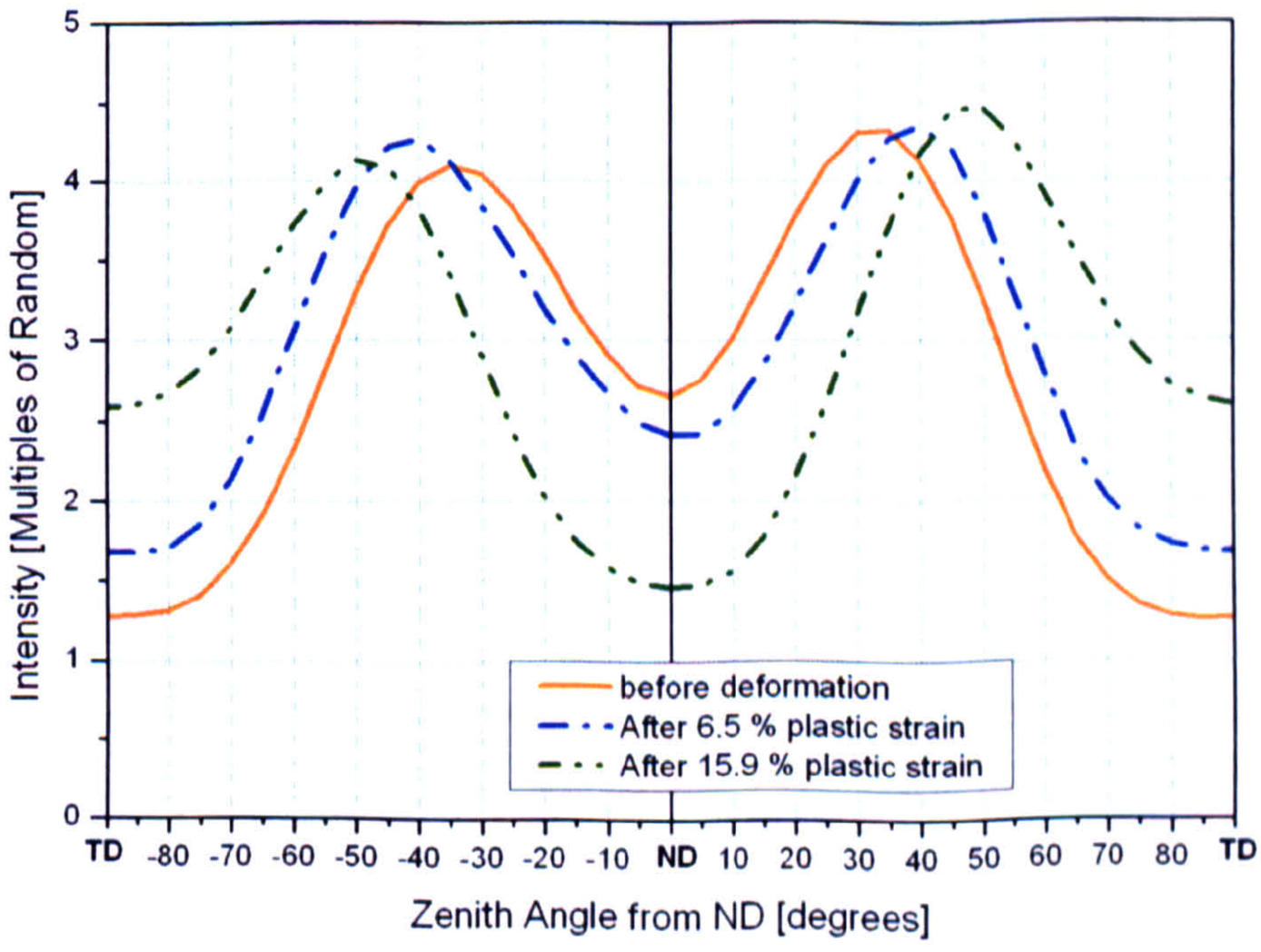

Figure 79 *Evolution of the basal intensity for a TD-ND-TD zenith scan during TD compression*

7.2.1.c Compression along RD

From the data presented in Chapter 5.2, it is during compression along RD that most changes happen in terms of diffraction intensity. In order to capture better the texture evolution in this case, four samples were studied. The tests had a slightly different deformation rate: the first two were compressed up to 1.3% and 4% plastic strain with a rate of approximately $0.6x10^{-3}$ s^{-1} while the other two were compressed to 8.3% and 15.9% with a rate of $1.4x10^{-3}$ s^{-1}. The response of the samples is represented in Figure 80. The increasing hardening rate described in chapter 5.2.3.a is again visible here.

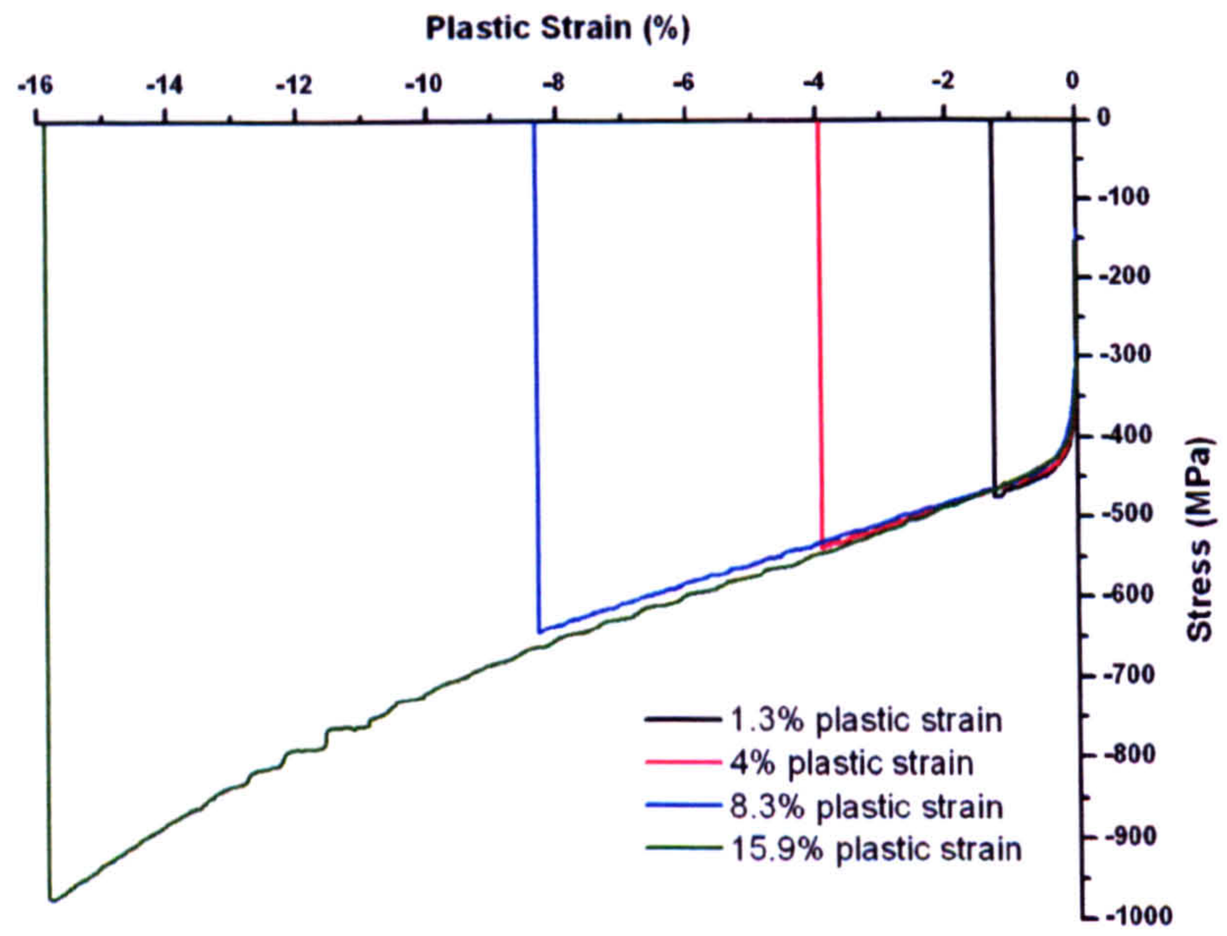

Figure 80 Stress-Strain curves for the samples compressed along RD

Figure 81 shows the pole figures for the different compression levels. After ε^p =1.3% (Figure 81 (a)), the texture shows little difference with that of the as received material. After 4%, the intensity of the {00.2} eyes is down to below 4 multiples of random, while some intensity appears in the RD. As the deformation increases, the eyes are increasingly weakened while the poles in the RD intensify. For {10.0} pole figures, intensity is lost in the vicinity of RD while some poles appear in the ND-TD plane, and especially along TD.

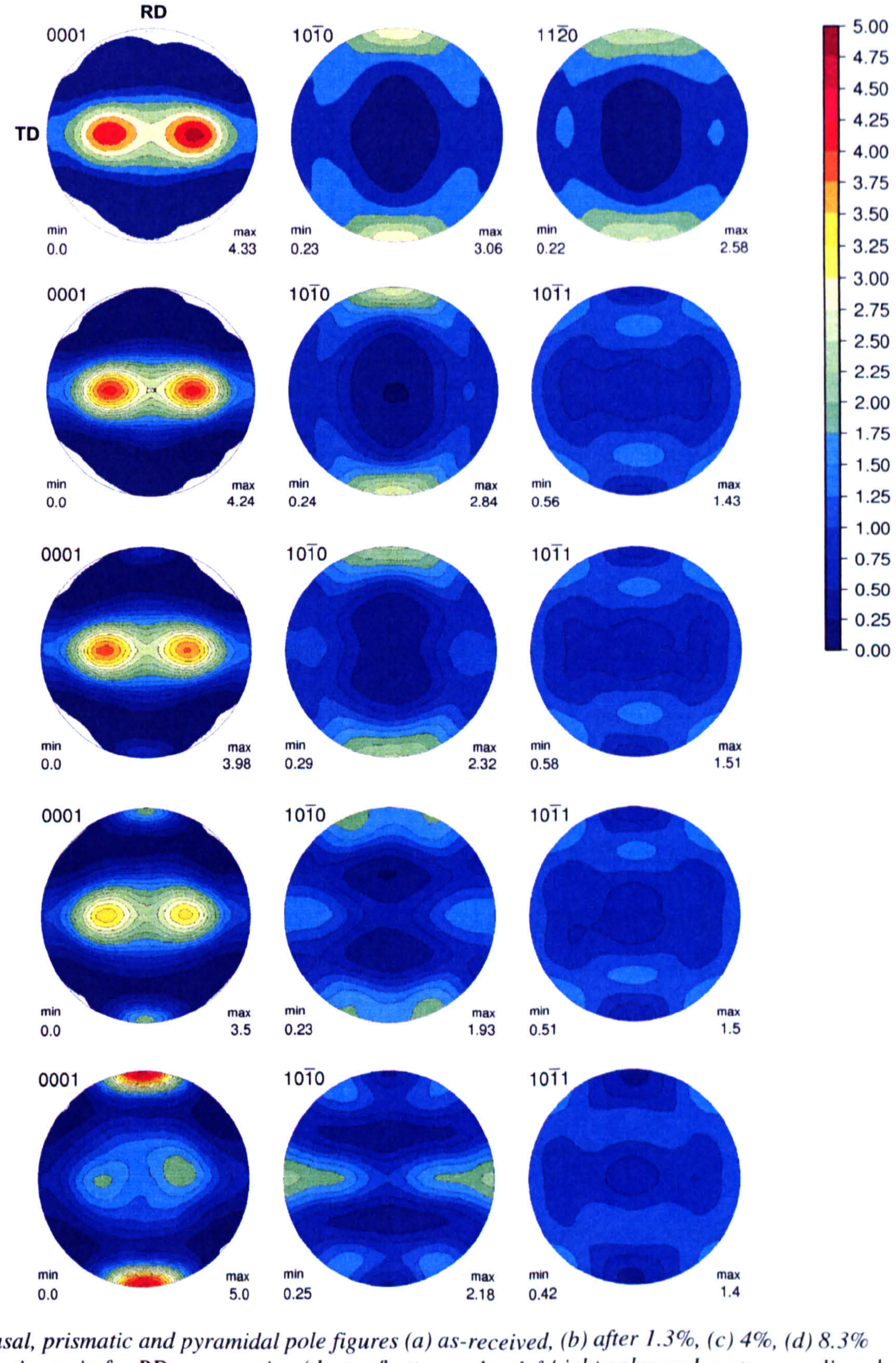

Figure 81 Basal, prismatic and pyramidal pole figures (a) as-received, (b) after 1.3%, (c) 4%, (d) 8.3% and (e) 15.9% plastic strain for RD compression (the top/bottom poles, left/right poles and centre are aligned with RD, TD and ND respectively)

Once more we have plotted a TD-ND-TD zenith angle scan of the basal pole figure (Figure 83). This time however we also performed the scan in the RD-TD plane as it is where the most significant intensity changes happen (Figure 83).

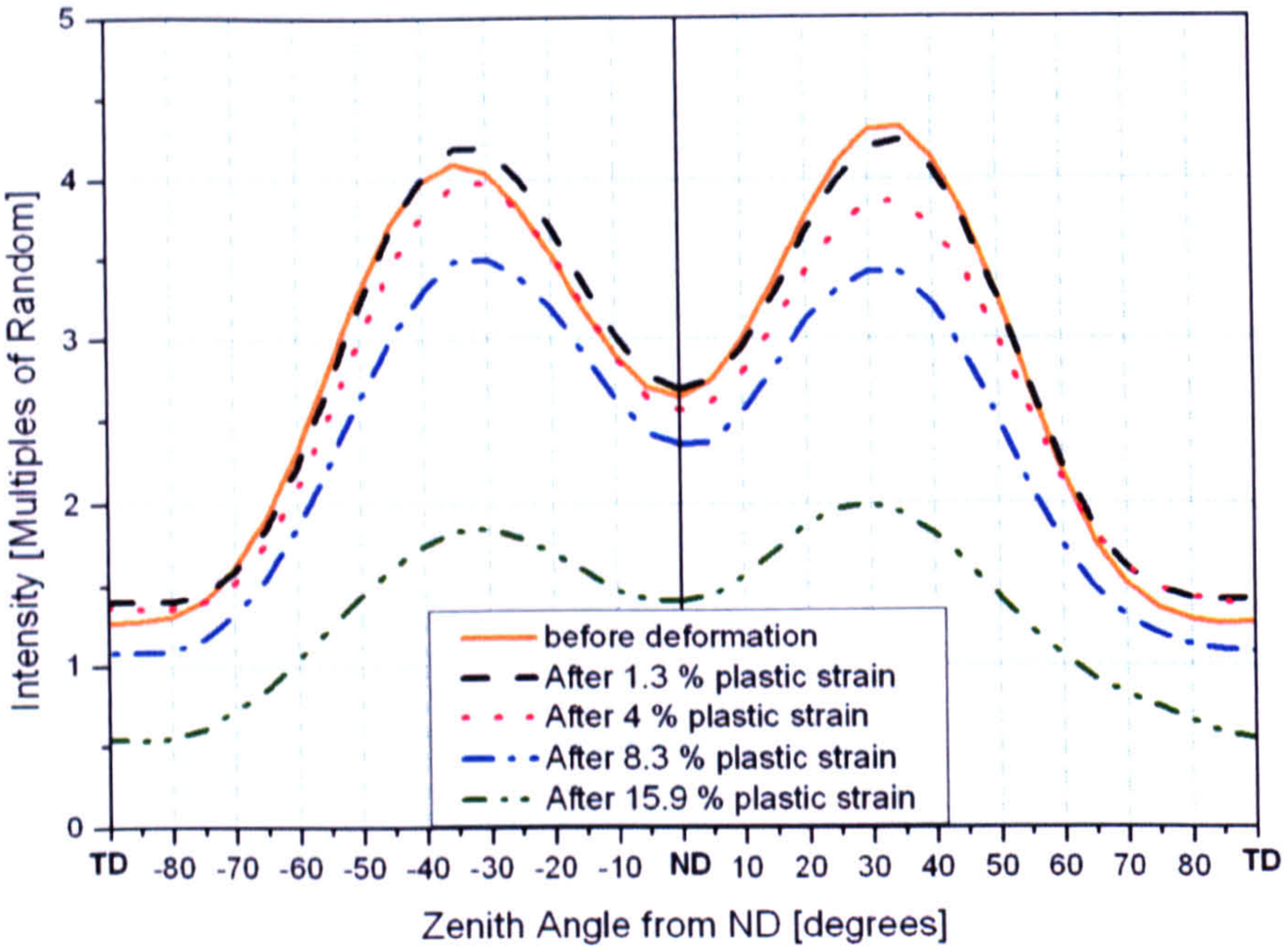

Figure 82 Evolution of the basal intensity for a TD-ND-TD zenith scan during RD compression

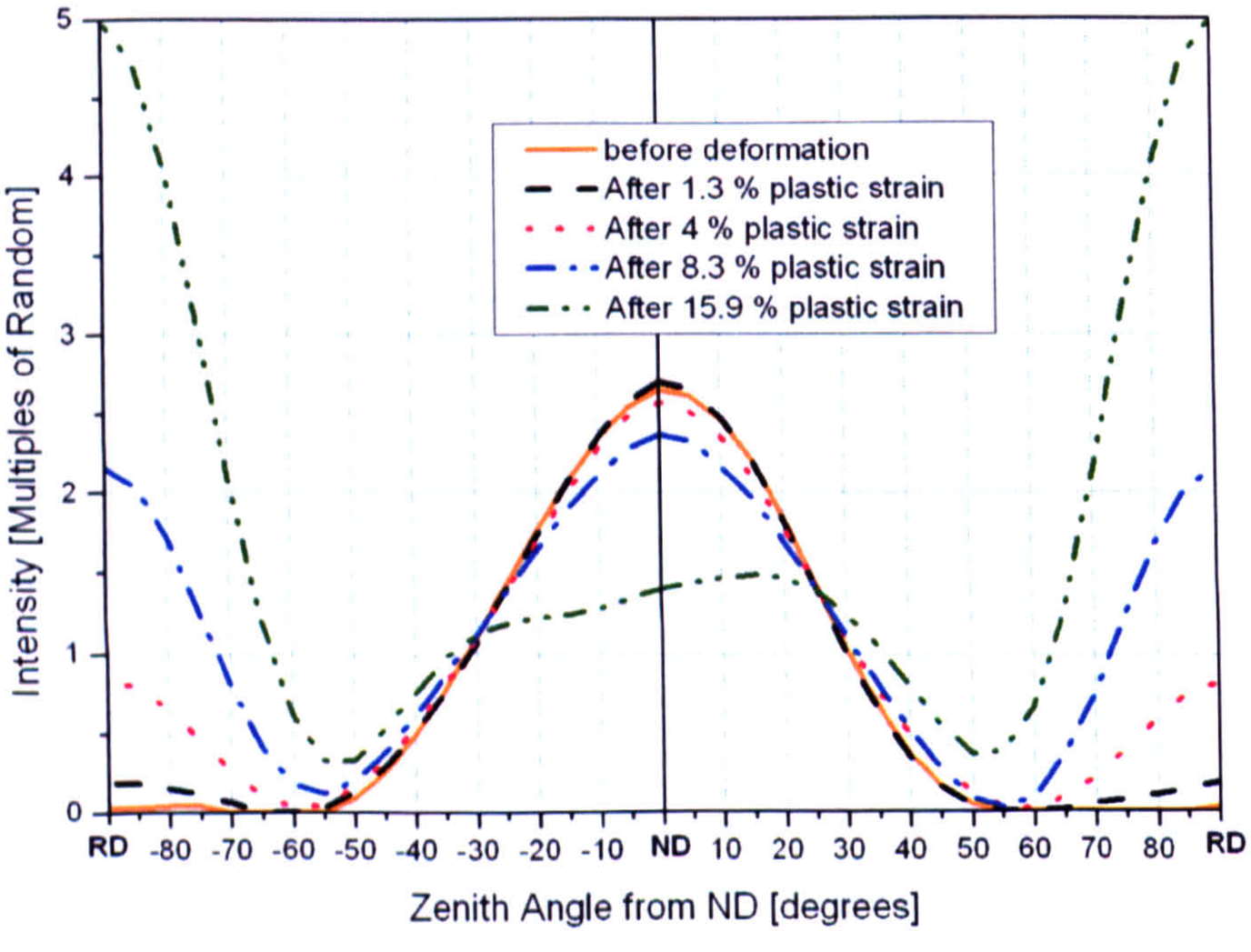

Figure 83 Evolution of the basal intensity for a RD-ND-RD zenith scan during RD compression

The transfer of {00.2} intensities from the ND-TD plane to the RD is not gradual. This suggests that the most drastic texture changes observed are not due to slip but rather to twinning. Indeed the crystal rotation induced by slip in constrained grains is an incremental function of the amount of slip. So slip induced crystal rotation is characterized by an incremental displacement of the poles on a pole figure. On the other hand twinning introduces a finite amount of rotation and will be characterized by a finite displacement of

the poles on the pole figure. Tensile twinning in Zr crystals tilts the lattice by nearly 90°, which corresponds to the amount of rotation necessary to bring the basal planes from the ND-TD plane to the RD as observed here.

7.2.2 Zr-2.5%Nb

A similar study has been carried out on the Zr-2.5%Nb material described in Chapter 4. The compression coupons were cubes of 4mm. They were compressed in the same Instron machine used for the Zry-4 samples with a strain rate of $2x10^{-3}$ s^{-1}. For each processing direction, two samples were compressed at different levels of strain and the textures measured on the HIPPO diffractometer. The β phase peaks were not visible in the diffraction spectra. On ENGIN-X, the peaks were very low and broad and difficult to identify and fit (Figure 46). The lower counting time of the HIPPO measurements can explain why they don't appear on the spectra as they are lost in the background noise. As a consequence, only the texture of the α phase is studied here.

7.2.2.a Compression along AD

Two coupons were compressed along the Axial direction (AD) to 6.5% and 15% plastic strain respectively. The stress/strain curve is plotted on Figure 84. The noise in the curves is a result of slight strain rate variations during the test.

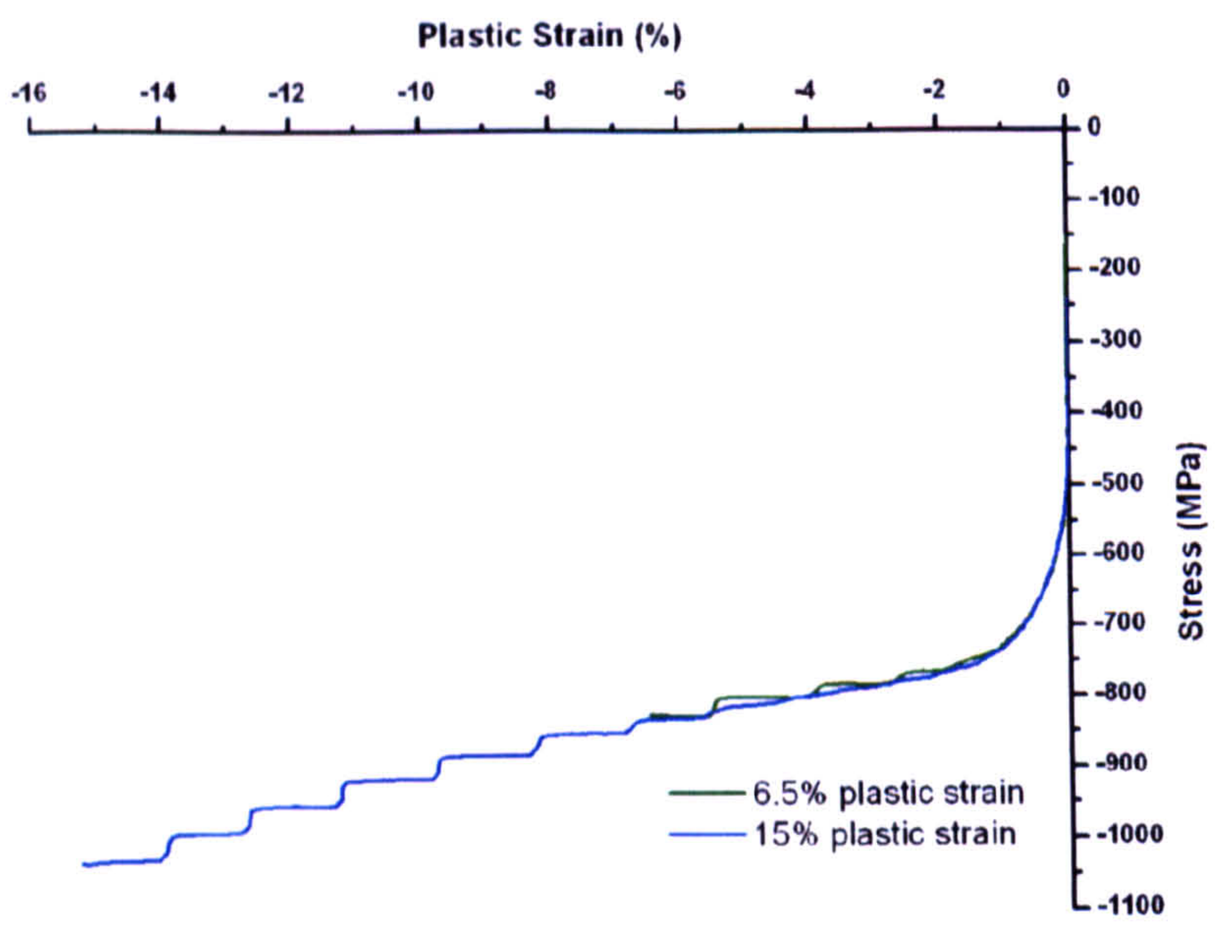

Figure 84 Stress-Strain curves for the Zr-2.5Nb samples compressed along AD

The pole figures measured in each sample are represented on Figure 85. The texture changes are quite significant and seem to show a grains rotation from an $\{00.2\}_{HD}$ to a $\{00.2\}_{AD}$ orientation: the $\{10.0\}_{AD}$ and $\{00.2\}_{HD}$ intensities decrease in favour of $\{00.2\}_{AD}$. There are no intermediate $\{00.2\}$ intensities in the HD/AD plane during compression which suggests that it is an abrupt reorientation induced by tensile twinning, as was observed during RD compression of Zry-4.

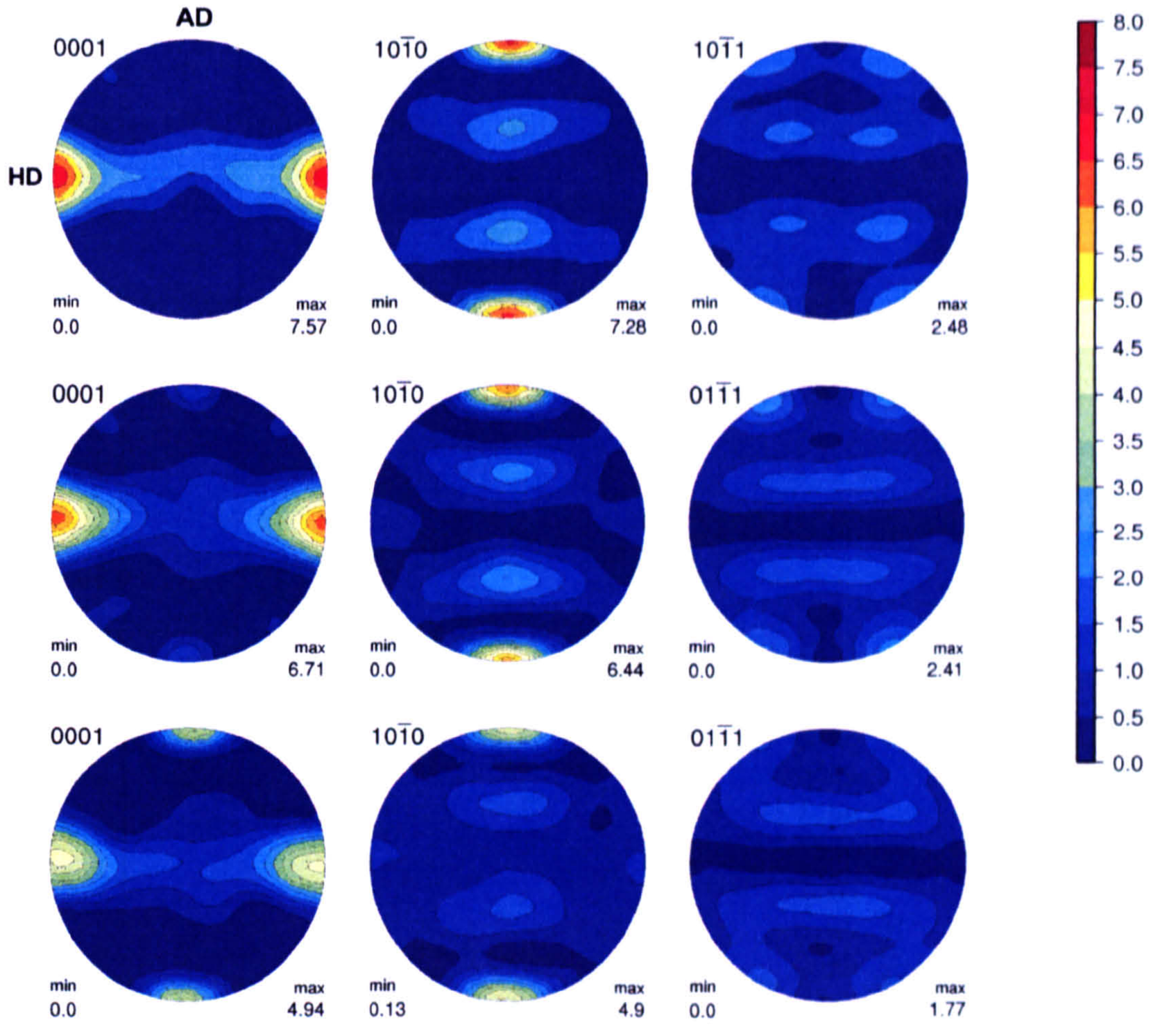

(a)

(b)

(c)

Figure 85 Basal, prismatic and pyramidal pole figures (a) as-received, (b) after 6.5% and (c) 15 % plastic strain for AD compression (the top/bottom poles, the left/right poles and the centre are AD, HD and RaD respectively)

7.2.2.b Compression along RaD

The mechanical response of the two coupons compressed along the radial direction is shown on Figure 86. In terms of plastic strain, they were compressed up to 6.2% and 16.2%.

As shown on Figure 87, the texture evolution is relatively marginal during RaD compression. The only noticeable change is that the maximum intensities for each pole figure seem to reduce with increasing deformation. It suggests that RaD compression slightly weakens the texture without affecting the main features. It is actually not a surprising result as the process of extrusion implies compression in the same direction, so the texture is already stabilised for this type of deformation. Of course during extrusion the

material is under more complicated triaxial loading conditions so the texture is still affected by uniaxial RaD compression.

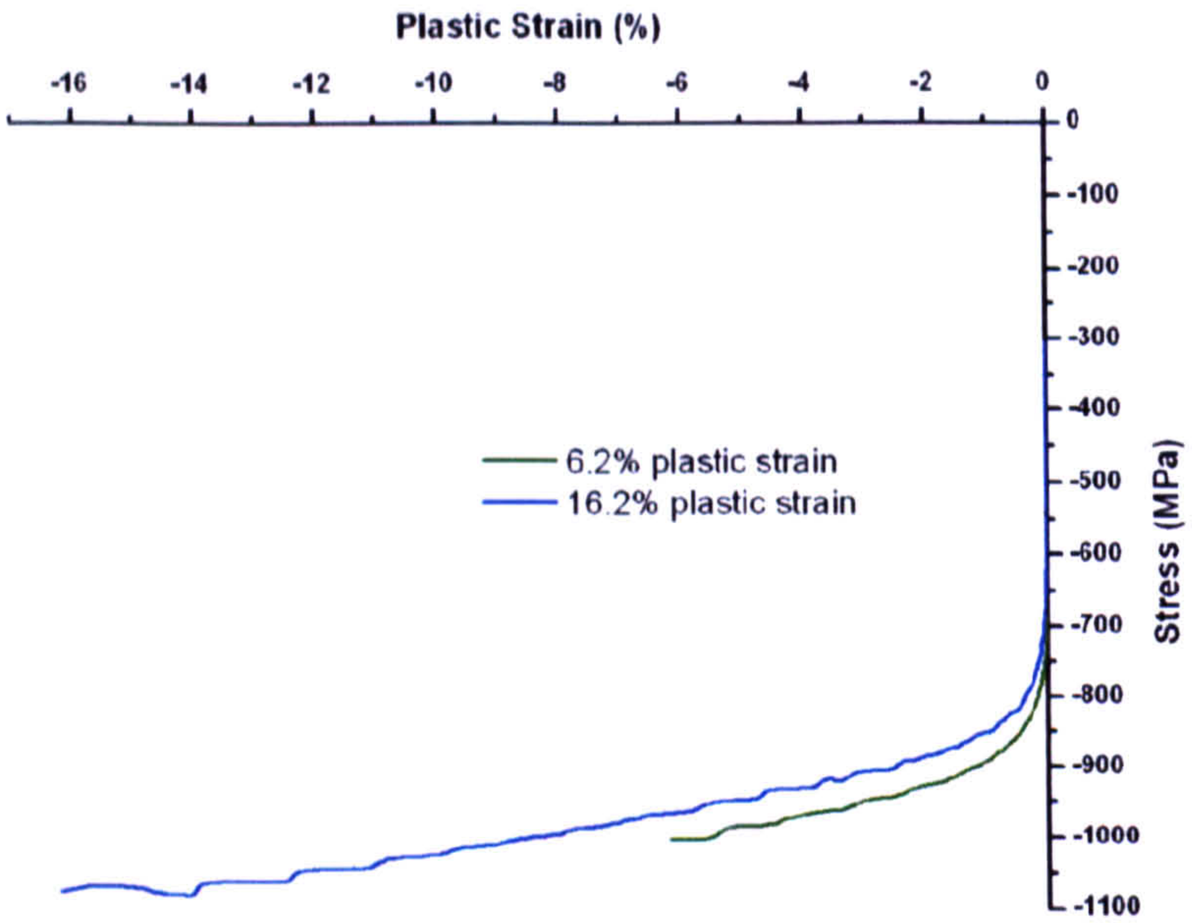

Figure 86 Stress-Strain curves for the Zr-2.5Nb samples compressed along RaD

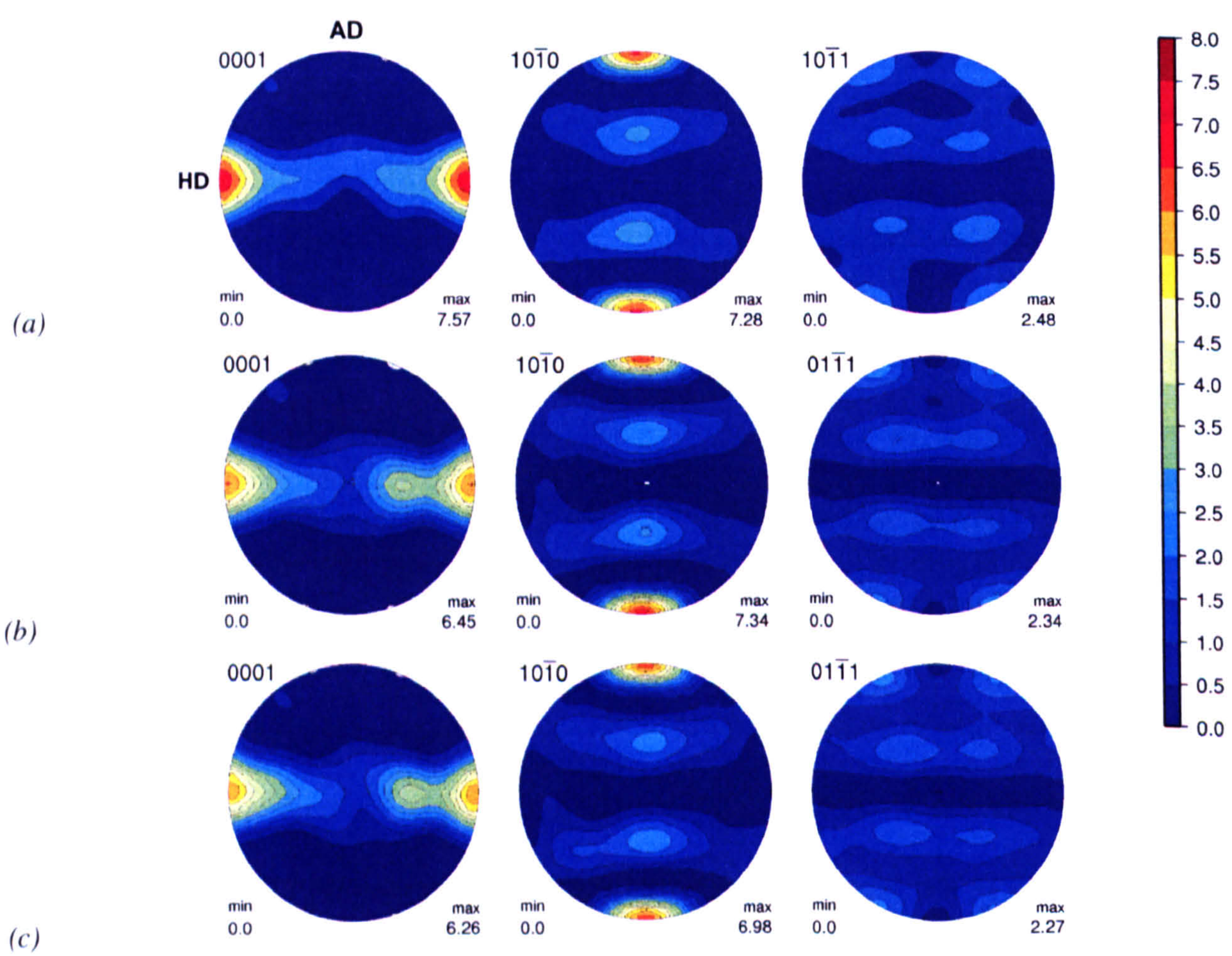

Figure 87 Basal, prismatic and pyramidal pole figures (a) as received, (b) after 6.2% and (c) 16.2% plastic strain for RaD compression (the top/bottom poles, the left/right poles and the centre are AD, HD and RaD respectively)

7.2.2.c Compression along HD

For compression along HD, the ductility is quite low and the material fails between approximately 7% and 7.5% plastic strain. The first coupon was compressed up to 2.2% plastic strain while the second one was brought to failure at 7.1%. The macroscopic flow curves are represented on Figure 88 and the corresponding final textures on Figure 89.

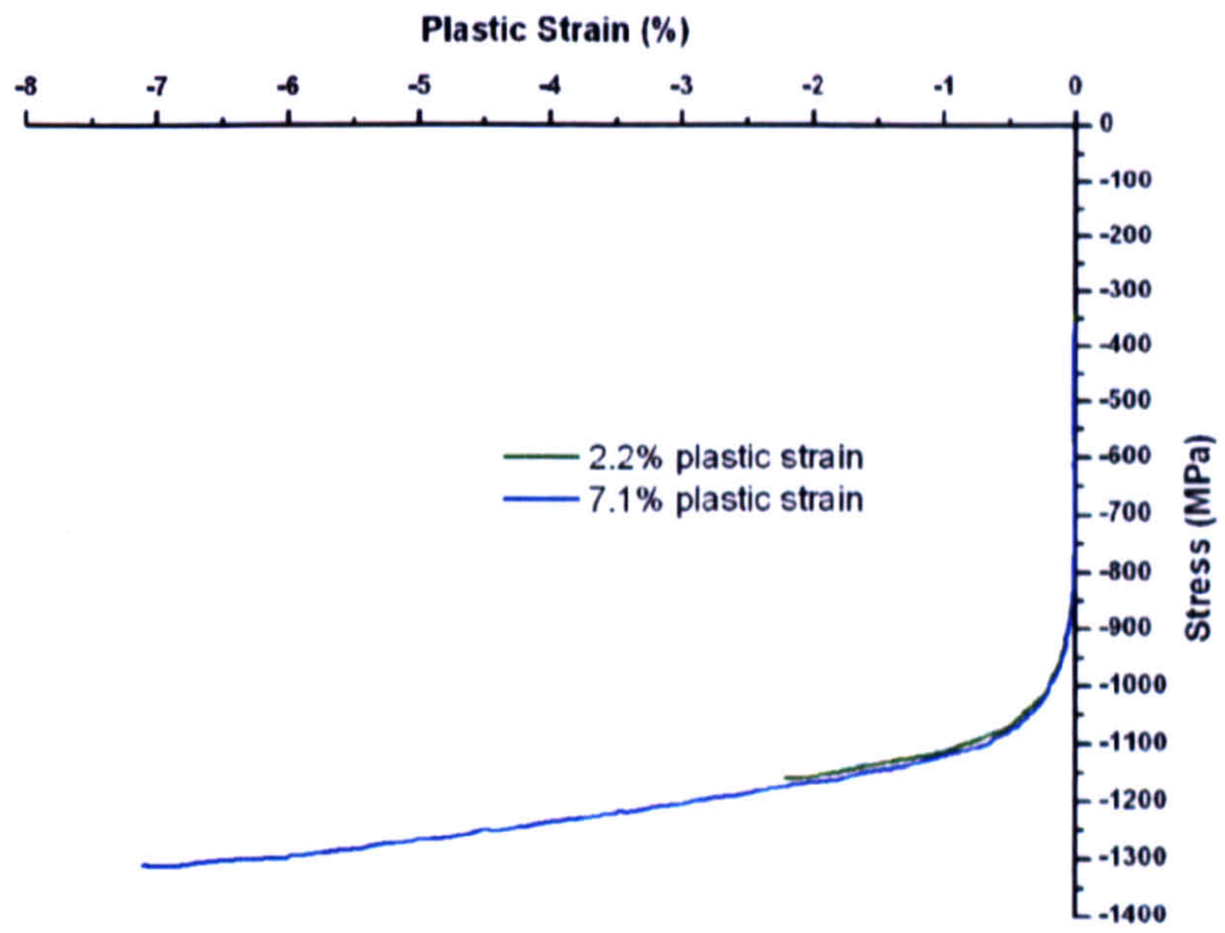

Figure 88 Stress-Strain curves for the Zr-2.5Nb samples compressed along HD

Despite the comparatively small levels of deformation, the texture changes quite significantly between the different coupons.

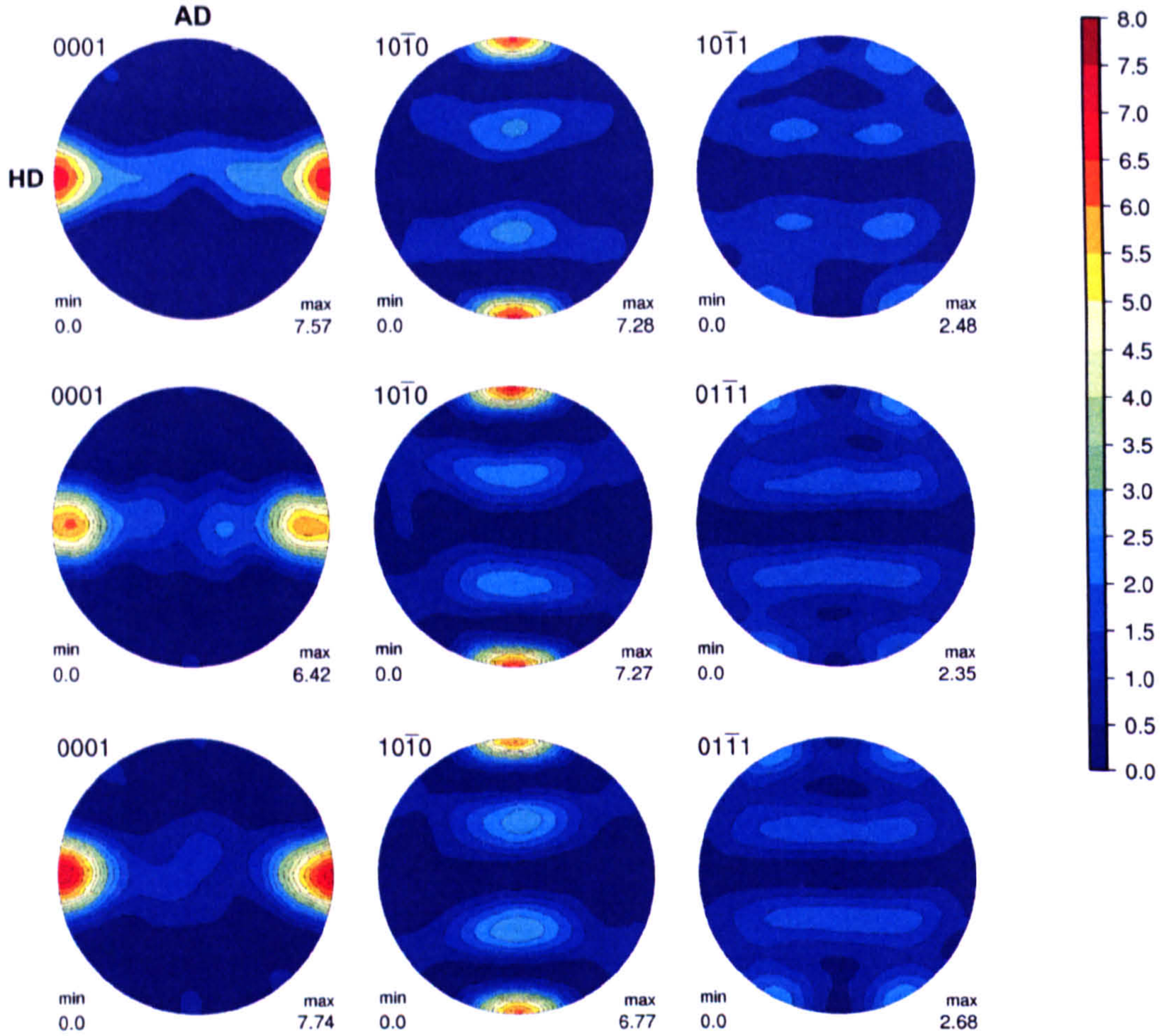

(a)

(b)

(c)

Figure 89 Basal, prismatic and pyramidal pole figures (a) as-received, (b) after 2.2% and (c) 7.1% plastic strain for HD compression (the top/bottom poles, the left/right poles and the centre are AD, HD and RaD respectively)

7.3 Discussion

7.3.1 Experimental uncertainties

It is important to analyse the causes of uncertainties in the results presented here. First, the mechanical tests were not performed with an ideal rigorousness: the strain rates were not perfectly standardised between the tests (there were some slight variations from test to test) and the strain was not measured on the samples directly. The control was also not flawless and for some tests there were fluctuations in the strain rate. The method of ex-situ compression itself also comports some inherent limitations and the results are prone to the error introduced by local texture variations. Indeed, although the samples have been taken in the same region of the plate/tube, the spatial texture variations are added to the

deformation induced texture evolution. However we still believe they are of lower order than the changes occurring during deformation. Finally and as mentioned in previous Sections, the sharp textures measured at HIPPO can be smoothed because of the large detector panel areas.

7.3.2 Volume fraction of twinning

We have seen that during RD compression of Zry-4, the intensities of {00.2} pole figure are transferred from the ND-TD plane to the RD direction and that this evolution is most probably due to tensile twinning. Twinning is energetically advantageous only if there is a strain reduction in the compression direction, which corresponds to the case where the mechanism tilts the basal planes towards that direction. Given the loading conditions, the grains see most compression along the RD. So the most favourable cases of twinning during compression along RD will tilt basal planes from the ND-TD plane towards the RD. From there we make the assumption that the intensities that appear in the RD are exclusively due to twinning (15.9% plastic deformation is a relatively small amount of deformation for slip induced texture changes) and represent all the twinning activity. This can give a basis to attempt to calculate the volume fraction of twinning as a function of the deformation.

When looking at Figure 83, the region around RD affected by large intensity changes extends to 35° from RD. Figure 90 shows intensity variations for azimuth scans at a zenith angle of 90°, i.e. in the RD-TD plane. Here the phenomenon extends to +/- 45° from RD. We can thus define windows near the RD pole of the pole figure which are affected by large increases in intensity during RD compression. On Figure 91, the windows are represented on the pole figure grid. Assuming only and all the twinned grains contribute to the intensities in these windows, we will compute the volume fraction of twinned grains.

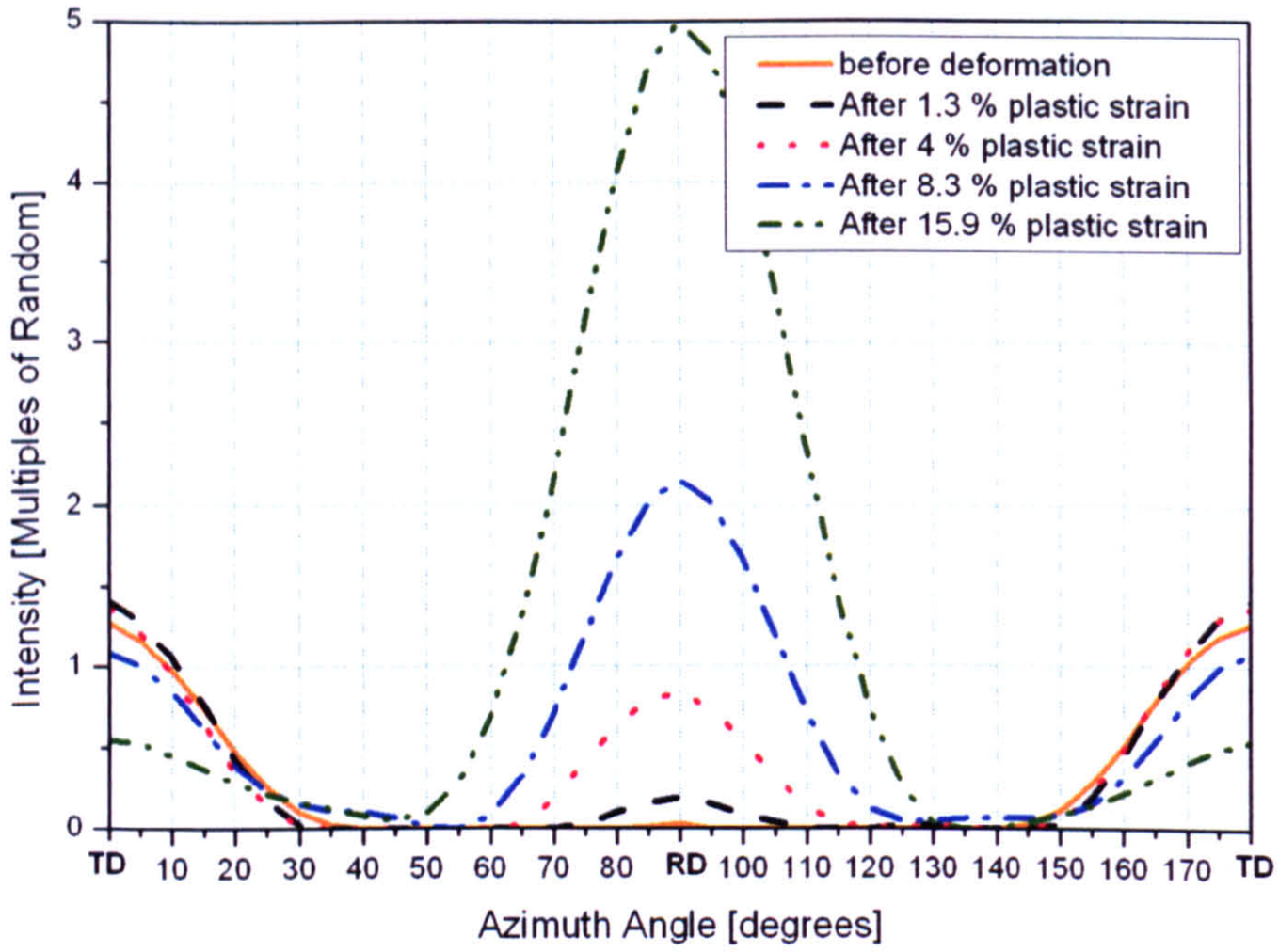

Figure 90 *Evolution of the basal intensity for a TD-RND-TD azimuth scan during RD compression*

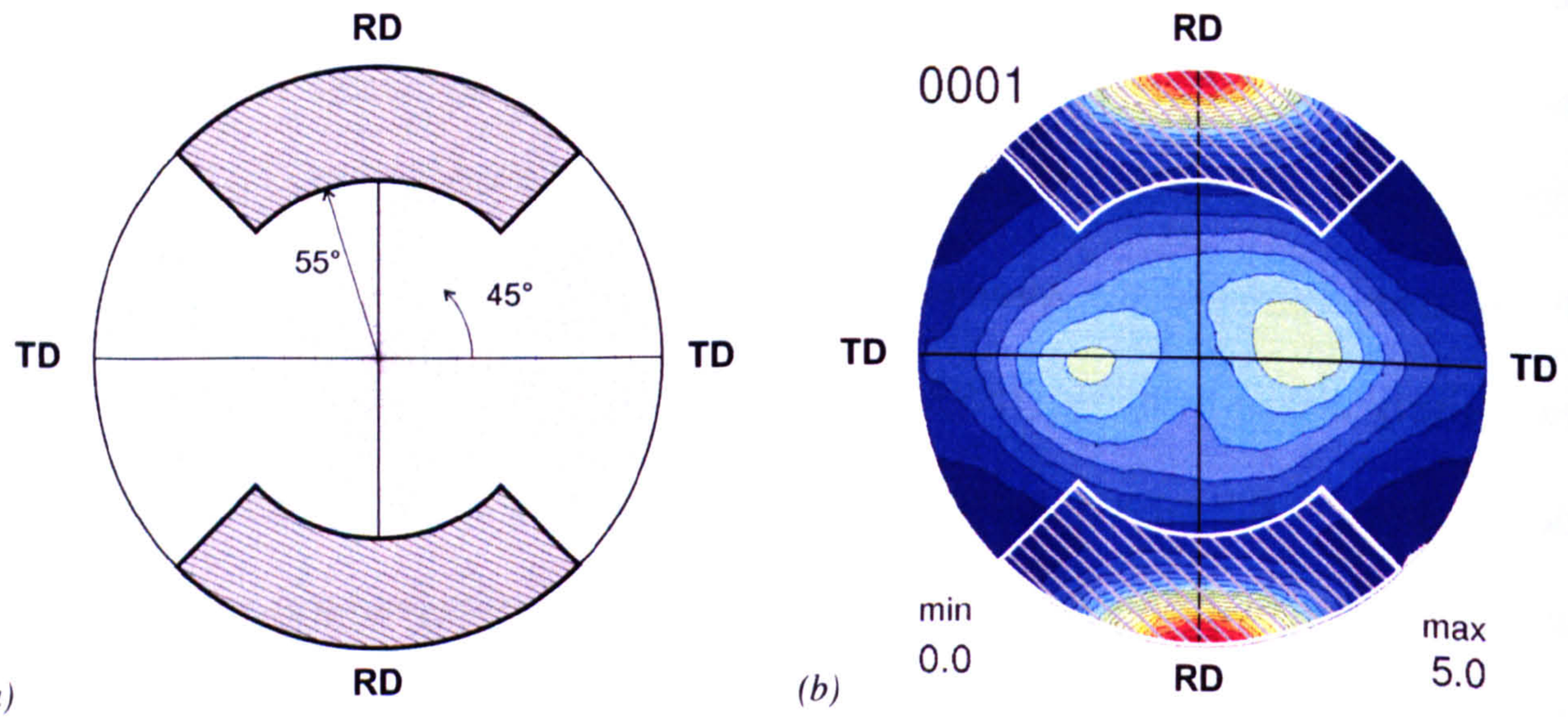

Figure 91 *Windows used for the calculation of VFT (a) on the equal area grid and (b) on the {00.2} pole figure of the sample compressed at 15.9%*

The volume fraction of {00.2} reflections oriented in the windows defined in Figure 91 can be computed as follow:

Eq. 23
$$v_{\{00.2\}} = \int_{\alpha=55\pi/180}^{\pi/2} \left(\int_{\beta=\pi/4}^{3\pi/4} I(\alpha,\beta).\sin\alpha.d\beta + \int_{\beta=5\pi/4}^{7\pi/4} I(\alpha,\beta).\sin\alpha.d\beta \right) d\alpha$$

Effectively the pole figures returned by PopLA proved to be not perfectly normalized (error of less than 5%). The most probable explanation lies in the fact that the negative densities have been truncated off the pole figures. The pole figures were calculated with the GSAS function polfplot from the spherical harmonic coefficients, and as the truncation is performed by GSAS after normalisation, the average values over the pole figure will differ from 1 (the values would be higher, which is the case except for the last compression test). We decided to normalize the pole figures again for the purpose of calculating the volume fractions. If the intensities are normalized, the intensity integrated over the whole surface of the pole figure is equal to the integral of unity over the same surface, i.e:

$$\int I dA = \int dA \qquad \textit{Eq. 24}$$

For a pole figure, the surface element $dA = \sin\alpha.d\alpha.d\beta$, and for normalised pole figures:

$$\int I dA = \int_{\alpha=0}^{\pi/2}\int_{\beta=0}^{2\pi} \sin\alpha.d\alpha.d\beta = 2\pi \qquad \textit{Eq. 25}$$

Hence for normalising the pole figures, the intensities were corrected with the factor $\frac{2\pi}{\int I dA}$. Another method for renormalizing the pole figures would have been to run the WIMV function in GSAS. The renormalization was not performed for the representation of the pole figures and the small error must be taken into account when looking at them.

The pole figure is in the form of discrete data with a cell size of 5°x5°. The integrals can be separated in sums of integrals over each cell and Eq. 23 becomes:

$$v_{\{00.2\}} = \sum_{k=12}^{18}\left(\sum_{l=10}^{27}\int_{\alpha=i*k}^{i(k+1)}\int_{\beta=i*l}^{i(l+1)} I(\alpha,\beta).\sin\alpha.d\beta.d\alpha + \sum_{l=56}^{63}\int_{\alpha=i*k}^{i(k+1)}\int_{\beta=i*l}^{i(l+1)} I(\alpha,\beta).\sin\alpha.d\beta.d\alpha\right) \qquad \textit{Eq. 26}$$

where $i = 5\pi/180$ is the angular increment expressed in radians.

As the intensity is constant on each cell:

Eq. 27

$$\upsilon_{\{00.2\}} = \sum_{k=12}^{18}\left(\sum_{l=10}^{27}\left(I(k,l)\int_{\alpha=i*k}^{i(k+1)}\int_{\beta=i*l}^{i(l+1)}\sin\alpha.d\beta.d\alpha\right)+\sum_{l=56}^{63}\left(I(k,l)\int_{\alpha=i*k}^{i(k+1)}\int_{\beta=i*l}^{i(l+1)}\sin\alpha.d\beta.d\alpha\right)\right)$$

$$\text{.....} = \sum_{k=12}^{18}\left(\sum_{l=10}^{27}\left(I(k,l).i.\left[\cos(i.k)-\cos(i(k+1))\right]\right)+\sum_{l=56}^{63}\left(I(k,l).i.\left[\cos(i.k)-\cos(i(k+1))\right]\right)\right)$$

Then the volume fraction of twinning at a given applied strain ε is:

Eq. 28 $$\upsilon_{twinning} = \upsilon_{\{00.2\}}(\varepsilon) - \upsilon^{init}_{\{00.2\}}$$

The initial volume fraction $\upsilon^{init}_{\{00.2\}} = 0.0051$, which means that 0.5% of grains are oriented such as their basal planes {00.2} are close to RD. Figure 92 is the evolution of the computed VFT as a function of the applied plastic strain. After 15.9% plastic strain, approximately 32% of the volume of the material is composed of twins.

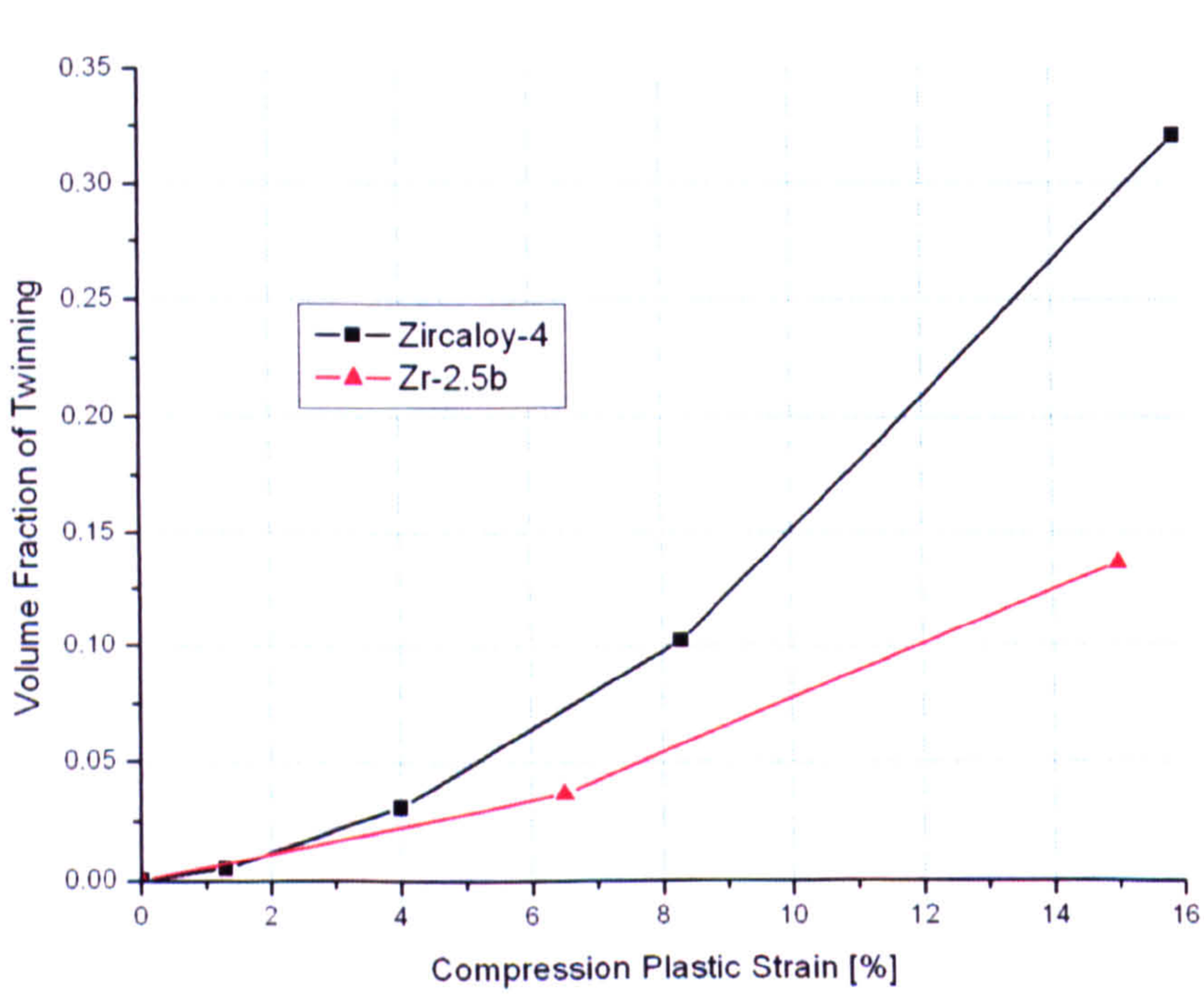

Figure 92 Volume fraction of twinned grains as a function of the applied strain for RD compression in Zry-4 and AD compression in Zr-2.5%Nb

For compression of Zr-2.5%Nb along the axial direction, the texture changes also indicate twinning activation and one can compute the volume fraction of twinning from the pole figures. With similar considerations a window of twinned grains was defined in the basal

pole figures, with a radial width of +/- 35° and an azimuthal width of +/- 30° from the AD pole. The results are shown on Figure 92. After 15% of plastic strain, 13.6% of the volume is composed of twins. It is substantially less than what was experienced in Zircaloy-4 during RD compression. The initial texture is different in the two materials and it can be a factor in the twinning activation. However the texture is much stronger in Zr-2.5Nb so intuitively it doesn't seem to justify the smaller amount of twinning. Another difference is the grain size and shape: the grains in Zry-4 are quite equiaxed whereas they have a platelet shape with a very small dimension radially in the Zr-2.5%Nb pressure tube. It has been demonstrated before that in small grain materials, twinning is not favoured [72]. Moreover, twins created in small grains have less volume available for propagation and a same volume fraction of twinning requires more twins in a fine grained material than in a coarse grained one. Finally Zr-2.5%Nb is dual phase and the second phase might have a constraint effect that doesn't encourage twinning in the α grains.

The maximum longitudinal strain from twinning in a polycrystal is given by the equation $\varepsilon_{twin} \approx \sqrt{1/2}\ s\upsilon_{twin}$ [43, 86]. The contribution of tensile twinning to the plastic strain can be thus calculated from the volume fraction of twinning and with the shear strain $s = 0.167$ for tensile twinning in zirconium (as computed in section 3.2.3.b). Figure 93 shows the partitioning of the plastic strain from tensile twinning and from the other modes (assumed to be slip modes only) during RD compression of Zry-4. Initially the strain is mostly assumed by slip. At 15.9% of plastic strain, tensile twinning is responsible for a strain of 3.78%, which means that around 24% of the plastic strain has been provided by tensile twinning alone.

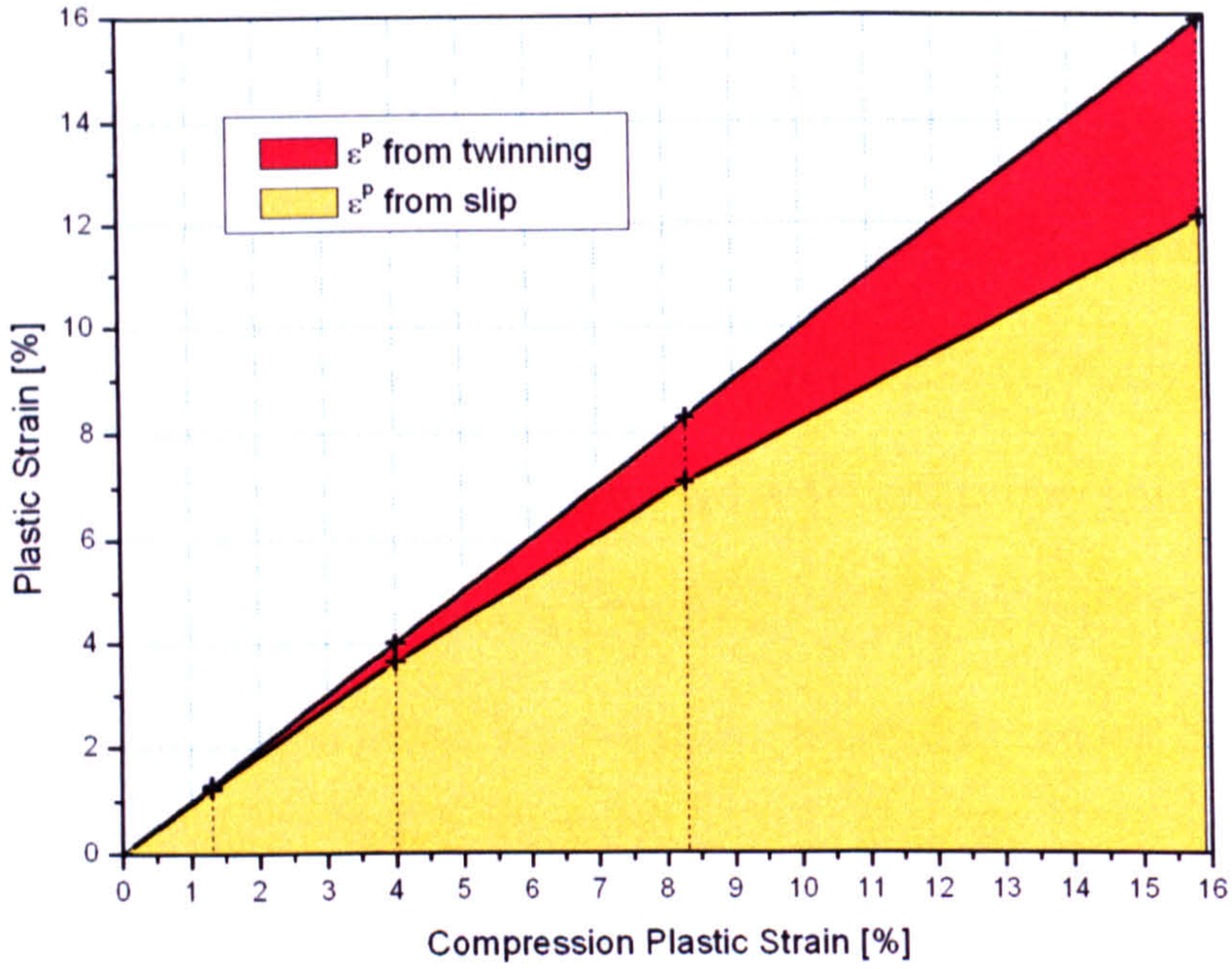

Figure 93 Proportion of the plastic strain provided by twinning and slip during RD compression of Zry-4.

The method of calculation of the VFT doesn't allow discrimination between nucleation and propagation of twinning, as VFT is purely a volume quantity and it is not indicative of the actual number of twins or their average size.

A good topic for future work would be to carry out some EBSD mapping on compressed samples to try and determine the VFT with a micrographic approach. It would also help getting an idea of how the VFT is shared between twinned grains. A limitation in this approach would be the difficulty of obtaining good quality surface for good quality Kikuchi patterns and a high rate of indexing necessary for mapping. There is also the possibility that the surface preparation can introduce artefacts. The technique would probably be valid for relatively high levels of deformation.

7.4 Conclusion

For all types of compression tests and on both materials, it was observed that the basal poles tend to align towards the compression direction. The texture changes are abrupt when Zry-4 and Zr-2.5%Nb are compressed in directions deprived of basal reflections. It is

believed that twinning is mostly responsible for such reorientations. In the other cases it is probably due to a combination of slip and twinning. For uniaxial tests that have common features with the mechanical loading experienced by the material during the manufacturing process, the texture changes are small. Indeed the initial texture is already close to a stabilised texture for these mechanical loadings.

Assuming that the new basal intensities along the compression directions that appeared during radial and axial compression in Zry-4 and Zr-2.5%Nb are a result of twinning, the volume fraction of twinned grains was computed at different levels of plastic strain. It seems that twinning is more activated in Zry-4 than in Zr2.5%Nb: after 15% plastic strain, twins represent approximately 30% of the volume of Zry-4 while Zr-2.5%Nb counts only 14%. The different initial textures and grain shapes can justify this observation. It could also be that in Zr-2.5%Nb the second phase introduces different constraints on the α grains which activate less twinning as a consequence.

Conclusions

This thesis aimed to shed more light on the mechanisms of deformation in zirconium alloys, and more specifically in Zircaloy-4 and Zr-2.5%Nb. This study has important applications both for optimising manufacturing and for assessing in-service life of components, i.e. increasing safety levels and efficiency by improving the components properties and reducing the factors of safety. Texture and deformation are highly intertwined and affect each other. Understanding this relationship can help find adequate manufacturing processes so that the resulting texture improves the service life. Although the experiments and modelling reported in this thesis were not carried out in the same environmental conditions as those found in the core of a nuclear reactor, they are necessary steps towards a good evaluation of the mechanical behaviour in service conditions. Before carrying out the same tests under irradiation (which would imply complicated measures regarding safety, sample manipulations, etc...) and temperature, it is important to gain expertise in more simple experimental conditions.

The main experimental procedure consisted of in-situ unixaxial compression on Zry-4 rolled plate and Zr-2.5%Nb tube: at different levels of applied stress (or strain), the elastic strains relative to the initial state were derived from diffraction measurements. This was performed for several diffraction reflections in order to evaluate the influence of the grains crystal orientations on their mechanical behaviour. The microscopic responses of the α phase were qualitatively similar for both the single and dual phase alloys. In the elastic regime, all the α phase reflections showed similar behaviours as expected from the low crystal anisotropy in hcp materials. In the compression direction, the lattice strain in the prismatic reflection saturated relatively early while the basal reflections were quickly under more load than the aggregate and yielded at higher stress. These results evidenced low elastic and a strong plastic anisotropy in the α grains. After unloading at around 10%

total strain, the relative intergranular residual strains could reach 0.2% to 0.5%. The results differed quantitavely for a given material depending on the compression direction, which indicates that texture is affecting the local behaviours. The Zr2.5%Nb was studied before and after heat treatment. It was found that in both cases, the second phase was very hard. This result disagrees with the assumption made by some authors that it is a soft phase.

Texture was also responsible for bringing the crystal anisotropy to the macroscopic level Tensile twinning was identified in both alloys as a major deformation mechanism. The peak intensity variations observed in the diffraction spectra during compression along the processing directions deprived from {00.2} reflections (rolling and axial directions for Zircaloy-4 and Zr-2.5%Nb respectively) were the first indicator. During compression the intensity of {10.0} decreased while that of {00.2} increased in the spectra collected in the compression directions. It was then confirmed by texture measurements performed at different levels of plastic strain: basal intensities were transferred to the compression direction. Although slip can introduce some texture changes, only twinning can explain the abrupt changes observed in these cases. For compression along the other directions, the texture changes are less drastic, which is indicative that less twinning is activated. To date there is little evidence in the literature of twinning in the dual phase Zr-2.5%Nb. An analysis was performed on the basal pole figures to obtain more quantitative information about the amount of twinning. It was computed that after a compression of 15% plastic strain along RD and AD respectively, tensile twins represent around 30% of the volume in Zircaloy-4 while they account for only 13% of the volume of Zr-2.5%Nb. It remains to be investigated whether this difference is a result of the presence of the second phase or is governed by other characteristics such as texture or grain shape. For a compression test along RD on Zry-4, the prismatic reflection showed a sudden relaxation at the early stages of twinning. It was hypothesised that twinning nucleation might have happened in a significant proportion of potential parent grains over a short period of time, and that the

strain relaxation associated with nucleation would have been transferred from the grain level to the average family reflection. After this nucleation period, most of the mechanism of twinning would be propagation.

An Elasto-Plastic Self Consistent (EPSC) model was used in order to simulate the compression of Zry-4. The model was used to solve an inverse problem and find the parameters of crystal plasticity that yield the best agreement between computed and experimental data. The refinement was not successful at determining a set of parameters common for all compression tests. Some reasons were discussed as well as some ways of improving model fitting. However the best set of parameters found for compression along the normal direction of the plate was in good agreement with what was read in the literature for other single phase alloys.

The model was also used as a novel approach for dealing with a different problem met in diffraction for stress measurements: how to derive the macroscopic stresses from the diffraction elastic strains. The result showed that some techniques commonly used in the literature give errors of around 15%.

Future work

The work presented in this thesis can be extended in several directions, and here are a few tracks that would generate good future work.

Several authors mention that the strain rate affects the deformation mechanisms and some of the experimental results presented in this thesis suggest that the effect would be visible in the way the elastic strain is partitioned between the diffraction reflections. It would be interesting to run a set of uniaxial loading tests in situ and at different strain rates. To cover a large range of strain rates, a combination of neutron and synchrotron radiation could be used: the former for the slow tests and the latter for the fast tests. The tests would have to be run in a continuous mode, i.e. without holds, and the diffraction measurements would be averages over a small range of stress and strain.

The mechanism of twinning and its nucleation could be studied in more detail by performing diffraction measurements with a fine measurement increment. This would require the use of a technique with a good time resolution, such as synchrotron diffraction. This would help understand how the load is shared between the grains at the onset of twinning. To see the effect on the mesoscopic scale (i.e., at the level of families of grains), twinning would have to be easily activated on a large scale, so the compression tests would have to be performed along a direction deprived from basal reflection. With the recent and continuous improvements in tomography techniques, we can also imagine setting up a microtomography experiment to spot twins at the early stage of the mechanism. Combined with diffraction this could give a better idea of the amount of relaxation experienced by the grains during twin nucleation.

As demonstrated in this thesis, there are several limitations in the EPSC model in its present form. Recently some improvements have been brought, particularly regarding the way twinning is modelled. By applying these upgrades, it would be interesting to see how

the modelling of Zry-4 is improved. Some authors have also developed models for two phase materials which could be applied to simulating the deformation of Zr-2.5%Nb for comparison with the single phase Zry-4. An interesting extension to the dual phase model would consist of implementing the new twinning model. Finally, there is still a lack in the way the inverse problem is solved to find the hardening parameters that yield the best agreement with the experimental data. It would be very useful to develop a search method, using for example a genetic algorithm optimisation method.

Appendix A - Considerations on diffraction

A.1 Fitting the diffraction data from HIPPO

The refinement procedure for fitting the HIPPO diffraction data is substantially more complicated than that of ENGIN-X spectra. Indeed a set of parameters must yield a good fit of 98 histograms. The process is comprised of several steps as described below:

1. Refine the background for each histogram (modelled by a GSAS function type 1 with 8 terms).
2. Switch to LeBail mode and refine the lattice parameters with the background fixed.
3. Refine simultaneously the lattice parameters, the background and the DIFC.
4. Refine the DIFA only.
5. Refine the width parameter σ_1.
6. Switch to Rietveld mode and refine the background with the profile and DIFC coefficients fixed.
7. Insert the zero pole figure constraint.
8. Refine the spherical harmonics coefficients up to the 6^{th} order.
9. Refine the isotropic displacement factor and the atomic position with SH coefs fixed.
10. Repeat steps 9 and 10 with incrementally higher SH coefficients if necessary

We would like to thank Dr. S.Vogel at LANSCE for providing a routine including all these steps.

Note: DIFA, DIFC and ZERO are the coefficients used to link the d-spacing (d) to the time of flight (TOF) via the relationship:

$TOF=DIFA*d^2+DIFC*d+ZERO$

Appendix B - Considerations on the EPSC modelling

B.1 Derivation of the self consistent equation

The basic system of equations is:

- the aggregate incremental constitutive equation:

$$\dot{\Sigma} = L : \left(\dot{\mathrm{E}} - \mathrm{A}\dot{T}\right) \qquad \textit{Eq. 7-29}$$

- the crystal incremental constitutive equation:

$$\dot{\sigma} = L_c : \left(\dot{\varepsilon} - \alpha\dot{T}\right) \qquad \textit{Eq. 7-30}$$

- the equation for grain/matrix interaction:

$$\dot{\sigma} - \dot{\Sigma} = -\tilde{L} : \left(\dot{\varepsilon} - \dot{\mathrm{E}}\right) \qquad \textit{Eq. 7-31}$$

- the assumption that the aggregate is represented by the grains average:

$$\dot{\Sigma} = \left\langle \dot{\sigma} \right\rangle \qquad \textit{Eq. 7-32}$$

Combining Eq. 7-29 and Eq. 7-30 into Eq. 7-31:

$$\dot{\varepsilon} = \left(L_c + \tilde{L}\right)^{-1} : \left(L + \tilde{L}\right) : \dot{\mathrm{E}} + \left(L_c + \tilde{L}\right)^{-1} : \left(L_c\alpha - L\mathrm{A}\right)\dot{T} \qquad \textit{Eq. 7-33}$$

$$\dot{\varepsilon} = A_c : \dot{\mathrm{E}} + \left(L_c + \tilde{L}\right)^{-1} : \left(L_c\alpha - L\mathrm{A}\right)\dot{T}$$

Where A_c is called Hill's 4th order concentration tensor

Note 1: One could also have used $\dot{\mathrm{E}} = \left\langle \dot{\varepsilon} \right\rangle$ instead of Eq. 7-32. However this leads to using inverse of L_c for each grain which brings inversion problems if some L_c are singular. Hutchinson recommends using the previous formulation (see [33] p253).

Note 2: In his code C.Tomé uses a self consistent equation slightly different: $L = \left\langle L_c : A_c \right\rangle \left\langle A_c \right\rangle^{-1}$. The result is the same as when convergence is reached, $\langle A_c \rangle = 0$. This formulation helps the convergence.

B.2 Schematic flow chart of the EPSC scheme

Flow charts describing the EPSC scheme are presented on the next to pages. The second chart develops the equations.

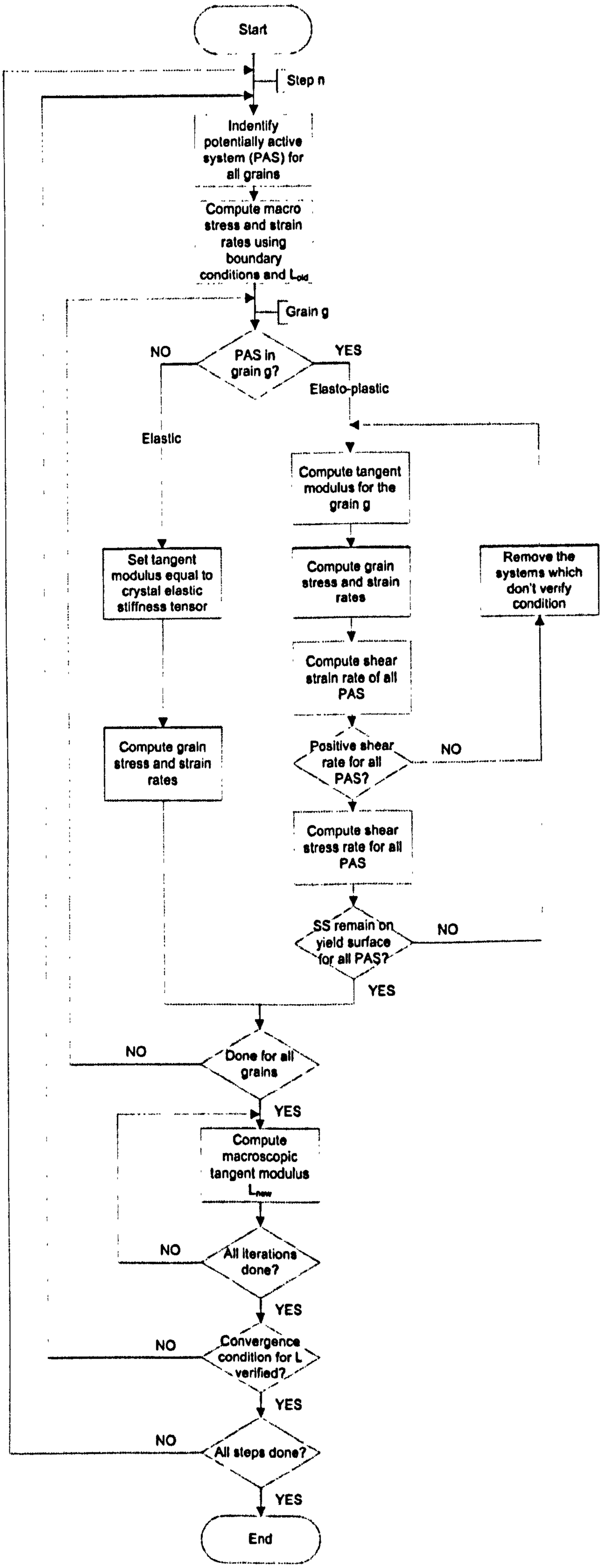
Start
Step n
Indentify potentially active system (PAS) for all grains
Compute macro stress and strain rates using boundary conditions and L_{old}
Grain g
PAS in grain g?
NO
YES
Elasto-plastic
Elastic
Compute tangent modulus for the grain g
Set tangent modulus equal to crystal elastic stiffness tensor
Compute grain stress and strain rates
Remove the systems which don't verify condition
Compute shear strain rate of all PAS
Positive shear rate for all PAS?
NO
Compute grain stress and strain rates
Compute shear stress rate for all PAS
SS remain on yield surface for all PAS?
NO
YES
NO
Done for all grains
YES
Compute macroscopic tangent modulus L_{new}
NO
All iterations done?
YES
NO
Convergence condition for L verified?
YES
NO
All steps done?
YES
End

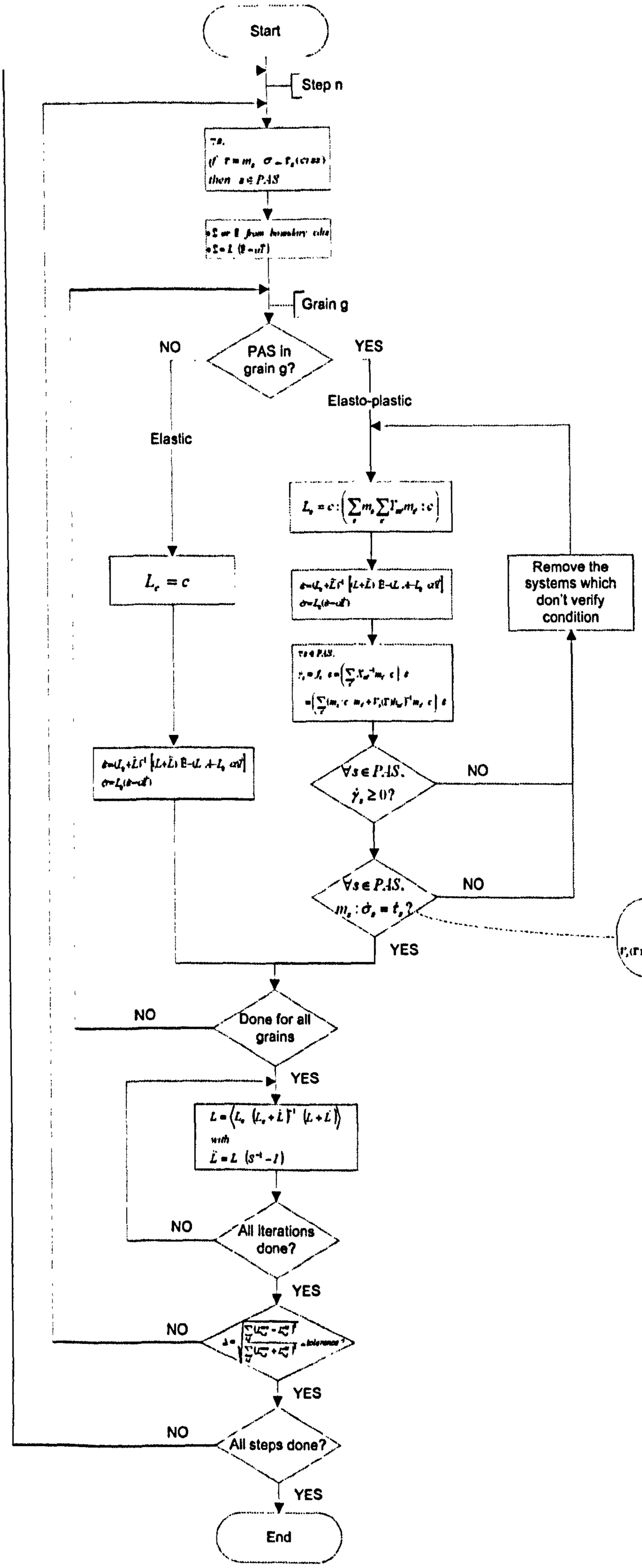
Start
Step n
Grain g
PAS in grain g?
NO
YES
Elastic
Elasto-plastic
$L_c = c$
$L_s = c:\left(\sum_s m_s \sum_\sigma \Gamma_\sigma m_s : c\right)$
Remove the systems which don't verify condition
$\forall s \in PAS.$ $\dot{\gamma}_s \geq 0$?
NO
$\forall s \in PAS.$ $m_s : \dot{\sigma}_s = t_s$?
NO
YES
$L = \langle L_c \left(I + \tilde{L}\Gamma\right)^{-1} \left(I + \tilde{L}\right) \rangle$
with
$\tilde{L} = L\,(s^{-1} - I)$
Done for all grains
NO
YES
All iterations done?
NO
YES
All steps done?
NO
YES
End

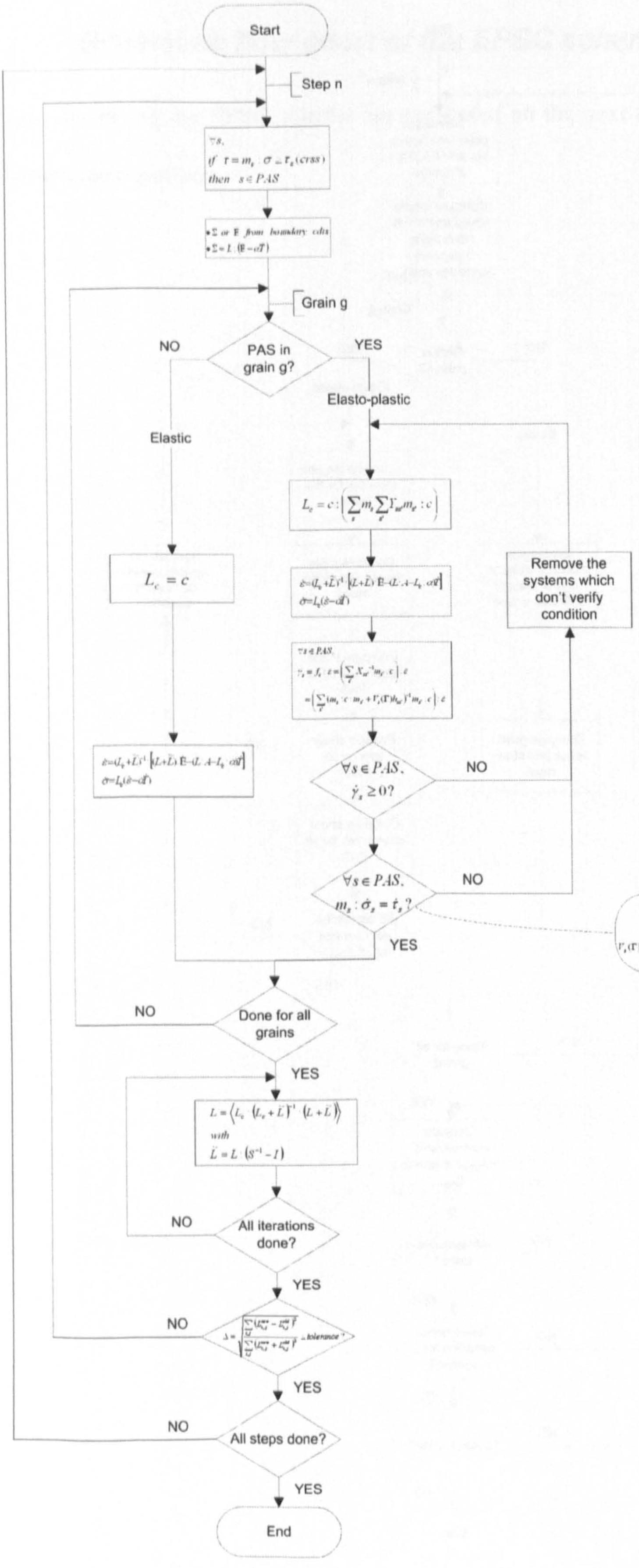
Start
Step n
$\forall s,$
$if\ \ \tau = m_s : \sigma = \tau_s(crss)$
$then\ \ s \in PAS$
$\bullet \Sigma$ or $\dot{\mathbf{E}}$ from boundary cdts
$\bullet \dot{\Sigma} = L : (\dot{\mathbf{E}} - \alpha \dot{T})$
Grain g
NO
PAS in grain g?
YES
Elasto-plastic
Elastic
$L_c = c : \left(\sum_s m_s \sum_{s'} \Gamma_{ss'} m_{s'} : c \right)$
$L_c = c$
$\dot{\varepsilon} = (L_0 + \tilde{L})^{-1} : \left[(L + \tilde{L}) : \dot{\mathbf{E}} - L : A - L_0 : \alpha \dot{T} \right]$
$\dot{\sigma} = L_0 : (\dot{\varepsilon} - \alpha \dot{T})$
$\forall s \in PAS,$
$\dot{\gamma}_s = f_s : \varepsilon = \left(\sum_{s'} X_{ss'}^{-1} m_{s'} : c \right) : \varepsilon$
$= \left(\sum_{s'} (m_s : c : m_{s'} + \Gamma_s(\Gamma) h_{ss'})^{-1} m_{s'} : c \right) : \varepsilon$
$\forall s \in PAS,$
$\dot{\gamma}_s \geq 0 ?$
NO
Remove the systems which don't verify condition
$\forall s \in PAS,$
$m_s : \dot{\sigma}_s = \dot{\tau}_s ?$
NO
YES
$\tau_s = \sum_{s'} \Gamma_s(\Gamma) h_{ss'} \tilde{\gamma}_s$
and
$\Gamma_s(\Gamma) = \frac{\Delta \tau_s}{\Delta \Gamma} = \theta_1 + \left(\theta_0 - \theta_1 + \Gamma \frac{\theta_1 \theta_0}{\tau_s} \right) e^{-\Gamma \frac{\theta_0}{\theta_1}}$
NO
Done for all grains
YES
$L = \left\langle L_0 : \left(L_0 + \tilde{L} \right)^{-1} : \left(L + \tilde{L} \right) \right\rangle$
$with$
$\tilde{L} = L : \left(S^{-1} - I \right)$
NO
All iterations done?
YES
NO
$\Delta = \sqrt{\frac{\sum_{ij} (L_{ij}^{n+1} - L_{ij}^{n})^2}{\sum_{ij} (L_{ij}^{n+1} + L_{ij}^{n})^2}} < tolerance$
YES
NO
All steps done?
YES
End

B.3 Link between the coordinate systems

There are several coordinate systems used at different stages in the model. The sample is referenced by the three processing directions {X,Y,Z}. In the case of the rolled plate of Zry-4, the system is {RD,TD,ND}. The EPSC scheme has its own coordinate system: $\{X_1,X_2,X_3\}$. Finally the texture of the material is given with reference to a measurement coordinate system {x,y,z} (corresponding to the chamber coordinate system for an EBSD measurement for example). It is very important to understand how these coordinate systems are linked so that the results of the simulation can be comparable to experimental data.

The texture information consist of a weight file where the Euler angles are referenced to {x,y,z}. Inputing the texture information into the model is thus results in imposing that $\{X_1,X_2,X_3\}\equiv\{x,y,z\}$. On the other hand {x,y,z} is linked to {X,Y,Z} by the way the sample was oriented during the texture measurement.

In the EPSC model, the directions for which the lattice strains are exported are defined with reference to the EPSC coordinate system $\{X_1,X_2,X_3\}$ using a latitude angle χ from X_3 and a longitude angle η from X_1. In the case of the modelling of Zircaloy-4 presented in Chapter 6, we have the relations:

Sample	χ	η	EPSC
TD	90	0	X1
RD	90	90	X2
ND	0	0	X3

B.4 Matlab GUI

To ease the refinement of the EPSC hardening parameters, a Graphical User Interface (GUI) was developed using Matlab. It allowed selecting the deformation modes to use for the calculation and setting their hardening parameters. The EPSC could then be run from the GUI and the results of the simulation were represented along with the experimental data. The graphs could be selected as macroscopic or microscopic flow curves. The effect of changing the variables on the responses could be thus directly and easily seen.

A screenshot of the GUI is shown in Figure 94.

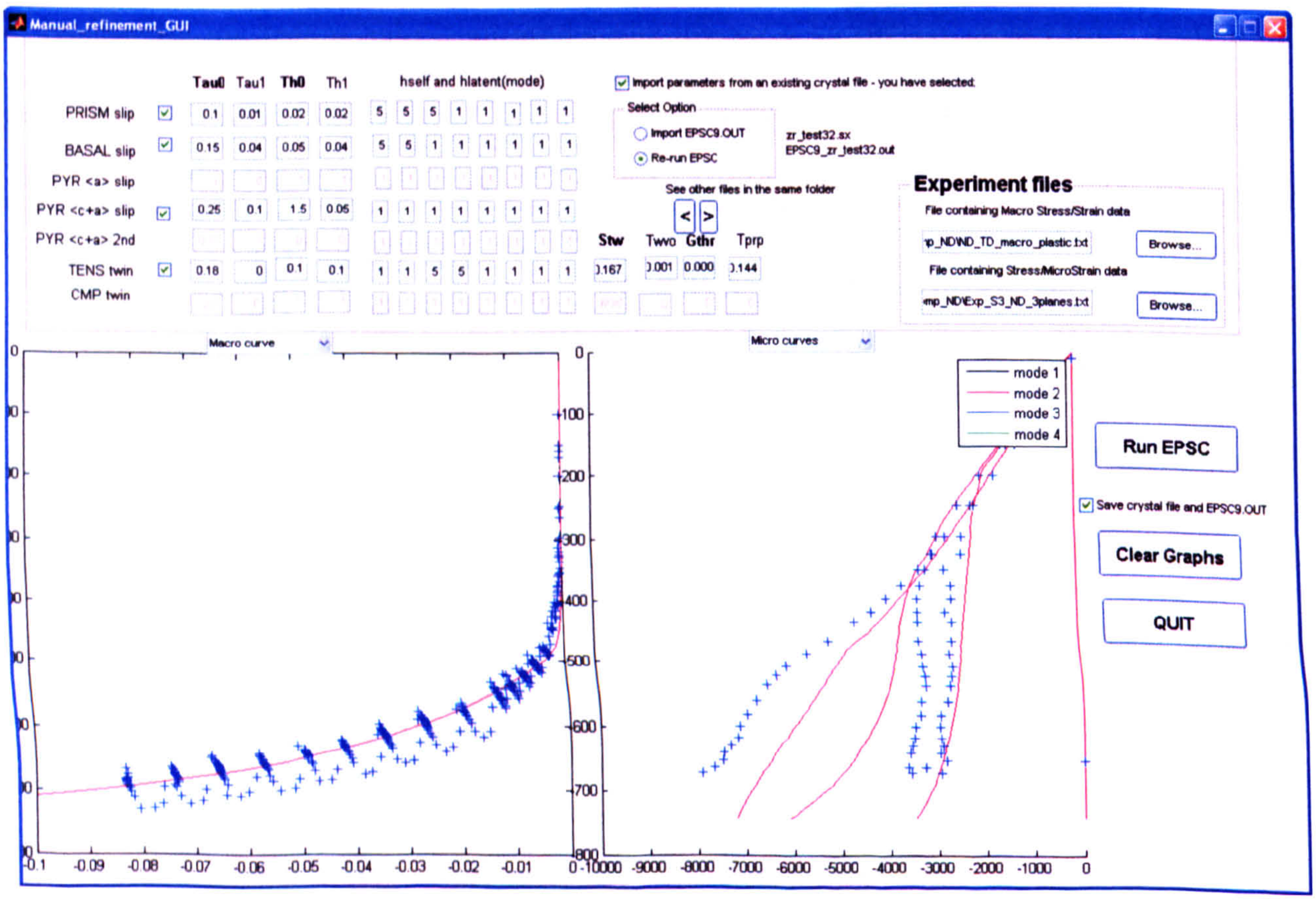

Figure 94 Matlab GUI for refining the EPSC hardening parameters manually.

Appendix C - Miller-Bravais indices

For Hexagonal systems, the Miller-Bravais indexing is generally used to reference crystallographic planes and directions. This system differs slightly from the Miller indices. The most obvious difference is that it counts four indices instead of the usual three. The reason for having a new system is due to the symmetry of the crystal and the non orthogonality of the coordinate system in a hexagonal unit cell: the $\mathbf{a_1}$ and $\mathbf{a_2}$ unit vectors are at 120°. As a result only part of the symmetry-equivalent planes and directions are represented by a simple indices permutations in the Miller formalism.

For referencing planes Bravais used (hkil), where i=–h–k. There is also a possibility of indexing the same plane with (hk.l). In this work we chose the latter option. The dot acts as a reminder that the cell is hexagonal. Its role is important especially when considering set of planes equivalent by symmetry using the notation {hk.l}. Indeed in the Bravais notation, {hkil} or {hk.l} represent all the equivalent planes, whereas in Miller indexing, {hkl} doesn't count all of them.

To represent the (hkil) plane in the unit cell:

- If the indices are non zero, the plane intercepts the axis a_1, a_2, a_3 and c at a/h, a/k, a/i, and c/l respectively (see Figure 95).
- If there are zero indices, the plane is parallel to the corresponding axis.

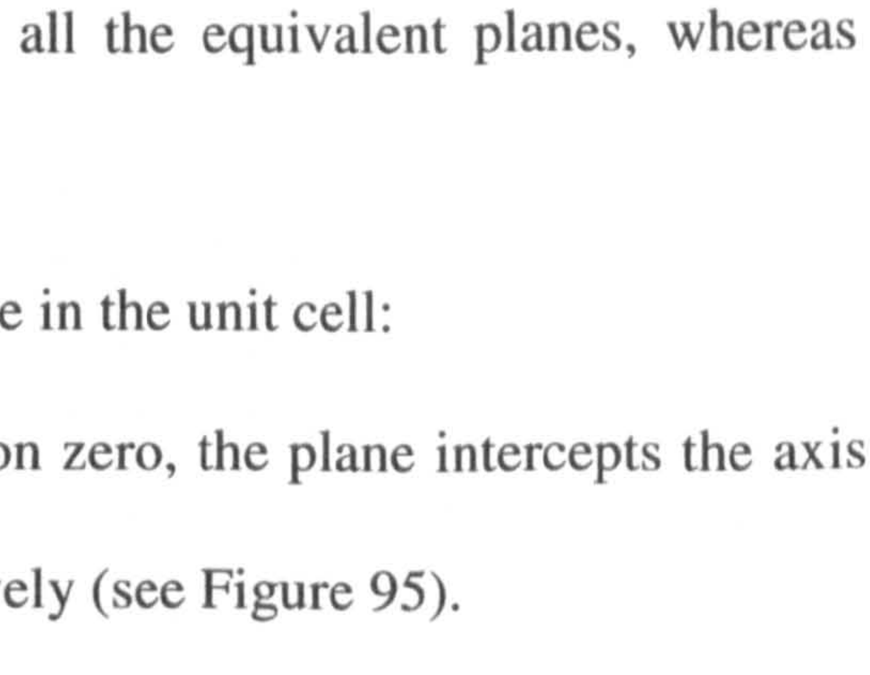

Figure 95 Lattice plane indexing in the Miller-Bravais convention

The Bravais referencing of crystallographic directions is much less intuitive than for planes. It is very important to be aware that a [uvtw] direction will generally not be normal to the (uvtw) plane. This is a major difference with the classic Miller indexing.

If [UVW] are the Miller indices and [uvtw] the Miller-Bravais indices for a same direction $\vec{n}$, we have the relationships:

$\vec{n} = U\vec{a}_1 + V\vec{a}_2 + W\vec{c}$ and $\vec{n} = u\vec{a}_1 + v\vec{a}_2 + t\vec{a}_3 + w\vec{c}$

And:

$$\begin{aligned} U &= u - t \\ V &= v - t \\ W &= w \end{aligned} \quad \text{and} \quad \begin{aligned} u &= (2U - V)/3 \\ v &= (2V - U)/3 \\ t &= -(u + v) \\ w &= W \end{aligned}$$

References

[1] I. C. Noyan, J. B. Cohen, *Residual Stress measurement by Diffraction and interpretation,* Springer/Sci-Tech/Trade, 1987.

[2] P. P. Ewald, *50 years of X ray Diffraction,* 1962.

[3] W. L. Bragg, J. J. Thomson, *The diffraction of short electromagnetic waves by a crystal,* Proceedings of the Cambridge Philosophical Society 17, 1914, pp.43-57.

[4] H. P. Klug, L. E. Alexander *X-Ray Diffraction Procedures: For Polycrystalline and Amorphous Materials,* John Wiley & sons, 1954.

[5] M. T. Hutchings, *Introduction to the characterization of residual stress by neutron diffraction,* CRC Press, Boca Raton, FL, 2005.

[6] A. D. Krawitz, *Introduction to diffraction in materials science and engineering,* John Wiley, New York, 2001.

[7] M. R. Daymond, M. A. M. Bourke, R. B. V. Dreele, B. Clausen, T. Lorentzen, *Use of Rietveld refinement for elastic macrostrain determination and for evaluation of plastic strain history from diffraction spectra,* Journal of Applied Physics 82, 1997, pp.1554-1562.

[8] M. R. Daymond, *The determination of a continuum mechanics equivalent elastic strain from the analysis of multiple diffraction peaks,* Journal of Applied Physics 96, 2004, pp.4263-4272.

[9] J. R. Santisteban, M. R. Daymond, J. A. James, L. Edwards, *ENGIN-X: A third-generation neutron strain scanner,* Journal of Applied Crystallography 39, 2006, pp.812-825.

[10] S. I. Campbell, F. A. Akeroyd, C. M. Moreton-Smith, *Open GENIE - Analysis and Control,* Condensed Matter, arXiv:cond-mat/0210442v2, 2002.

[11] A. C. Larson, R. B. V. Dreele, *General Structure Analysis System (GSAS),* Los Alamos National Laboratory Report, LAUR 86-748, 2004.

[12] H. M. Rietveld, *A Profile Refinement Method for Nuclear and Magnetic Structures,* Journal of Applied Crystallography 2, 1969, pp.65-&.

[13] A. W. Thompson, M. I. Baskes, W. F. Flanagan, *Dependence of Polycrystal Work-Hardening on Grain-Size,* Acta Metallurgica 21, 1973, pp.1017-1028.

[14] E. O. Hall, *The Deformation and Ageing of Mild Steel .3. Discussion of Results,* Proceedings of the Physical Society of London Section B 64, 1951, pp.747-753.

[15] N. J. Petch, *The Cleavage Strength of Polycrystals,* Journal of the Iron and Steel Institute 174, 1953, pp.25-28.

[16] H. J. Bunge, *3-Dimensional Texture Analysis,* International Materials Reviews 32, 1987, pp.265-291.

[17] E. Pantos, W. Kockelmann, L. C. Chapon, L. Lutterotti, S. L. Bennet, M. J. Tobin, J. F. W. Mosselmans, T. Pradell, N. Salvado, S. Buti, *Neutron and X-ray characterisation of the metallurgical properties of a 7th century BC Corinthian-type bronze helmet,* Nuclear Instruments and Methods in Physics Research Section B: Beam Interactions with Materials and Atoms 239, 2005, pp.16-26.

[18] E. Tenckhoff, *Deformation Mechanisms, Texture and Anisotropy in Zirconium and Zircaloy,* ASTM, Philadelphia, 1988.

[19] H. J. Bunge, M. Humbert, P. I. Welch, *Texture Transformation,* Textures and Microstructures 6, 1984, pp.81-96.

[20] W. G. Burgers, *On the process of transition of the cubic-body-centered modification into the hexagonal-close-packed modification of zirconium,* Physica 1, 1934, pp.561-586.

[21] V. Perovic, G. C. Weatherly, *The Beta to Alpha Transformation in a Zr-2.5 Wt-Percent Nb Alloy,* Acta Metallurgica 37, 1989, pp.813-821.

[22] H. R. Wenk, I. Lonardelli, D. Williams, *Texture changes in the hcp -> bcc -> hcp transformation of zirconium studied in situ by neutron diffraction,* Acta Materialia 52, 2004, pp.1899-1907.

[23] H. Hu, *Texture of Metals,* Texture 1, 1974, pp.233-258.

[24] K. Linga Murty, I. Charit, *Texture development and anisotropic deformation of zircaloys,* Progress in Nuclear Energy 48, 2006, pp.325-359.

[25] D. G. Carr, M. I. Ripley, T. M. Holden, D. W. Brown, S. C. Vogel, *Residual stress measurements in a zircaloy-4 weld by neutron diffraction,* Acta Materialia 52, 2004, pp.4083-4091.

[26] V. Randle, O. Engler, *Introduction to Texture Analysis: Macrotexture, Microtexture and Orientation Mapping,* Gordon and Breach Science Publishers, 2000.

[27] R. G. Ballinger, *The Anisotropic Mechanical Behavior of Zircaloy-2,* Massachussetts Institute of Technology, 1979.

[28] J. D. Eshelby, *The Determination of the Elastic Field of an Ellipsoidal Inclusion, and Related Problems,* Proceedings of the Royal Society of London. Series A, Mathematical and Physical Sciences 241, 1957, pp. 376-396.

[29] E. Kröner, *Zur plastischen verformung des vielkristalls (On the plastic deformation of polycrystals),* Acta Metallurgica 9, 1961, pp.155-161.

[30] B. Budianski, T. T. Wu, *Theoretical prediction of plastic strains of polycrystals,* Proc. 4th U.S. Nat. Cong. Appl. Mech., ASME 1962, pp.1175.

[31] O. Fassi-Fehri, A. Hihi, M. Berveiller, *Multiple site self consistent scheme,* International Journal of Engineering Science 27, 1989, pp.495-502.

[32] P. A. Turner, N. Christodoulou, C. N. Tome, *Modeling the mechanical response of rolled Zircaloy-2,* International Journal of Plasticity 11, 1995, pp.251-265.

[33] J. W. Hutchinson, *Elastic-Plastic Behaviour of Polycrystalline Metals and Composites,* Proceedings of the Royal Society of London Series a-Mathematical and Physical Sciences 319, 1970, pp.247-271.

[34] P. A. Turner, C. N. Tome, *A study of residual stresses in Zircaloy-2 with rod texture,* Acta Metallurgica et Materialia 42, 1994, pp.4143-4153.

[35] J. Goldak, L. T. Lloyd, C. S. Barrett, *Lattice Parameters, Thermal Expansions, and Grüneisen Coefficients of Zirconium, 4.2 to 1130 K,* Physical Review 144, 1966, pp.478 LP - 484.

[36] E. S. Fisher, C. J. Renken, *Single-Crystal Elastic Moduli and the hcp to bcc Transformation in Ti, Zr, and Hf,* Physical Review 135, 1964, pp.A482 LP - A494.

[37] A. Akhtar, *Basal Slip in Zirconium,* Acta Metallurgica 21, 1973, pp.1-11.

[38] A. Akhtar, *Compression of Zirconium Single-Crystals Parallel to C-Axis,* Journal of Nuclear Materials 47, 1973, pp.79-86.

[39] E. Tenchoff, *Review of Deformation Mechanisms, Texture, and Mechanical Anisotropy in Zirconium and Zirconium Base Alloys,* Journal of ASTM International 2, 2005.

[40] F. Xu, R. A. Holt, M. R. Daymond, *Evidence for basal < a >-slip in Zircaloy-2 at room temperature from polycrystalline modeling,* Journal of Nuclear Materials 373, 2008, pp.217-225.

[41] U. F. Kocks, D. G. Westlake, *The Importance of Twinning for the Ductility of CPH Polycrystals,* Transactions of the Metallurgical Society of AIME 239, 1967, pp.1107-1109.

[42] W. F. Hosford, *The mechanics of crystals and textured polycrystals,* Oxford Science Publications, Oxford, 1993.

[43] S. G. Song, G. T. Gray, *Influence of temperature and strain rate on slip and twinning behavior,* Metallurgical and Materials Transactions A 26A, 1995, pp.2665-2675.

[44] R. J. McCabe, G. Proust, E. K. Cerreta, A. Misra, *Quantitative analysis of deformation twinning in zirconium,* International Journal of Plasticity In Press, Corrected Proof, 2008.

[45] B. Clausen, C. N. Tome, D. W. Brown, S. R. Agnew, *Reorientation and stress relaxation due to twinning: modeling and experimental characterization for Mg.,* Acta Materialia 56, 2008, pp.2456-2468.

[46] D. W. Brown, S. R. Agnew, M. A. M. Bourke, T. M. Holden, S. C. Vogel, C. N. Tome, *Internal strain and texture evolution during deformation twinning in magnesium,* Materials Science and Engineering a-Structural Materials Properties Microstructure and Processing 399, 2005, pp.1-12.

[47] R. A. Lebensohn, C. N. Tome, *A Study of the Stress State Associated with Twin Nucleation and Propagation in Anisotropic Materials,* Philosophical Magazine a-Physics of Condensed Matter Structure Defects and Mechanical Properties 67, 1993, pp.187-206.

[48] R. Y. Zhang, M. R. Daymond, R. A. Holt, *A finite element model of deformation twinning in zirconium,* Materials Science and Engineering a-Structural Materials Properties Microstructure and Processing 473, 2008, pp.139-146.

[49] S. G. Song, G. T. Gray, *Structural Interpretation of the Nucleation and Growth of Deformation Twins in Zr and Ti .1. Application of the Coincidence Site Lattice (Csl) Theory to Twinning Problems in Hcp Structures,* Acta Metallurgica Et Materialia 43, 1995, pp.2325-2337.

[50] H. Francillette, B. Bacroix, M. Gasperini, J. L. Bechade, *Effect of initial textures on deformation mechanisms and texture evolutions of Zr[alpha] polycrystals deformed by channel-die compression tests,* Materials Science and Engineering A 234-236, 1997, pp.974-977.

[51] H. Francillette, A. Gavrus, R. A. Lebensohn, *A constitutive law for the mechanical behavior of Zr 702[alpha],* Journal of Materials Processing Technology 142, 2003, pp.43-51.

[52] R. A. Holt, M. R. Daymond, F. Xu, S. Cai, *Inter-granular and Inter-phase Constraints in Zirconium Alloys,* 15th International Symposium on Zirconium in the Nuclear Industry, Sunriver, USA, 2007.

[53] E. C. Oliver, M. R. Daymond, P. J. Withers, *Effects of texture and anisotropy on intergranular stress development in zirconium,* Icotom 14: Textures of Materials, Pts 1and 2 495-497, 2005, pp.1553-1558.

[54] M. Kiran Kumar, C. Vanitha, I. Samajdar, G. K. Dey, R. Tewari, D. Srivastava, S. Banerjee, *Textural and microstructural developments during fabrication of Zr-2.5Nb pressure tubes,* Journal of Nuclear Materials 335, 2004, pp.48-58.

[55] K. Kapoor, D. Lahiri, S. V. R. Rao, T. Sanyal, N. Saibaba, B. P. Kashyap, *Texture evolution in two phase Zr-2.5 wt-%Nb through modified route,* Materials Science and Technology 20, 2004, pp.1281-1289.

[56] L. Ortiz, R. Martinez, *Zircaloy Welding in OPAL Reactor Reflecor Vessel,* 15th Pacific Basin Nuclear Conference, Sydney, 2006.

[57] ATI Wha Chang, *Reactor grade zirconium alloys for nuclear waste disposal,* Technical data sheet, www.alleghenytechnologies.com/wahchang.

[58] M. Grange, *Fragilisation du Zircaloy-4 par l'hydrogene: Comportement, mécanismes d'endommagement, interaction avec la couche d'oxyde, simulation numérique*, PhD Thesis, Ecole des Mines de Paris, Paris, 1998.

[59] B. F. Kammenzind, B. M. Berquist, R. Bajaj, P. H. Kreyns, D. G. Franklin, *The Long-Range Migration of Hydrogen Through Zircaloy in Response to Tensile and Compressive Stress Gradients,* Zirconium in the Nuclear Industry: Twelfth International Symposium, ASTM, 1998.

[60] U. F. Kocks, C. N. Tomé, H.-R. Wenk, *Texture and Anisotropy,* Cambridge University Press, 1998.

[61] H.-R. Wenk, L. Lutterotti, S. C. Vogel, *Texture analysis with the new HIPPO TOF diffractometer,* Nuclear Instruments and Methods in Physics Research A 515, 2003, pp.575-588.

[62] M. T. Jovanovic, Y. Ma, R. L. Eadie, *An SEM study of beta-phase decomposition during the annealing of Zr-2.5% Nb alloy,* Journal of Nuclear Materials 244, 1997, pp.141-146.

[63] 'CANTEACH' web site, http://canteach.candu.org/.

[64] G. Choudhuri, D. Srivastava, K. R. Gurumurthy, B. K. Shah, *Optimization of stress relief heat treatment of PWHR pressure tubes (Zr-2.5Nb alloy),* Journal of Nuclear Materials 2007.

[65] M. Kiran Kumar, I. Samajdar, N. Venkatramani, G. K. Dey, R. Tewari, D. Srivastava, S. Banerjee, *Explaining absence of texture development in cold rolled two-phase Zr-2.5 wt% Nb alloy,* Acta Materialia 51, 2003, pp.625-640.

[66] J. A. Dann, M. R. Daymond, L. Edwards, J. A. James, J. R. Santisteban, *A comparison between Engin and Engin-X, a new diffractometer optimized for stress measurement,* Physica B: Condensed Matter, Proceedings of the Third European Conference on Neutron Scattering 350, 2004, pp.E511-E514.

[67] D. W. Brown, S. R. Agnew, M. A. M. Bourke, T. M. Holden, S. C. Vogel, C. N. Tomé, *Internal strain and texture evolution during deformation twinning in magnesium,* Materials Science and Engineering: A - Measurement and Interpretation of Internal/Residual Stresses 399, 2005, pp.1-12.

[68] M. A. Gharghouri, G. C. Weatherly, J. D. Embury, J. H. Root, *Study of the mechanical properties of Mg-7.7at.% Al by in-situ neutron diffraction,* Philosophical Magazine A 79, 1999, pp.1671-1695.

[69] O. Muránsky, D. G. Carr, P. Sittner, E. C. Oliver, *In situ neutron diffraction investigation of deformation twinning and pseudoelastic-like behaviour of extruded AZ31 magnesium alloy,* International Journal of Plasticity In Press, Accepted Manuscript, 2008.

[70] G. M. Benites, A. F. Guillermet, G. J. Cuello, J. Campo, *Structural properties of metastable phases in Zr-Nb alloys I. Neutron diffraction study and analysis of lattice parameters,* Journal of Alloys and Compounds 299, 2000, pp.183-188.

[71] G. M. Benites, A. F. Guillermet, *Structural properties of metastable phases in Zr-Nb alloys II. Systematics of the atomic volumes and interatomic distances,* Journal of Alloys and Compounds 302, 2000, pp.192-198.

[72] A. Salina Rodriguez, J. H. Root, *Texture Evolution in Zr-2.5 Nb Deformed in Uniaxial Compression,* Textures and Microstructures 14, 1991, pp.1239-1244.

[73] S. Cai, M. R. Daymond, R. A. Holt, M. A. Gharghouri, E. C. Oliver, *Evolution of Interphase, Intergranular Stresses in Zr-2.5Nb during Room Temperature Deformation,* Materials Science and Engineering A In Press, Accepted Manuscript, 2008.

[74] S. L. Raghunathan, A. M. Stapleton, R. J. Dashwood, M. Jackson, D. Dye, *Micromechanics of Ti–10V–2Fe–3Al: In situ Synchrotron Characterisation and Modelling,* Acta Materialia 55, 2007, pp.6861-6872.

[75] A. M. Stapleton, S. L. Raghunathan, I. Bantounas, H. J. Stone, T. C. Lindley, D. Dye, *Evolution of Lattice Strain in Ti–6Al–4V During Tensile Loading at Room Temperature,* Acta Materialia 56, 2008, pp.6186-6196.

[76] M. R. Daymond, H. G. Priesmeyer, *Elastoplastic deformation of ferritic steel and cementite studied by neutron diffraction and self-consistent modelling,* Acta Materialia 50, 2002, pp.1613-1626.

[77] S. Matthies, G. W. Vinel, *On the Reproduction of the Orientation Distribution Function of Texturized Samples from Reduced Pole Figures Using the Conception of a Conditional Ghost Correction,* Physica Status Solidi B-Basic Research 112, 1982, pp.K111-K114.

[78] F. Xu, R. A. Holt, M. R. Daymond, *Modeling lattice strain evolution during uniaxial deformation of textured Zircaloy-2,* Acta Materialia 56, 2008, pp.3672-3687.

[79] D. Dye, H. J. Stone, R. C. Reed, *A two phase elastic-plastic self-consistent model for the accumulation of microstrains in Waspaloy,* Acta Materialia 49, 2001, pp.1271-1283.

[80] S. Cai, M. R. Daymond, R. A. Holt, *Modeling the room temperature deformation of a two-phase zirconium alloy,* Acta Materialia 57, 2009, pp.407-419.

[81] A. B. Jimenez, J. L. Lazaro, J. R. Dorronsoro, *Finding Optimal Model Parameters by Discrete Grid Search,* Innovations in Hybrid Intelligent Systems, Salamanca, Spain, 2008.

[82] F. Xu, *Lattice Strain and Texture Evolution during Room-Temperature Deformation of Zircaloy-2,* PhD Thesis, Queen's University, Kingston, CA, 2007.

[83] J. R. Santisteban, L. Fernandez, H. Corsco, R. L. Martinez, L. Boccanera, L. Edwards, J. A. James, M. Turski, *Post-weld heat treatment stress relaxation in Zircaloy 4 plasma welds,* Residual Stresses Vii 524-525, 2006, pp.491-496.

[84] S. Matthies, J. Pehl, H. R. Wenk, L. Lutterotti, S. C. Vogel, *Quantitative texture analysis with the HIPPO neutron TOF diffractometer,* Journal of Applied Crystallography 38, 2005, pp.462-475.

[85] S. C. Vogel, C. Hartig, L. Lutterotti, R. B. Von Dreele, H. R. Wenk, D. J. Williams, *Texture measurements using the new neutron diffractometer HIPPO and their analysis using the Rietveld method,* Powder Diffraction 19, 2004, pp.65-68.

[86] S. Mahajan, D. F. Williams, *Deformation Twinning in Metals and Alloys,* International Metallurgical Reviews 18, 1973, pp.43-61.